GROUND-BASED SIMULATOR INPUT DATA FOR ADVANCED TANDEM-ROTOR HELICOPTERS

Roman T. Lytwyn, et al

Boeing Vertol Company

Prepared for:

Army Air Mobility Research and Development Laboratory

January 1974

DISCLAIMERS

The findings in this report are not to be construed as an official Department of the Army position unless so designated by other authorized documents.

When Government drawings, specifications, or other data are used for any purpose other than in connection with a definitely related Government procurement operation, the United States Government thereby incurs no responsibility nor any obligation whatsoever; and the fact that the Government may have formulated, furnished, or in any way supplied the said drawings, specifications, or other data is not to be regarded by implication or otherwise as in any manner licensing the holder or any other person or corporation, or conveying any rights or permission, to manufacture, use, or sell any patented invention that may in any way be related thereto.

Trade names cited in this report do not constitute an official endorsement or approval of the use of such commercial hardware or software.

DISPOSITION INSTRUCTIONS

Destroy this report when no longer needed. Do not return it to the originator.

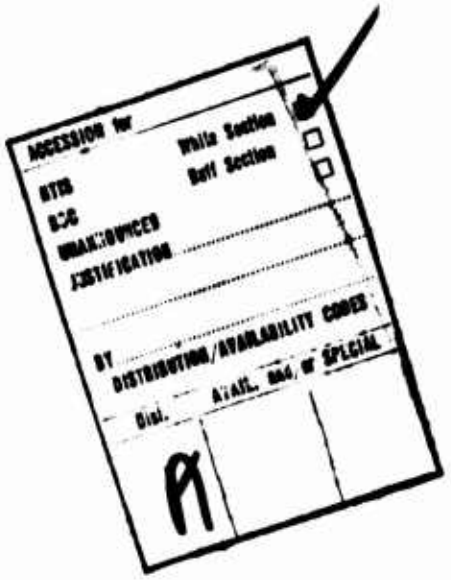

UNCLASSIFIED
Security Classification

AD 775 831

DOCUMENT CONTROL DATA - R & D

(Security classification of title, body of abstract and indexing annotation must be entered when the overall report is classified)

1. ORIGINATING ACTIVITY *(Corporate author)*
The Boeing Company, Vertol Division
Boeing Center, P.O. Box 16858
Philadelphia, Pennsylvania

2a. REPORT SECURITY CLASSIFICATION
Unclassified

2b. GROUP

3. REPORT TITLE

GROUND-BASED SIMULATOR INPUT DATA FOR ADVANCED TANDEM-ROTOR HELICOPTERS

4. DESCRIPTIVE NOTES *(Type of report and inclusive dates)*
Final Report

5. AUTHOR(S) *(First name, middle initial, last name)*

Roman T. Lytwyn
Fred White

6. REPORT DATE	7a. TOTAL NO. OF PAGES	7b. NO. OF REFS
January 1974	244	6

8a. CONTRACT OR GRANT NO.	9a. ORIGINATOR'S REPORT NUMBER(S)
DAAJ02-72-C-0095	USAAMRDL Technical Report 73-104
b. PROJECT NO. Task 1F162204AA4401	
c.	9b. OTHER REPORT NO(S) *(Any other numbers that may be assigned this report)*
d.	None

10. DISTRIBUTION STATEMENT

Approved for public release; distribution unlimited.

11. SUPPLEMENTARY NOTES	12. SPONSORING MILITARY ACTIVITY
	Eustis Directorate U.S. Army Air Mobility Research & Development Laboratory Fort Eustis, Virginia

13. ABSTRACT

Under USAAMRDL Contract DAAJ02-72-C-0095, four crane-type tandem-rotor helicopters with the gross weight capability of 50,000 lb, 80,000 lb, 120,000 lb, and 200,000 lb are defined in terms of rotor and fuselage parameters and the resulting dynamic characteristics. An automatic Precision Hover System (PHS) is synthesized and the hover hold system performance established analytically including aircraft position errors and pilot station acceleration environment as a function of low speed turbulence. In addition, pilot modeling techniques are utilized to analytically estimate the piloted performance and rating for various attitude and linear velocity control response modes without the aid of automatic hold functions. These estimated performance and rating levels are compared with similar data obtained from a piloted simulator evaluation on the Northrop Corporation (LAS/WAVS) Large Amplitude Simulator/Wide Angle Visual System. The comparison is conducted for the 50,000 pounds gross weight to establish the degree of validity associated with the preselected analytical approaches.

244

DD FORM 1 NOV 68 1473

UNCLASSIFIED
Security Classification

14. KEY WORDS	LINK A		LINK B		LINK C	
	ROLE	WT	ROLE	WT	ROLE	WT
Crane-Type Helicopters						
Advanced HLH Configurations						
Hover Performance						
Pilot Modeling Techniques						
Piloted Simulation						
External Load Equations of Motions						
Automatic Hover Hold System						

14. KEY WORDS	LINK A		LINK B		LINK C	
	ROLE	WT	ROLE	WT	ROLE	WT
Crane-Type Helicopters						
Advanced HLH Configurations						
Hover Performance						
Pilot Modeling Techniques						
Piloted Simulation						
External Load Equations of Motions						
Automatic Hover Hold System						

DEPARTMENT OF THE ARMY
U. S. ARMY AIR MOBILITY RESEARCH & DEVELOPMENT LABORATORY
EUSTIS DIRECTORATE
FORT EUSTIS, VIRGINIA 23604

This report has been reviewed by the Eustis Directorate, U. S. Army Air Mobility Research and Development Laboratory and is considered to be technically sound. The purpose of the program was to evaluate the effects of helicopter size on the helicopter's ability to hover in a position in load-carrying missions. The report is published for the exchange of information and appropriate application. The technical monitor for this contract was Mr. Robert P. Smith, Aeromechanics, Technical Applications Division.

Task 1F162204AA4401
Contract DAAJ02-72-C-0095
USAAMRDL Technical Report 73-104
January 1974

GROUND-BASED SIMULATOR INPUT DATA FOR ADVANCED TANDEM-ROTOR HELICOPTERS

Final Report

By

R. T. Lytwyn
F. White

Prepared by

Boeing Vertol Company
A Division of The Boeing Company
Philadelphia, Pennsylvania

for

EUSTIS DIRECTORATE
U.S. ARMY AIR MOBILITY RESEARCH AND DEVELOPMENT LABORATORY
FORT EUSTIS, VIRGINIA

SUMMARY

This report summarizes the hover performance studies for the Advanced Tandem Helicopters ranging in gross weight from Medium Lift Helicopters (MLH) of 50,000 pounds gross weight to Very High Lift Helicopters (VHLH) at 200,000 pounds, and describes the full flight envelope simulator math model for piloted simulation of these configurations. The programming and the model validation approaches are also discussed.

Four crane-type tandem rotor helicopters with the gross weight capability of 50,000 pounds, 80,000 pounds, 120,000 pounds, and 200,000 pounds are defined in terms of rotor and fuselage parameters and the resulting dynamic characteristics. An automatic Precision Hover System (PHS) is synthesized and the hover hold system performance established analytically including aircraft position errors and pilot station acceleration environment as a function of low speed turbulence. In addition, pilot modeling techniques are utilized to analytically estimate the piloted performance and rating for various attitude and linear velocity control response modes without the aid of automatic hold functions. These estimated performance and rating levels are compared with similar data obtained from a piloted simulator evaluation on the Northrop Corporation (LAS/WAVS) Large Amplitude Simulator/Wide Angle Visual System. The comparison is conducted for the 50,000 pounds gross weight to establish the degree of validity associated with the preselected analytical approaches.

The analytical results indicate that the tandem configurations (up to 200,000 pounds) can hold position with essentially the same accuracy regardless of the specific gross weight. This property is the result of the overwhelming dominance of the automatic control over the inherent aircraft characteristics, as well as of the basic dynamic similarity of all gross weight configurations.

Analysis of the hover hold capability in turbulence reveals that the piloted performance is mainly a function of specific control augmentation modes (command systems or control types), and is only weakly dependent on actual gross weight configuration. This is another indication of the dominance of the automatic pilot assist modes over the inherent dynamic response characteristics of helicopters in hover. In general, a good, precise, hover hold capability is obtainable with horizontal velocity command system involving very little attitude response.

The simulator evaluation of the 50,000-pound configuration confirms, in general, the basic analytical results relating to the piloted and the automatic system performance. In case of

piloted performance, the analysis predicts well the best obtainable hover hold capability for all command systems, but the average actual performance on simulator agrees exactly with the analytical predictions only for linear velocity type command systems. The difficulty in predicting piloted performance with marginal command systems (e.g.,attitude or acceleration types) stems from the uncertainty in assessing the pilot apprehension level resulting from display limitations, damping level preferences, and indirect visual and/or physical cues (e.g.,attitude changes during position control; rapid position display motion because of small scale, etc).

The general results of this research effort provide a validated basis for further analysis and piloted simulation of VHLH configurations regarding their performance capabilities, handling qualities criteria and automatic system requirements in hover and forward flight. The package containing MLH and VHLH configuration data provides the aircraft data for analytical studies. This data package, combined with the validated simulator model at the Northrop Corporation, Aircraft Division, LAS/WAVS facility, is suitable for further piloted simulator evaluation of hover and forward flight helicopter performance with and without externally slung loads. Finally, the analytical approach used here and validated against the piloted simulator results enables the designer to optimize his low speed control concepts inexpensively with a significant confidence level.

FOREWORD

This report constitutes the work of the Boeing Vertol Company in performance of U.S. Army Air Mobility Research and Development Laboratory Contract DAAJ02-72-C-0095 (DA Task 1F162204-AA4401). The work was performed from June 1972 through August 1973 with Mr. James M. Davis as the Program Manager, and Messrs. R.T. Lytwyn and F. White as the principal investigators. The Army technical representative was Mr. Robert P. Smith of Eustis Directorate, USAAMRDL, Fort Eustis, Virginia.

The ground-based simulator evaluation work was performed at the Northrop Corporation, Aircraft Division Aerosciences Laboratory in Hawthorne, California. The simulator mechanization was accomplished under the guidance of John B. Sinacori. Mr. A. Murakoshi was the principal application engineer, with Messrs. William Ross and Raymond Silvestri assisting him throughout the program.

Mr. A.P. Santa-Maria from the Boeing Vertol Experimental Flight Operations was the simulator test pilot on this program, and Mr. E. Low from the Aerodynamics Technology Staff performed the configuration definition work.

TABLE OF CONTENTS

LIST OF ILLUSTRATIONS

LIST OF TABLES

LIST OF SYMBOLS

A_{IC}	lateral cyclic pitch in body axis, rad
A_{ICF}	lateral cyclic pitch control input in body axes - forward rotor
A_{ICR}	lateral cyclic pitch control input in body axes - aft rotor
a	blade airfoil lift curve slope
a_o	rotor coning angle
a_1	longitudinal first harmonic flapping coefficient
$a_{XCG}, a_{YCG}, a_{ZCG}$	acceleration of aircraft center of gravity in the three body axes
a_{YP}, a_{ZP}	lateral and vertical acceleration at the cockpit pilot station, respectively
B_{IC}	longitudinal cyclic pitch in body axis, rad
B_{ICFR}, B_{ICRR}	longitudinal cyclic pitch in the shaft normal plane (S.N.P.) wind axes, forward and aft rotor respectively
B_{ITF}, B_{ITR}	longitudinal cyclic trim in the body axes, forward and aft rotor respectively
b_1	lateral first harmonic flapping coefficient
C_a	equivalent blade chord length for non-uniform downwash power correction (input for digital trim calculation)
C_{TS}	rotor thrust coefficient
c	blade chord length, ft
D	fuselage aerodynamic drag force
D_R	distance between forward and aft rotor hubs, ft
d	separation distance between external load hooks on the aircraft, ft

e	natural exponential base
e_β	blade flapping hinge offset, ft
f_e	equivalent flat plate drag area, ft^2
$f_{e_{REF}}$	reference configuration equivalent flat plate area, ft^2
$G_{B_{po}}$	longitudinal control pickoff gain setting on the simulator
G_h	altitude error feedback gain, in./ft
$G_{\dot{h}}$	altitude rate feedback gain, in./ft/sec
G_p	roll rate feedback gain, in./rad/sec
G_q	pitch rate feedback gain, in./rad/sec
G_r, G_R	yaw rate feedback gain, in./rad/sec
$G_{S_{po}}$	roll quickening gain setting on the simulator
G_X	longitudinal ground position error feedback gain, in./ft
$G_{\dot{X}}$	longitudinal ground speed feedback gain, in./ft/sec
G_Y	lateral ground position error feedback gain, in./ft
$G_{\dot{Y}}$	lateral ground speed feedback gain, in./ft/sec
$G_{\dot{Y}WO}$	$G_{\dot{Y}}$
G_θ	pitch attitude feedback gain, in./rad
G_ϕ	roll attitude feedback gain, in./rad
G_ψ	yaw attitude feedback gain, in./rad
g	gravity constant, 32.2 ft/sec^2
H_F, H_R	longitudinal (in plane of rotation) rotor forces, forward and aft rotor respectively
H_D	density altitude, ft

h	fuselage midsection height, ft
h_c	model cg vertical position for scaling wind tunnel test data relating to fuselage aerodynamic moments
h_e	altitude position error, ft
h_{er}	average vertical distance from aircraft cg to rotor hubs
h_F, h_R	vertical distance from aircraft cg to forward and aft rotor hub, respectively
h_H	differential height between forward and aft rotor hubs
$\dot{h}$	altitude rate, ft/sec
I_{XX}, I_{YY}, I_{ZZ}	aircraft moment of inertia about the roll, pitch, and yaw body axes, respectively, slug-ft^2
I_{XZ}	aircraft product of inertia, slug-ft^2
I_β	blade flapping moment of inertia, slug-ft^2
K_{LCP}	lateral cyclic stick pickoff gain factor
K_p	pilot control feedback gain
K_{SLV}	PHS lateral ground speed gain setting on simulator
K_{XLD}	PHS longitudinal ground position gain setting on simulator
K_{XLV}	PHS longitudinal ground speed gain setting on simulator
K_{YLD}	lateral position gain setting on the simulator
K_{ZLD}	vertical displacement gain setting on the simulator
K_{ZLV}	vertical velocity gain setting on the simulator
K_{δ_B}	longitudinal DCP control gain factor

$K_{X\delta_{BP}}$	differential collective pitch control gain setting on the simulator
$K_{X_{BP}}$	longitudinal cyclic pitch control gain setting on the simulator
$K_{X\delta_{BICF}}$	forward rotor gain setting for longitudinal cyclic pitch control on the simulator
$K_{X\delta_{BICR}}$	aft rotor gain setting for longitudinal cyclic pitch control on the simulator
$K_{\delta_{BIC}}$	longitudinal cyclic pitch control gain factor
L	fuselage aerodynamic lift force
L_{AIC}	total roll acceleration per unit lateral rotor disc tilt angle $L_{AIC} + L'_{AIC} + L''_{AIC}$
L'_{AIC}, L''_{AIC}	thrust tilt and centrifugal force contribution to L_{AIC}
L_t	integral scale of turbulence wave (gust)
L_v, L_p, L_r	roll acceleration per unit lateral velocity, roll rate, and yaw rate, respectively
$L_{\delta_S}, L_{\delta_R}$	roll acceleration per inch of cockpit lateral stick and pedal controls, respectively
ℓ	average horizontal distance from aircraft cg to rotor hubs
ℓ_c	model cg horizontal position for sealing wind tunnel test data relating to fuselage aerodynamic moments
ℓ_F, ℓ_R	horizontal distance from aircraft cg to the forward and aft rotor hubs, respectively
$\mathscr{L}$	fuselage aerodynamic roll moment
M	fuselage aerodynamic pitch moment
M_u, M_v, M_q	pitch acceleration per unit longitudinal velocity, vertical velocity, and pitch rate, respectively
$M_{\delta_B}, M_{\delta_C}$	pitch acceleration per inch of cockpit control - longitudinal and vertical control velocity

m	total aircraft mass, slugs
N	number of blades per rotor
N_v, N_p, N_r	yaw acceleration per unit lateral velocity, roll rate, and yaw rate, respectively
$N_{\delta_s}, N_{\delta_r}$	yaw acceleration per inch of cockpit lateral stick and pedal controls, respectively
N_{δ_R}	N_{δ_r}
N_{AIC}	yaw acceleration per unit lateral rotor disc tilt angle
p	aircraft body axes oriented roll rate, rad/sec
q	aircraft body axes oriented pitch rate, rad/sec
q_d	dynamic pressure, lb/ft^2
R	rotor radius, ft
R_{REF}	reference configuration rotor radius, ft
r	aircraft body oriented yaw rate, rad/sec
r_{rs}, r_{sp}, r_{dr}	characteristic roots of lateral-directional aircraft dynamics
r_w, r_q, r_{qu}	characteristic roots of longitudinal-vertical aircraft dynamics
s	complex (Laplace) variable
T	rotor thrust force, lb
T_I	pilot model adjustable lag time constant, sec
T_L	pilot model adjustable lead time constant, sec
T_{L_2}	lateral stick control pickoff washout time constant, sec
T_{L_3}	lateral stick control pickoff lag time constant, sec
T_N	pilot model constant neuromuscular lag time, sec

U	longitudinal aircraft velocity
U_o	steady (trim) longitudinal aircraft velocity
$U_g, \bar{U}_g$	longitudinal gust velocities, instantaneous and average, respectively
V	airspeed
V_{as}	characteristic turbulence airspeed (for hover, V_{as} = average wind speed), ft/sec
V_T	blade tip speed, ft/sec
v	lateral aircraft velocity, ft/sec
$v_g, \bar{v}_g$	lateral gust velocities, instantaneous and average, respectively
W_G	aircraft gross weight, lb
w	vertical aircraft velocity
w_o	steady (trim) aircraft velocity
w_g	vertical gust velocity
X	longitudinal aircraft displacement response signal
X_c	longitudinal displacement command signal
X_e	longitudinal hover position error due to turbulence
X_I	North-South aircraft position with respect to a fixed ground reference point
$\dot{X}_I$	longitudinal aircraft ground speed
X_{Ie}	longitudinal aircraft ground position error, ft
X_{sc}	longitudinal scope position display driving variable
X_u, X_w, X_q	longitudinal acceleration per unit longitudinal and vertical velocity and pitch rate, respectively

$X_{\delta_B}, X_{\delta_c}$	longitudinal acceleration per inch of cockpit control, longitudinal and collective stick, respectively
x	aircraft body oriented longitudinal axis
$\bar{x}$	aircraft average longitudinal ground position error in turbulence
x_{LOAD}	longitudinal axis of external load
Y	lateral aircraft displacement response signal
Y_c	lateral displacement command signal
Y_e	lateral hover position error due to turbulence, ft
Y_I	East-West aircraft position error with respect to a fixed ground reference point, ft
Y_{Ie}	lateral aircraft ground position error, ft
$\dot{Y}_I$	lateral aircraft ground speed, ft/sec
Y_{sc}	lateral scope position display driving variable
Y_p	pilot model transfer function
Y_v, Y_p, Y_r	lateral acceleration per unit lateral velocity, roll rate, and yaw rate, respectively
$Y_{\delta_S}, Y_{\delta_R}$	lateral acceleration per inch of lateral stick and pedal control, respectively
Y_{δ_r}	$Y_{\delta R}$
y	aircraft body oriented lateral axis
$\bar{y}$	aircraft average lateral ground position error in turbulence
y_{LOAD}	lateral external load body oriented axis
Z_u, Z_w, Z_q	vertical acceleration per unit longitudinal and vertical velocity, and pitch rate, respectively
$Z_{\delta_B}, Z_{\delta_c}$	vertical acceleration per inch of longitudinal and collective stick control, respectively

Z_{θ_c}	vertical aircraft acceleration per unit of blade collective pitch angle
z	aircraft body oriented vertical axis
z_{LOAD}	vertical external load body oriented axis
α	fuselage aerodynamic angle of attack
α_{CA}	angle of attack of rotor control axis
β	fuselage angle of sideslip
γ	Locke number = 1/2 pca $R^4/I\beta$
δ_3	blade pitch-flap coupling angle
δ_B	longitudinal stick control, inches
δ_c	collective control, inches of equivalent stick
δ_{BIC}	longitudinal cyclic control due to pilot input
δ_r (or δ_R)	pedal control, inches
δ_s	lateral stick control, inches
θ	aircraft pitch attitude
θ_{AS}, θ_{AP}	total control signals at aft rotor swiveling and pivoting actuators, respectively
θ_{BF}, θ_{BR}	longitudinal blade pitch angles due to cockpit DCP input
θ_{CF}, θ_{CR}	collective blade pitch angles due to cockpit collective stick input
θ_e	aircraft pitch attitude error feedback
θ_{FS}, θ_{FP}	total control signals at forward rotor swiveling and pivoting actuators, respectively
θ_o	steady (trim) aircraft pitch attitude

θ_{OF}, θ_{OR}	blade root collective pitch angles at forward and aft rotors
θ_{RF}, θ_{RR}	directional blade cyclic pitch angles due to cockpit control inputs
θ_{SF}, θ_{SR}	blade lateral cyclic pitch angles due to lateral stick control, forward and aft rotor, respectively
θ_{TF}, θ_{TR}	root collective pitch angles at full down position of collective stick, forward and aft rotor, respectively
λ	instantaneous rotor inflow ratio
λ_o	steady (trim) rotor inflow ratio
$\lambda_{SL}, \dot{\lambda}_{SL}, \ddot{\lambda}_{SL}$	lateral cable angle, angular rate and acceleration, respectively
μ	rotor advance ratio
$\mu_{SL}, \dot{\mu}_{SL}, \ddot{\mu}_{SL}$	longitudinal cable angle, angular rate and acceleration, respectively
$\nu_{SL}, \dot{\nu}_{SL}, \ddot{\nu}_{SL}$	lateral differential cable angle, angular rate and acceleration, respectively
ρ	air density at H_D, slugs/ft^3
ρ_o	sea level air density, slugs/ft^3
σ	rotor solidity ratio
σg	turbulence intensity RMS, ft/sec
σ_{u_g}	longitudinal gust magnitude, RMS or standard deviation
σ_{v_g}	lateral gust magnitude, RMS or standard deviation
σ_{w_g}	vertical gust magnitude, RMS or standard deviation
σ_x	aircraft longitudinal position error, RMS or standard deviation
σ_y	aircraft lateral position error, RMS or standard deviation

σ_β	blade mass moment about the flapping hinge
τ	inherent pilot model reaction time delay, sec
$\tau_{\dot{h}}$	PHS altitude rate feedback time constant, sec
τ_{QL}	pitch rate feedback lag time constant, sec
τ_{QWO}	pitch rate feedback washout time constant, sec
τ_p	roll rate feedback time constant in SAS, sec
τ_R	yaw rate feedback time constant in SAS, sec
τ_w	vertical aircraft response time constant, sec
$\tau_{\dot{x}}$	PHS longitudinal velocity feedback time constant, sec
$\tau_{\dot{y}_{WO}}$	PHS lateral velocity feedback time constant, sec
τ_{δ_B}	longitudinal DCP control shaping time constant, sec
$\tau_{\delta_{BIC}}$	longitudinal cyclic control shaping time constant, sec
$\tau_{\phi_{WO}}$	roll attitude feedback time constant (washout), sec
Φ_{aYP}	power spectral density of lateral acceleration at the pilot station due to turbulence
Φ_{aZP}	power spectral density of vertical acceleration at the pilot station due to turbulence
Φ_g	general expression for power spectral density of turbulence
$\Phi_{u_g}, \Phi_{v_g}, \Phi_{w_g}$	power spectral densities of longitudinal, lateral, and vertical gust
Φ_x, Φ_y	power spectral density of longitudinal and lateral aircraft position error due to turbulence
ϕ	aircraft roll attitude

ϕ_e	aircraft roll attitude feedback error
ψ	aircraft yaw attitude
ψ_e	aircraft yaw attitude error feedback
ψ_{sc}	scope display driving variable for yaw position
Ω	rotor rotational frequency, rad/sec
ω	angular frequency, rad/sec
ω_g	characteristic turbulence frequency, $\omega_g = 1.5\ V_{as}/L_t$
ω_{CUTOFF}	cutoff frequency for gust spectral integration, rad/sec

INTRODUCTION

BACKGROUND

Potential applications for large helicopters with external load capability include the stacking of containers on trucks or ships, bridge placement, and modular housing construction. A high degree of precision is required from the helicopter if these types of operations are to be performed in a timely and safe manner.

The ability of a helicopter to hover accurately with respect to a fixed reference point depends on the inertial and aerodynamic characteristics of the aircraft, the design of the automatic flight control system, and the response of the rotor and flight control system. At present, no experience with large helicopters (80,000 pounds and larger gross weights) exists which would indicate their potential capabilities or limitations during precise hover hold missions. As the size of the helicopter is increased, larger rotors are required which must operate at lower rpm. This leads to lower, rotor-induced frequencies, which might conceivably alter the basic responses normally experienced with existing medium-gross-weight aircraft. Pure extrapolation to a larger size contains a sufficient number of unknown factors affecting the flying qualities to warrant a closer analytical and simulator evaluation of the performance of such aircraft during precise hover hold missions. The questions of aircraft size effect on the pilot's ability to perform these missions must be addressed in analyses and simulations. The control system pilot-assist requirements, as well as the automatic hover hold functions, must be synthesized and evaluated.

The sensitivity of these helicopters to turbulence levels must also be established if an all-weather operational capability is to be ensured. The acceleration environment at the crew station should be investigated since the cockpit position with respect to aircraft center of gravity will increase with the helicopter size, and too large acceleration levels will interfere with the precise piloting task.

OBJECTIVES AND SCOPE

The main objective of the analytical portion of this investigation is the evaluation of helicopter size effects on its capability to perform precise hover position hold missions. For this purpose, the study defines parametrically four tandem-rotor helicopter configurations with the gross weight capability of 50,000, 80,000, 120,000, and 200,000 pounds, and synthesizes the automatic control system functions for precise hover capability and pilot control augmentation (assist functions). A single precision hover system (PHS) and

stability augmentation system (SAS) is used for all gross weight configurations. Several pilot-assist functions are designed using different combinations of longitudinal cyclic pitch (DCP), with conventional lateral cyclic control. Automatic feedback functions are also included to provide the pilot with direct acceleration, velocity, or altitude control on the stick. A full-flight envelope mathematical model is utilized to perform piloted evaluation and to compare the results with analytical predictions. The hover position hold capabilities and pilot station accelerations are defined as a function of turbulence level, pilot control augmentation modes, and gross weight configurations. The unpiloted aircraft position hold capabilities with PHS augmentation are compared with the piloted performance without ground position and velocity hold. Several test points are compared directly with the piloted simulator results in terms of turbulence effects, control assist functions, and pilot station acceleration levels.

DEVELOPMENT OF PARAMETRIC CHARACTERISTICS FOR ADVANCED TANDEM-ROTOR HEAVY LIFT HELICOPTER CONFIGURATIONS

The four tandem-rotor helicopters defined in this section are based on scaling the existing HLH designs up into the VHLH gross weight region. The ground rules for scaling of the aerodynamic performance and fuselage aerodynamic forces and moments are discussed below, and the dynamic characteristics of the basic aircraft are presented on page 13.

ADVANCED TANDEM-ROTOR HEAVY LIFT HELICOPTER (HLH) CONFIGURATIONS

Sizing Ground Rules and Aircraft Parameters

The four HLH configurations shown in Figure 1 are based on the scaling of the Boeing-Vertol Model 301 Heavy Lift Helicopter, with a design gross weight of from 120,000 pounds to the equivalent of tandem-rotor helicopters at higher and lower gross weights. As such, they are based on the following scaling ground rules:

1. Disc loading = 8.9 lb/ft^2
2. Rotor overlap = 23.8% of rotor diameter
3. Rotor solidity = 0.0923
4. Tip speed = 750 fps
5. All reference lengths, except the main landing gear, are proportional to design gross weight. The main landing gear is assumed to be constant in order to accommodate an 8-by-8-by 20-ft cargo container.
6. All reference areas, except the equivalent flat plate area (f_e), are proportional to design gross weight. The flat plate area, (f_e), is based on the following:
   - Main landing gear flat plate area varies as the square root of gross weight.
   - All other items vary linearly with gross weight.
7. Engine and transmission ratings are proportional to design gross weight.
8. Moments of inertia are scaled from the Model 301 Heavy Lift Helicopter data, using the length and area proportionality described above.

NORMAL GROSS WT:

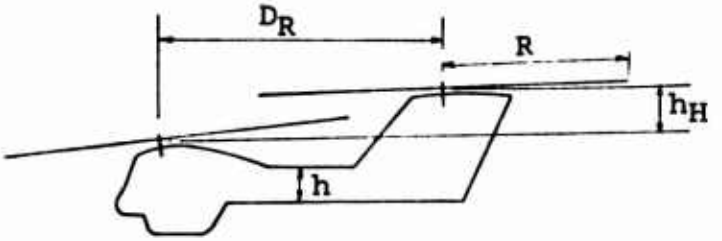

50,000 LB
R = 29.90 FT
D_R = 45.57 FT
h = 6.0 FT
h_H = 6.83 FT

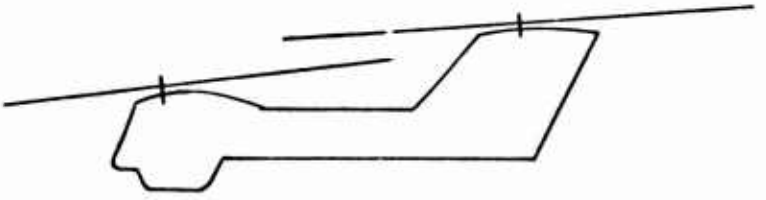

80,000 LB
R = 37.82 FT
D_R = 57.64 FT
h = 7.6 FT
h_H = 8.63 FT

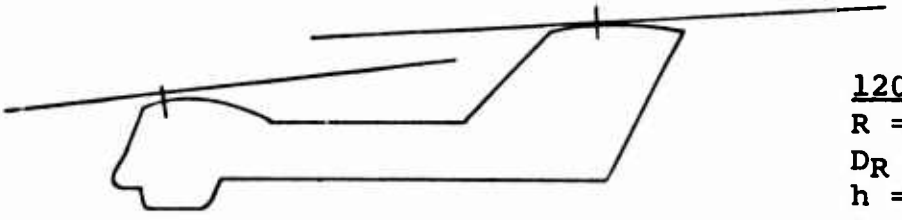

120,000 LB
R = 46.32 FT
D_R = 70.59 FT
h = 9.35 FT
h_H = 10.57 FT

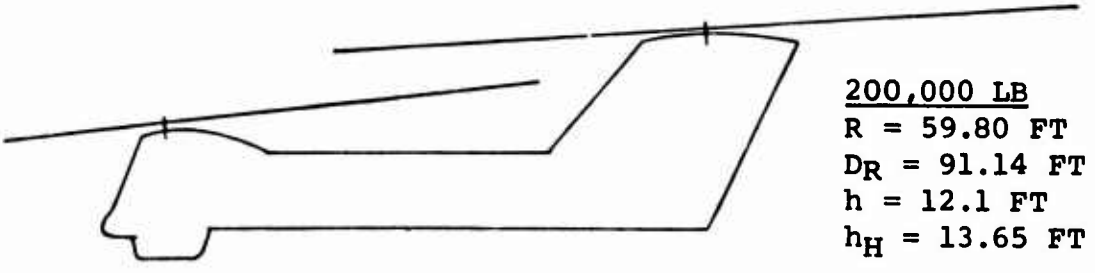

200,000 LB
R = 59.80 FT
D_R = 91.14 FT
h = 12.1 FT
h_H = 13.65 FT

Figure 1. Advanced Tandem-Rotor HLH Configuration Data.

The aircraft parameters defining each design gross weight configuration are summarized in Table I.

The disc loading of 8.9 pounds per square foot represents more realistically the current tandem-rotor helicopter designs, while attempting to keep the downwash velocity sufficiently small at reasonable power level requirements.

Fuselage Aerodynamics and Scaling Factors

Tables II through VII summarize the fuselage aerodynamic forces and moments for the baseline HLH configuration at 120,000 pounds gross weight. The tables are based on wind tunnel test results for a solid model of a tandem-rotor heavy lift helicopter. Data presented in the tables are functions of fuselage angle of attack, α, and fuselage sideslip angle, β. Tabular force and moment information is expressed in the body axis in the form: drag (D/qd), sideforce (Y/qd), lift (L/qd), pitching moment (M/qd), rolling moment ($\mathcal{L}$/qd), and yawing moment (N/qd), with α from -90° to $+90^{\circ}$, and β from -90° to $+90^{\circ}$. From 90° to 180°, the curves are assumed to be mirror image values of 0° to 90°.

Moment data is expressed about a center-of-gravity location at which the wind tunnel model was tested. Moment corrections proportional to the distance to the c.g. location being flown with the full force simulation model are applied to the stored data.

Tabular fuselage data usually does not account for rotor hub drag, momentum drag, and leakage drag and therefore must be adjusted to the correct level before being used. A Δf_e correction is applied to the tabulated lift, drag, and side force data to account for these items.

The fuselage aerodynamic data shown in Tables II through VII are already corrected for the rotor hub drag, and are based on the total equivalent flat plate area of 138.0 sq ft. This represents very closely the 120,000-pound configuration, and the tables can be used directly for that configuration gross weight. For configurations other than the 120,000 pounds, the following scale factors should be applied to arrive at the corresponding fuselage aerodynamic tables:

$$D/_{qd} = \left(\frac{f_e}{f_{eREF}}\right) \left(D/_{qd}\right)_{TABLE\ II}$$

$$Y/_{qd} = \left(\frac{R}{R_{REF}}\right)^2 \left(Y/_{qd}\right)_{TABLE\ IV}$$

TABLE I. ADVANCED TANDEM-ROTOR HLH CONFIGURATION PARAMETERS

Item	Units	Value			
Design Gross Weight	Lb	50,000	80,000	120,000	200,000
Equiv. Flat Plate Area (Airframe)	Sq Ft	82.1	110.0	141.7	195.1
Disc Loading	Lb/Sq Ft	8.9	8.9	8.9	8.9
Rotor Radius, R	Ft	29.90	37.82	46.32	59.80
Rotor Chord	Ft	2.167	2.741	3.357	4.333
Blades per Rotor	-	4	4	4	4
Flap Hinge Offset	Ft	1.408	1.781	2.182	2.817
Blade Twist	Deg	-12	-12	-12	-12
Blade Airfoil Cutout	-	.1636	.1636	.1636	.1636
Tip Speed	Ft/Sec	750	750	750	750
Dist. Between Rotors (Waterline)	Ft	45.57	57.64	70.59	91.14
Vertical Hub Separation	Ft	6.825	8.633	10.573	13.65
C_a (Ratio)	Ft	1.943	2.457	3.010	3.886
I_β - Flapping Moment	Slug-Ft^2	1,828	5,945	16,932	63,724
σ_β - Weight Moment	Ft-Lb	3,099	7,969	18,587	54,026
I_{xx}	Slug-Ft^2	67,120	138,950	266,820	622,250
I_{yy}	Slug-Ft^2	384,350	929,340	2,014,820	5,400,340
I_{zz}	Slug-Ft^2	331,930	849,670	1,911,530	5,310,230
Fuselage Width - Constant Section	Ft	6.5	8.235	10.1	13.0
Fuselage Height - Constant Section	Ft	6.0	7.6	9.35	12.1
Fwd. Shaft Angle	Deg	6	6	6	6
Aft Shaft Angle	Deg	3	3	3	3
Blade Lock No. = $1/2\ \rho ac\ R^4/I_\beta$	-	5.78	5.78	5.58	5.32
I_F, l_R - Horiz. Dist. from A/C c.g. to Rotor	Ft	22.79	28.82	35.29	45.57
h_F (Vert. Dist. from A/C c.g. to Fwd. Rotor)	Ft	7.5	7.8	8.2	9.0
h_R (Vert. Dist. from A/C c.g. to Rear Rotor)	Ft	14.33	16.43	18.77	22.65
Estimated Empty Gross Weight (TOGW)	Lb	29,000	43,000	62,000	101,000
l_c (midpoint c.g. location)	Ft	2.0	2.0	2.0	2.0
h_c (midpoint c.g. location)	Ft	0	0	0	0

TABLE II. BASELINE TANDEM-ROTOR HLH FUSELAGE DRAG TABLES, D/qd
REFERENCE: STA. 596", WATER LINE 164"
120,000-POUND GROSS WEIGHT

β,deg \ α,deg	-90.0	-49.3	-29.3	-19.3	-9.3	-4.3	0.7	5.7	10.7	20.7	30.7	50.7	90.0
-90	10	-35	-35	-35	-35	-35	-35	-35	-35	-35	-35	-35	-10
-60	0	10	50	55	60	60	60	65	75	75	65	10	0
-50	0	-30	50	70	75	80	80	85	90	90	65	-35	0
-40	0	-45	20	45	55	60	60	65	75	70	40	-45	0
-30	0	-35	15	35	45	50	50	55	70	70	40	-35	0
-20	0	-20	50	65	75	80	80	85	105	110	75	-20	0
-15	0	-15	65	91	104	108	111	120	136	139	95	-15	0
-10	0	-15	75	106	120	124	128	136	153	154	110	-15	0
-6	0	-10	80	113	127	131	134	142	160	161	115	-10	0
-2	0	-10	80	116	130	134	137	145	164	164	115	-10	0
0	0	-10	80	117	131	135	138	145	164	164	115	-10	0
2	0	-10	80	116	130	134	137	145	164	164	115	-10	0
6	0	-10	80	113	127	131	134	142	160	161	115	-10	0
10	0	-15	75	106	120	124	128	136	153	154	110	-15	0
15	0	-15	65	91	104	108	111	120	136	139	95	-15	0
20	0	-20	50	65	75	80	80	85	105	110	75	-20	0
30	0	-35	15	35	45	50	50	55	70	70	40	-35	0
40	0	-45	20	45	55	60	60	65	75	70	40	-45	0
50	0	-35	50	70	75	80	80	85	90	90	65	-35	0
60	0	10	50	55	60	60	60	65	75	75	65	10	0
90	10	-35	-35	-35	-35	-35	-35	-35	-35	-35	-35	-35	10

TABLE III. BASELINE TANDEM-ROTOR HLH FUSELAGE LIFT TABLES, L/qd
120,000-POUND GROSS WEIGHT

β,deg \ α,deg	-90.0	-49.3	-29.3	-19.3	-9.3	-4.3	0.7	5.7	10.7	20.7	30.7	50.7	90.0
-90	-780	-150	-150	-150	-150	-150	-150	-150	-150	-150	-150	-150	390
-60	-750	-720	-595	-485	-355	-315	-280	-235	-190	-95	-20	240	850
-50	-750	-615	-565	-475	-345	-300	-250	-195	-120	10	135	490	850
-40	-750	-555	-435	-335	-185	-125	-80	-15	65	230	355	645	850
-30	-750	-560	-380	-240	-50	15	65	135	225	390	495	710	850
-20	-750	-605	-400	-235	-20	55	105	185	270	425	535	730	850
-15	-750	-620	-420	-255	-36	42	96	181	265	424	535	735	850
-10	-750	-635	-435	-276	-57	19	75	165	252	417	530	730	850
-6	-750	-640	-445	-286	-70	5	60	151	242	410	530	730	850
-2	-750	-640	-450	-291	-77	-3	51	142	236	406	530	730	850
0	-750	-640	-450	-292	-79	-5	50	140	235	405	530	730	850
2	-750	-640	-450	-291	-77	-3	51	142	236	406	530	730	850
6	-750	-640	-445	-286	-70	5	60	151	242	410	530	730	850
10	-750	-635	-435	-276	-57	19	75	165	252	417	530	730	850
15	-750	-620	-420	-255	-36	42	96	181	265	424	535	735	850
20	-750	-605	-400	-235	-20	55	105	185	270	425	535	730	850
30	-750	-560	-380	-240	-50	15	65	135	225	390	495	710	850
40	-750	-555	-435	-335	-185	-125	-80	-15	65	230	355	645	850
50	-750	-615	-565	-475	-345	-300	-250	-195	-120	10	135	490	850
60	-750	-720	-595	-485	-355	-315	-280	-235	-190	-95	-20	240	850
90	-780	-150	-150	-150	-150	-150	-150	-150	-150	-150	-150	-150	390

TABLE IV. BASELINE TANDEM-ROTOR HLH FUSELAGE SIDEFORCE TABLES, Y/qd 120,000-POUND GROSS WEIGHT

β,deg \ α,deg	-90.0	-49.3	-29.3	-19.3	-9.3	-4.3	0.7	5.7	10.7	20.7	30.7	50.7	90.0
-90	790	1030	1030	1030	1030	1030	1030	1030	1030	1030	1030	1030	790
-60	0	855	995	1030	1040	1045	1050	1045	1040	1025	985	840	0
-50	0	660	810	855	870	875	880	875	870	850	805	645	0
-40	0	470	620	665	685	690	695	690	685	665	615	460	0
-30	0	315	425	470	490	495	500	495	490	470	425	310	0
-20	0	205	270	290	300	305	310	305	300	290	270	200	0
-15	0	150	205	217	226	228	230	228	226	215	205	145	0
-10	0	100	130	142	152	153	153	153	152	140	130	100	0
-6	0	65	80	90	92	93	93	93	92	89	80	65	0
-2	0	25	30	33	35	35	35	35	35	33	30	25	0
0	0	0	0	0	0	0	0	0	0	0	0	0	0
2	0	-25	-30	-33	-35	-35	-35	-35	-35	-33	-30	-25	0
6	0	-65	-80	-90	-92	-93	-93	-93	-92	-89	-80	-65	0
10	0	-100	-130	-142	-152	-153	-153	-153	-152	-140	-130	-100	0
15	0	-150	-205	-217	-226	-228	-230	-228	-226	-215	-205	-145	0
20	0	-205	-270	-290	-300	-305	-310	-305	-300	-290	-270	-200	0
30	0	-315	-425	-470	-490	-495	-500	-495	-490	-470	-425	-310	0
40	0	-470	-620	-665	-685	-690	-695	-690	-685	-665	-615	-460	0
50	0	-660	-810	-855	-870	-875	-880	-875	-870	-850	-805	-645	0
60	0	-855	-995	-1030	-1040	-1045	-1050	-1045	-1040	-1025	-985	-840	0
90	-790	-1030	-1030	-1030	-1030	-1030	-1030	-1030	-1030	-1030	-1030	-790	0

TABLE V. BASELINE TANDEM-ROTOR HLH FUSELAGE PITCH MOMENT TABLES, M/qd 120,000-POUND GROSS WEIGHT

β,deg \ α,deg	-90.0	-49.3	-29.3	-19.3	-9.3	-4.3	0.7	5.7	10.7	20.7	30.7	50.7	90.0
-90	1000	-500	-500	-500	-500	-500	-500	-500	-500	-500	-500	-500	-4300
-60	3500	-2800	-3800	-4000	-3900	-3800	-3600	-3500	-3400	-2900	-2000	-700	-4000
-50	3500	-2700	-3200	-3200	-3000	-2800	-2600	-2500	-2300	-1700	-1000	-500	-4000
-40	3500	-3900	-3500	-3200	-2900	-2600	-2400	-2100	-2000	-1500	-900	-1500	-4000
-30	3500	-4000	-4900	-4500	-4000	-3500	-3200	-3000	-3000	-2500	-2000	-1100	-4000
-20	3500	-2800	-4200	-4200	-4000	-3800	-3500	-3200	-3000	-2200	-1100	200	-4000
-15	3500	-2300	-3600	-3400	-3150	-2950	-2550	-2300	-2150	-1350	-200	600	-4000
-10	3500	-2000	-3000	-2850	-2500	-2300	-1950	-1600	-1450	-700	300	900	-4000
-6	3500	-1800	-2700	-2500	-2200	-1950	-1600	-1300	-1150	-350	600	1000	-4000
-2	3500	-1700	-2500	-2350	-2000	-1750	-1400	-1100	-950	-200	700	1100	-4000
0	3500	-1700	-2500	-2300	-1950	-1700	-1350	-1050	-900	-150	800	1200	-4000
2	3500	-1700	-2500	-2350	-2000	-1750	-1400	-1100	-950	-200	700	1100	-4000
6	3500	-1800	-2700	-2500	-2200	-1950	-1600	-1300	-1150	-350	600	1000	-4000
10	3500	-2000	-3000	-2850	-2500	-2300	-1950	-1600	-1450	-700	300	900	-4000
15	3500	-2300	-3600	-3400	-3150	-2950	-2550	-2300	-2150	-1350	-200	600	-4000
20	3500	-2800	-4200	-4200	-4000	-3800	-3500	-3200	-3000	-2200	-1100	200	-4000
30	3500	-4000	-4900	-4500	-4000	-3500	-3200	-3000	-3000	-2500	-2000	-1100	-4000
40	3500	-3900	-3500	-3200	-2900	-2600	-2400	-2100	-2000	-1500	-900	-1500	-4000
50	3500	-2700	-3200	-3200	-3000	-2800	-2600	-2500	-2300	-1700	-1000	-500	-4000
60	3500	-2800	-3800	-4000	-3900	-3800	-3600	-3500	-3400	-2900	-2000	-700	-4000
90	1000	-500	-500	-500	-500	-500	-500	-500	-500	-500	-500	-500	-4300

TABLE VI. BASELINE TANDEM-ROTOR HLH FUSELAGE ROLL MOMENT TABLES, $\mathcal{L}/qd$
120,000-POUND GROSS WEIGHT

β,deg \ α,deg	-90.0	-49.3	-29.3	-19.3	-9.3	-4.3	0.7	5.7	10.7	20.7	30.7	50.7	90.0
-90	2300	2500	2500	2500	2500	2500	2500	2500	2500	2500	2500	2500	1250
-60	0	2200	2100	2200	2300	2200	2200	2000	1800	1500	1300	1200	0
-50	0	3000	2200	2200	2200	2100	2000	1800	1500	1200	1200	1800	0
-40	0	3000	3200	3000	2900	2700	2600	2400	2100	1700	1800	1800	0
-30	0	2200	2800	3000	3000	3000	2900	2600	2200	1800	1700	1200	0
-20	0	1300	1700	1900	2000	2000	2000	1800	1500	1200	1000	800	0
-15	0	1000	1200	1350	1400	1350	1300	1250	1000	850	800	600	0
-10	0	700	900	950	950	900	850	800	750	600	500	400	0
-6	0	400	500	550	600	550	550	500	450	400	300	300	0
-2	0	100	200	200	200	200	200	200	150	150	100	100	0
0	0	0	0	0	0	0	0	0	0	0	0	0	0
2	0	-100	-200	-200	-200	-200	-200	-200	-150	-150	-100	-100	0
6	0	-400	-500	-550	-600	-550	-550	-500	-450	-400	-300	-300	0
10	0	-700	-900	-950	-950	-900	-850	-800	-750	-600	-500	-400	0
15	0	-1000	-1200	-1350	-1400	-1350	-1300	-1250	-1000	-850	-800	-600	0
20	0	-1300	-1700	-1900	-2000	-2000	-2000	-1800	-1500	-1200	-1000	-800	0
30	0	-2200	-2800	-3000	-3000	-3000	-2900	-2600	-2200	-1800	-1700	-1200	0
40	0	-3000	-3200	-3000	-2900	-2700	-2600	-2400	-2100	-1700	-1800	-1800	0
50	0	-3000	-2200	-2200	-2200	-2100	-2000	-1800	-1500	-1200	-1200	-1800	0
60	0	-2200	-2100	-2200	-2300	-2200	-2200	-2000	-1800	-1500	-1300	-1200	0
90	-2300	-2500	-2500	-2500	-2500	-2500	-2500	-2500	-2500	-2500	-2500	-2500	-1250

TABLE VII. BASELINE TANDEM-ROTOR HLH FUSELAGE YAW MOMENT TABLES, N/qd

β,deg \ α,deg	-90.0	-49.3	-29.3	-19.3	-9.3	-4.3	0.7	5.7	10.7	20.7	30.7	50.7	90.0
-90	-3700	-9000	-9000	-9000	-9000	-9000	-9000	-9000	-9000	-9000	-9000	-9000	-100
-60	0	-2500	-2100	-2300	-2100	-1800	-1500	-1000	-700	-400	-300	-100	0
-50	0	-6000	-3100	-2500	-2000	-1600	-1200	-800	-500	-100	-100	-100	0
-40	0	-4600	-6000	-6000	-4900	-3900	-2800	-1800	-800	0	100	200	0
-30	0	-2900	-4100	-4600	-4200	-3300	-2400	-1400	-500	100	200	400	0
-20	0	-1900	-2400	-2600	-2300	-1800	-1200	-600	-100	400	500	500	0
-15	0	-1400	-1900	-1950	-1700	-1250	-850	-350	100	500	600	600	0
-10	0	-900	-1200	-1300	-1050	-750	-450	-100	250	550	600	500	0
-6	0	-600	-700	-800	-500	-300	-50	150	300	450	500	400	0
-2	0	-200	-200	-300	-100	0	50	100	150	200	200	200	0
0	0	0	0	0	0	0	0	0	0	0	0	0	0
2	0	200	200	300	100	0	-50	-100	-150	-200	-200	-200	0
6	0	600	700	800	500	300	50	-150	-300	-450	-500	-400	0
10	0	900	1200	1300	1050	750	450	100	-250	-550	-600	-500	0
15	0	1400	1900	1950	1700	1250	850	350	-100	-500	-600	-600	0
20	0	1900	2400	2600	2200	1800	1200	600	100	-400	-500	-500	0
30	0	2900	4100	4600	4000	3300	2400	1400	500	-100	-200	-400	0
40	0	4600	6000	6000	5000	3900	2800	1800	800	0	-100	-200	0
50	0	6000	3100	2500	2000	1600	1200	800	500	100	100	-100	0
60	0	2500	2100	2300	2000	1800	1500	1000	700	400	300	100	0
90	3700	9000	9000	9000	9000	9000	9000	9000	9000	9000	9000	9000	100

$$L/_{qd} = \left(\frac{R}{R_{REF}}\right)^2 \left(L/_{qd}\right)_{TABLE\ III}$$

$$M/_{qd} = \left(\frac{R}{R_{REF}}\right)^3 \left(M/_{qd}\right)_{TABLE\ V}$$

$$\mathcal{L}/_{qd} = \left(\frac{R}{R_{REF}}\right)^3 \left(\mathcal{L}/_{qd}\right)_{TABLE\ VI}$$

$$N/_{qd} = \left(\frac{R}{R_{REF}}\right)^3 \left(N/_{qd}\right)_{TABLE\ VII}$$

where

$f_{e_{REF}} = 138.0\ ft^2$

f_e = tabulated in TABLE I

$R_{REF} = 45.0$ ft

R = tabulated in TABLE I

These scaling formulas are based on the assumptions that all non-dimensional aerodynamic force and moment coefficients are constant for each gross weight configuration. Only the scalings of reference lengths and areas are required, and these are proportional to rotor radius and (rotor radius)^2 respectively.

DYNAMIC CHARACTERISTICS

The stability derivations presented in this section are based on the standard Boeing-Vertol trim and stability digital program A-97. The program computes the helicopter trim by means of an iterative solution to the six steady-state equations, summing all forces and moments about the fixed body axis. A numerical approach to the solution of the rotor flapping and force equations is used, allowing for the automatic accounting of blade stall, reverse flow, and compressibility effects. The simplifications or assumptions contained in the rotor analysis include the following:

- Induced velocity distribution is assumed to be uniform.
- Blade lag and all elastic degrees of freedom are neglected.

- Nonsteady aerodynamic and spanwise flow effects are neglected.

The stability derivatives and control powers are then obtained numerically by evaluating the changes in the helicopter forces and moments from their trim value caused by a small perturbation in an independent parameter. These derivatives are quasi-static; i.e., the rotor is assumed to reach its new steady-state condition instantaneously as the perturbation is applied.

The stability derivatives data are presented for sea-level standard conditions (midpoint c.g. position) in hover at all design gross weights and all estimated empty gross weights. An analysis is then made of the effects of scaling on important hover derivatives and the associated dynamic properties. All control sensitivity data are based on constant cockpit control-to-blade pitch angle mechanical ratios consistent with the typical tandem-rotor HLH configuration.

Stability Derivatives

A summary of stability derivatives for all design gross weight configurations in hover is shown in Table VIII. The most important derivatives, which define the helicopter dynamics in hover, are plotted in Figures 2 and 3. The following discussion elucidates the scaling properties of the major derivatives plotted in these figures.

Longitudinal Axis

The most important derivatives in hover are represented by the vertical damping, Z_w, the pitch damping, M_q, and the pitch acceleration due to longitudinal velocity, M_u. These derivatives, together with the control sensitivities Z_{δ_C} and M_{δ_B}, determine the aircraft response to pilot input in hover.

The vertical damping, Z_w, is determined by the sensitivity of rotor thrust to vertical velocity. According to Reference 1, this derivative in hover can be approximated by the formula

$$Z_w = -\left[\frac{8}{V_T\left(\frac{2C_T}{a\sigma}S\right)\left(1-\frac{a\sigma}{16\lambda_o}\right)}\right]$$

TABLE VIII. ADVANCED TANDEM-ROTOR HLH STABILITY DERIVATIVES

Hover, midpoint C.G., sea level, standard day
750 ft/sec tip speed

Param. No.	Param. Symbol	Units	Configuration 50,000 Lb		80,000 Lb		120,000 Lb		200,000 Lb	
			Design Gross Weight	Empty Gross Weight	Design Gross Weight	Empty Gross Weight	Design Gross Weight	Empty Gross Weight	Design Gross Weight	Empty Gross Weight
1	θ_o	deg	2.842	2.804	2.805	2.769	2.779	2.743	2.757	2.719
2	B_{ITF}	deg	-.40	-.40	-.40	-.40	-.40	-.40	-.40	-0.40
3	B_{ITR}	deg	-2.80	-2.80	-2.80	-2.80	-2.80	-2.80	-2.80	-2.80
4	Xu	$1/sec$	-.01802	-.01260	-.01756	-.01180	-.01718	-.01127	-.01682	-.01088
5	Xw	$1/sec$	.00791	.01389	.00794	.01476	.00806	.01537	.00815	.01577
6	Xq	ft/sec	.6444	-.06072	.7521	-.2741	.8774	-.4917	1.0839	-.7951
7	X_{δ_B}	$\frac{ft/sec^2}{in.}$	.1389	.2303	.1-91	.2448	.1412	.2564	.1440	.2655
8	X_{δ_C}	$\frac{ft/sec^2}{in.}$	.2926	.4631	.2925	.4950	.2965	.5172	.3015	.5341
9	Z_u	$1/sec$	.01010	.01762	.01013	.01876	.00998	.01886	.00995	.01815
10	*Zw	$1/sec$	-.2230	-.3556	-.2229	-.3771	-.2246	-.3900	-.2263	-.3975
11	Zq	ft/sec	-1.0901	-1.5102	-1.2620	-2.0971	-1.5525	-2.6327	-1.9504	-3.295
12	Z_{δ_B}	$\frac{ft/sec^2}{in.}$	.1270	.1418	.1196	.1394	.0991	.1171	.0786	.0883
13	*Z_{δ_C}	$\frac{ft/sec^2}{in.}$	-7.306	-11.478	-7.308	-12.151	-7.346	-12.585	-7.397	-12.881
14	*Mu	$1/ft\text{-}sec$	.00485	.00457	.00396	.00361	.00332	.00304	.00266	.00243
15	Mw	$1/ft\text{-}sec$	-.00406	-.00401	-.00335	-.00314	-.00278	-.00254	-.00217	-.00196
16	*Mq	$1/sec$	-.7648	-.8166	-.8053	-.8400	-.8468	-.8804	-.8900	-.9209
17	*M_{δ_B}	$\frac{1/sec^2}{in.}$	.2667	.2946	.2241	.2401	.1920	.2040	.1561	.1642
18	M_{δ_C}	$\frac{1/sec^2}{in.}$	-.1261	-.1213	-.1031	-.0949	-.0840	-.0757	-.0646	-.0572
19	Yv	$1/sec$	-.01939	-.01472	-.01892	-.01395	-.01860	-.01360	-.01827	-.01335
20	Yp	ft/sec	-.9316	-.4400	-1.1161	-.4147	-1.3287	-.3988	-1.6800	-.3962
21	Yr	ft/sec	-.03489	-.01400	-.03977	-.00541	-.0401	-.0057	-.0380	.0238
22	Y_{δ_s}	$\frac{ft/sec^1}{in.}$	1.3351	1.3372	1.3143	1.3164	1.3038	1.3050	1.2964	1.2942
23	Y_{δ_R}	$\frac{ft/sec^1}{in.}$	-.06059	-.08461	-.05521	-.07885	-.05509	-.08080	-.05830	-.08427
24	*Lv	$1/ft\text{-}sec$	-.00761	-.00618	-.00672	-.00526	-.00608	-.00456	-.00535	-.00400
25	*Lp	$1/sec$	-.5681	-.6473	-.6508	-.7676	-.7564	-.9035	-.9137	-1.1346
26	Lr	$1/sec$	.02801	.02171	.03631	.01354	.04388	.01156	.05379	.01423
27	*L_{δ_s}	$\frac{1/sec^2}{in.}$	.5376	.6412	.4813	.5838	.4406	.5290	.3931	.4788
28	L_{δ_R}	$\frac{1/sec^2}{in.}$	-.1949	-.2091	-.1852	-.1891	-.1751	-.1704	-.1608	-.1531
29	Nv	$1/ft\text{-}sec$	.0000528	.0000271	.0000556	.0000115	.0000293	.0000193	.0000272	.0000154
30	Np	$1/sec$	-.000647	-.001963	-.000444	-.00371	0.	-.00451	.000309	-.00397
31	*Nr	$1/sec$	-.08745	-.04756	-.08608	-.04190	.08512	-.03903	-.08443	-.03858
32	N_{δ_s}	$\frac{1/sec^2}{in.}$	.000628	.000905	.000785	.000966	.000648	.000829	.000435	.000719
33	*N_{δ_R}	$\frac{1/sec^2}{in.}$	.2305	.1541	.1796	.1116	.1454	.0867	.1119	.0657

*Denotes the most important stability derivatives

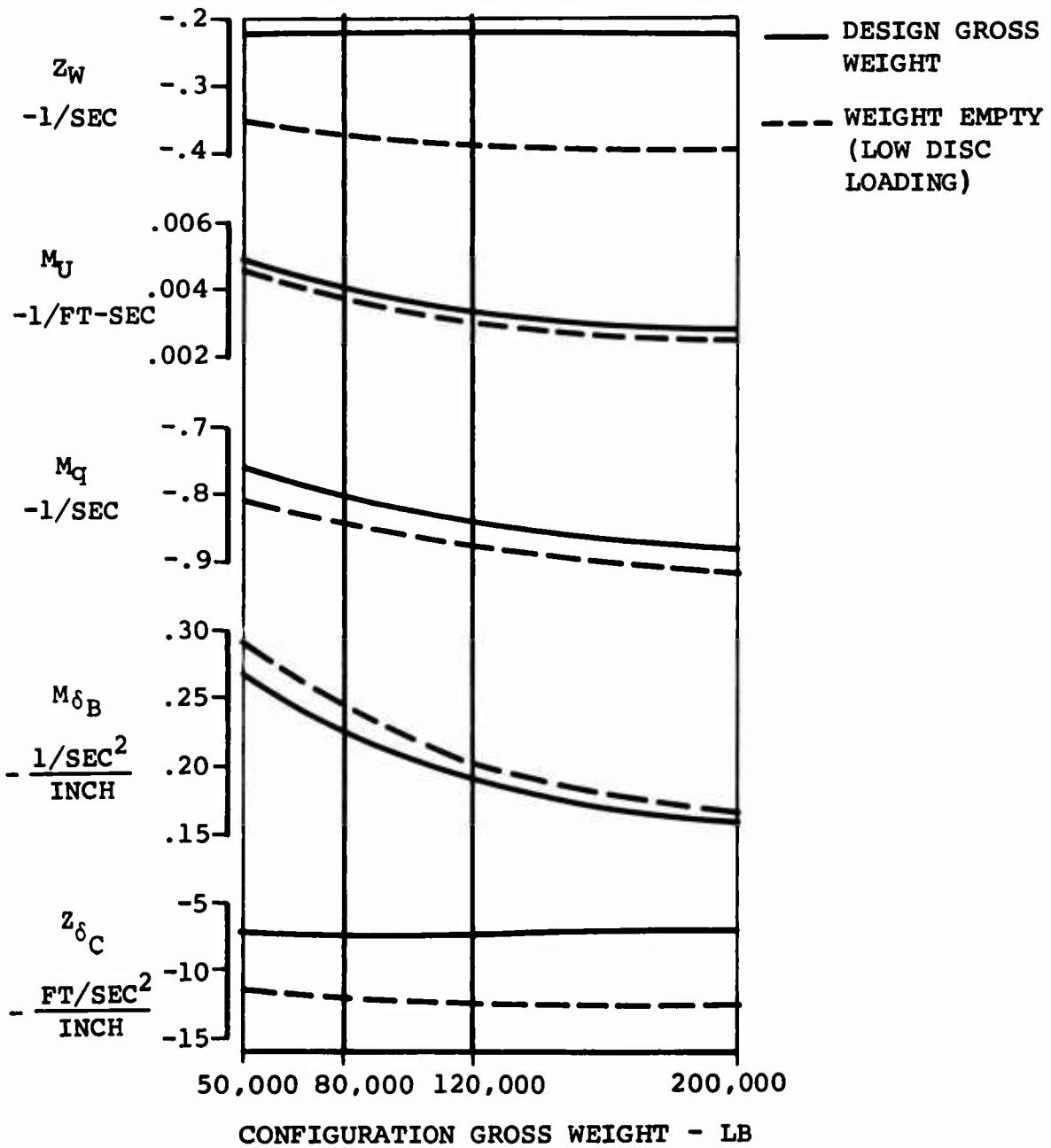

Figure 2. Major Longitudinal Stability Derivatives in Hover.

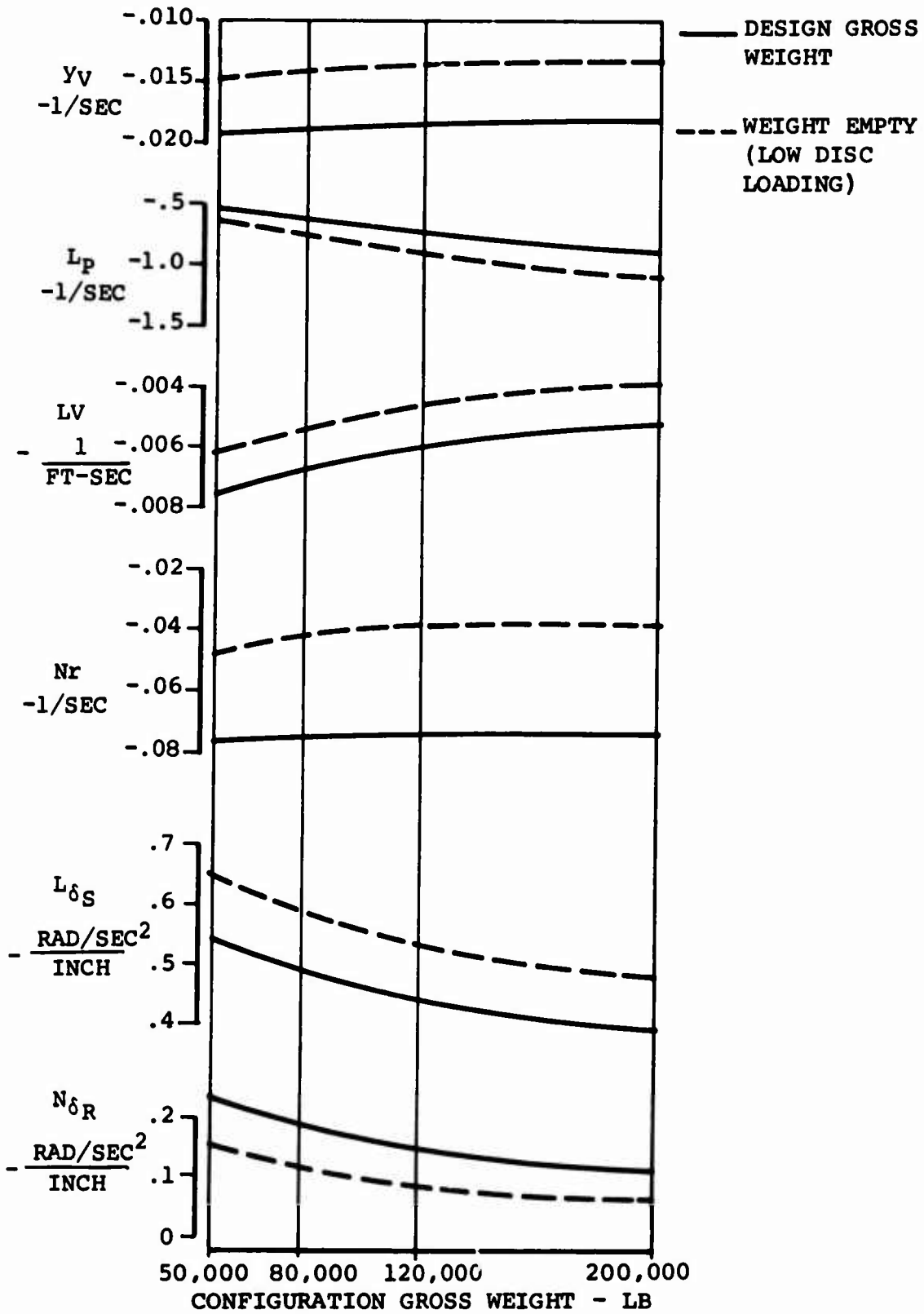

Figure 3. Major Lateral-Directional Stability Derivatives in Hover.

Since the tip speed, V_T, the disc loading, and the blade-chord-to-rotor radius ratio are constant with the configuration gross weight, the vertical damping remains nearly constant with gross weight (see Figure 2). The factor

$$\left(\frac{2C_{T_S}}{a\sigma}\right) \propto \frac{\text{Disc Loading}}{\frac{C}{R}\ Npa\ V_T^2}$$

so at lower disc loading, the vertical damping will increase for a given configuration. This is really the reflection of decreasing helicopter mass as the gross weight of a given configuration is reduced. The slight increase in Z_w for the empty weight configuration with higher design gross weights represents the smaller ratio of empty-to-design gross weight factor for heavier helicopters.

The pitch damping, M_q, in hover is proportional to the vertical damping, so

$$M_q \cong Z_w \left(\frac{\ell^2 m}{I_{yy}}\right)$$

Again, since Z_w is constant with configuration design gross weight, M_q should scale as the factor in brackets. For the particular inertia and aircraft dimension scaling noted in Table I, the scaling factor increases by about 15% from the 50,000-pound to the 200,000-pound configuration. This scaling property is reflected in the increased M_q with configuration design gross weight. At the empty gross weight (low disc loading), the increased M_q is due to lower pitch inertia.

The pitch acceleration due to forward speed, M_u, can be approximated in hover (Reference 1) by the formula

$$M_u = \frac{8g}{V_T}\left(\frac{2C_{T_S}}{a\sigma}\right)\left(\frac{h_{er}m}{I_{yy}}\right)$$

so M_u will scale according to the factor $(h_{er}m/I_{yy})$. The aircraft dimensional and inertia scaling shown in Table I results in a decreasing M_u with the configuration gross weight. The slight decrease in M_u at empty gross weight is due to lower disc loading and lower pitch inertia.

The vertical control sensitivity, Z_{δ_C}, is proportional to the rotor thrust derivative with respect to the blade pitch setting. In hover (Reference 1),

$$Z_{\delta_C} \propto Z_{\delta_C} \cong -\frac{g}{3}\left[\frac{1}{\left(\frac{2C_T}{a\sigma}s\right)\left(1-\frac{a\sigma}{8}\frac{1}{\lambda_o}\right)}\right]$$

so the vertical control sensitivity, Z_{δ_C}, remains nearly constant for all design gross weight configurations (Figure 2) and increases with the lower disc loading (empty gross weight). The increased Z_{δ_C} at low gross weight is again the direct result of lower mass at constant thrust derivative with respect to collective pitch.

The longitudinal stick sensitivity, M_{δ_B}, is directly proportional to Z_{δ_C} in tandem-rotor helicopters, because the pitch control in tandem-rotor helicopters is derived mainly from differential change in blade collective pitch angle on the forward and rear rotors. The variation of M_{δ_B} with aircraft size can then be expressed in the proportional form

$$M_{\delta_B} \propto Z_{\theta_C}\left(\frac{\ell m}{I_{yy}}\right)$$

and M_{δ_B} will scale as the factor $(\ell m/I_{yy})$. For the particular parameters shown in Table I, M_{δ_B} will decrease by more than 40% as the aircraft configuration gross weight is increased from 50,000 pounds to 200,000 pounds.

Lateral-Directional Axis

The most important lateral-directional derivatives in hover are represented by the roll damping, L_p, the yaw damping, L_r, and the roll acceleration due to side velocity, L_v. These derivatives, together with the control sensitivities, L_{δ_S} and N_{δ_R}, define the basic aircraft response to the pilot input in hover.

The roll damping, L_p, is a function of rolling moment due to rotor disc lateral tilting brought about by aircraft roll rate. An approximate expression, valid in hover, is given by

$$L_p \cong -\left(\frac{4}{\gamma V_T}\right)R\left[\frac{h_{er}W_G}{I_{xx}} + \frac{N\sigma_\beta}{RI_{xx}}\left(\frac{e_\beta}{R}\right)V_T^2\right]$$

As shown in Table I, V_T is constant and γ is nearly constant for all gross weight configurations. L_p will then scale as the rotor radius multiplied by the expression in brackets. The expression in brackets is plotted in Figure 4 in terms of

THRUST TILT CONTRIBUTION: $L'_{AIC} = \frac{her\ W_G}{I_{xx}}$

CENTRIFUGAL MOMENT CONTRIBUTION: $L''_{AIC} = \frac{N\sigma\beta V_T^2}{RI_{xx}}\left(\frac{e\beta}{R}\right)$

W_G = TOTAL GROSS WEIGHT

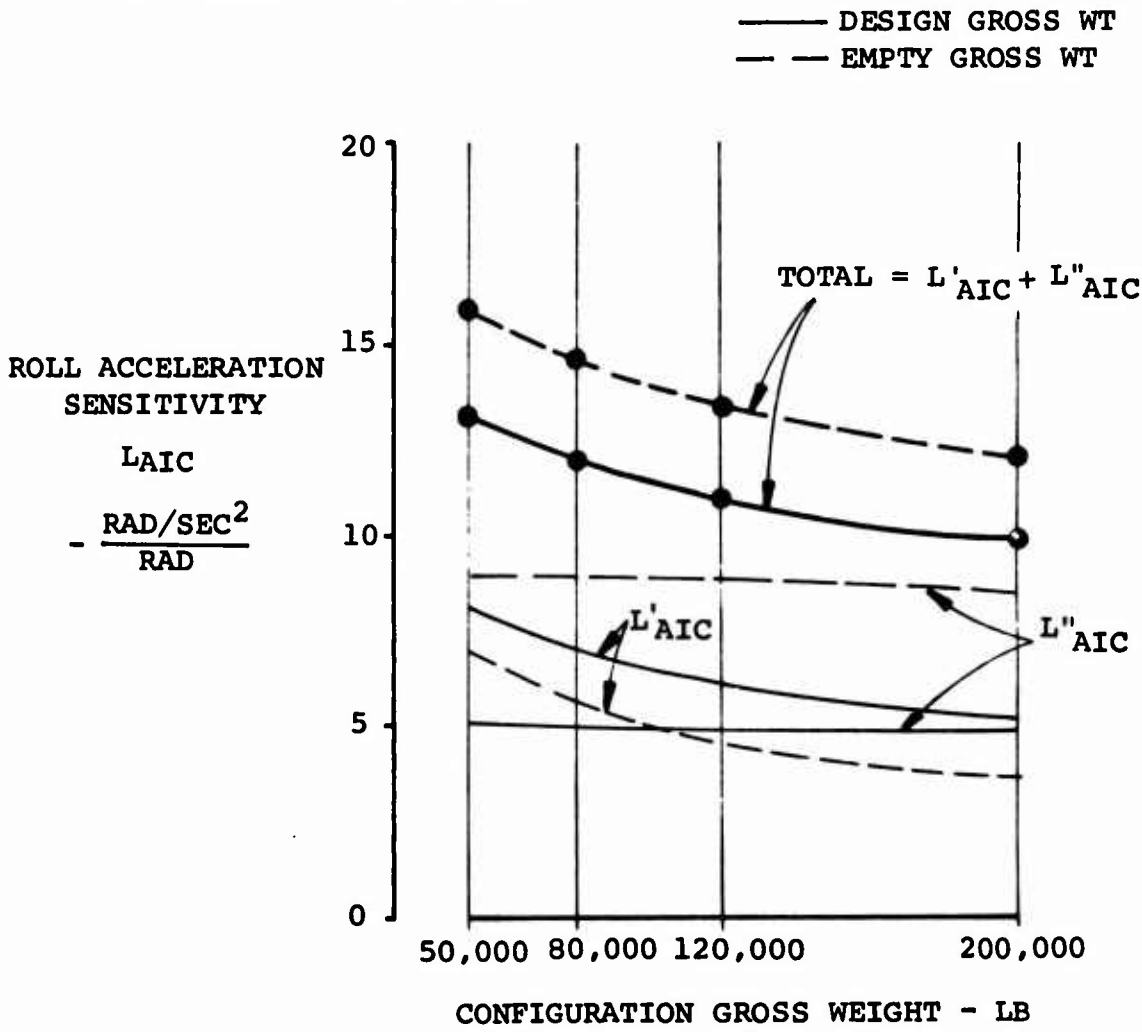

Figure 4. Average Roll Acceleration Sensitivities to Rotor Disc Tilt in Hover.

the rotor thrust tilt contribution, $L'_{A_{1C}}$, and the centrifugal moment part, $L''_{A_{1C}}$, and as the sum $(L'_{A_{1C}} + L''_{A_{1C}})$, the total roll acceleration sensitivity. As shown in the figure, the total sensitivity decreases with the configuration gross weight, but the decrease is much less than the inverse ratio of rotor radii. L_p will then increase with configuration gross weight as shown in Figure 3. At empty gross weights, the higher L_p is a reflection of the dominant contribution of the centrifugal forces to the rolling moment, which scales as the inverse ratio of roll inertia.

The yaw damping, N_r, is related to the rotor disc tilt brought about by lateral translational velocities at forward and aft rotors. As such, it is a direct function of Y_v of each rotor, which can be approximated in hover by the formula

$$Y_v \cong - \frac{8g}{V_T} \left(\frac{2C_T s}{a\sigma} \right)$$

then

$$N_r \propto Y_v \frac{\ell^2 m}{I_{zz}}$$

At constant disc loading and constant (C/R), Y_v will remain constant for all gross weight configurations. At lower disc loading (e.g., weight empty), Y_v will decrease proportionately to the disc loading. The yaw damping will then scale with configuration gross weight as the ratio $(\ell^2 m/I_{zz})$, which, for the parametric aircraft definition given in Table I, is equal to unity at the design gross weight, and somewhat less than unity at the empty gross weights. Consequently, the yaw damping, N_r, remains nearly constant with the design gross weight and is decreased uniformly at lower disc loading.

The roll acceleration due to sideward velocity, L_v, is also directly related to the rotor disc tilt brought about by the side velocity. As such, its dependence on design gross weight configurations can be related to Y_v in the proportional form

$$L_v \propto Y_v \left(\frac{h_{er} m}{I_{xx}} \right)$$

The scaling factor $(h_{er} m/I_{xx})$ decreases with the design gross weight, while Y_v remains constant. The derivative L_v will then decrease at higher design gross weights. It will also decrease proportionately with the disc loading.

The lateral cyclic control sensitivity, L_{δ_s}, is a direct function of the lateral rotor disc tilt per unit of cyclic pitch angle. In general, the rolling moment per unit cyclic pitch comprises two most powerful contributions: the lateral component of the thrust, and the hub moment due to the offset flapping hinges. At hover, L_{δ_s} can be approximately defined in terms of roll moment per unit lateral cyclic in the form

$$L_{\delta_s} \propto L_{AIC} \cong \frac{1}{I_{xx}}\left[h_{er} W_G + \frac{N\sigma_\beta}{R}\left(\frac{e_\beta}{R}\right)V_T^2\right]$$

The first term in the brackets represents the contribution of the thrust tilt, while the second is the centrifugal force moment. The first factor will scale with the design gross weight as $(h_{er}W_G/I_{xx})$, and will therefore decrease with increasing design gross weight, diminishing slightly at empty gross weights (see Figure 4). The second factor remains constant at all configuration gross weights, but scales as $\left(\frac{1}{I_{xx}}\right)$ from normal gross weight to weight empty. This centrifugal force contribution will remain essentially constant with disc loading.

The yaw control sensitivity, N_{δ_R}, for a tandem-rotor helicopter is generated by the lateral cyclic pitch applied differentially on forward and aft rotors. As such, it can be expressed by the following approximate formula, based on thrust tilt, above:

$$N_{\delta r} \propto N_{AIC} = \ell W_G/I_{zz}$$

$N_{\delta r}$ will then scale as the factor $(\ell W_G/I_{zz})$, and will therefore decrease with the increased configuration gross weight. The diminishing property of $N_{\delta r}$ at empty gross weight (see Figure 3) is attributable to the particular geometric and inertial scaling properties of the configurations, rather than to disc loading effects.

Dynamic Properties of Basic Aircraft Configurations

The dynamic characteristics discussed in this section are based on aircraft rigid-body behavior as defined by the uncoupled longitudinal and lateral-directional stability derivatives listed in Table VIII. An approximation of the characteristic roots in hover, based on Reference 1, is used to elucidate the variations in these roots with configuration gross weight and disc loading. The complete dynamic characteristics, without simplifications, are tabulated in Table IX.

TABLE IX. LATERAL-DIRECTIONAL AND LONGITUDINAL ROOTS IN HOVER

Mode \ Configuration		50,000 Lb		80,000 Lb		120,000 Lb		200,000 Lb	
		Full Gr Wt	Wt Empty	Full Gr Wt	Wt Empty	Full Gr Wt	Wt Empty	Full Gr Wt	Wt Empty
Lateral-Directional									
Roll Subsidence		-.891	-.900	-.920	-.957	-.975	-1.042	-1.074	-1.223
Spiral		-.0871	-.0472	-.0857	-.0415	-.0848	-.0386	-.0840	-0.0385
Dutch Roll	Frequency Rad/Sec	.501	.455	.468	.411	.437	.370	.394	+0.322
	Real Part I/Sec	.152	.119	.125	.0876	.0998	.0623	.0708	+0.0374
Longitudinal									
Pitch Subsidence		-.945	-.976	-.952	-.970	-.967	-.987	-.985	-1.005
Vertical		-.222	-.352	-.228	-.372	-.224	-.384	-.225	-.392
Oscillatory	Frequency Rad/Sec	.390	.375	.353	.336	.323	.307	.288	.273
	Real Part I/Sec	.0806	.0715	.0639	.0565	.0510	.0451	.0383	.0337

Longitudinal Dynamics

The longitudinal dynamics in hover can be approximated by the following expressions for the corresponding characteristic roots:

Vertical Mode: $r_w = Z_w$

Pitch Subsidence Mode: $r_q = M_q$

Pitch - Longitudinal Oscillations ($M_q < 0$):

$$r_{qu} = \frac{1}{2}\left(\frac{M_u g}{M_q^2}\right) \pm \left(\sqrt{\frac{M_u g}{|M_q|}}\right) i$$

Vertical Mode: This mode determines the aircraft vertical velocity response to collective stick, with the time constant equal to

$$\tau_w = \frac{1}{|Z_w|}$$

Figure 2 shows that the vertical response at normal gross weight remains constant for all configurations with a time constant of 4.5 seconds. At weight empty, the vertical time constant will shorten to less than 3.0 seconds. Such time constants are too long for precise vertical control, and collective control augmentation will be required for precise hover tasks.

Pitch Subsidence Mode: As shown in Table IX, the pitch subsidence mode remains nearly constant for all gross weight configurations with a time constant of 1 second. Pitch damping augmentation will be required in order to improve pure pitch control and reduce the pitch time constant to a reasonable magnitude.

Longitudinal Oscillatory Mode: This mode does not determine the actual aircraft response to pilot inputs, but its unstable character is generally detrimental to control in any turbulence level. The frequency and the damping ratio of this mode are functions of the ratio of M_u to M_q alone, so the mode changes very little with gross weight configuration and disc loading. The unstable feature of this mode in all hovering helicopters is easily suppressed by pitch damping augmentation through the differential collective pitch feedback.

Lateral-Directional Dynamics

The lateral-directional dynamics in hover can be described by the following approximate expressions for the characteristic roots (poles):

Roll Subsidence Mode: $r_{rs} = L_p$

Spiral (Yaw) Mode: $r_{sp} = N_r$

Dutch Roll Mode: $r_{dr} = \frac{1}{2}\left(\frac{L_v g}{L_p^2}\right) \pm \left(\sqrt{\frac{L_v g}{|L_p|}}\right) i$

The roll subsidence mode is the primary response mode around which the pilot controls the helicopter in roll and sideward motion. As shown in Table IX, the time constant of this mode, equal to $|1/r_{rs}|$, remains between 1.1 and 0.9 second for all gross weight configurations. As such, it is generally too long for precise control, so roll rate feedback is generally required to improve the roll control on tandem, fully articulated rotors.

The spiral or yaw mode in hover determines the aircraft response to pedals. In tandem-rotor helicopters this mode is nearly neutrally stable (see Table IX) because of insignificant directional stability in hover. For precise control, all gross weight configurations will require stability augmentation in the yaw axis.

The Dutch roll mode is an unstable oscillatory mode dominated by roll and sideward motion with some yaw. The unstable character of this motion is generally detrimental to aircraft control in any turbulence in hover. In hover the mode can be stabilized usually by a tight roll feedback loop (rate and attitude).

FULL-FLIGHT ENVELOPE MATHEMATICAL MODEL

The airframe and the control system analytical models outlined in this section are the same as the standard Boeing-Vertol model utilized for the piloted simulation of the Model 347 helicopter and for Heavy Lift Helicopters. As such, the model contains all the basic features of tandem-rotor helicopters, including a simplified external load suspension system utilizing two longitudinally disposed cables. Only the basic features of the model are described in this report. A detailed description of the model is contained in Reference 5.

AIRFRAME DYNAMIC MODEL

The airframe and rotor dynamic model used for the full-flight envelope tandem helicopter simulation is described in this section. To illustrate how this model works, brief descriptions of each major calculation have been prepared and are presented below in the general order in which they are performed, starting with equations of motion and working back around to the forces and moments which drive these motion equations.

Figure 5 illustrates, in block diagram format, how the various calculations in the model are related. Shown at the far right-hand side of the chart are the equations of motion being fed by the summed forces and moments. Other portions of the diagram are associated with the computational steps described below.

Airframe Calculation Summary

1. Basic equations of motion are solved, providing linear and angular accelerations about all three axes. Euler angle rotations are performed to orient the airframe in inertial space.

2. Remote velocity is resolved into the body axis to provide fuselage angle of attack and sideslip information. Effect of wind on velocity resolution is considered, as is forward rotor downwash interference on fuselage.

3. Remote velocity is resolved through rotor shaft incidence angle (and is corrected for aircraft pitching motion) to derive rotor shaft normal plane (S.N.P.) wind axis velocities and sideslip (β) values.

4. Rotor advance (μ) and inflow (λ) ratios are computed. Inflow ratio calculations account for rotor-on-rotor interference.

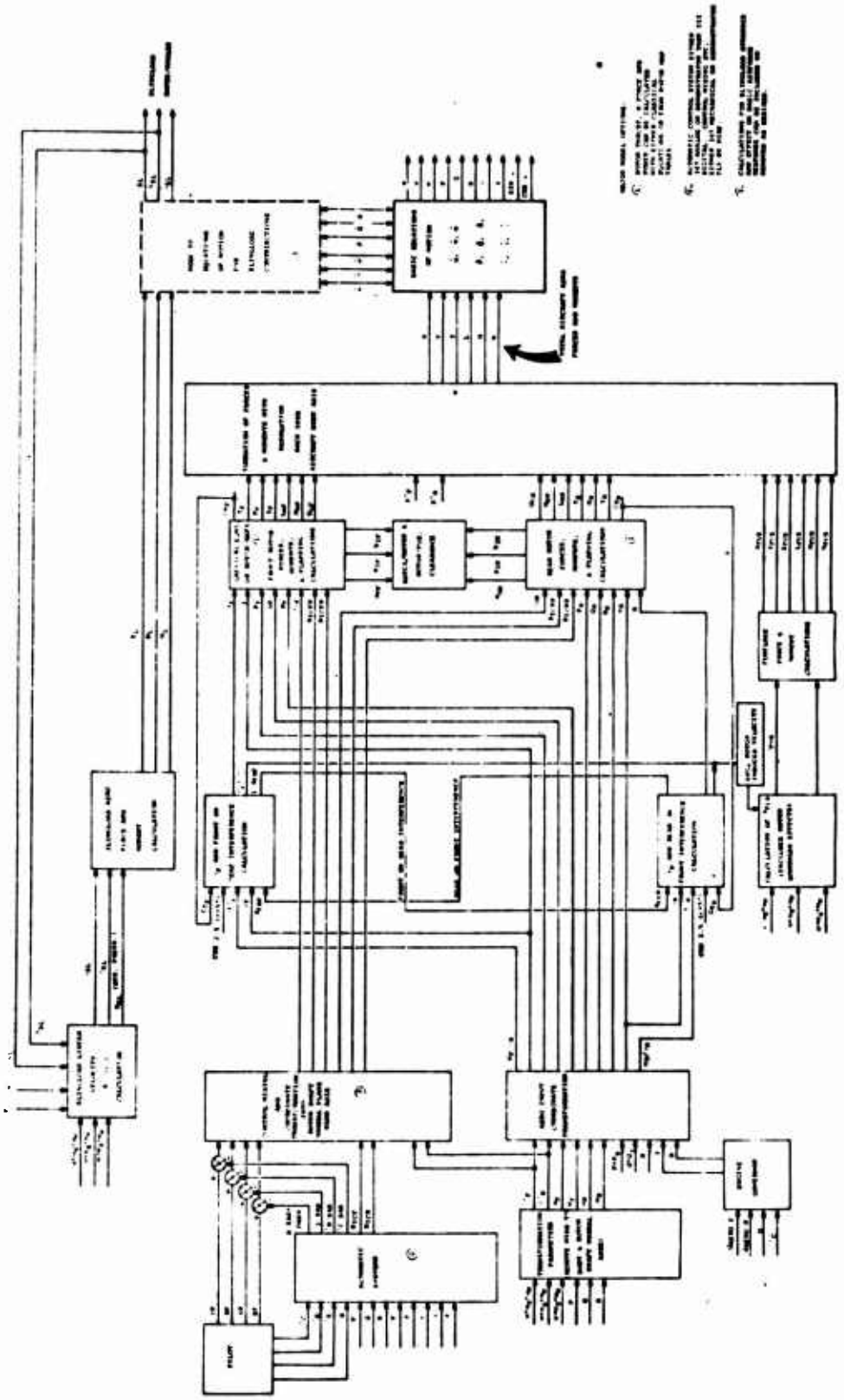

Figure 5. Tandem-Rotor Helicopter Aircraft Mathematical Model.

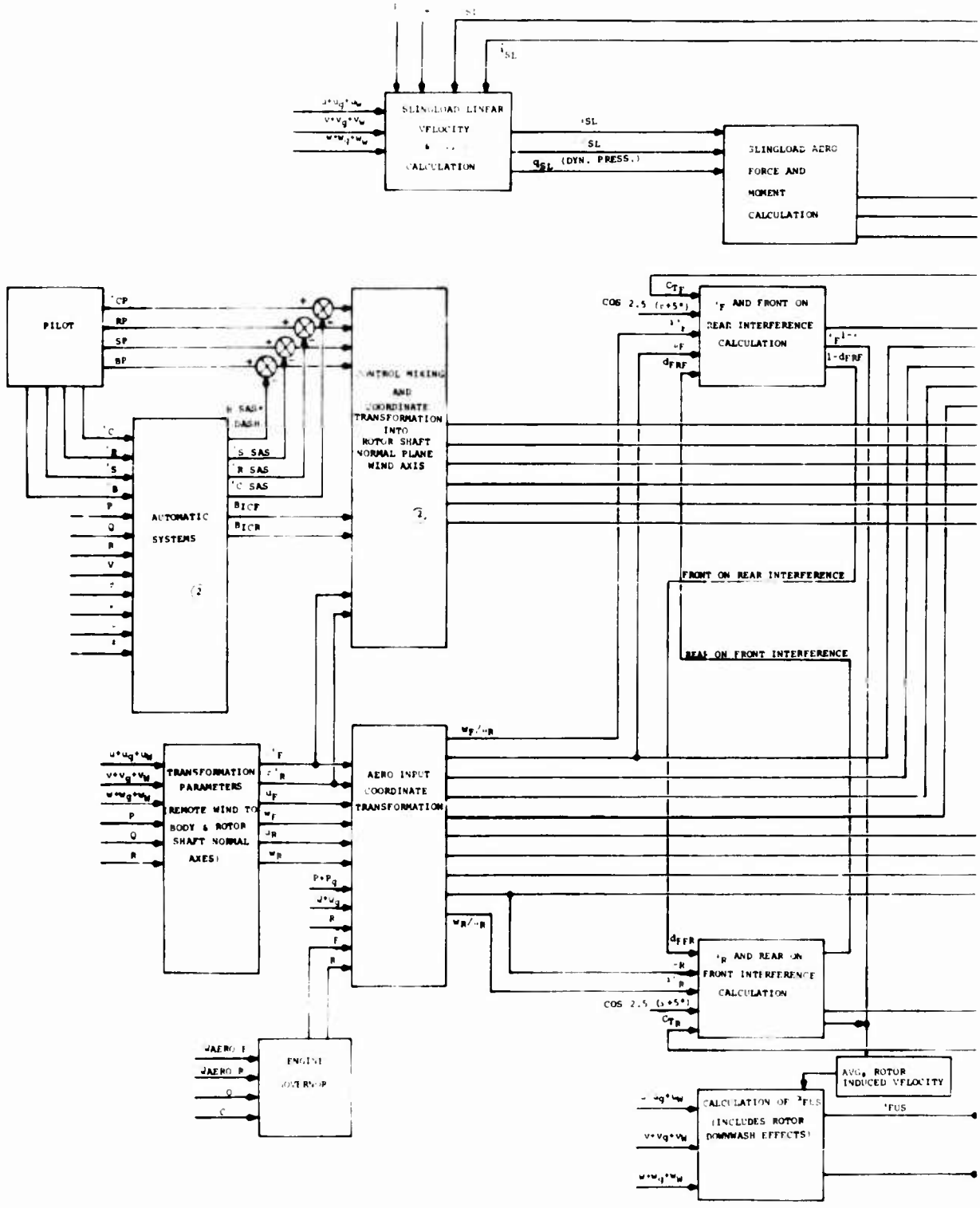

Figure 5. Tandem-Rotor Helicopter Aircraft Mathematical Model.

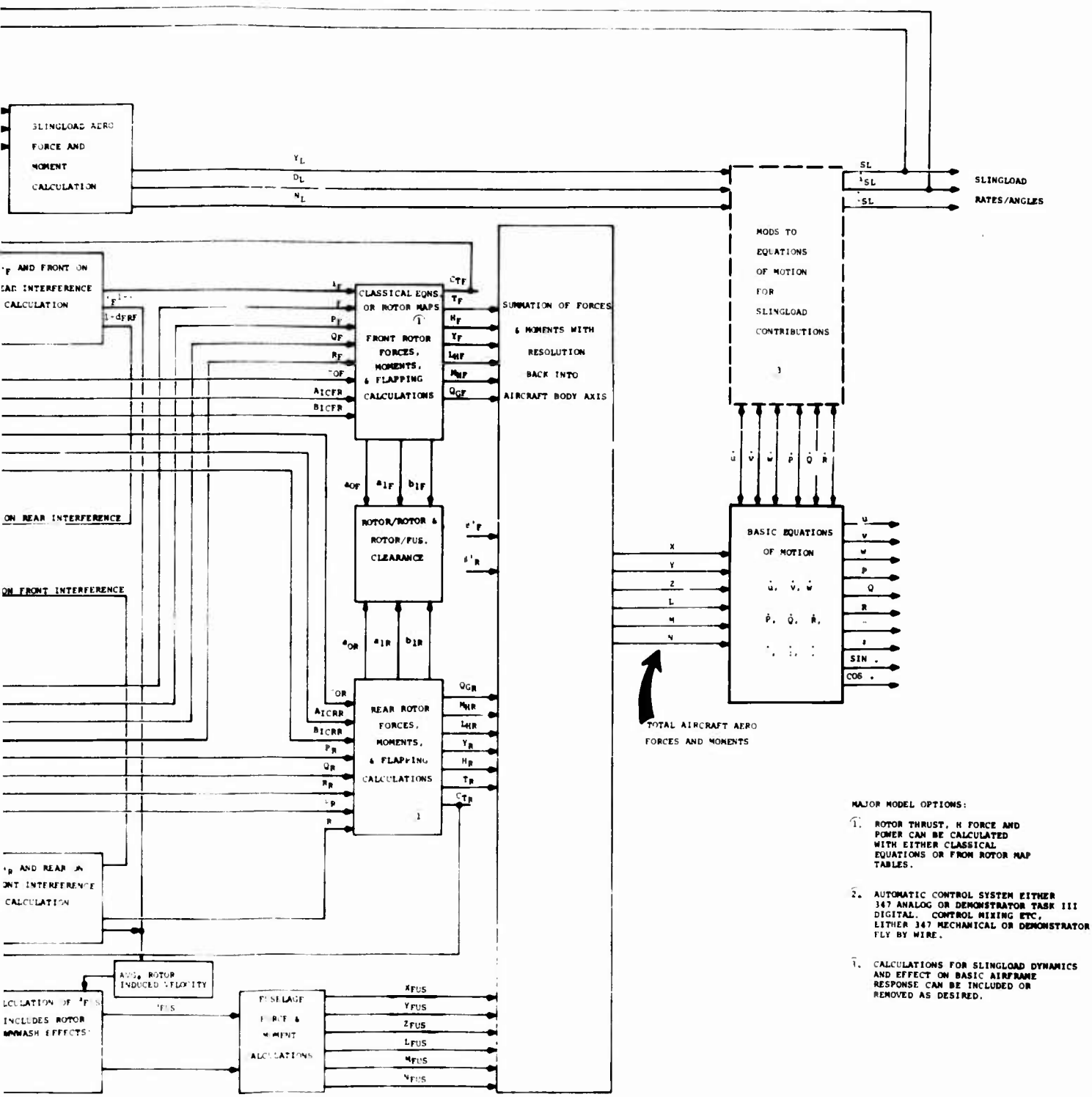

MAJOR MODEL OPTIONS:

1. ROTOR THRUST, H FORCE AND POWER CAN BE CALCULATED WITH EITHER CLASSICAL EQUATIONS OR FROM ROTOR MAP TABLES.

2. AUTOMATIC CONTROL SYSTEM EITHER 347 ANALOG OR DEMONSTRATOR TASK III DIGITAL. CONTROL MIXING ETC, EITHER 347 MECHANICAL OR DEMONSTRATOR FLY BY WIRE.

3. CALCULATIONS FOR SLINGLOAD DYNAMICS AND EFFECT ON BASIC AIRFRAME RESPONSE CAN BE INCLUDED OR REMOVED AS DESIRED.

aft

5. Control axis angle of attack (α_{CA}) for each rotor is calculated. Rotor-rotor interference effects are included.

6. Rotor input collective and cyclic controls (θ_o, B_{1C}, A_{1C}) are compiled, and both longitudinal and lateral cyclics are resolved through the rotor sideslip angle to align controls orthogonal to the local wind. Forward rotor cyclic inputs are corrected for delta three (δ_3) hinging effects.

7. Coning (a_o), longitudinal (a_1), and lateral (b_1) first-harmonic flapping coefficients are computed, and first-order dynamic lags are applied to account for rotor system flapping response.

8. Rotor forces and moments are computed using either:

   a. The classical equation method, with forces resolved perpendicular and parallel to the shaft normal plane and aligned with the S.N.P. wind axis, or

   b. The rotor map approach with thrust, power and rotor propulsive force derived from tabular isolated rotor or wind tunnel data and expressed in the rotor wind axis.

9. Fuselage aerodynamic forces and moments are calculated from tabular wind tunnel derived data.

10. Rotor aerodynamic forces and moments are resolved through rotor sideslip and shaft incidence angles back into the aircraft body axis. Summation of these resolved forces and moments with body axis fuselage forces and moments is performed, and to these values are added the moments imposed upon the airframe by individual rotor forces. The force and moment sums are inserted into the equations of motion to again compute the airframe acceleration set.

11. Engine governor response to aerodynamic rotor power requirements is computed, along with individual rotor speed degrees of freedom. Rotor shaft windup spring rates are accounted for in the governor model.

On the left-hand side of Figure 5 are shown the cockpit and automatic system control inputs. The automatic systems are not covered in this report in order to keep the rather complicated airframe calculation discussion as simple as possible for clarity. Reference 5 presents a comprehensive explanation of all control system functions along with the appropriate modeling equations.

TANDEM-ROTOR MECHANICAL CONTROL SYSTEM MODEL

The hybrid mechanization of the mechanical and automatic control system model is described in this section. It includes the 347 conventional mechanical control system.

Figure 6 shows a functional block diagram explaining the operation of a typical tandem-rotor helicopter mechanical control system. Shown on the left-hand side of the diagram are the lateral (δ_S), longitudinal (δ_B), directional (δ_R), and collective (δ_C) cockpit control inputs made by the pilot or generated analytically.

Before controls are mixed mechanically, the high-authority differential airspeed hold (DASH) input is summed with the longitudinal stick, and the lower directional SAS is added to the pilot pedal input as shown on the chart. Control mixing then takes place, with collective pitch inputs (resulting from δ_B and δ_C inputs) going to each head, along with lateral cyclic pitch which is related to δ_R and δ_S inputs. Note that the collective (θC_F, θC_R) and differential collective (θB_F and θB_R) controls are referenced to the full-down collective position on each rotor head (θT_F and θT_R).

After the mechanical control mixing is accomplished, SAS inputs are summed, and the controls are passed through a second-order upper boost model. The boost actuators are designated as being either swiveling or pivoting, depending upon their primary function on the actual aircraft (note the S or P subscripts). For both rotors, the boost actuators operate either together, to produce collective pitch, or differentially, to produce lateral cyclic pitch.

After being processed through the upper boost system, control inputs are "unmixed", so they can be used in the "classical" equations or with the rotor maps. Before the lateral (A_{1C}) controls are transformed into the S.N.P. wind axis, longitudinal (B_{1C}) inputs are added. Longitudinal cyclic pitch for each rotor is put in according to "q" sensed schedules which vary with calibrated airspeed. Longitudinal cyclic may be put in by the pilot in conjunction with the AFCS.

Longitudinal cyclic actuator dynamics as shown in Figure 6 are modeled with a simple first-order lag. Because of the relatively high frequencies involved in the SAS actuators, no dynamics associated with their operation are included.

All equations describing the conversion of cockpit controls to the equivalent blade pitch angle, control mixing equations to accommodate the SAS motion reference, and the final conversion to the blade pitch angles used for rotor map readings are detailed in Reference 5.

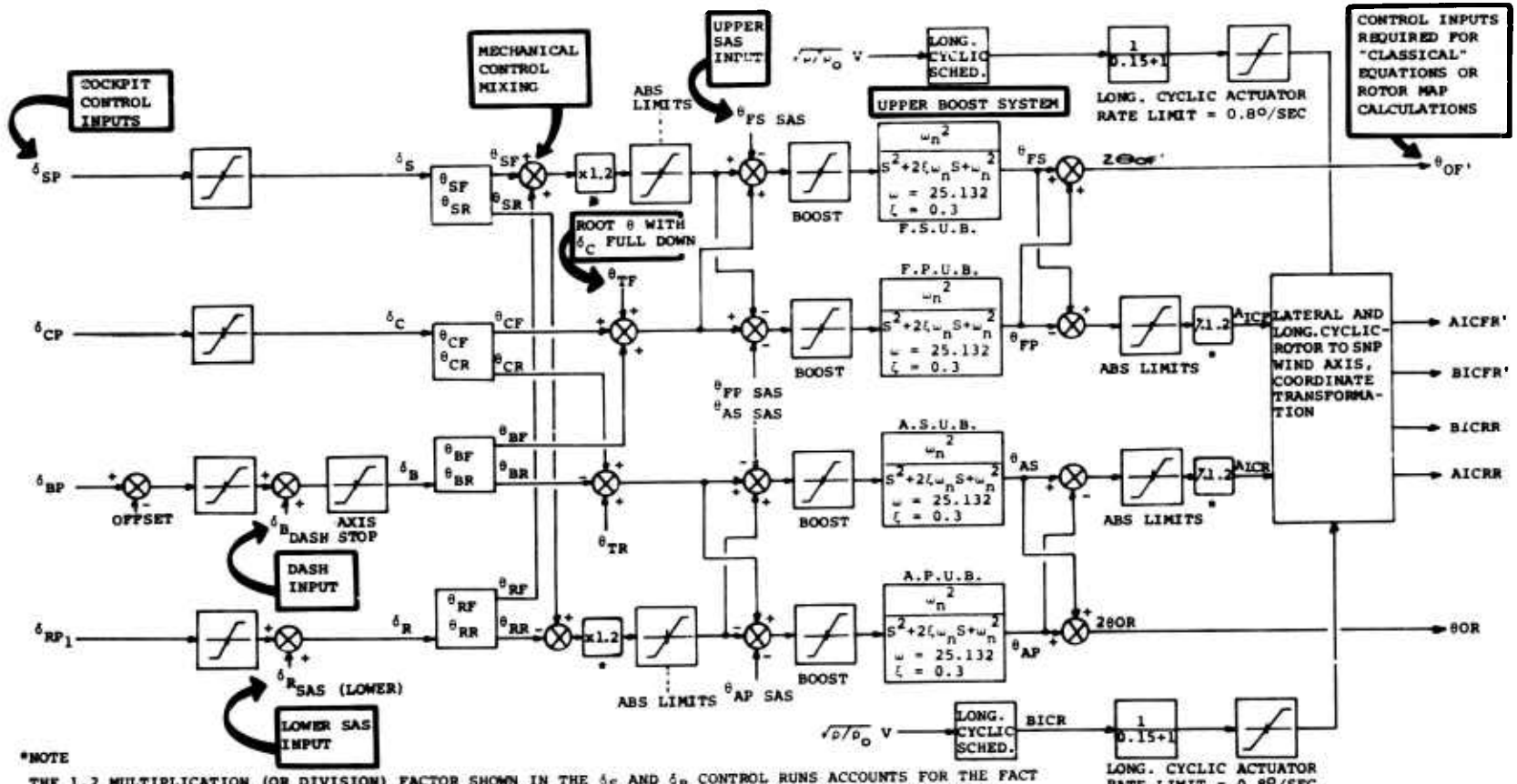

Figure 6. Tandem-Rotor Helicopter Mechanical Control System Functional Block Diagram.

SMALL-MOTION EXTERNAL LOAD MODEL

The aircraft equations of motion shown schematically in Figure 5 include a simplified external load model based on a two-poir suspension system. The modified equations are shown in this section together with load aerodynamic properties.

The simplified external load model is based on three additiona degrees of freedom which permit longitudinal, lateral and yaw motions of the load, all measured with respect to the airframe The three load degrees of freedom are defined by cable angles (see Figure 7) μ_{SL}, λ_{SL} and ν_{SL}.

The three additional equations of motion for the sling load compute angular acceleration of the cables, i.e., $\ddot{\mu}_{SL}$, $\ddot{\lambda}_{SL}$, and $\ddot{\nu}_{SL}$. Along with these changes are terms added into the original six airframe equations of motion reflecting coupling, which is expressed as a function of μ_{SL}, $\dot{\mu}_{SL}$, λ_{SL}, $\dot{\lambda}_{SL}$, ν_{SL}, and $\dot{\nu}_{SL}$.

The external load equations are based on derivations in Reference 5. As such, they are the simplest ones and are valid for relatively small angular motions (15° or less) of the two-poin parallel cable suspension. A general external load model, based on total force approach, which includes the tether restraints with elastic or inextensible cable, is described in detail in Appendix I.

FULL-FORCE EXTERNAL LOAD MODEL

While the small-motion external load analytical model describe in Reference 5 is adequate for most hover and forward flight simulation tasks in which cable tensions remain nearly constant, it is difficult to adapt to special transition conditions such as may be encountered during external load lift-off, from both cable unloaded through partial cable tension, to the fully airborne state. For this reason, a different set of equations has been derived to accommodate the simulation of these special flight conditions. These equations treat the external load as an independent rigid body, with its own six degrees of freedom, and specify a set of helicopter and external load forces which couple the two bodies by means of two arbitrarily located elastic or inextensible cables. The detailed derivation, based on the Lagrangian approach applicable to the system with constraint equations, is presented in Appendix I.

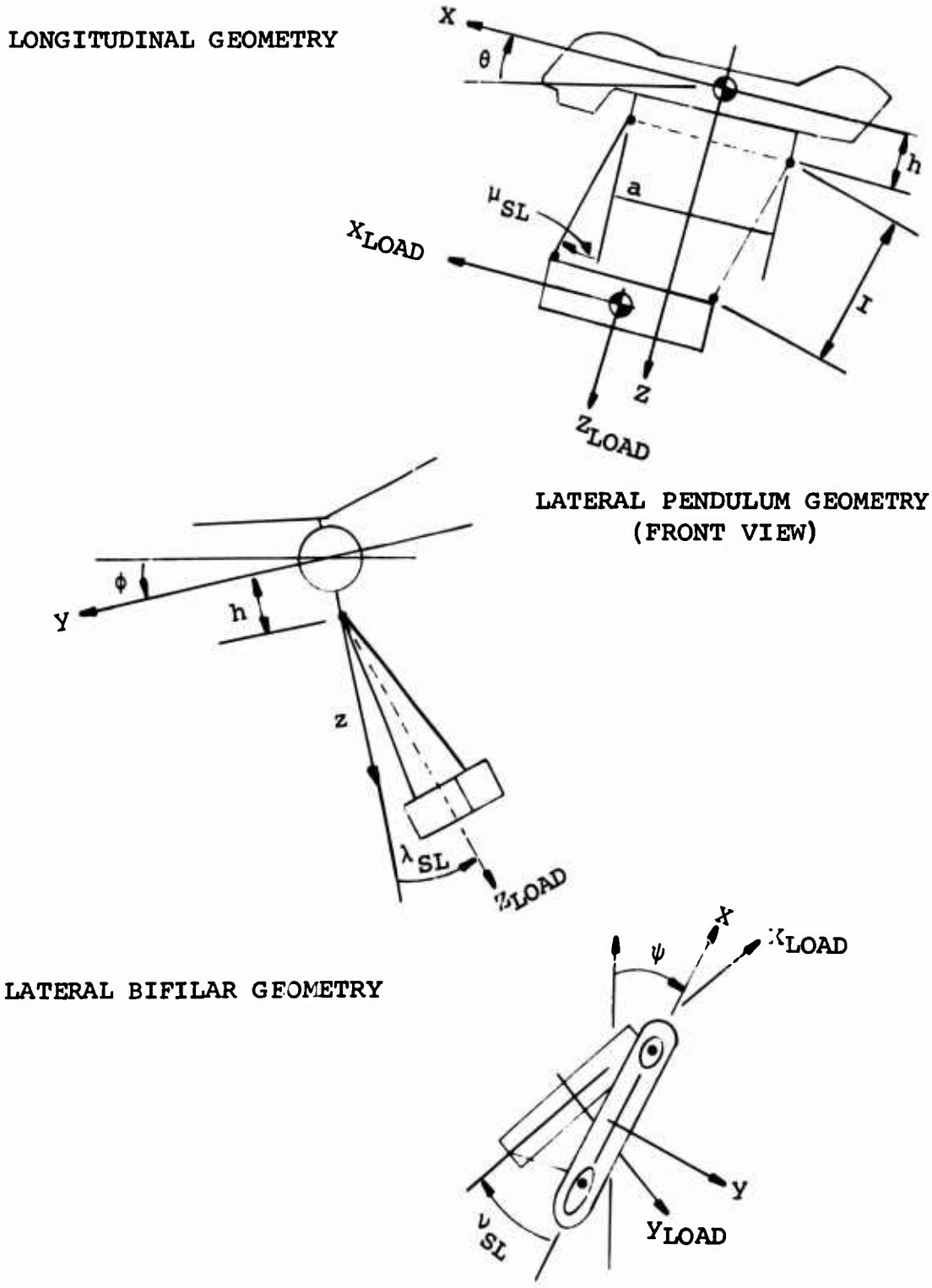

Figure 7. Simplified External Load Model Geometry.

Figure 8 illustrates the model for the combined external load and helicopter system. The formulation is sufficiently general to accommodate the following features:

- Arbitrary location of two hooks on the aircraft and attachment points on the load.
- Elastic or inextensible cables.
- All inertia properties of the external load.

In the preliminary evaluation of the elastic cables versus the inextensible cable formulation, it was established that the simulation of elastic cables will be simpler for two basic reasons: first, in the case of inextensible cables, the solution of constraint equations, arising from forcing the cables to be infinitely stiff in axial direction, will require more computation to restrain the motion, including the computation of linear position, velocities, and accelerations along the direction of cables; second, when the cables become transiently unstressed (slack), the return to the stressed state with inextensible cables will require the computation of impulsive forces which must be applied to effect a stepwise change in linear and angular (aircraft and load) velocities resulting from sudden tautness of the cables. The elastic cable formulation requires only a continuous tracking of cable stretch magnitudes and rates. The transient cable slacking and stressing will be automatically accommodated by cable elastic forces alone.

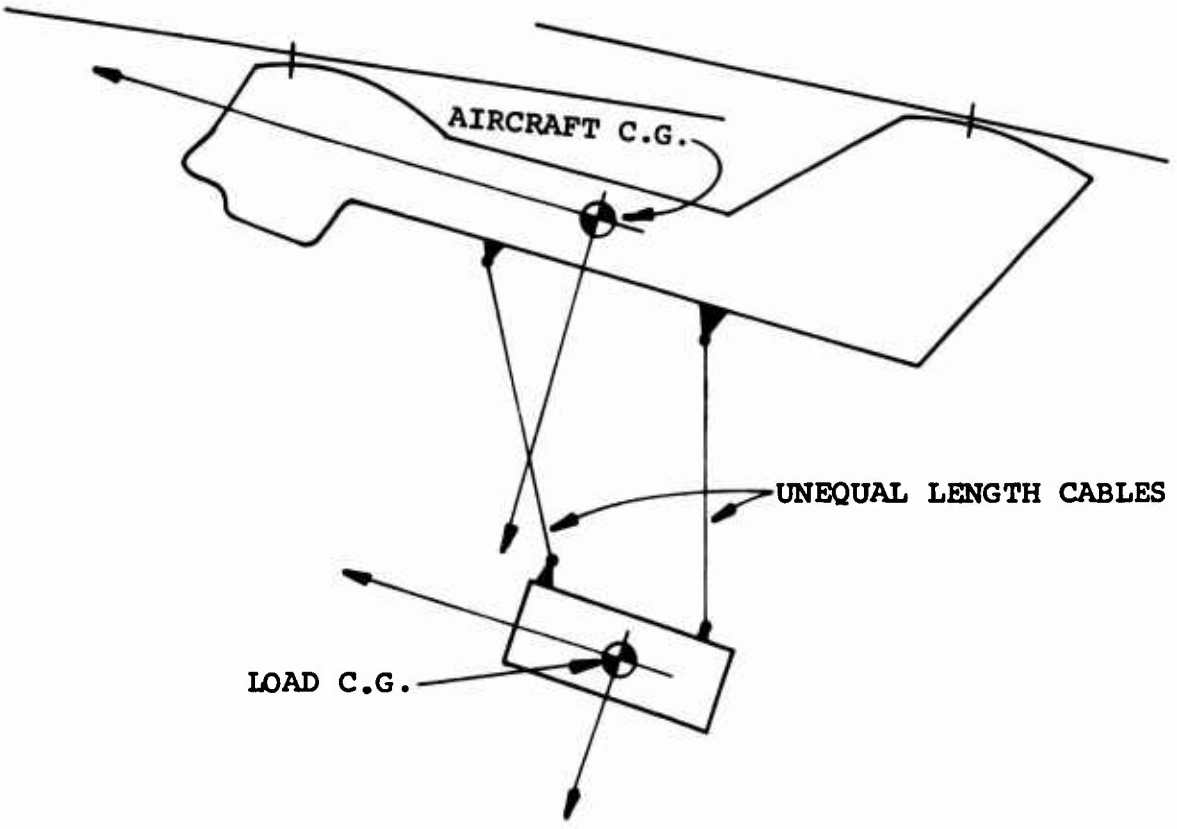

Figure 8. Full Force External Load Model (Side View).

ANALYTICAL STUDY OF ADVANCED TANDEM-ROTOR HELICOPTER (ATH) HOVER PERFORMANCE

The procedure that was followed in analyzing comparable precision hover performance of a hover hold system and a pilot was:

1. Investigate unaugmented helicopter characteristics.
2. Improve helicopter handling qualities through stability augmentation loops.
3. Synthesize hover hold system and estimate hover hold performance in turbulence.
4. With hover hold system off, estimate pilot-in-the-loop hover hold performance and pilot workload in turbulence.

UNAUGMENTED AIRCRAFT

To represent the motion of the rigid-body helicopter, a set of small-perturbation differential equations was used. The equations, as presented in Figure 9, represent the unaugmented helicopter, separated into longitudinal-vertical motion and lateral-directional motion. This separation of axes was maintained throughout the analysis. In later sections, these equations were modified and added to, to include the effects of gusts, augmentation, and pilot model. The equations are in first-order form suitable for state matrix evaluations.

Longitudinal-Vertical Motion

Figure 10 shows the effect that helicopter size has on the longitudinal-vertical eigenvalues (roots of the characteristic equation). As shown, the vertical, or plunging, mode (Z_w) remains relatively constant with increasing size. The short-term pitching mode (M_q) also remains relatively constant. However, the unstable second-order response, which is reflective of the long-term speed and attitude changes, shows a slight decrease in instability and a slight reduction in frequency.

Lateral-Directional Motion

Figure 11 shows the effect that helicopter size has on the lateral-directional eigenvalues. The stable aperiodic mode that corresponds to N_r shows little effect in changing size. The other aperiodic mode is predominantly roll rate damping (L_p) and shows a slight decrease in time to half amplitude with increasing size. The eigenvalue at the origin corresponds to the neutral stability associated with heading

(1) $\dot{u} = X_u U + X_w W + (Xq - W_o)q - g\theta$

(2) $\dot{w} = Z_u U + Z_w W + (Zq + U_o)q$

(3) $\dot{q} = M_u U + M_w W + M_q q$

(4) $\dot{\theta} = q$

(a) LONGITUDINAL-VERTICAL EQUATIONS

(1) $\dot{V} = Y_v V + (Y_p + W_o)p + (Y_r - U_o)r + g\,\phi$

(2) $\dot{p} = \left(\frac{I_{XX}I_{ZZ}}{I_{ZZ}I_{XX} - I_{XZ}^2}\right)\left[\left(L_v + \frac{I_{XZ}}{I_{XX}} N_v\right) V + \left(L_p + \frac{I_{XZ}}{I_{XX}} N_p\right)p + \left(L_r + \frac{I_{XZ}}{I_{XX}} N_r\right) r\right]$

(3) $\dot{r} = \left(\frac{I_{XX}I_{ZZ}}{I_{ZZ}I_{XX} - I_{XZ}^2}\right)\left[\left(N_v + \frac{I_{XZ}}{I_{ZZ}} L_v\right) V + \left(N_p + \frac{I_{XZ}}{I_{ZZ}} L_p\right)p + \left(N_r + \frac{I_{XZ}}{I_{ZZ}} L_r\right) r\right]$

(4) $\dot{\phi} = p$

(5) $\dot{\Psi} = r$

(b) LATERAL-DIRECTIONAL EQUATIONS

Figure 9. Linear Aircraft Equations of Motion.

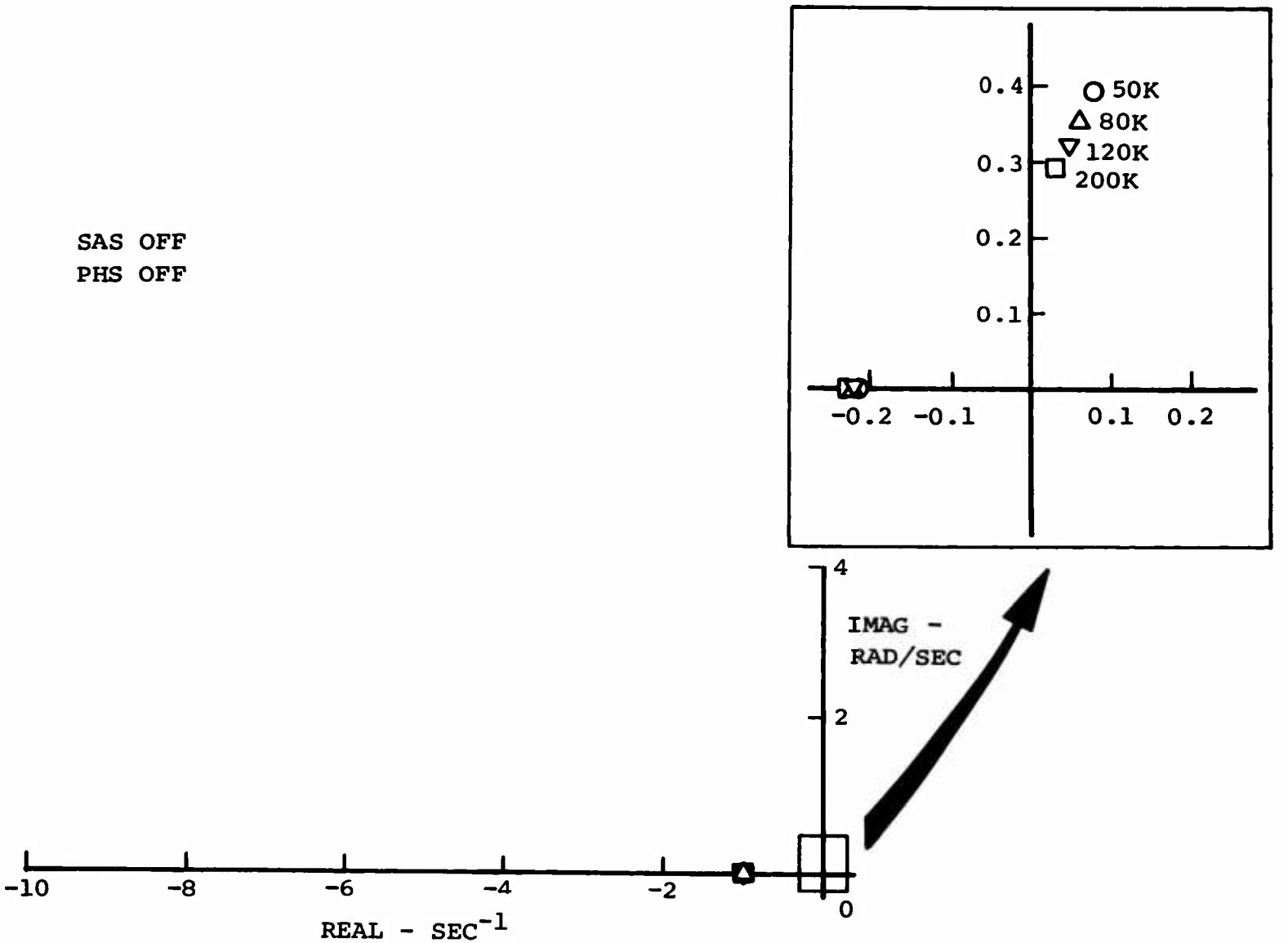

Figure 10. Longitudinal System Effect of Gross Weight.

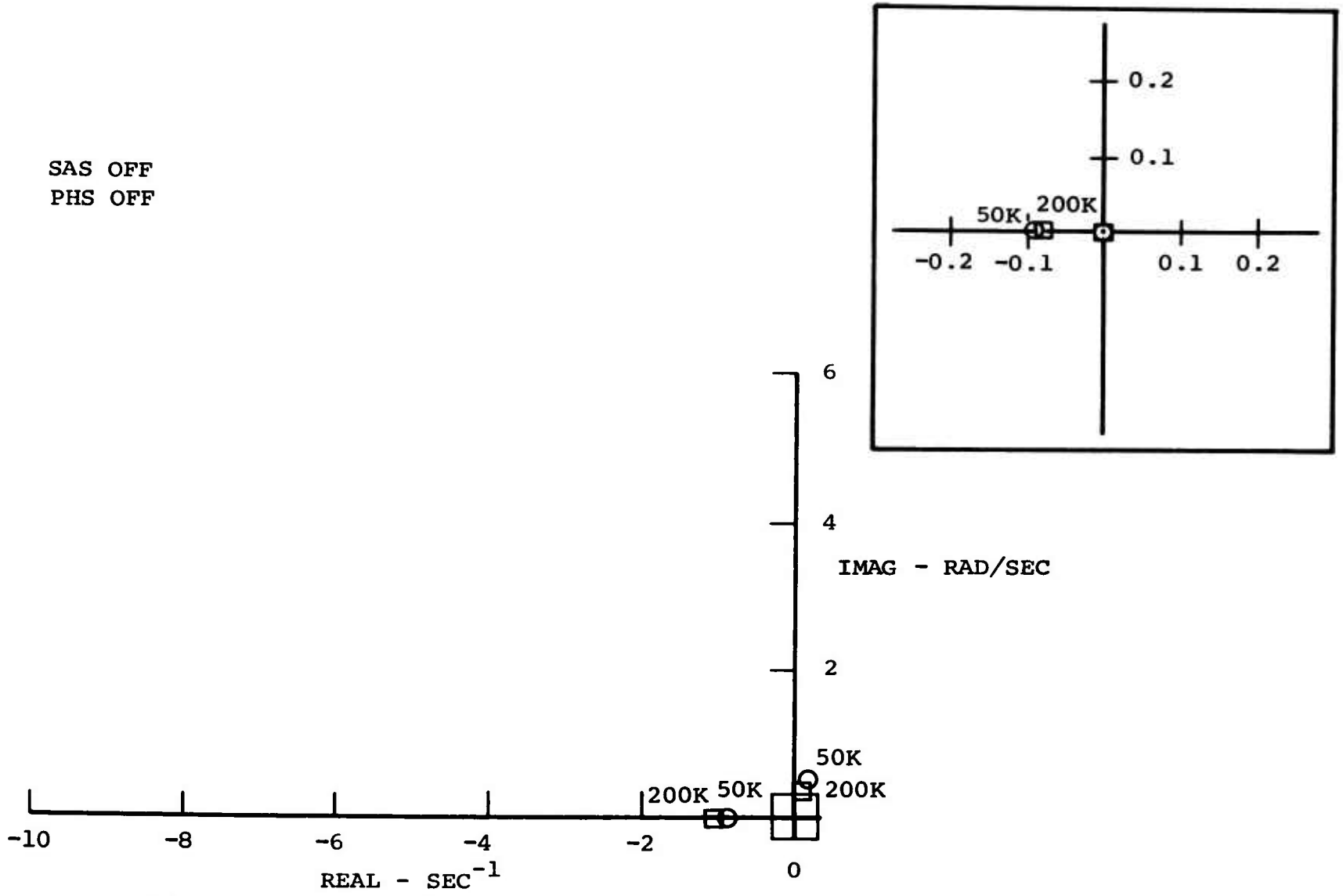

Figure 11. Lateral-Directional System Effect of Gross Weight.

changes. The slightly unstable second-order pair of eigenvalues is reflective of long-term changes in lateral velocity and bank angle. A slight decrease in frequency is evident with increasing size.

STABILITY AUGMENTATION

Stability augmentation in the form of feedback loops was added to the control system to improve helicopter responses. To shorten the time required to synthesize a good system, guidelines for choosing shaping and loop gains are taken, for the most part, from work done on the heavy lift helicopter and the Model 347.

Loop Closures

To show the effect of these feedback loops, one loop at a time will be closed with various loop gains. For this purpose only the 50,000-pound normal-gross-weight configuration will be analyzed.

Longitudinal-Vertical System

Figure 12 is a block diagram of the feedback loops added to the longitudinal-vertical system to improve pitch rate damping and to stabilize the long-term second-order response. An altitude rate feedback loop into collective could have been added at this time to improve vertical damping. However, the vertical mode is almost completely uncoupled from the longitudinal modes, and thus will be improved when the precision hover loops are added. Closing the pitch rate feedback loop first, Figure 13 shows the effect that loop gain has on the locations of the eigenvalues. Increasing loop gain causes the eigenvalues corresponding to the pitch rate damping mode and feedback lag to combine and form a second-order coupled response. The eigenvalues representing the vertical damping mode and feedback washout are only slightly affected. The long-term unstable pair of eigenvalues moves slightly toward the imaginary axis, but remains unstable for the range of gains chosen. The maximum gain shown is the final value chosen for closure of this loop, and all subsequent loop closures.

With the rate loop closed, Figure 14 shows the effect of closing the pitch attitude loop. As loop gain increases, the higher frequency pitch mode tends to decrease in frequency. However, the more predominant effect of this loop closure is to stabilize the long-term response. As loop gain increases, the unstable pair of eigenvalues crosses the imaginary axis, approaches the real axis, and splits into two aperiodic modes. As gain is further increased, one of the aperiodic modes decreases in time constant while the other increases. The

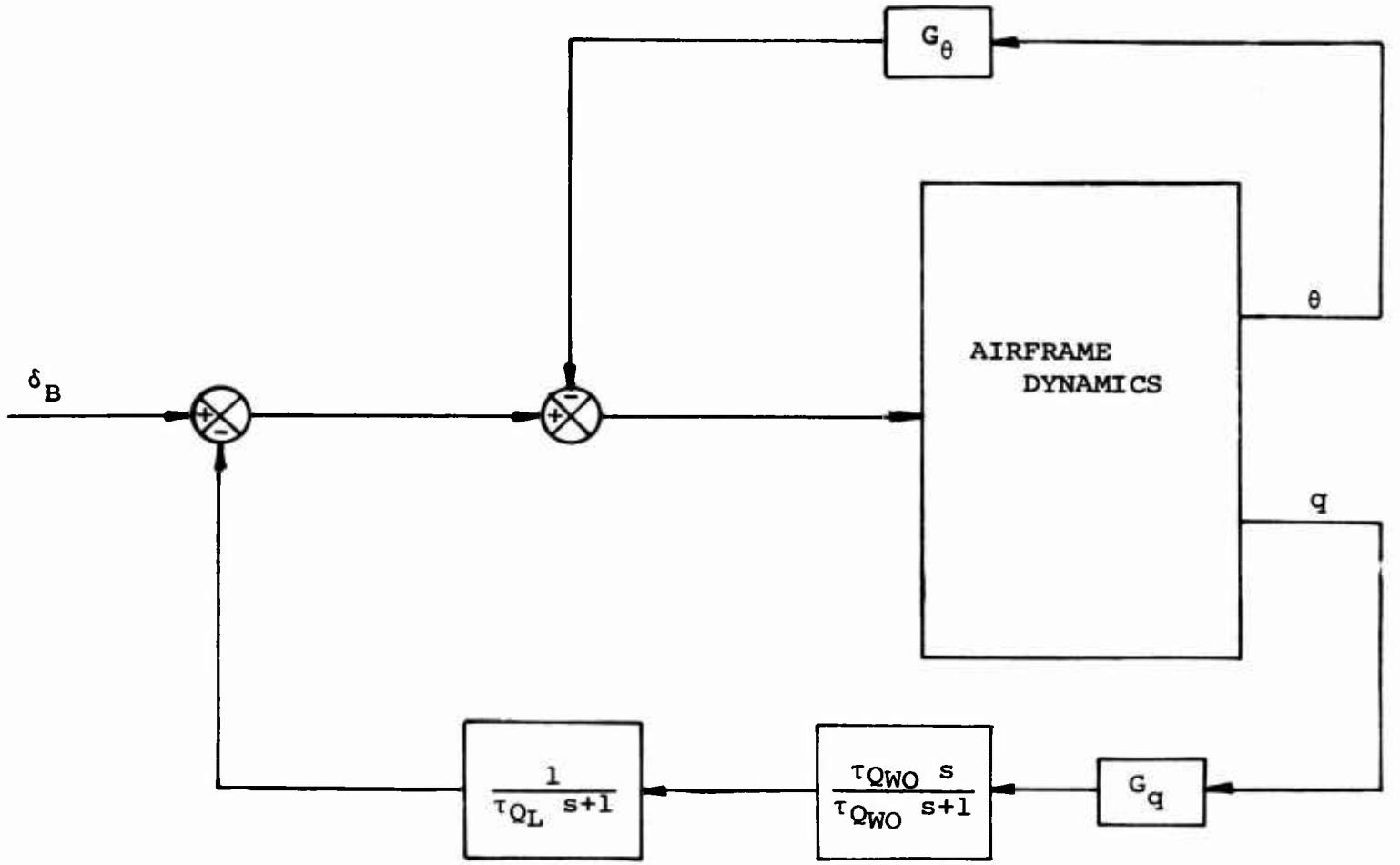

Figure 12. Longitudinal-Vertical Stability Augmentation.

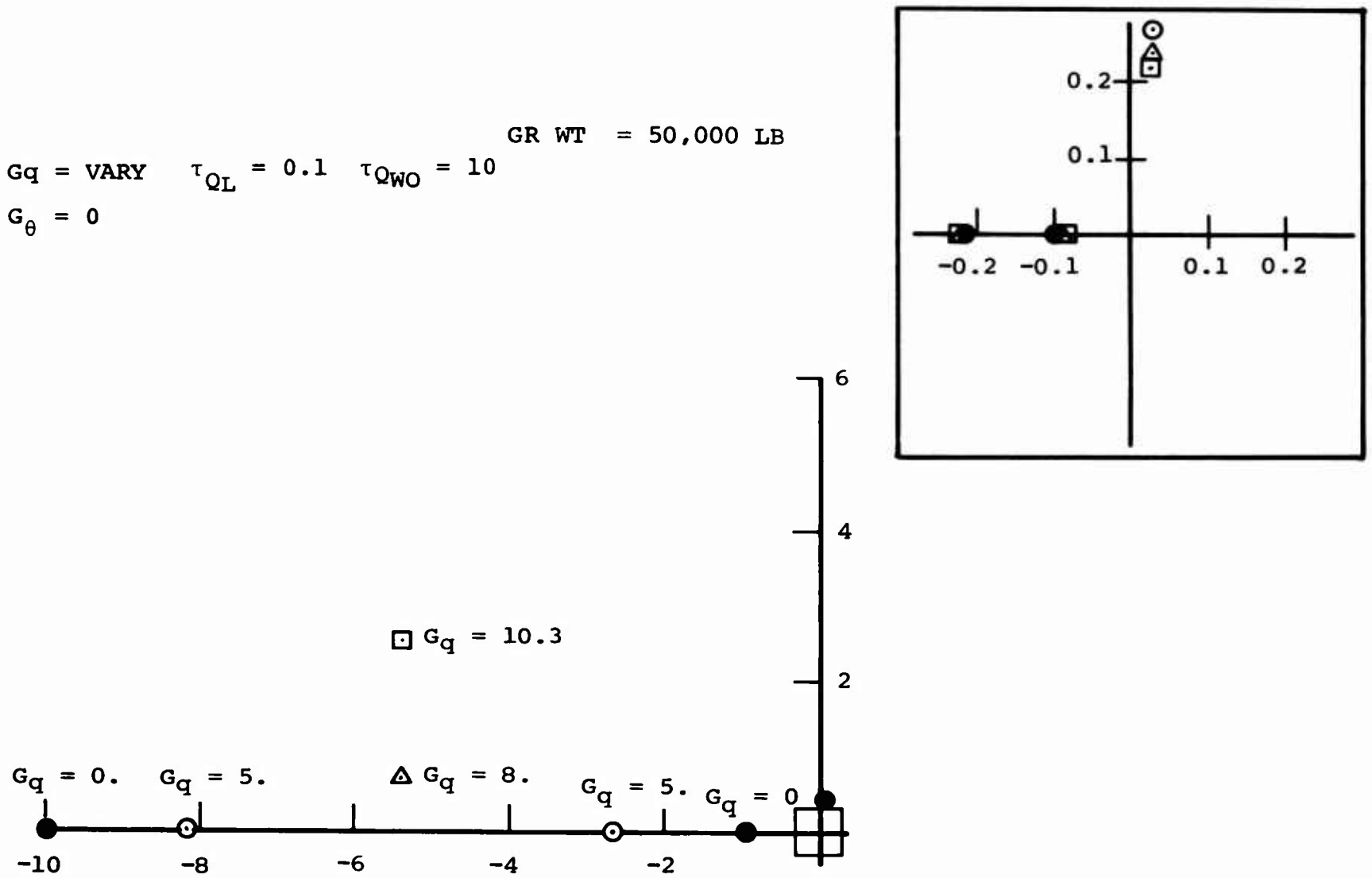

Figure 13. Longitudinal System - Effect of Pitch Rate Feedback.

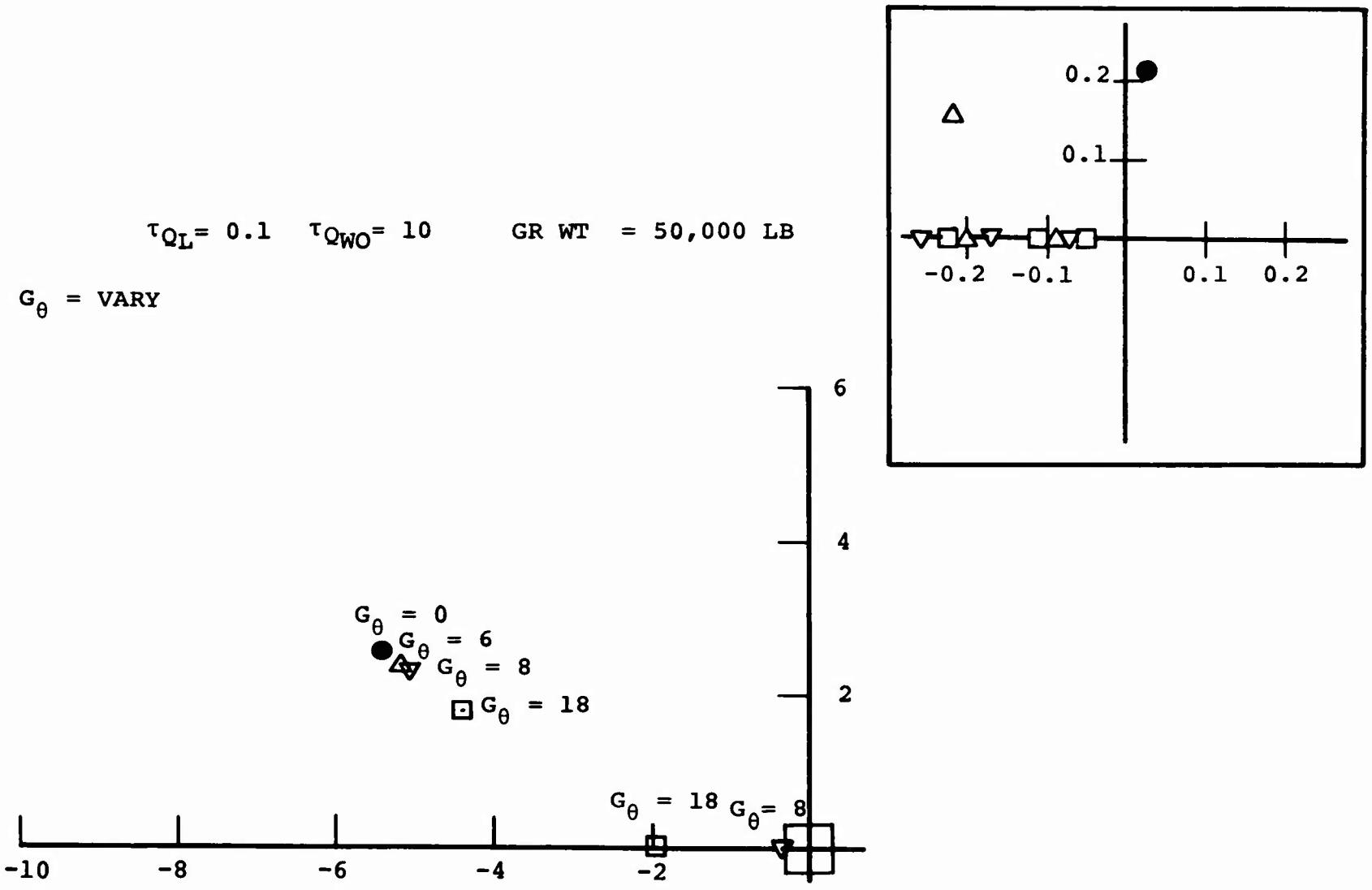

Figure 14. Longitudinal System - Effect of Pitch Attitude Feedback.

eigenvalue corresponding to the uncoupled washout time constant slightly increases its time constant. Again, as with the pitch rate feedback loop, pitch attitude feedback into differential collective has little effect on the vertical damping mode.

Lateral-Directional System

Figure 15 is a block diagram showing the selected lateral-directional stability augmentation loops. Figure 16 shows the effect of closing the roll rate loop. The effect is similar to that of the pitch rate loop closure, in that the roll rate damping (L_p) mode combines with the feedback lag to form a second-order coupled response. The effect of roll rate feedback on the directional modes is small. The effect of this loop on the long-term second-order lateral mode is a slight improvement in the stability.

Figure 17 is the result of closing the roll attitude loop with the roll rate loop closed. As the gain increases, the higher frequency roll rate mode decreases in damping. The long-term unstable oscillation becomes stable, approaches the real axis, and splits into two aperiodic modes. As loop gain is further increased, one eigenvalue becomes more negative, reflecting the tight bank angle hold, while the other eigenvalue combines with the washout time constant to form a lightly damped long-term, low-frequency oscillation. The directional modes are only slightly affected by this roll attitude loop.

Figure 18 is the result of adding yaw rate feedback to the previously closed loops. As yaw rate feedback gain increases, only the mode corresponding to N_r is affected. The time to half amplitude of this mode decreases by a factor of about twenty.

Figure 19 shows the effect of now closing the yaw attitude loop. As can be seen, only the yaw rate mode and the neutrally stable heading mode are affected. As gain increases, these two modes combine to form a second-order response.

Figure 20 is the result of adding an inertial lateral velocity feedback loop. The value of this loop can be seen in the improved long-term pair of eigenvalues. As gain increases, this mode increases in damping ratio until it splits into two aperiodic modes.

Effect of Helicopter Size With SAS ON

With all the loops closed as shown in Figures 12 and 15, the effect of increasing the helicopter size will now be investigated.

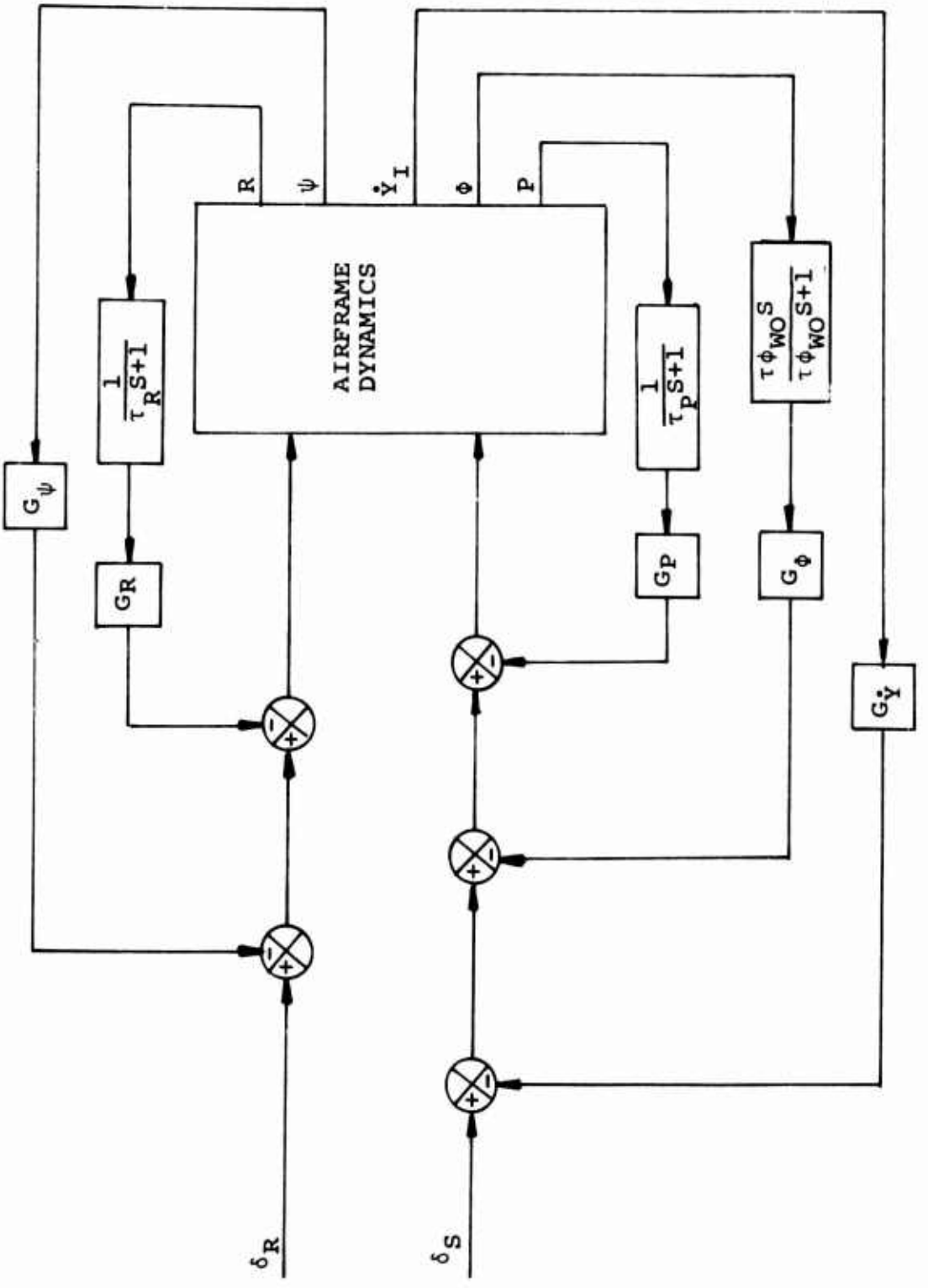

Figure 15. Lateral-Directional Stability Augmentation.

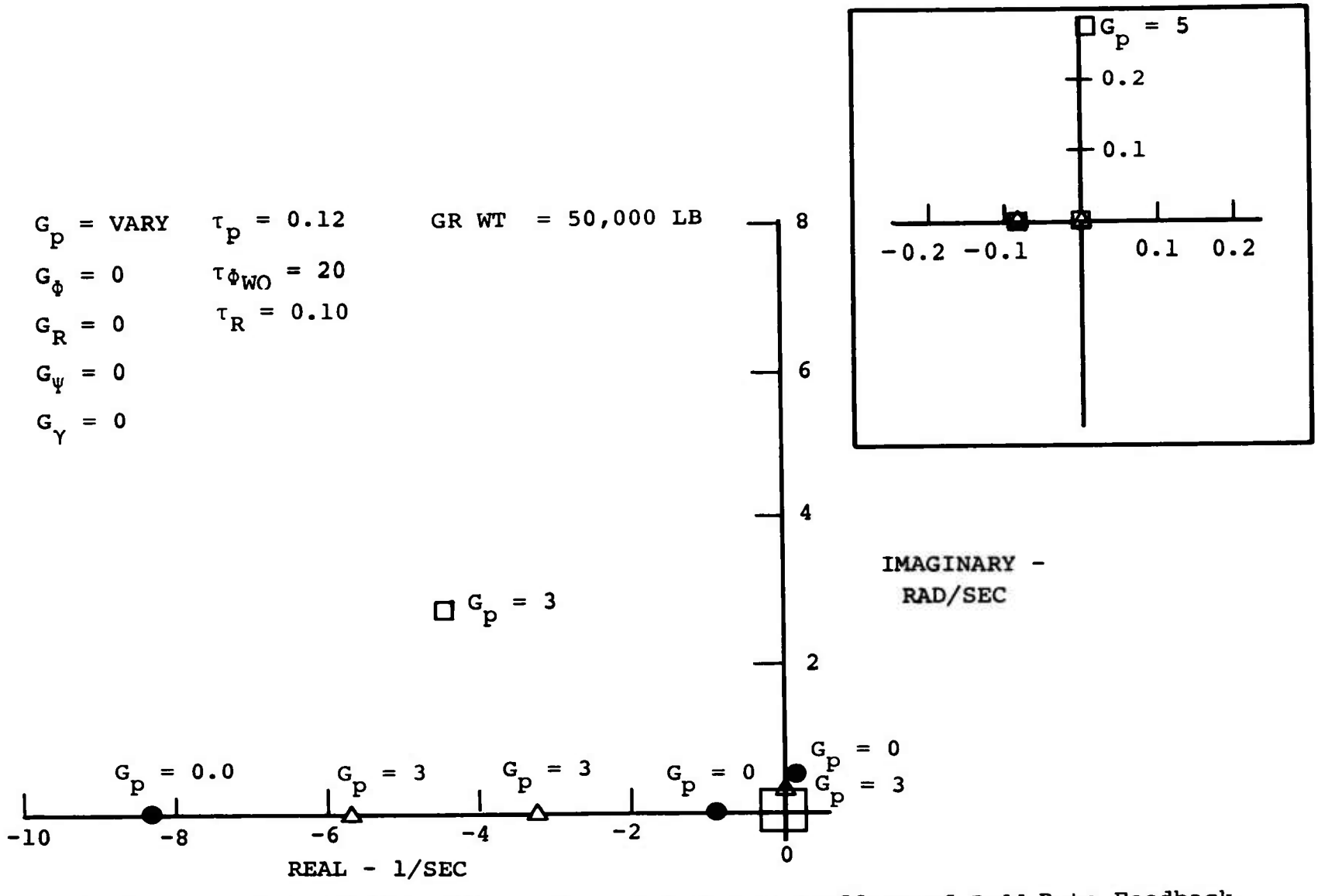

Figure 16. Lateral-Directional System Root Locus Effect of Roll Rate Feedback.

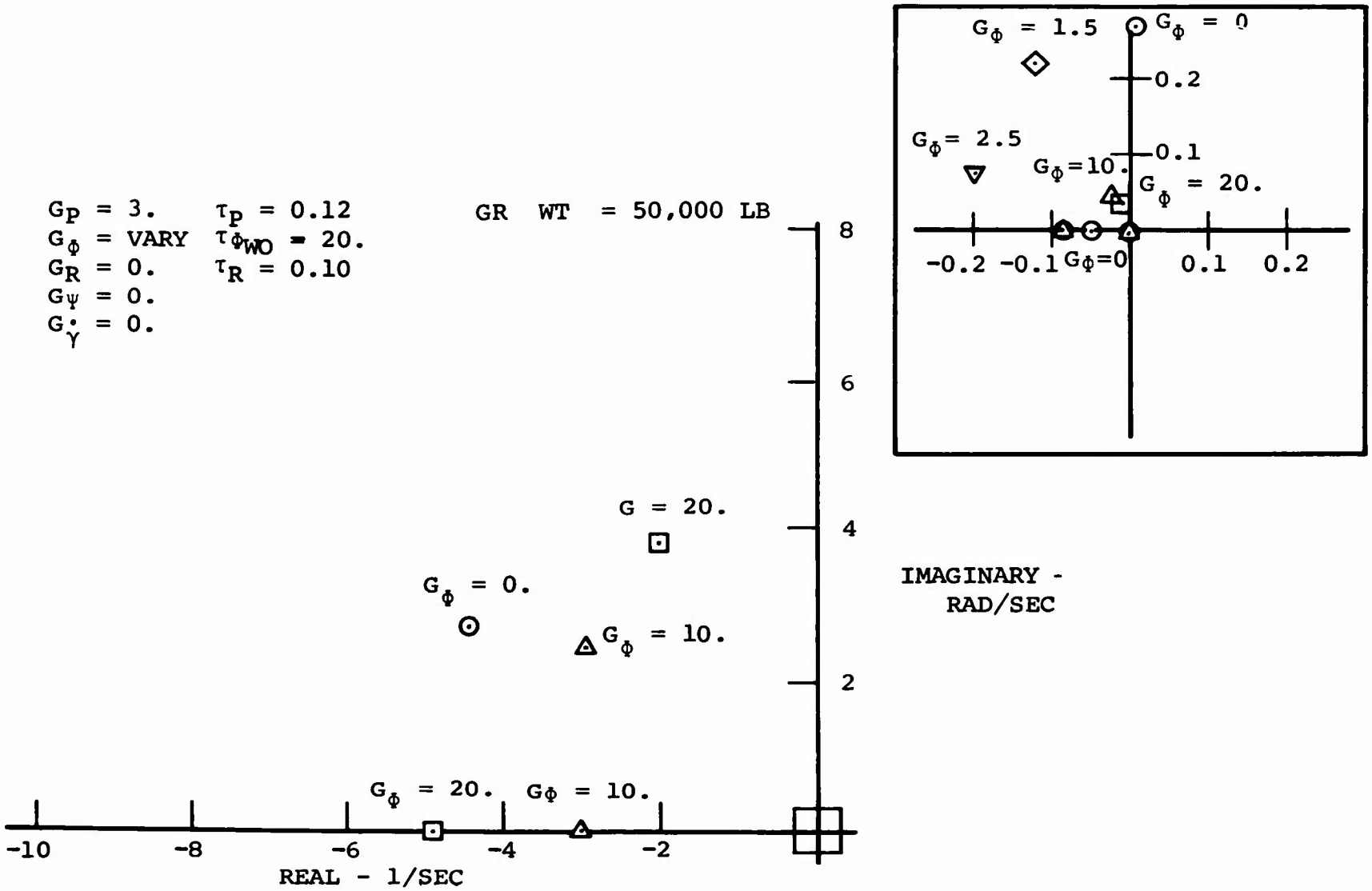

Figure 17. Lateral-Directional System Root Locus Effect of Roll Attitude Feedback.

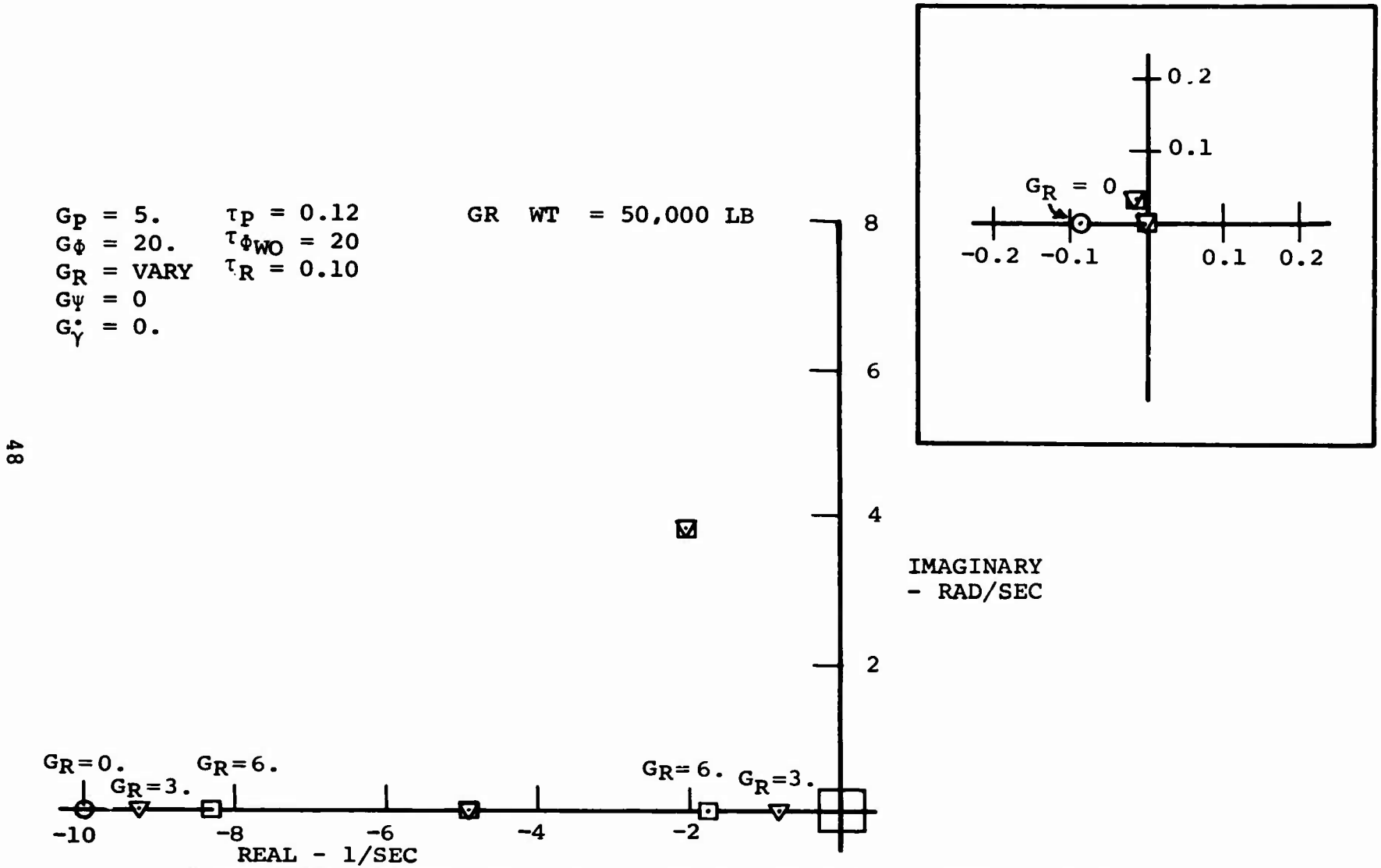

Figure 18. Lateral-Directional System Root Locus Effect of Yaw Rate Feedback.

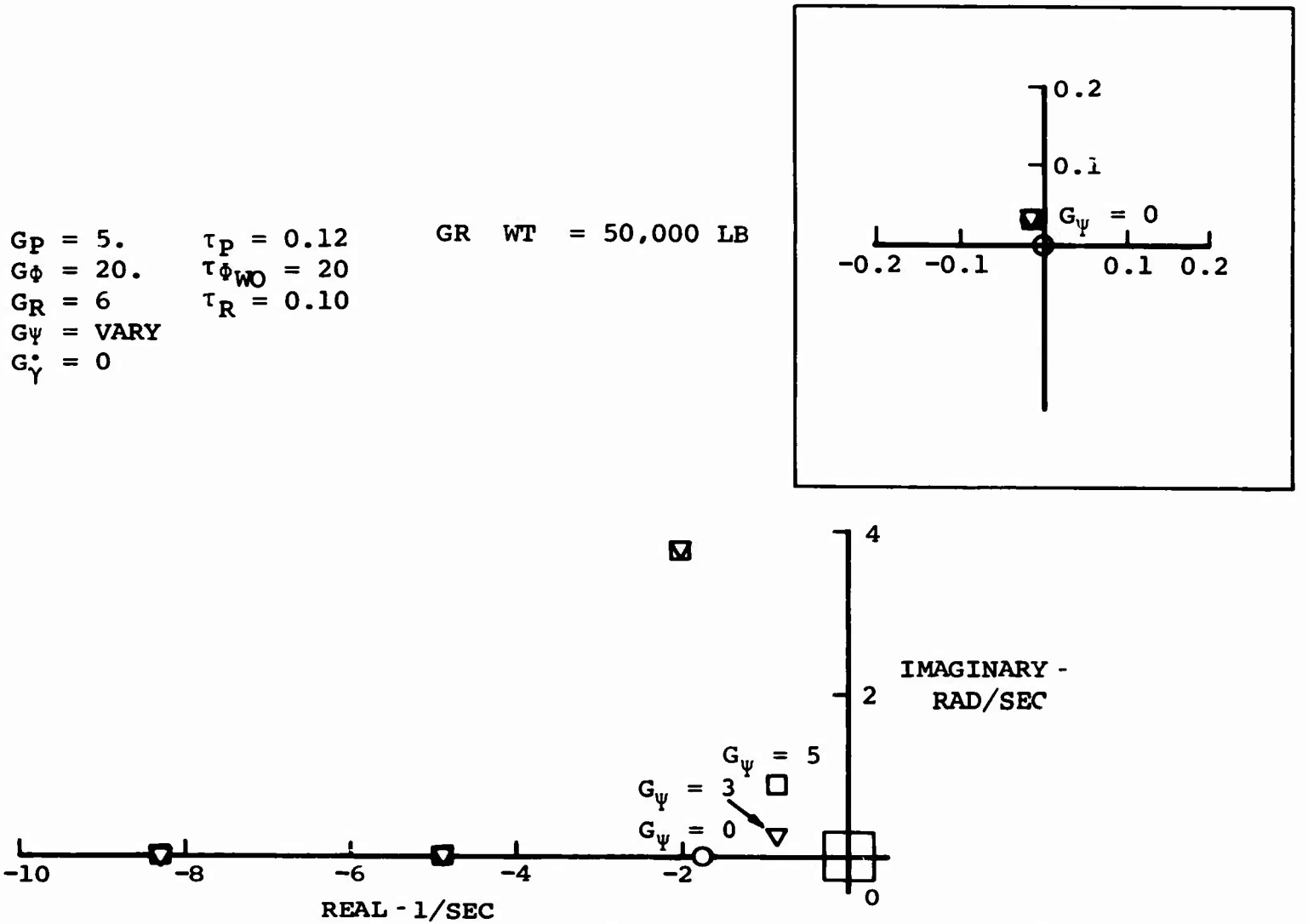

Figure 19. Lateral-Directional System Root Locus Effect of Heading Feedback.

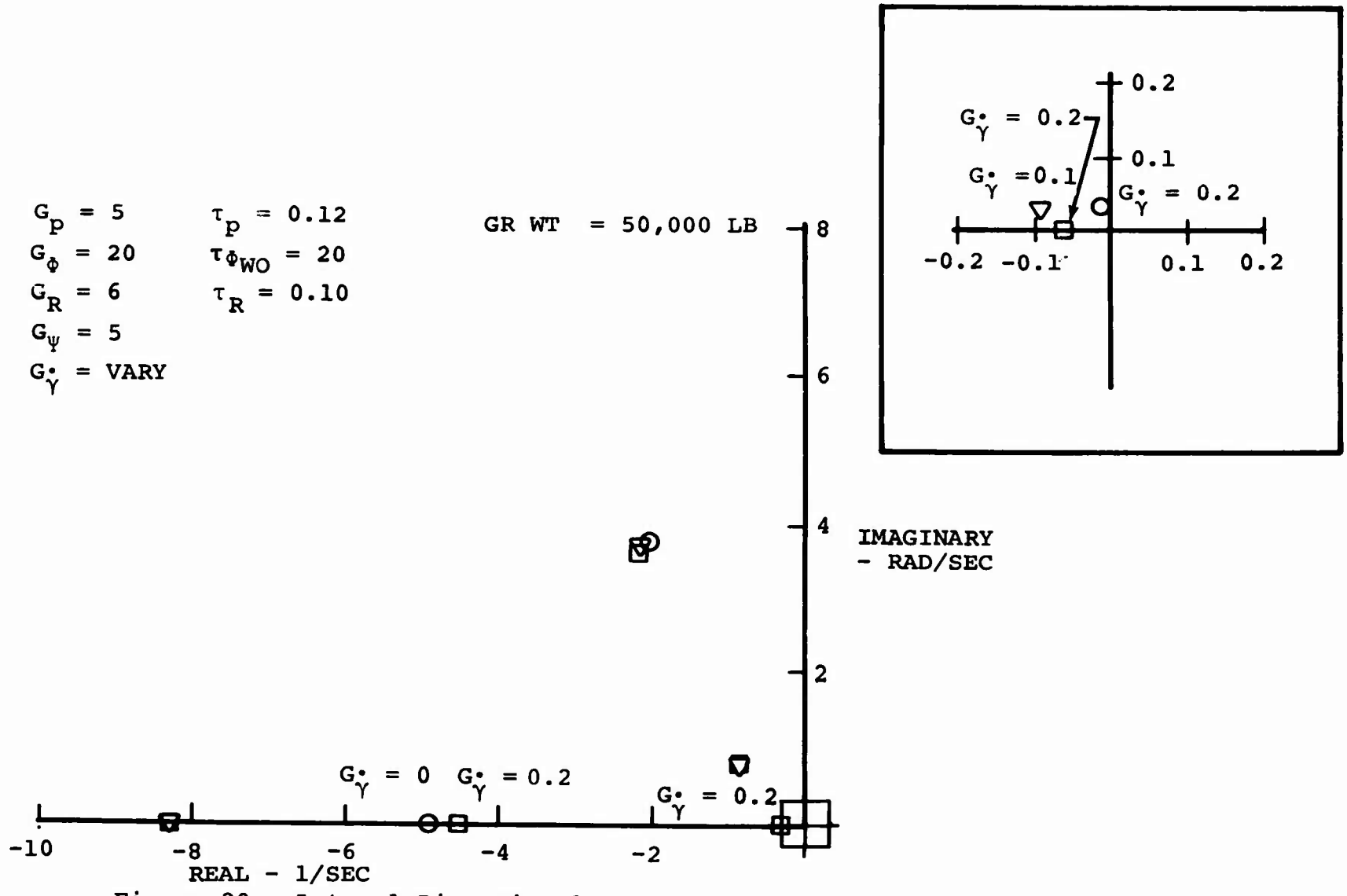

Figure 20. Lateral-Directional System Root Locus Effect of Lateral Velocity Feedback.

Longitudinal-Vertical Motion

Figure 21 is a plot of the longitudinal-vertical eigenvalues with SAS ON for four different gross weights. As size increases, it appears that the higher frequency pitch mode approaches the real axis and splits into two aperiodic modes. As gross weight continues to increase, one of the aperiodic eigenvalues becomes more negative while the other moves in the direction of the origin until it combines with an aperiodic pitch attitude mode and forms a second-order response at a lower frequency.

Lateral-Directional Motion

Figure 22 shows the effect of increasing helicopter size on the lateral-directional eigenvalues. Both of the second-order responses, lateral and directional, maintain almost constant damping, but experience a reduction in frequency.

UNPILOTED HOVER HOLD PERFORMANCE

In the previous paragraphs, the helicopter was augmented by feedback loops to improve its handling qualities. Even though the helicopter, with these loops closed, is now stable, there is no guarantee that it will return to its original position in space when disturbed. To provide position hold, position errors can be used to feed inputs into the control system. These inputs can be provided either automatically through feedback loops or by the pilot through optically sensed errors. This section deals with the automatic concept.

Loop Closures

Feedback loops were added to the longitudinal-vertical system and the lateral-directional system to provide automatic hover hold capability. As was done before, the effect of closing these loops one at a time was analyzed using the 50,000-pound configuration.

Longitudinal-Vertical System

Figure 23 is a block diagram of the selected feedback loops to provide longitudinal and vertical position hold. Note that the longitudinal signals are fed back into longitudinal cyclic and not differential collective, as were pitch rate and pitch attitude. This is done because longitudinal cyclic is a more effective longitudinal control, with less pitch coupling. Although the longitudinal and lateral positions were the primary interest in this report, vertical hold capability was included for completeness. Since it has been shown that the vertical motion is almost completely uncoupled from the longitudinal motion, any improvement in vertical position hold capability

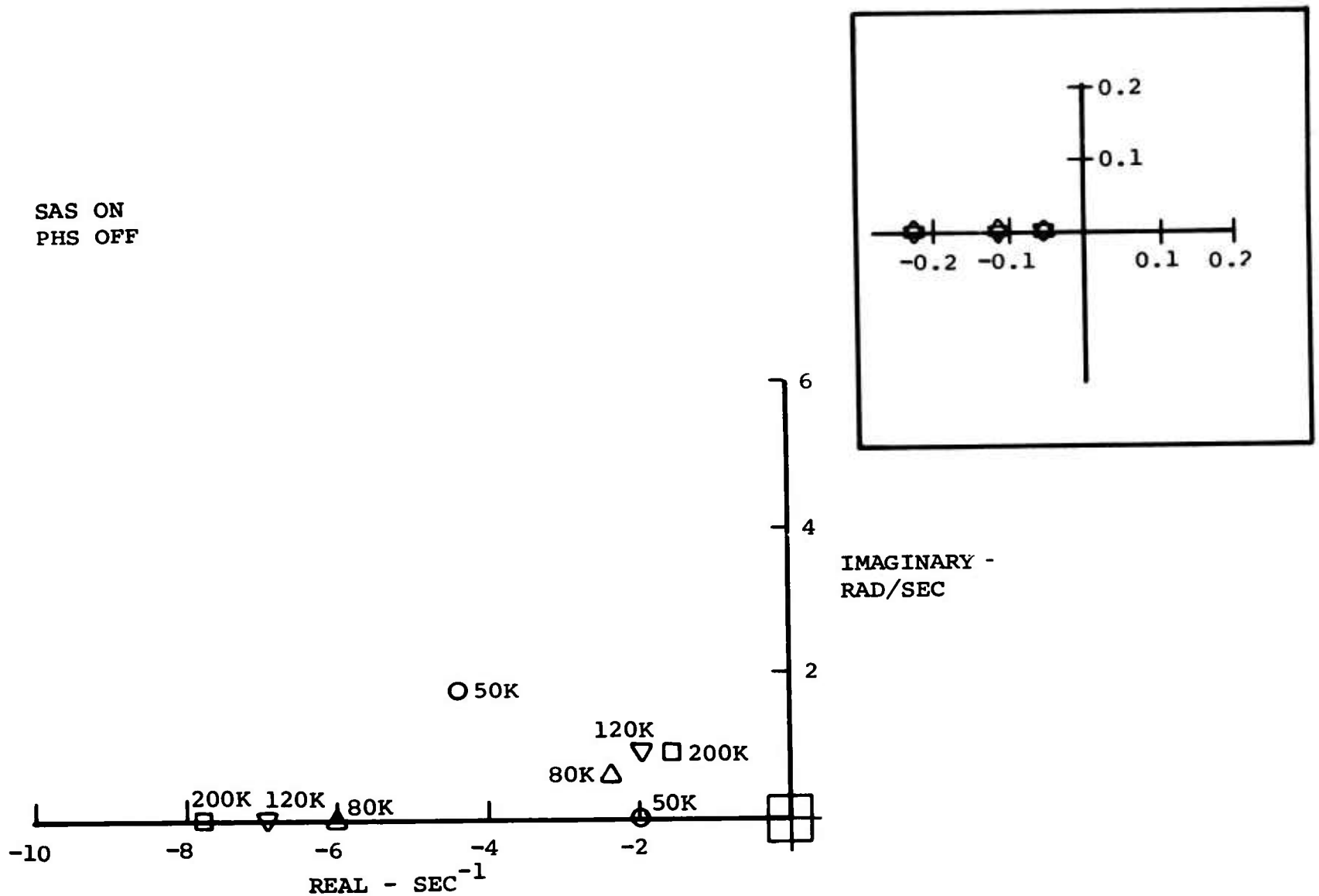

Figure 21. Longitudinal System - Effect of Gross Weight.

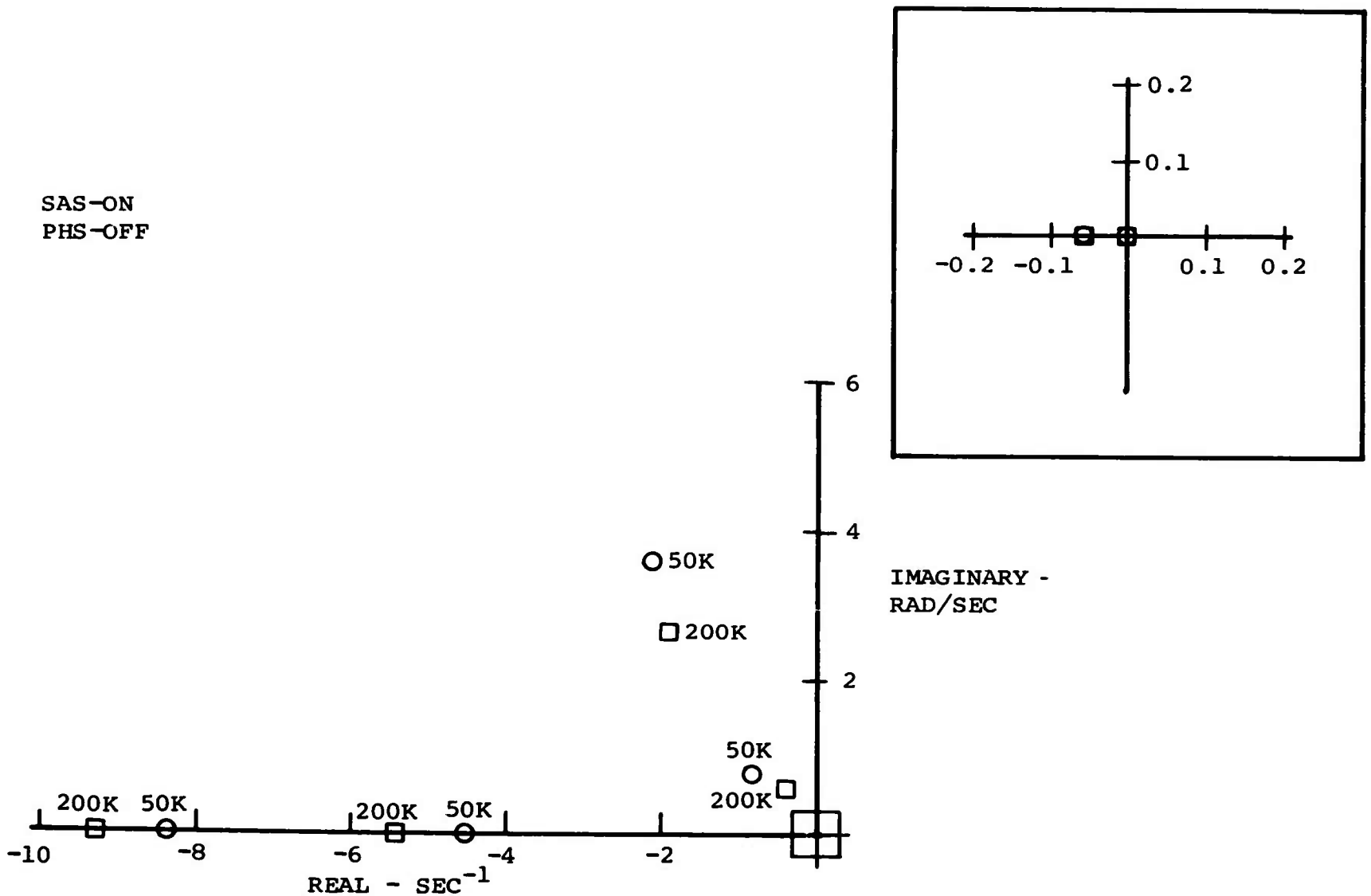

Figure 22. Lateral-Directional System - Eigenvalues Effect of Gross Weight.

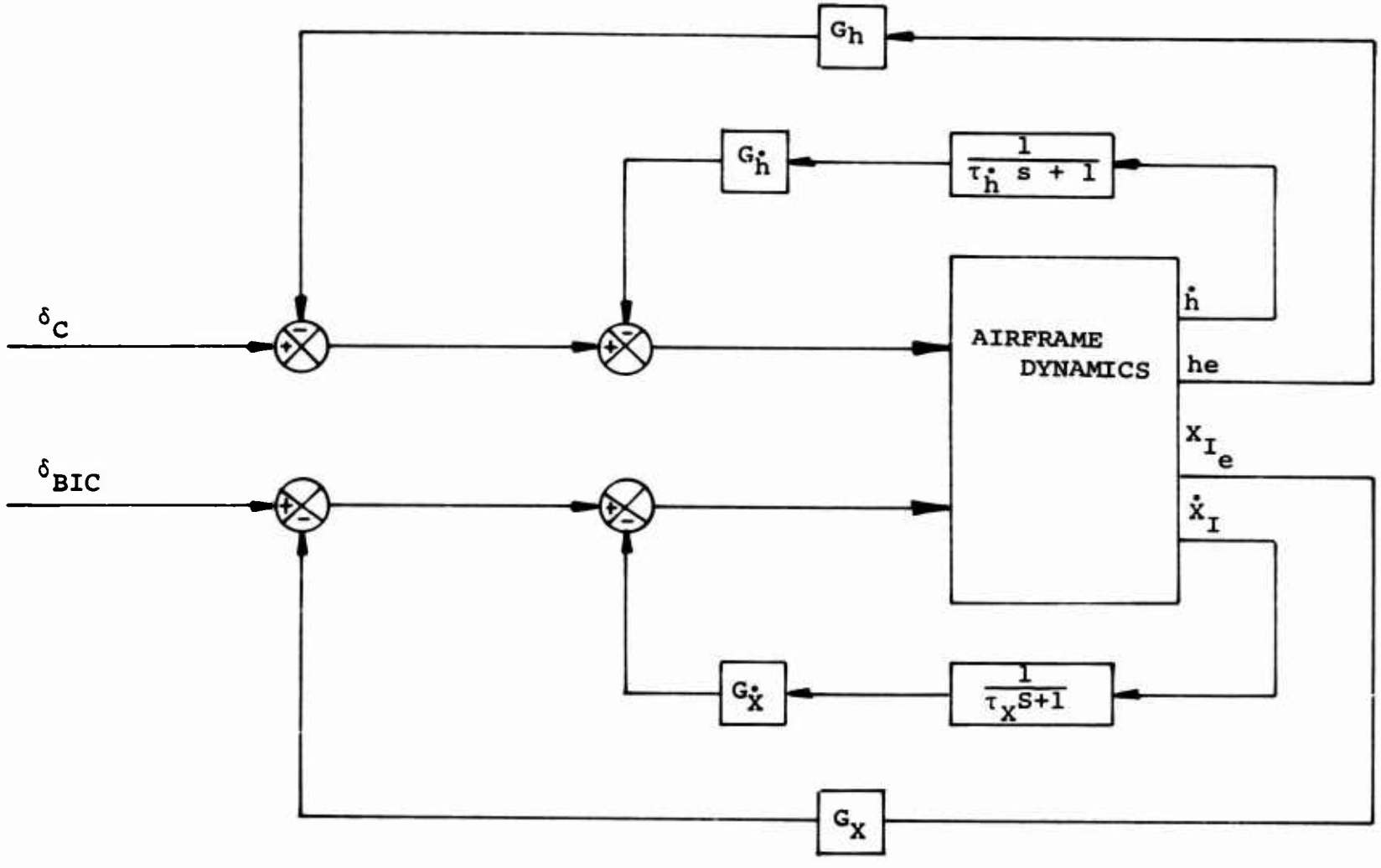

Figure 23. Longitudinal-Vertical Precision Hover System.

can be done with a simple one-degree-of-freedom model, independent of the results obtained here for the longitudinal and lateral system.

Closing the inertial longitudinal velocity loop first, Figure 24 shows the result of various feedback gains. As can be seen, the high-frequency pitch mode is affected by this loop closure, indicating that this mode is now strongly coupled with longitudinal velocity. Increasing loop gain tends to decrease the damping in this mode while increasing the frequency. This loop closure also causes the eigenvalue associated with velocity damping to increase negatively until it combines with the pitch attitude mode to form a second-order response. Further increases in loop gain cause this mode to increase in frequency at fairly constant damping ratio. This implies that the rise time will decrease and the settling time will decrease while the overshoot remains constant. This is a desirable condition for a tight and rapid control system, provided the damping level is sufficient to keep overshoot within tolerances. The eigenvalues that appear at the origin represent the neutral stability of altitude and longitudinal position. These loops are yet to be closed.

Now, with the longitudinal velocity loop closed, the longitudinal position loop is closed, Figure 25. Increasing the loop gain moves the neutrally stable eigenvalue from the origin and drives it along the negative real axis, thus decreasing its response time constant. A final time constant of about 1 second is reached. One eigenvalue, representing altitude, still remains at the origin.

Figure 26 shows the effect of closing the altitude rate loop. The effect of this loop closure with ever-increasing gain is to drive the vertical damping time constant down, with the altitude eigenvalue remaining at the origin.

The final longitudinal-vertical system loop closure is the altitude loop (Figure 27). The effect is to cause the aperiodic modes representing vertical velocity and vertical position to combine into a second-order response. Further increase in gain causes the coupled response to decrease in damping and increase in frequency.

Lateral System

Figure 28 is a block diagram of the selected feedback loops to provide lateral position hold. Figure 29 shows the effect of adding a lateral velocity feedback through a washout. The high-frequency roll rate mode increases in damping while slightly decreasing in damped natural frequency. As gain increases, two lateral aperiodic modes combine to form a second-order lateral response. Further gain increases cause the

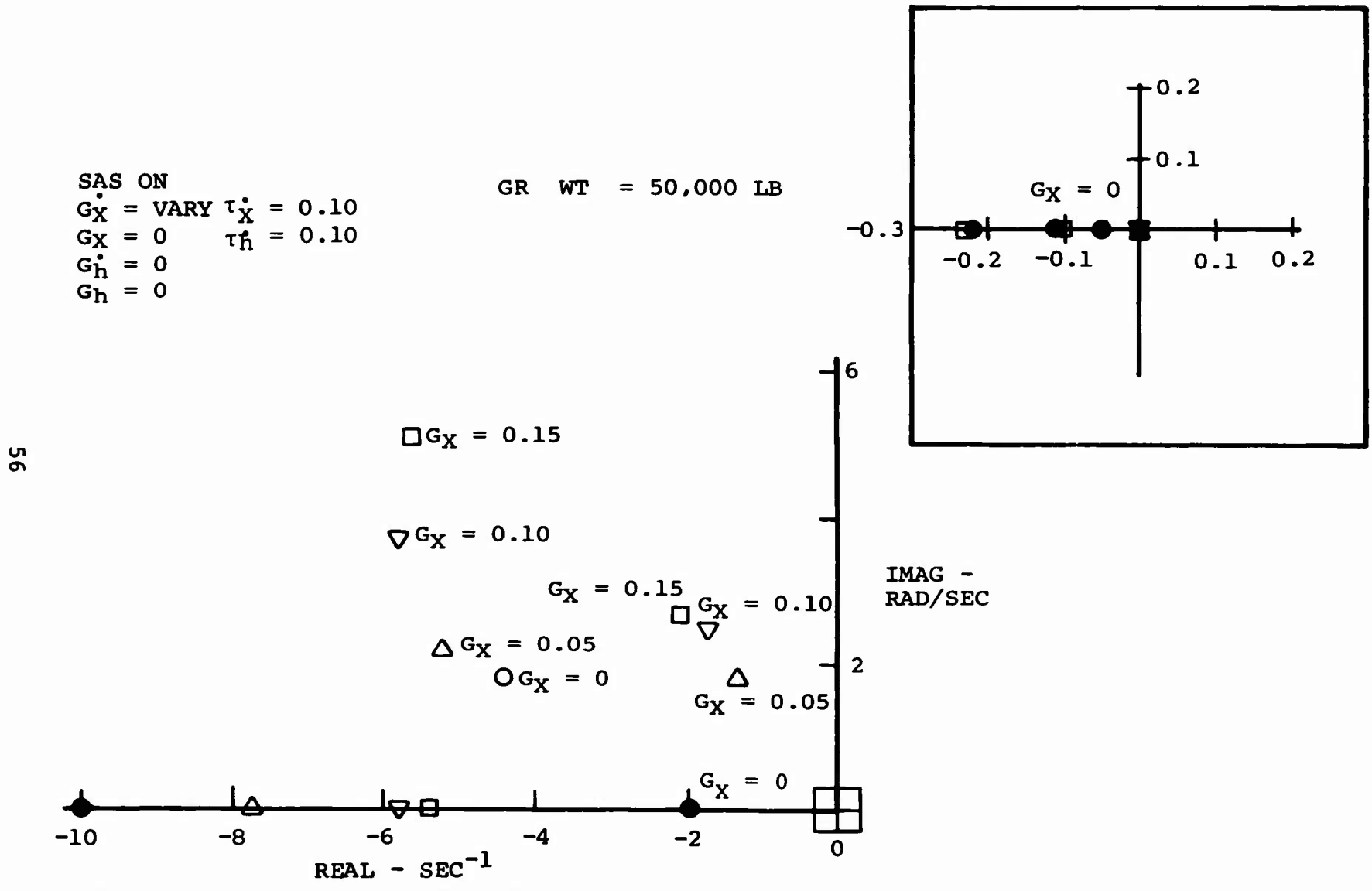

Figure 24. Longitudinal System - Effect of Longitudinal Ground Speed Feedback.

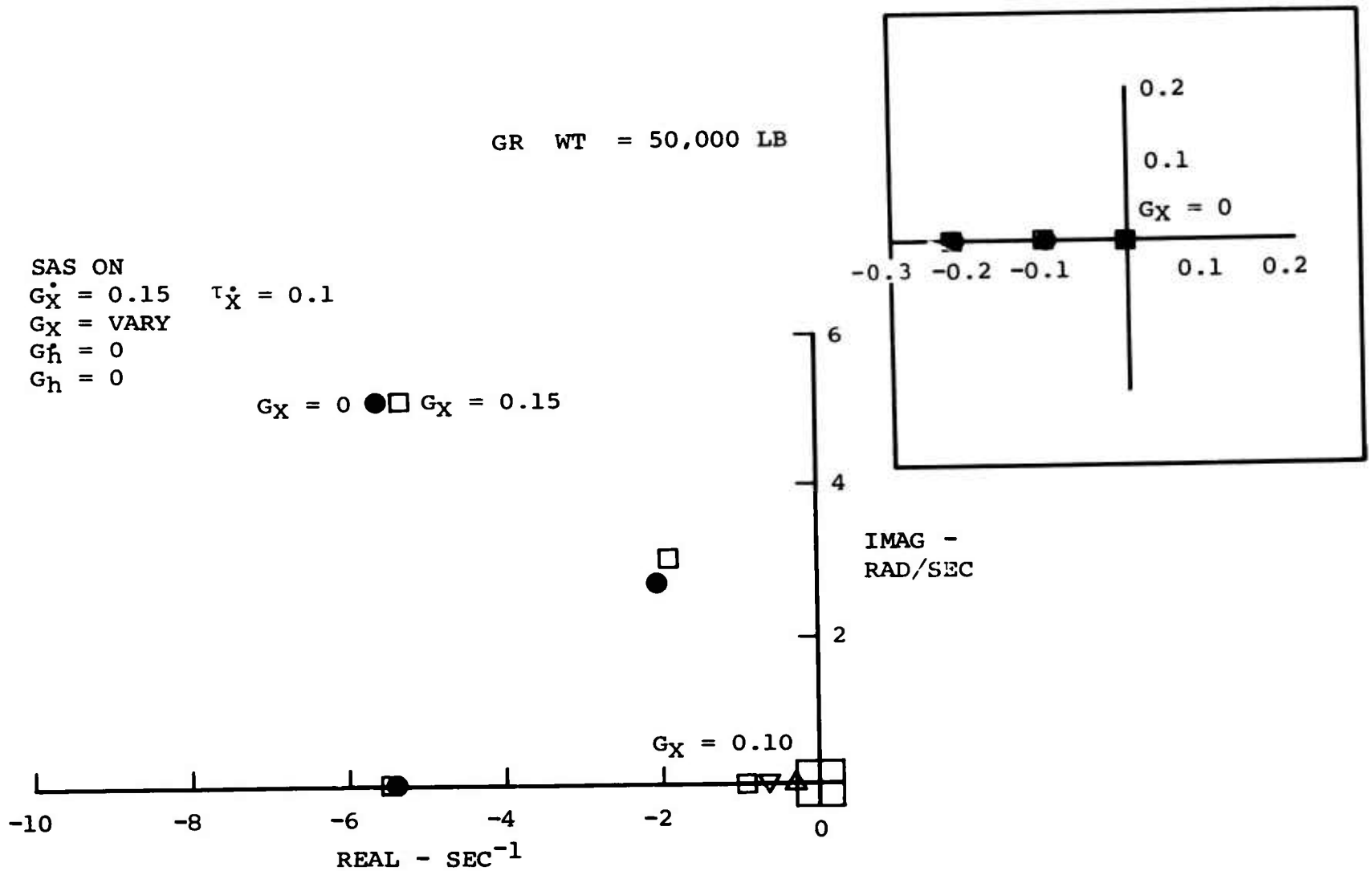

Figure 25. Longitudinal System - Effect of Longitudinal Position Feedback.

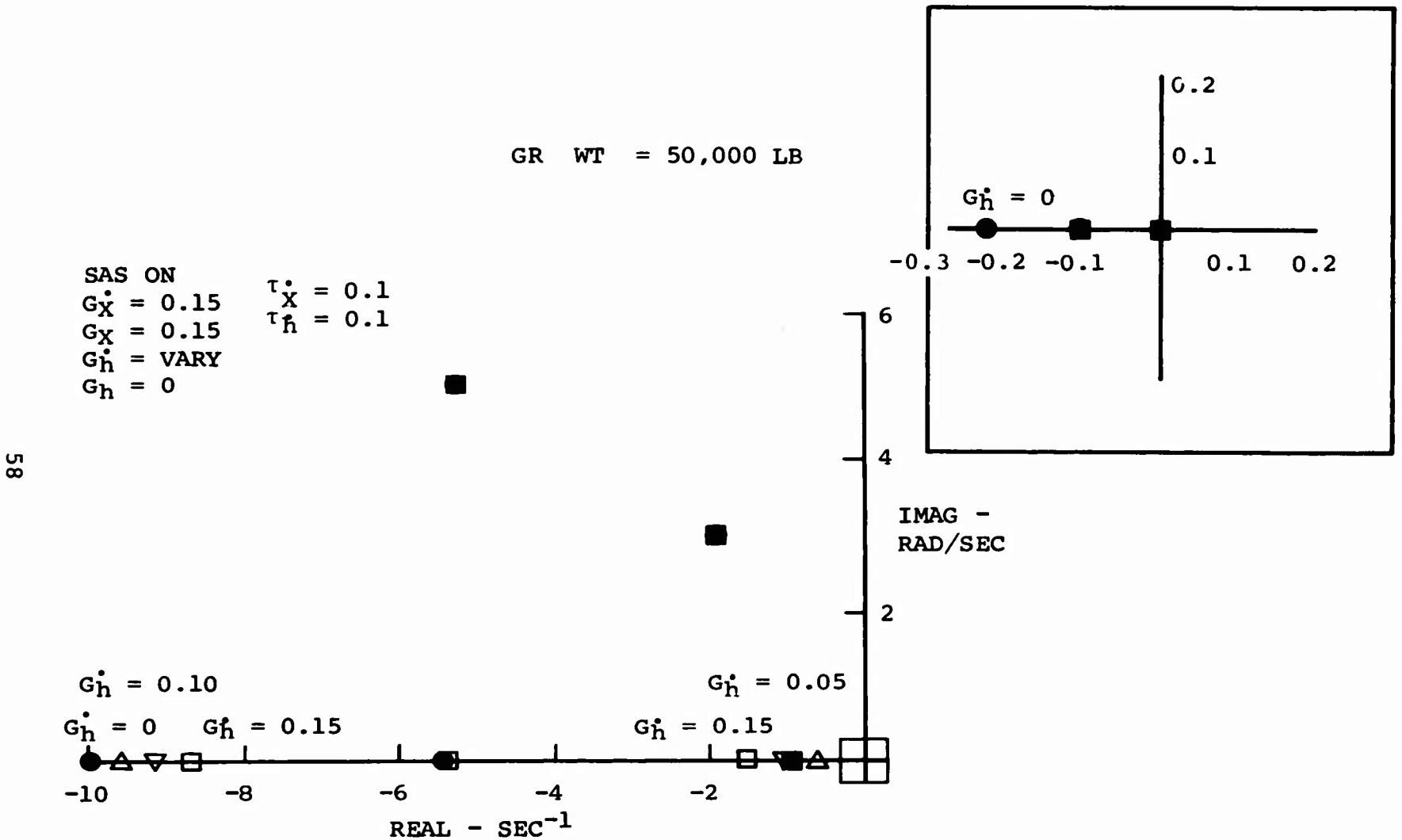

Figure 26. Longitudinal System - Effect of Altitude Rate Feedback.

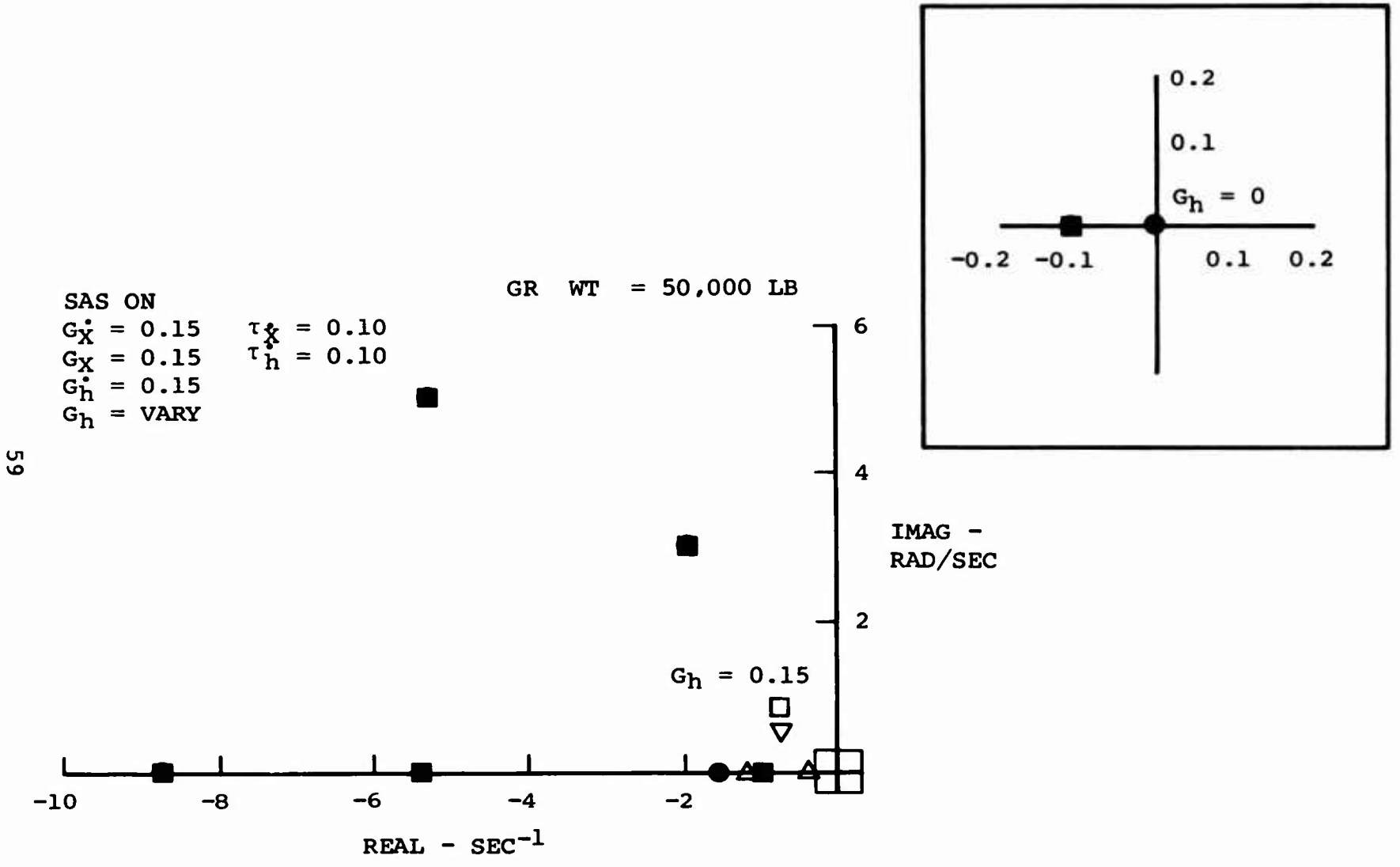

Figure 27. Longitudinal System - Effect of Altitude Feedback.

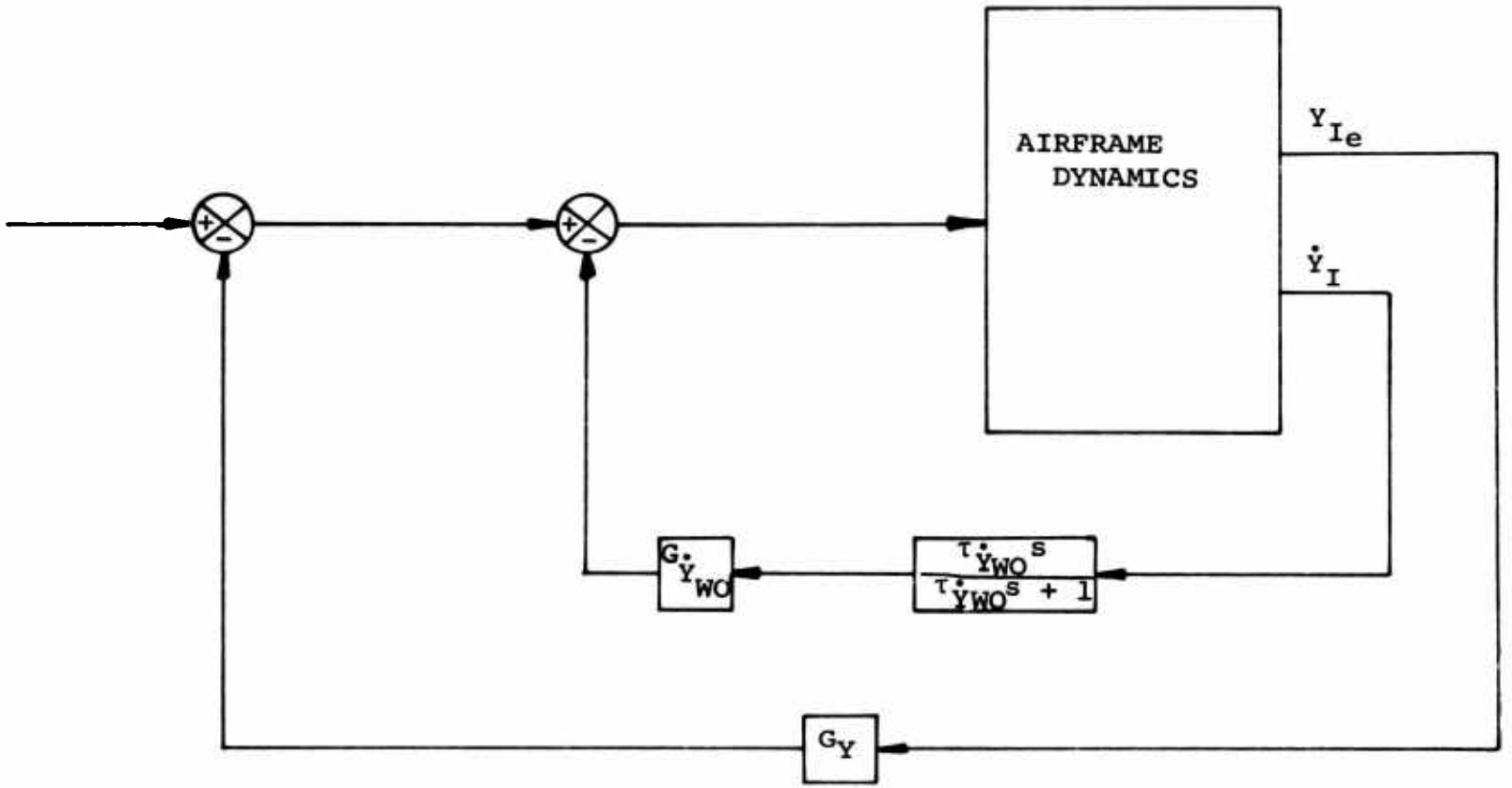

Figure 28. Lateral Precision Hover System.

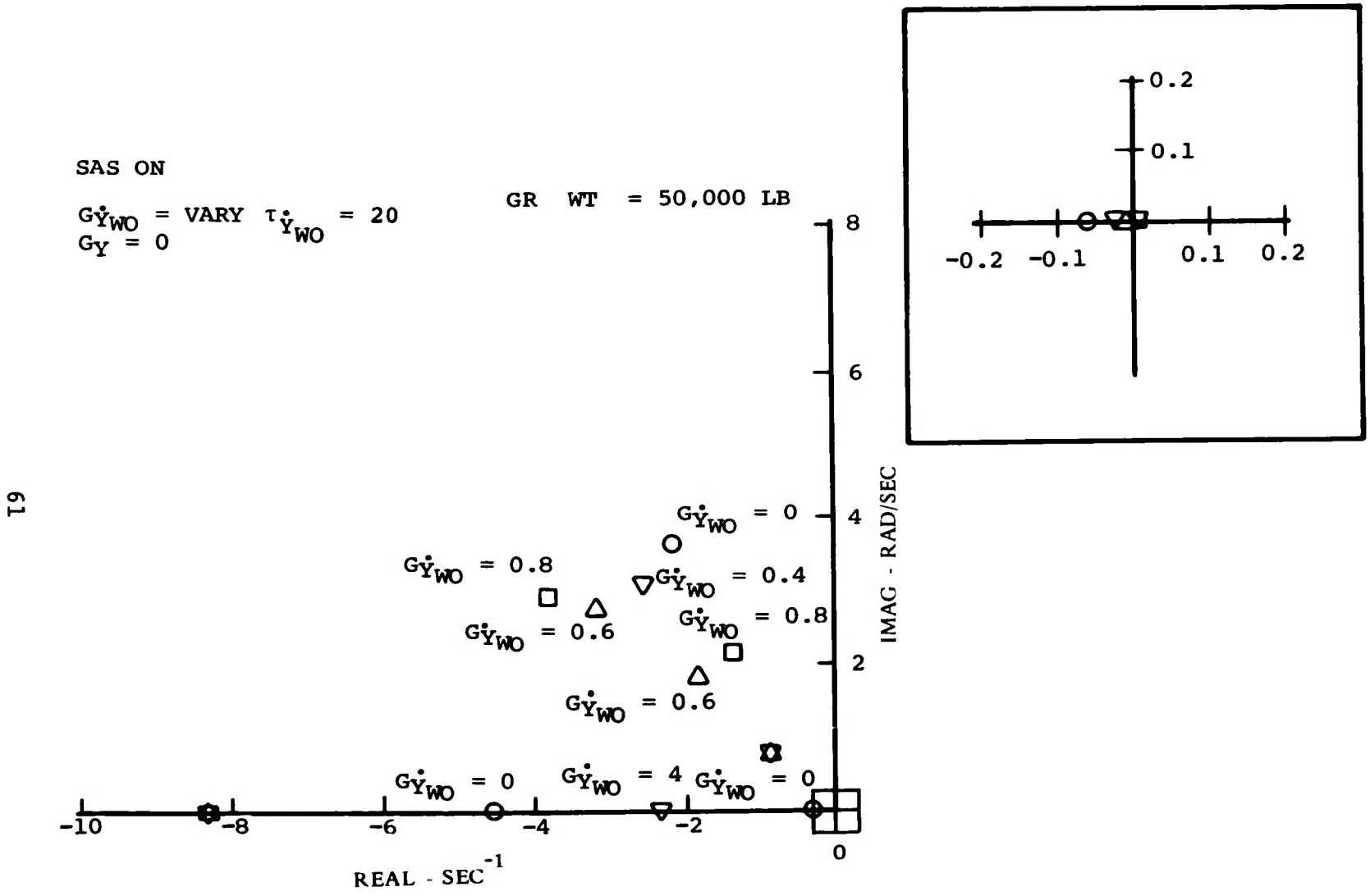

Figure 29. Lateral-Directional System - Root Locus Effect of Lateral Velocity Through Washout Feedback.

damping of this mode to decrease. One other lateral aperiodic mode is driven toward the origin. The second-order directional mode is unaffected.

Figure 30 is the result of closing the lateral position loop with all other loops closed. The higher frequency roll mode is only slightly affected. The lower frequency roll-velocity mode maintains approximately constant damping while decreasing in frequency. The neutrally stable eigenvalue at the origin representing lateral position is pushed out the negative real axis, consequently quickening its response. The effective washout time constant is increased, and the eigenvalue is driven closer toward the origin. The second-order directional mode is unaffected.

Effect of Helicopter Size With PHS ON

With all the feedback loops representing the stability augmentation and the precision hover systems closed, the effect of helicopter size was investigated.

Longitudinal-Vertical Motion

Figure 31 shows the effect of increasing helicopter size on the longitudinal-vertical responses. Increasing size has almost no effect on the second-order vertical response, due to the little change in Z_w. The higher frequency second-order longitudinal response did not change much either. This points out the strong dependence of this mode on longitudinal cyclic control sensitivity, which is relatively invariant with size. However, the lower frequency second-order longitudinal response shows a marked decrease in frequency at almost constant damping. This effect is due to the dependence of this mode on DCP control sensitivity, which decreases with increasing size, and also to a lesser degree, to a decrease in longitudinal cyclic pitch control sensitivity.

Lateral-Directional Motion

Figure 32 shows the effect on lateral-directional responses due to increased helicopter size. The high-frequency roll mode increases in damping and decreases in frequency. This effect is probably due to increasing L_p and decreasing L_{δ_s} with increasing size. The lower frequency second-order roll-velocity mode shows only a slight decrease in damping. This is probably due to the strong dependence of this mode on lateral control sensitivity (Y_{δ_s}), which remains relatively constant. The second-order directional mode shows a slight decrease in damping and a definite decrease in frequency, which correspond to the slight decrease in N_r and definite decrease in N_{S_R} with size.

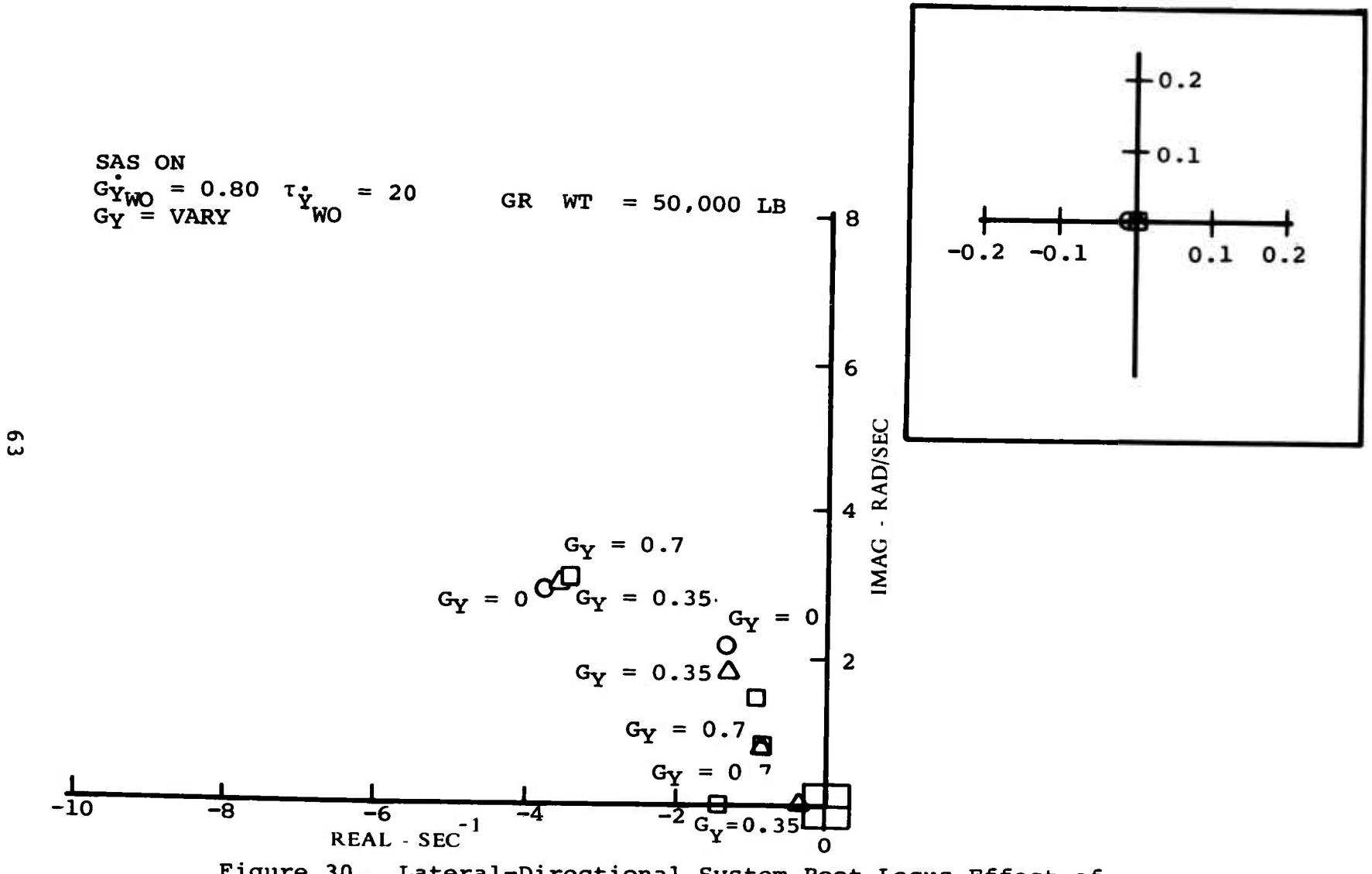

Figure 30. Lateral-Directional System Root Locus Effect of Lateral Position Feedback.

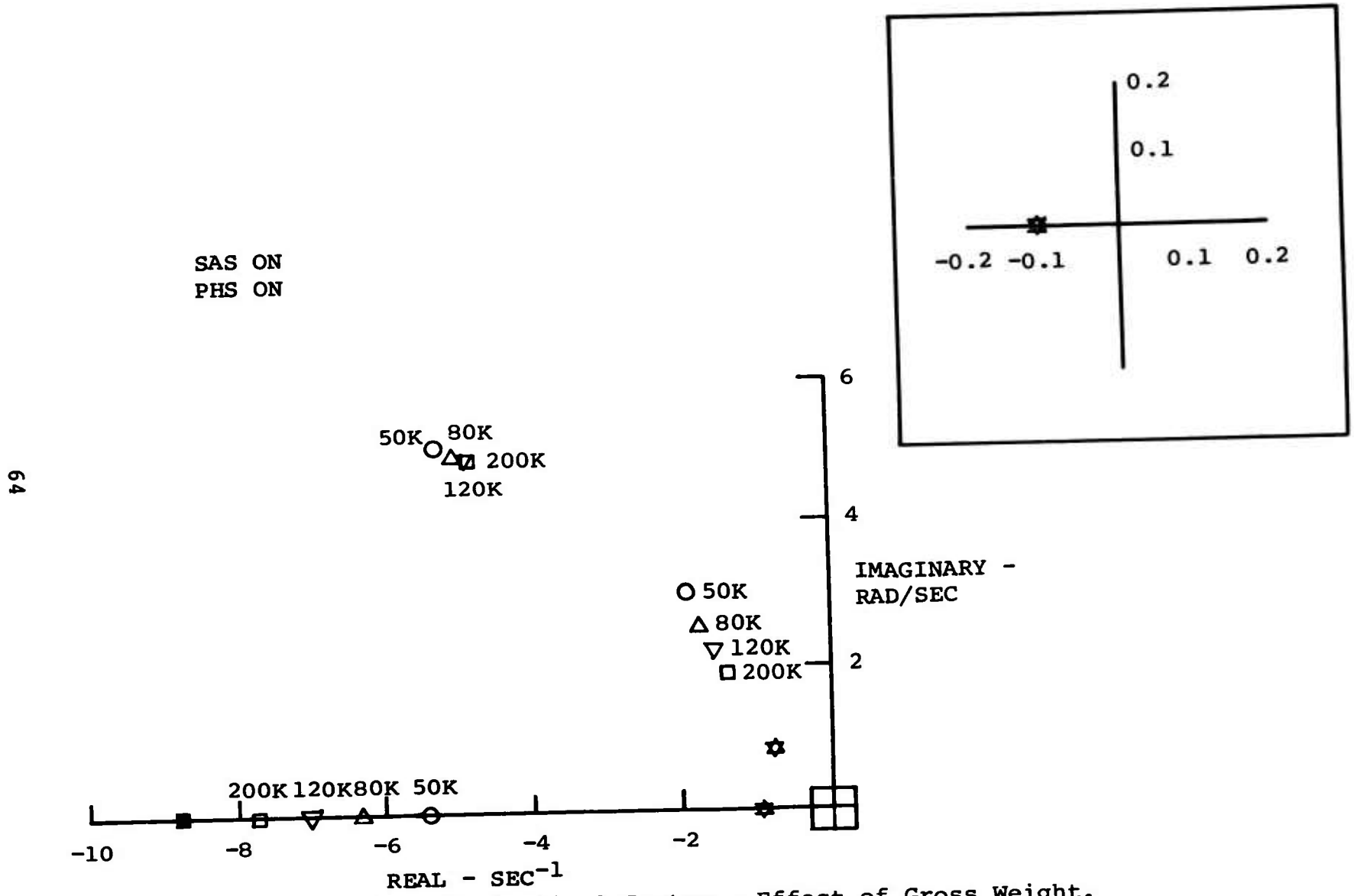

Figure 31. Longitudinal System - Effect of Gross Weight.

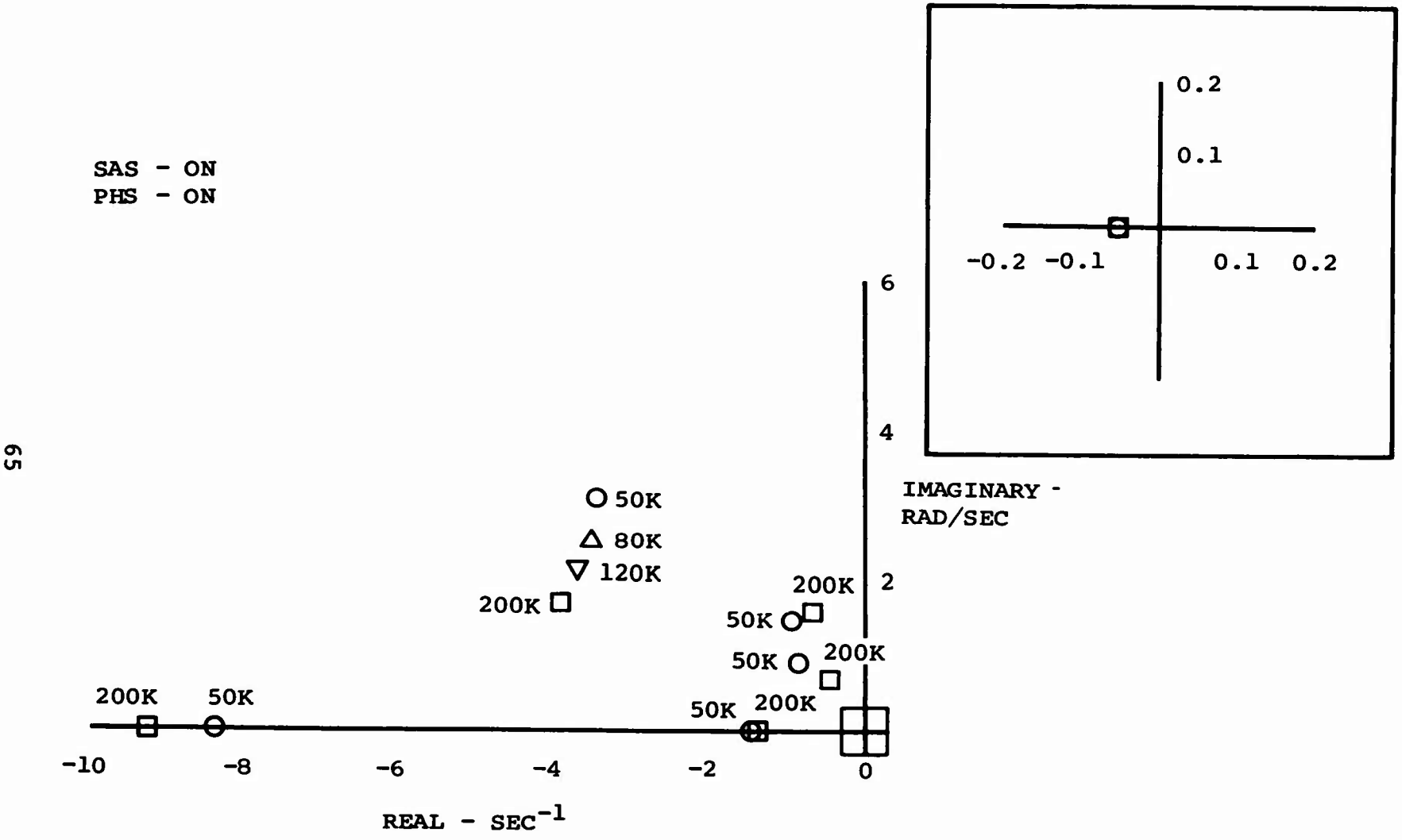

Figure 32. Lateral-Directional System Eigenvalues Effect of Gross Weight.

Low-Speed Gust Model

One way to investigate the hold performance of a helicopter and control system is to calculate the position root-mean-square (rms) error of the helicopter subjected to random velocity disturbances (turbulence). For this purpose, a one-dimensional gust model was chosen. Random U-gusts were used to evaluate the longitudinal-vertical motion, while random V-gusts were used for the lateral-directional motion.

The one-dimensional gust spectrum chosen for this analysis is

$$\Phi(\omega) = \frac{2\omega_g \sigma_g^2}{\omega^2 + \omega_g^2}$$

where

$$\omega_g = \frac{3}{2} \frac{V_{as}}{L_t}$$

The quantity L_τ is generally considered to be proportional to altitude at low altitudes and equal to 1000 feet at altitudes above 1000 feet. The parameter ω_g, gust break frequency, is chosen to be $\pi/10$, agreeing with References 2 and 3. The value of σ_g is chosen to be 5 ft/sec for most of the study. However, since the rms of any response is proportional to σ_g, the result for any other value of σ_g is easily obtained. Figure 33 is a plot of this gust spectrum and shows a very sharp drop-off with frequency.

Hover Hold Performance in Turbulence

Using the gust model just described and the fully augmented helicopter, the performance of the helicopter in turbulence was investigated.

Longitudinal-Vertical Performance

Figure 34 is the fully augmented (SAS ON and PHS ON) longitudinal-vertical system. Figure 35 shows the modulus squared of the transfer function, which represents the longitudinal position error of the 50,000-pound helicopter to longitudinal gust as a function of frequency. This plot shows the maximum value occurring at about 0.1 rad/sec. Figure 36 is the longitudinal position spectrum, which is obtained by multiplying the modulus squared of Figure 35 and the gust spectrum of Figure 33. The predominant effect of the gust spectrum can be seen in the rapid attenuation with frequency of Figure 36. If the curve of Figure 36 is calculated for frequencies between minus infinity and plus infinity, then integrated between these limits,

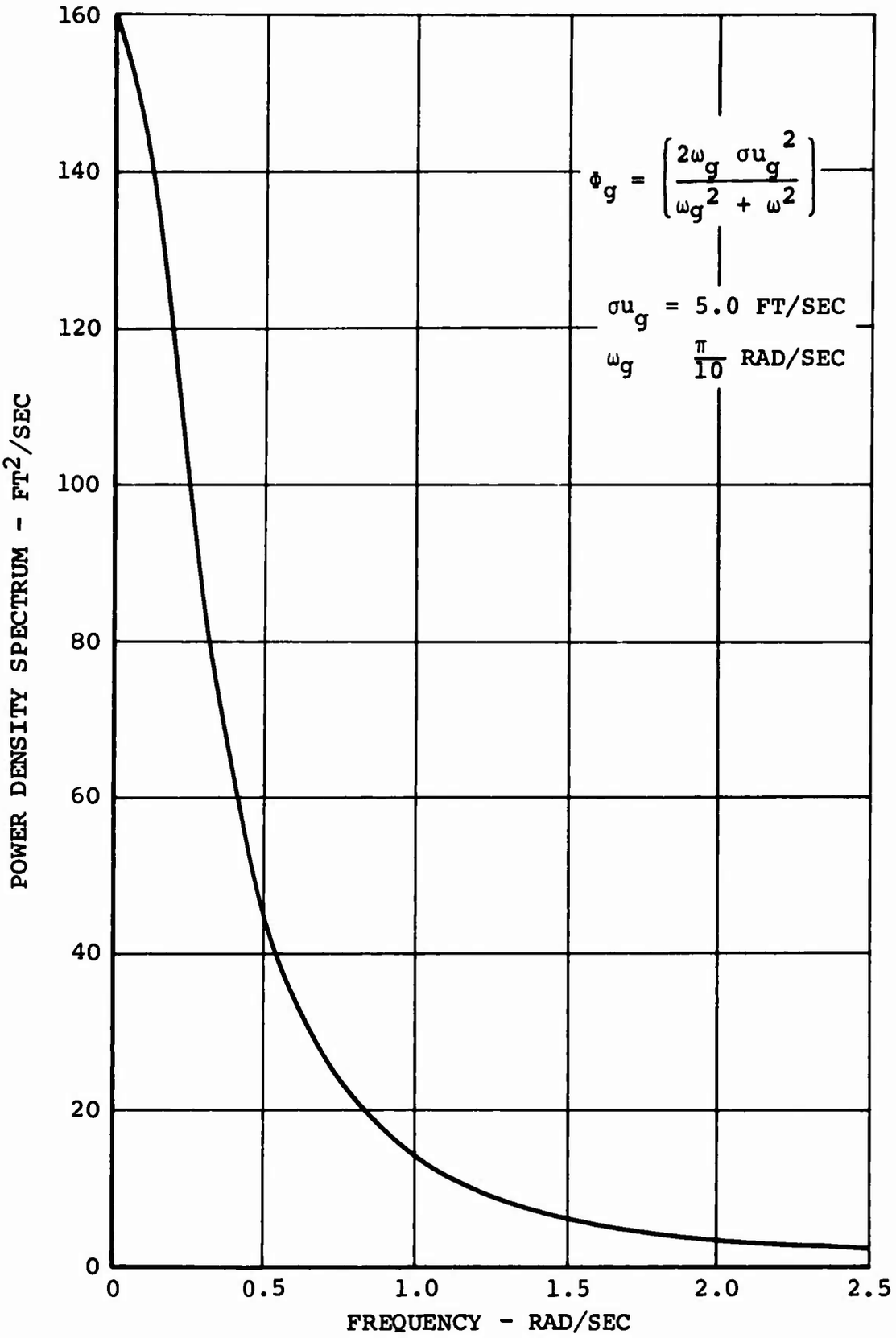

Figure 33. Gust (Turbulence) Power Spectrum.

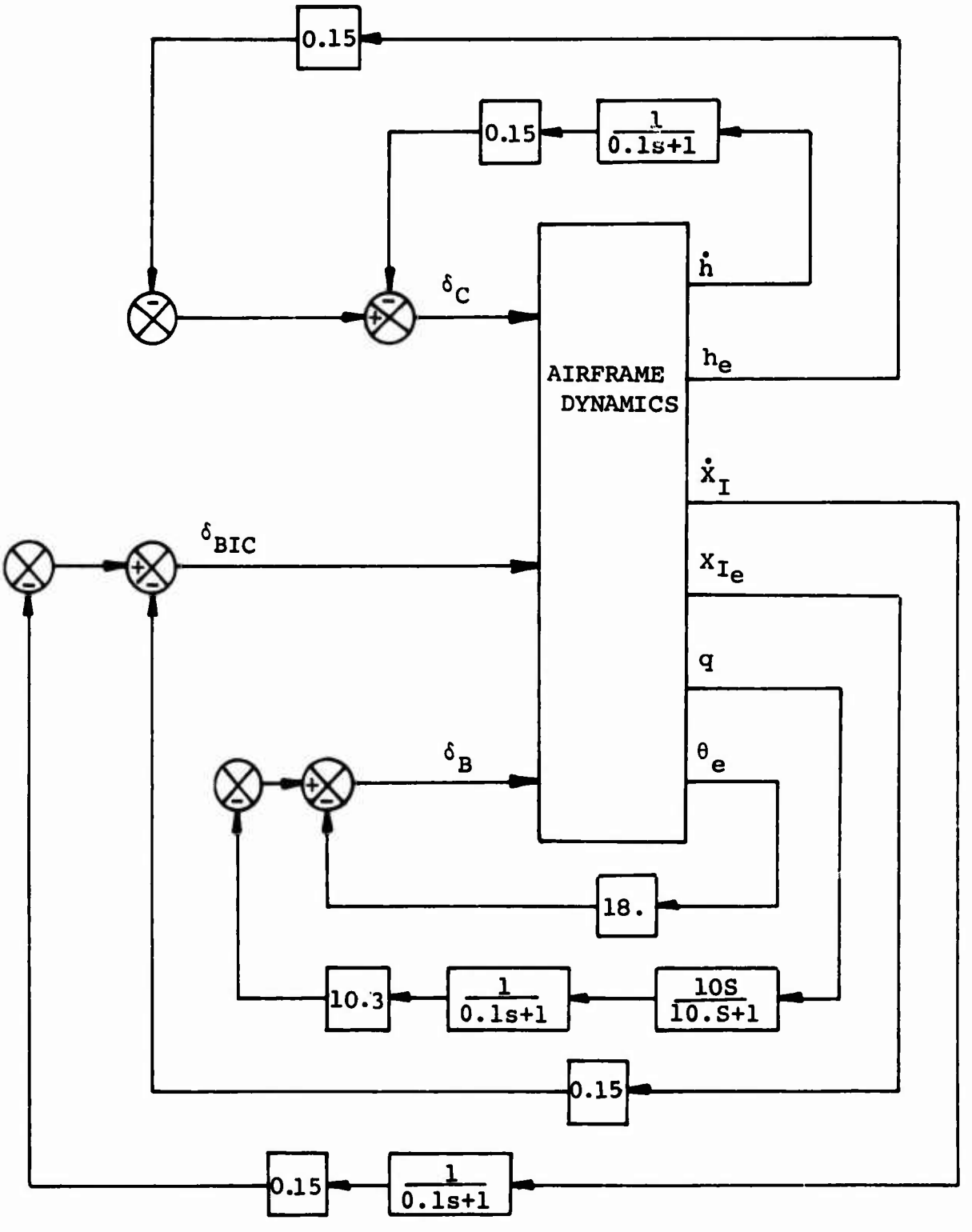

Figure 34. Longitudinal-Vertical System - Complete Block Diagram.

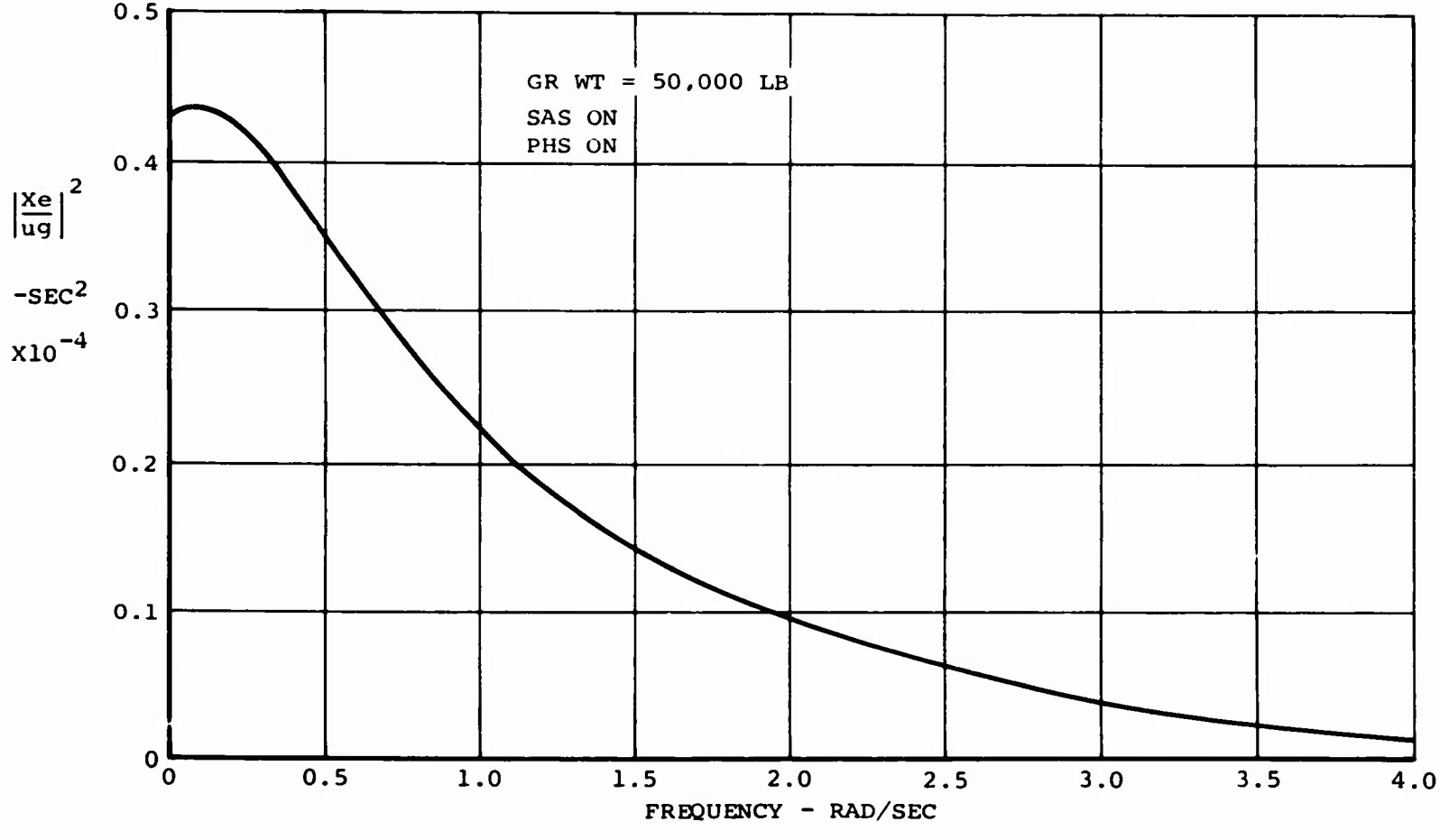

Figure 35. Modulus of Ratio of Longitudinal Position Error to Longitudinal Gust.

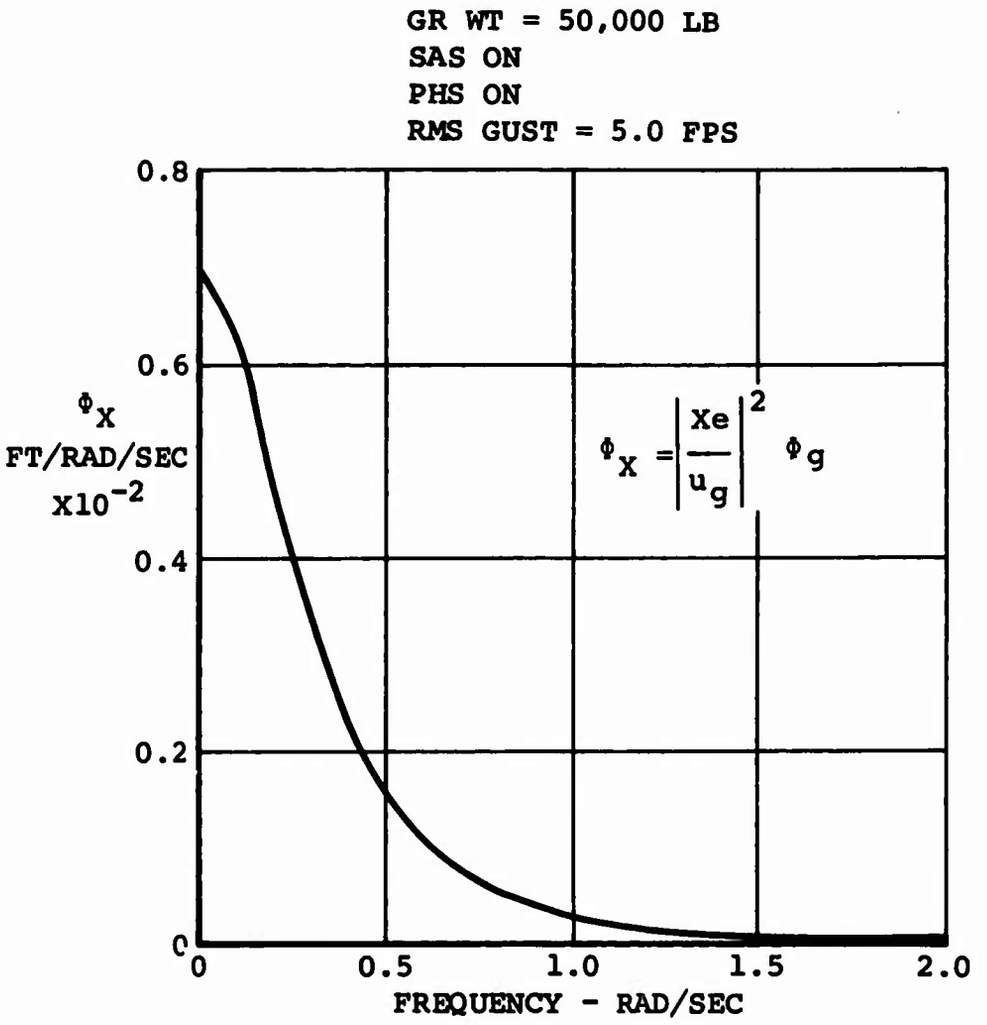

Figure 36. Power Spectrum of Longitudinal Position Error to Longitudinal Gust Ratio.

and finally divided by 2π, the result would be the root-mean-square response of position error due to the gust spectrum. However, since the position power spectrum is greatly attenuated with frequency, an adequate approximation to the rms can be obtained by truncating the integration at some cutoff frequency. Figure 37 shows the result of varying cutoff frequency on rms position error. As can be seen, an asymptotic value is rapidly approached above 1.0 rad/sec.

A measure of the relative comfort and discomfort of the pilot is the rms normal acceleration levels. Figure 38 is similar to Figure 35 except that the transfer function is now vertical acceleration at pilot station over longitudinal gust. As can be seen, the maximum value is obtained at a much higher frequency than position error. This is due to the pitch acceleration at the predominant high-frequency pitch mode. But as shown in Figure 39, the power spectrum of this function due to the gust spectrum is quite attenuated above 4 rad/sec. Figure 40 shows that the rms pilot acceleration is relatively constant above a cutoff frequency of 18 rad/sec.

Table X presents the rms values of the longitudinal position error, vertical position error, pitch attitude error, longitudinal acceleration at c.g., vertical acceleration at c.g., and vertical acceleration at pilot station as a function of helicopter size. The effect of size is minimal on all parameters, with the greatest effect appearing in pilot station acceleration, which shows a slight increase in size, probably due to increasing distance between c.g. and pilot station.

Lateral-Directional Performance

Figure 41 is the fully augmented, SAS ON and PHS ON, lateral-directional system. Figure 42 is the lateral position error transfer function due to lateral gust for the 50,000-pound configuration. The peak value for this function occurs at a slightly higher frequency than did the longitudinal position error, and does not drop off as rapidly with frequency. Figure 43 is the corresponding lateral position power spectrum as a result of the gust spectrum and shows a slightly shallower attenuating slope than did the longitudinal position spectrum. As a result of this shallower slope, the rms lateral position error approaches a higher value than did the longitudinal position rms value, Figure 44.

Figure 45 is the modulus squared of lateral acceleration at the pilot station. The first peak in this function roughly occurs at the lower frequency lateral velocity mode, while the second and smaller peak is influenced by the higher frequency lateral mode. Figure 46 is the result of imposing the gust spectrum on the acceleration modulus. The gust spectrum

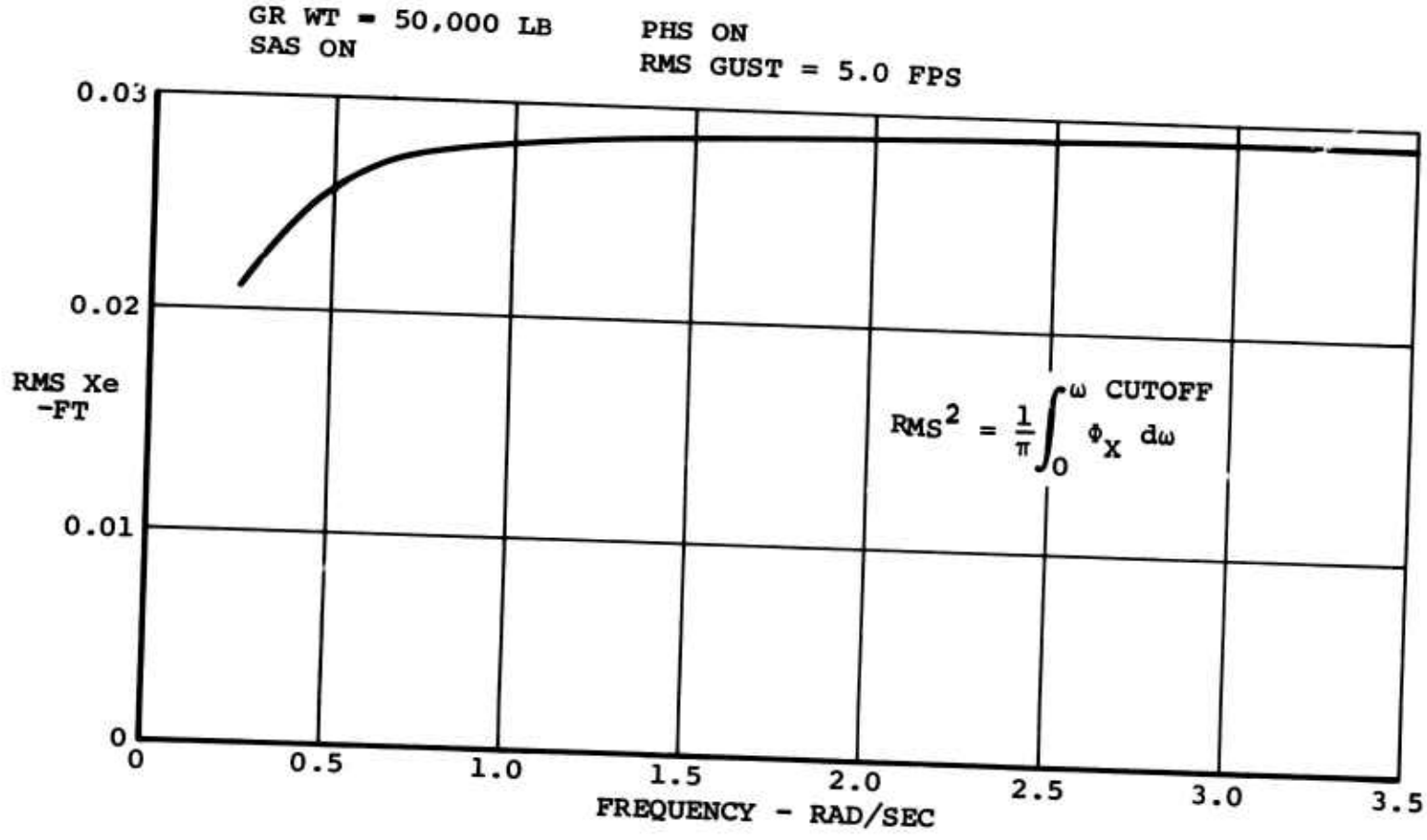

Figure 37. RMS Longitudinal Position Error to a Longitudinal Gust Versus Integration Cutoff Frequency.

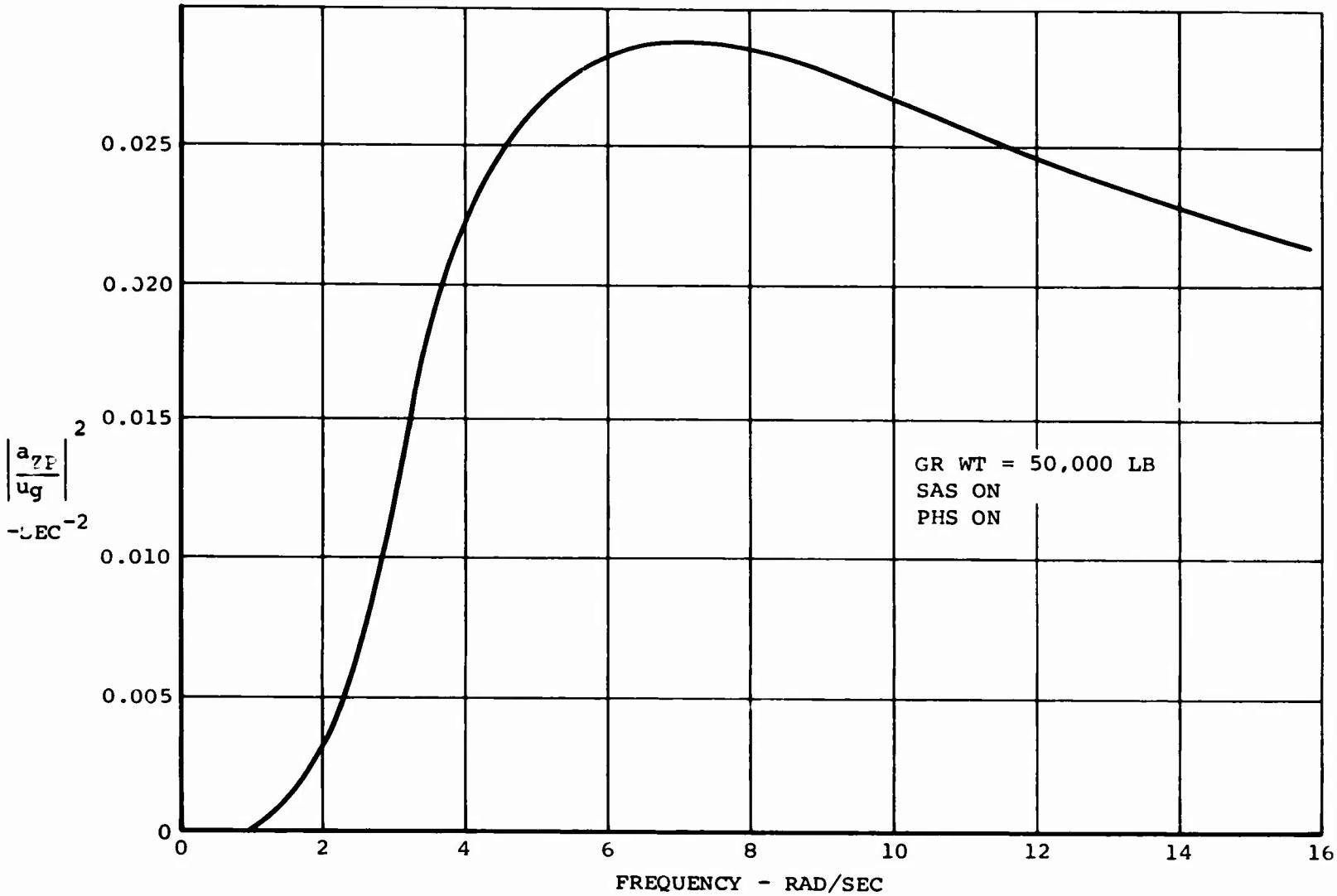

Figure 38. Modulus of Ratio of Vertical Acceleration at Pilot Station to Longitudinal Gust.

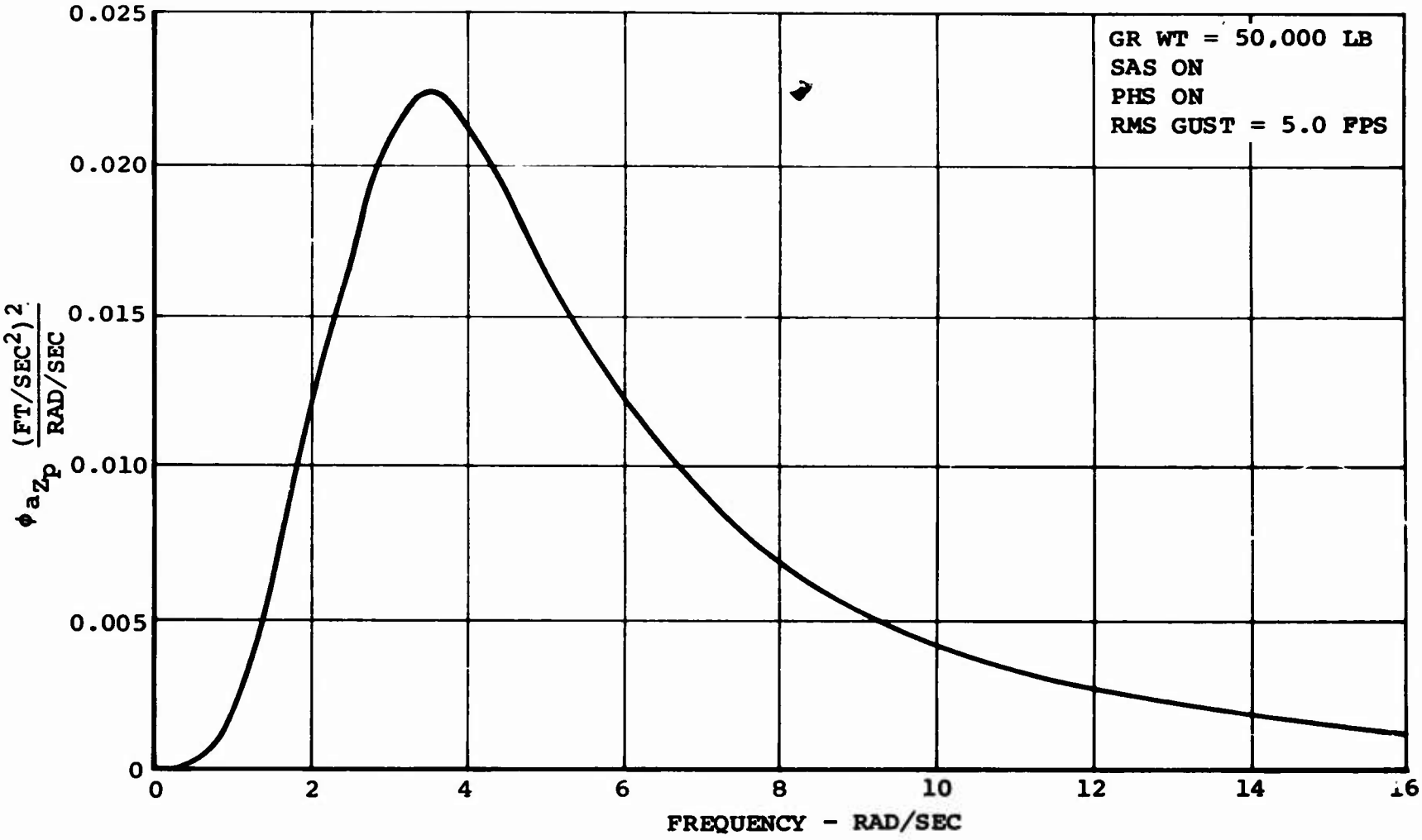

Figure 39. Power Spectrum of Vertical Acceleration at Pilot Station Due to Longitudinal Gust.

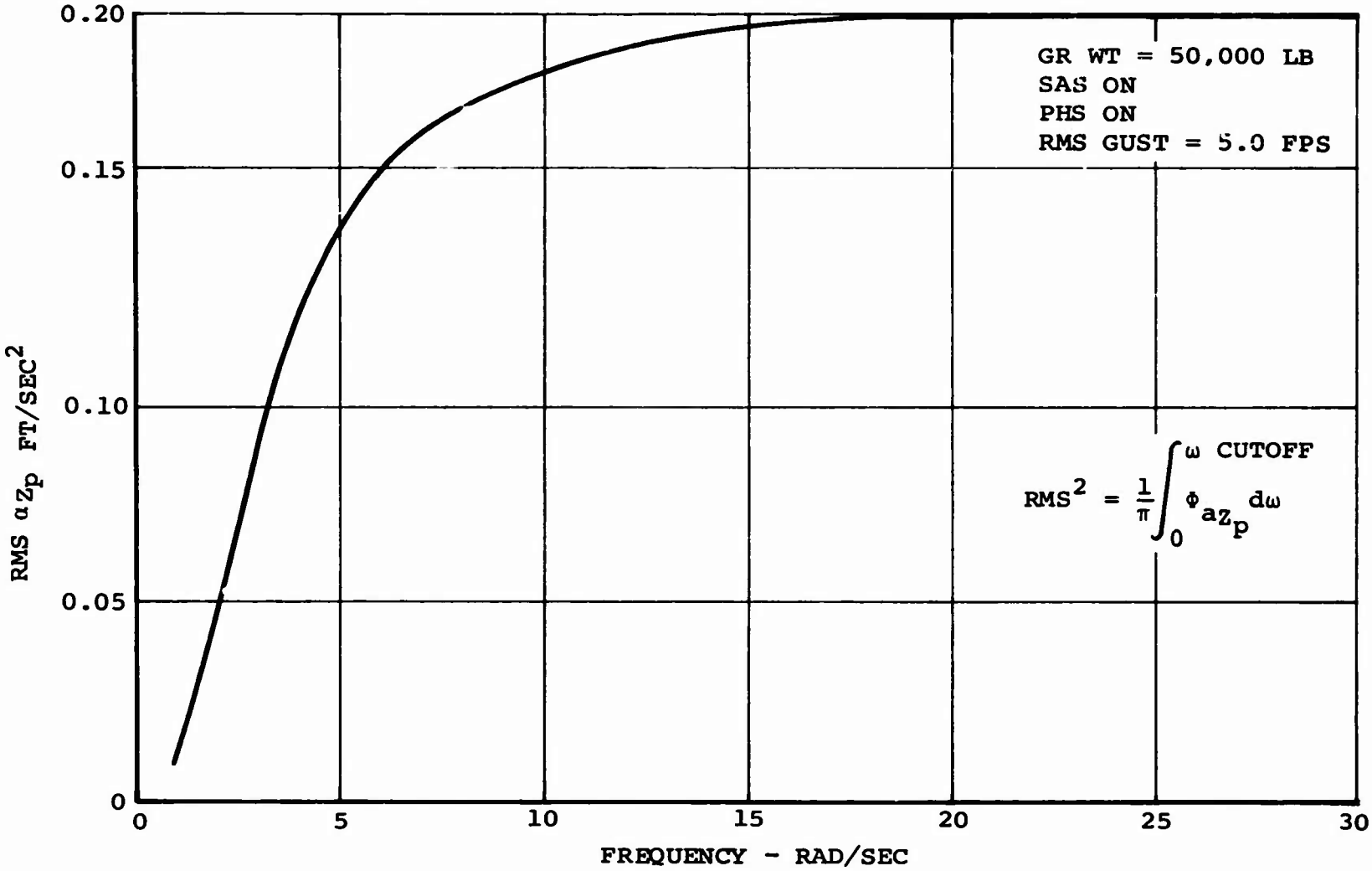

Figure 40. RMS Vertical Acceleration at Pilot Station Due to Longitudinal Gust Versus Integration Cutoff Frequency.

TABLE X. LONGITUDINAL-VERTICAL MOTION EFFECT OF GROSS WEIGHT ON RMS RESPONSES TO GUST

SAS ON, PHS ON

Gross Weight (Lb)	50,000	180,000	120,000	200,000
Xe (Ft)	0.03	0.03	0.03	0.03
Ze (Ft)	0.05	0.05	0.05	0.05
θ_e (Deg)	0.13	0.13	0.13	0.14
$\alpha_{x_{c.g.}}$ (Ft/Sec^2)	0.015	0.015	0.014	0.014
$\alpha_{z_{c.g.}}$ (Ft/Sec^2)	0.025	0.025	0.025	0.025
α_{z_p} (Ft/Sec^2)	0.206	0.207	0.199	0.215

GUST MODEL

One-Dimensional Longitudinal Spectrum

$$\Phi_{ug} = \frac{2\omega g\ \sigma ug^2}{\omega^2 + \omega g^2}$$

$\sigma ug = 5.0$ Ft/Sec

$\omega g = \pi/10$ Rad/Sec

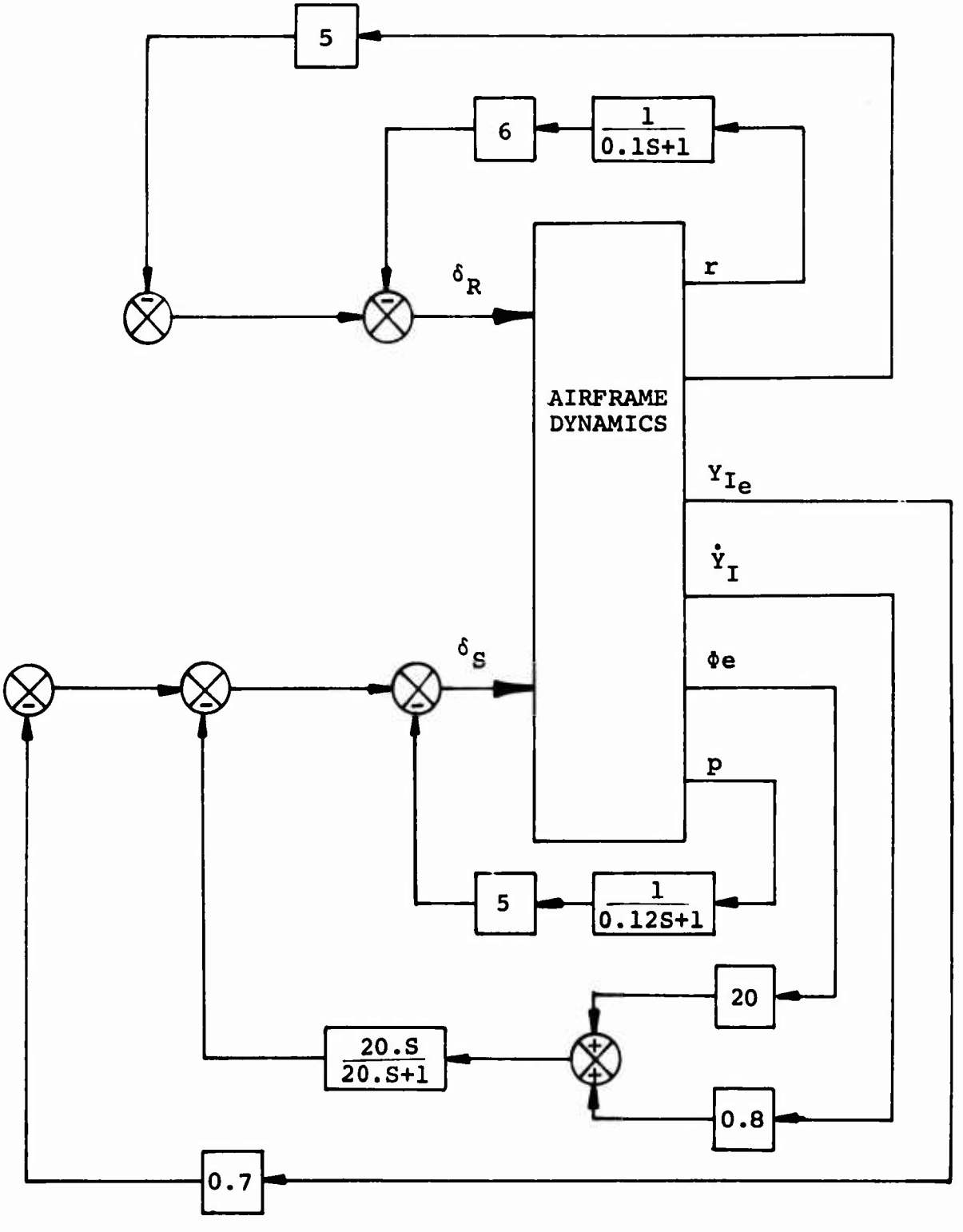

Figure 41. Lateral-Directional System (Complete Block Diagram).

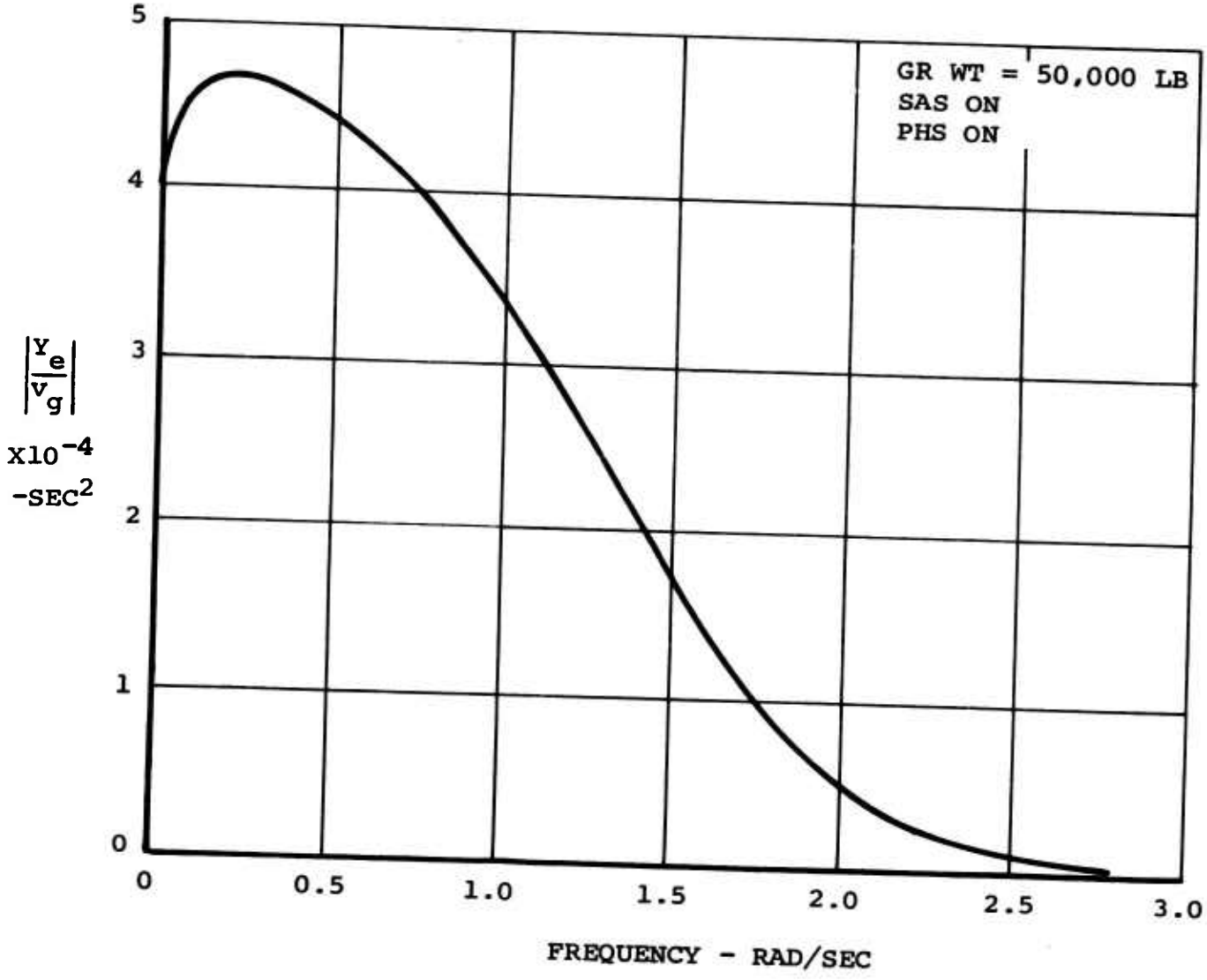

Figure 42. Modulus of Ratio of Lateral Position Error to Lateral Gust.

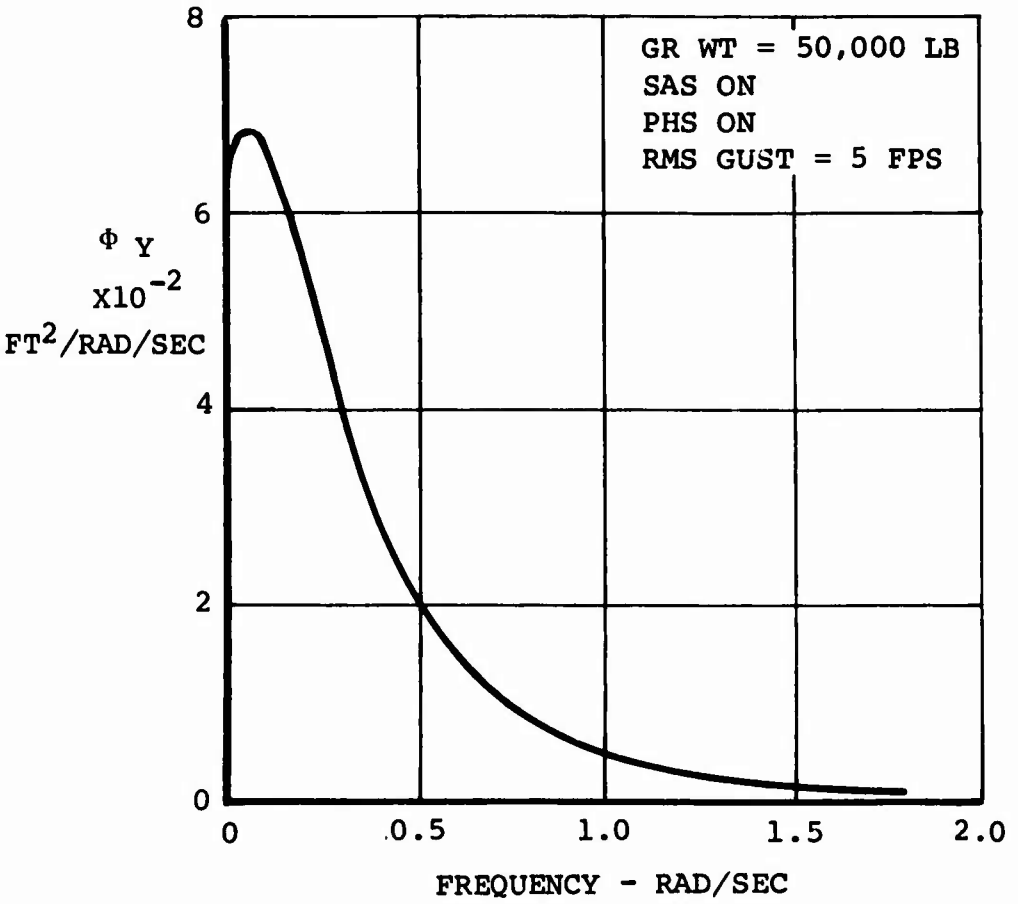

Figure 43. Power Spectrum of Lateral Position Error Due to Lateral Gust.

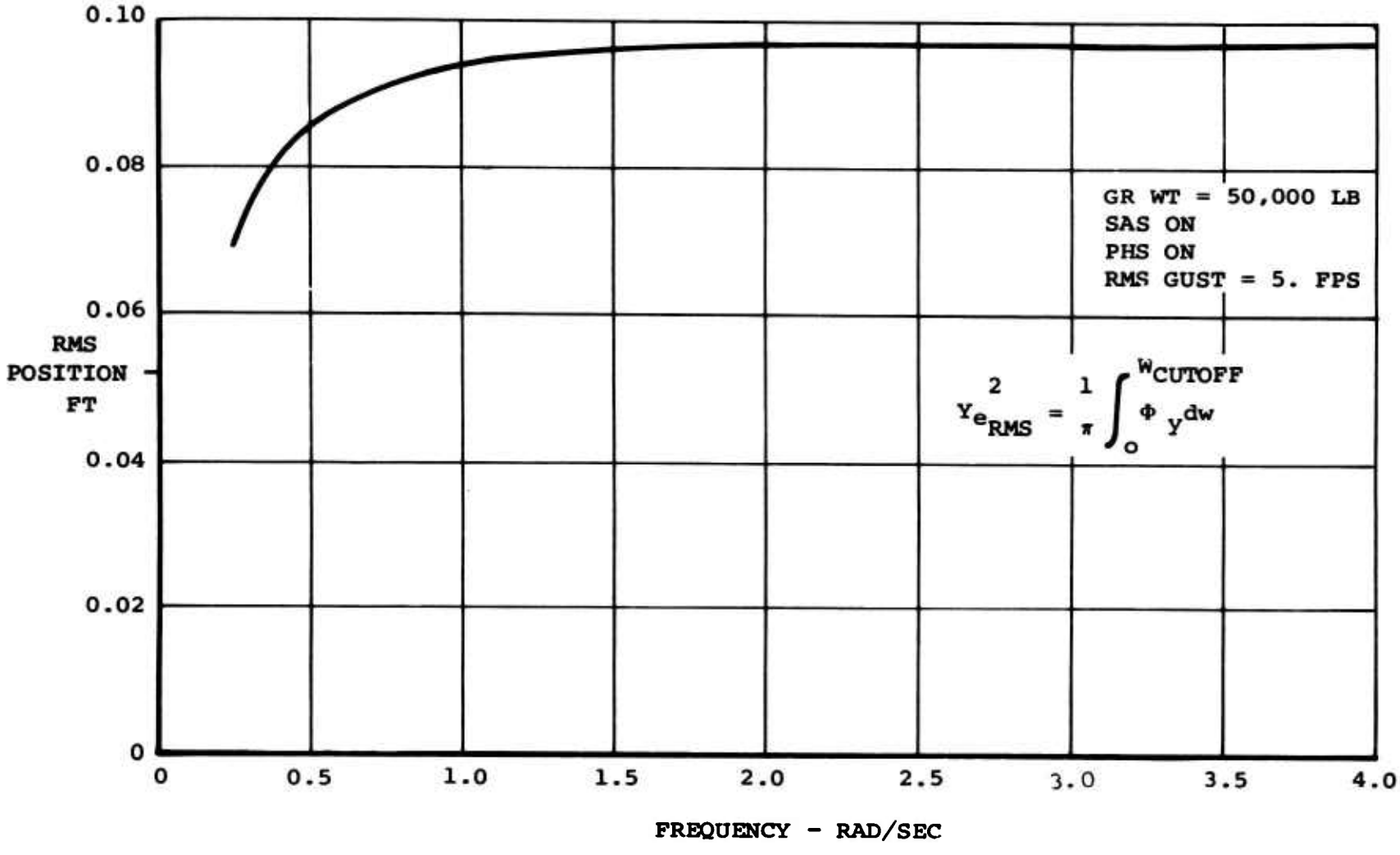

Figure 44. RMS Lateral Position Error Due to Lateral Gusts Versus Integration Cutoff Frequency.

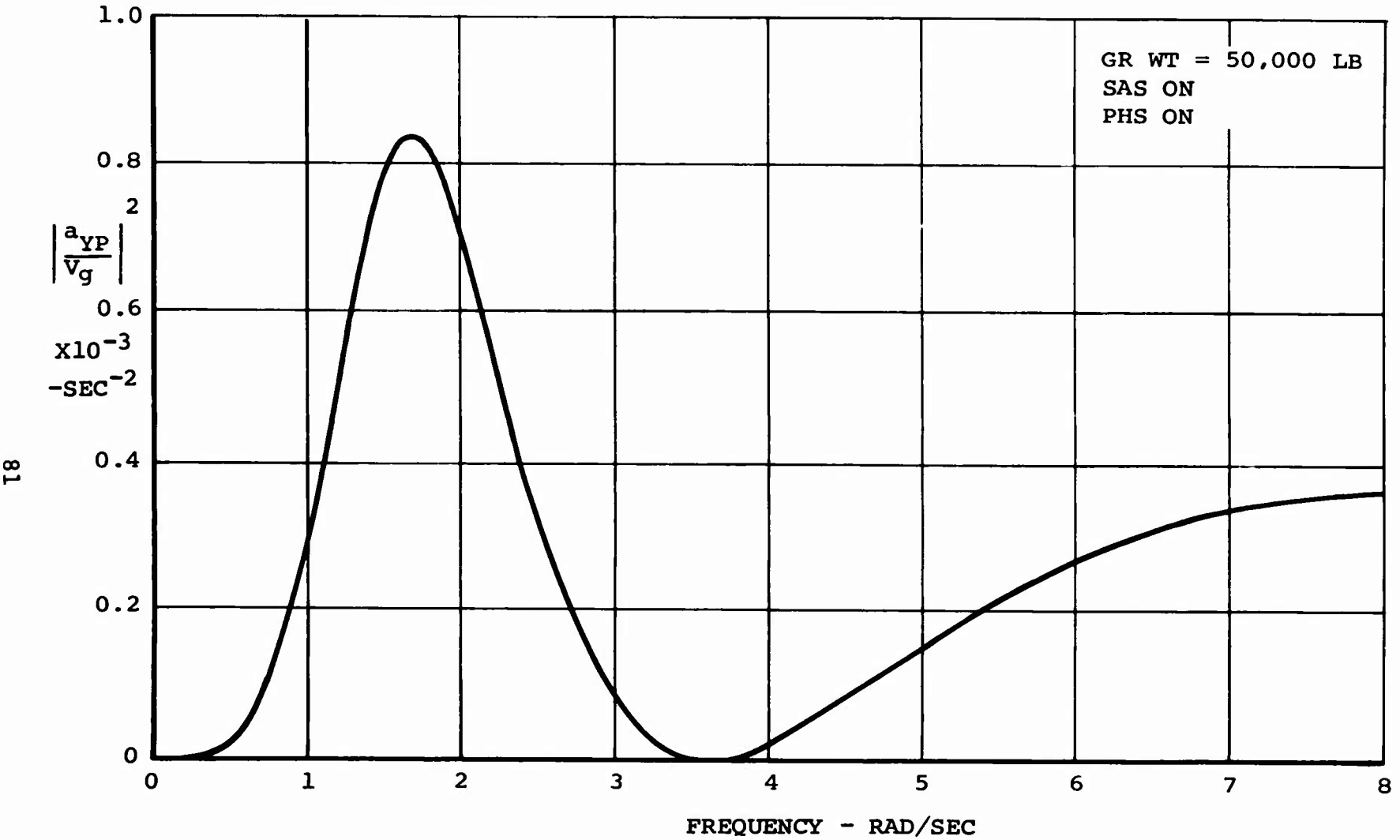

Figure 45. Modulus of Ratio of Lateral Acceleration at Pilot Station to Lateral Gust.

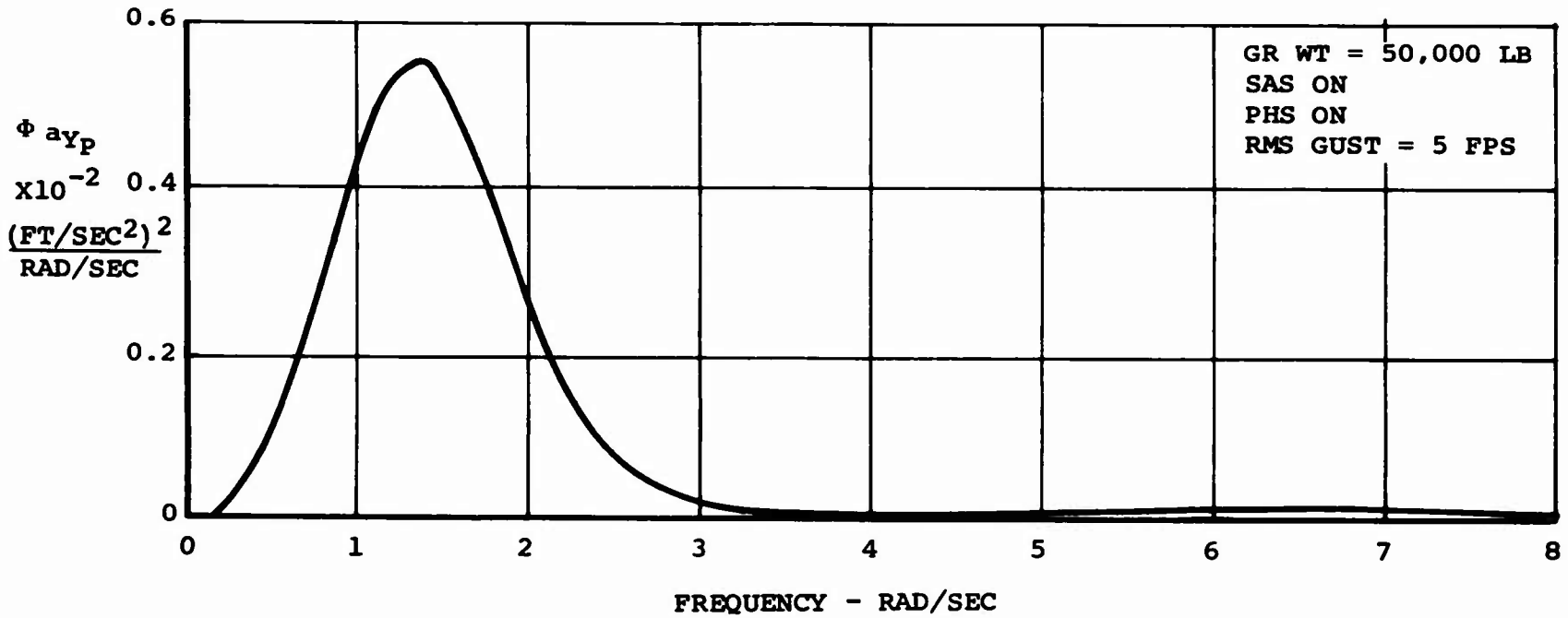

Figure 46. Power Spectrum of Lateral Acceleration at Pilot Station Due to Lateral Gusts.

almost eliminates the second peak. Finally, the effect of cutoff frequency is shown in Figure 47.

Table XI presents the rms values for the lateral position error, bank angle error, heading error, lateral acceleration at c.g., and lateral acceleration at pilot station as a function of helicopter size. As evident from the table, helicopter size has little effect.

PILOTED HOVER HOLD PERFORMANCE

The ability of the pilot to perform the precision hover task with the automatic hold system off is investigated in this section. A linear pilot model is for this purpose.

Pilot Model

The pilot transfer function model conventionally employed in handling quality analyses consists of the general form

$$Y_p = \frac{K_p\ (T_L S + 1)\ e^{-\tau s}}{(T_N S + 1)\ (T_I S + 1)}$$

together with adjustment rules for the parameters K_p, T_L, and T_I. The fixed parameters τ and T_N represent reaction-time and neuromuscular lag. General rules for the selection of these five pilot parameters are presented in Figure 48, which is reproduced from Reference 4.

From comments made in Reference 5 and preliminary results here, it was determined that the adjustable pilot lag, T_I, was not desirable for position loop closures in the crossover frequency range of interest. Figure 49 is representative of the effect that pilot lag has on closed-loop stability. Thus, $T_I = 0$ is used during the analysis.

The actual block diagram of the pilot model used in this study is shown in Figure 50. The transport lag, $e^{-\tau s}$, is represented by the first-order Pade's approximation. Values for the fixed parameters τ and T_N are chosen as 0.15 second and 0.10 second, respectively.

Control Options and Pilot-Assist Functions

In evaluating the pilot's ability to perform the precision hover task, several control options and assist functions will be considered. Figure 51 is a block diagram showing the control options and assist functions in the longitudinal axis. Three longitudinal options will be studied. Referring to Figure 51,

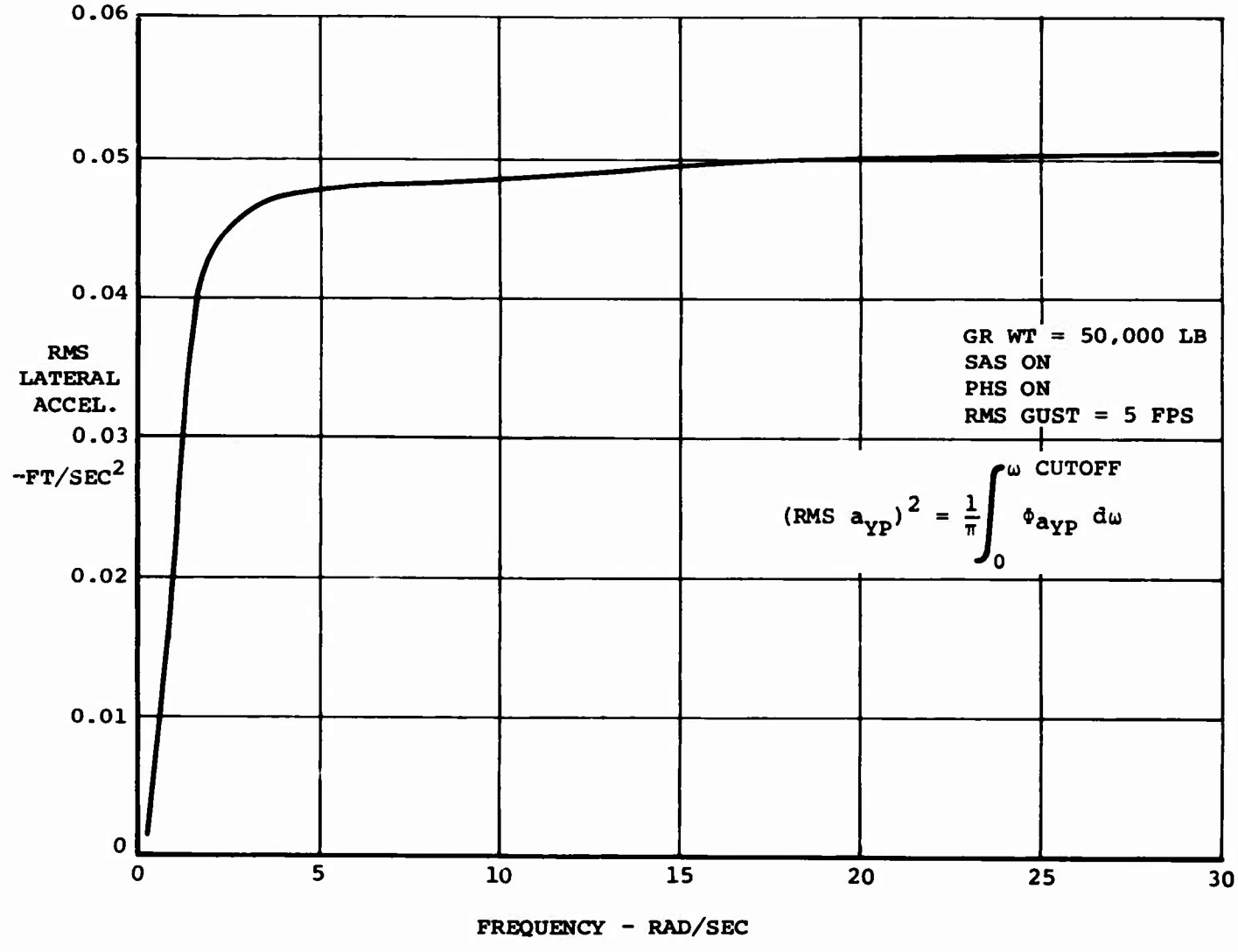

Figure 47. RMS Lateral Acceleration at Pilot Station Due to Lateral Gusts Versus Cutoff Frequency.

TABLE XI. LATERAL-DIRECTIONAL MOTION EFFECT OF GROSS WEIGHT ON RMS RESPONSES TO GUST

SAS ON, PHS ON

Gross Weight (Lb)	50,000	80,000	120,000	200,000
Ye (Ft)	0.097	0.096	0.096	0.095
Φe (Deg)	0.120	0.120	0.120	0.120
Ψe (Deg)	0.0115	0.0115	0.0115	0.0172
$\alpha_{Y_{C.G.}}$ (Ft/Sec^2)	0.054	0.053	0.053	0.052
α_{Y_P} (Ft/Sec^2)	0.051	0.050	0.050	0.048

GUST MODEL

One-Dimensional Lateral Spectrum

$$\Phi_{v_g} = \frac{2\omega g \sigma v g^2}{\omega^2 + \omega g^2}$$

σvg = 5.0 Ft/Sec

ωg = /10 Rad/Sec

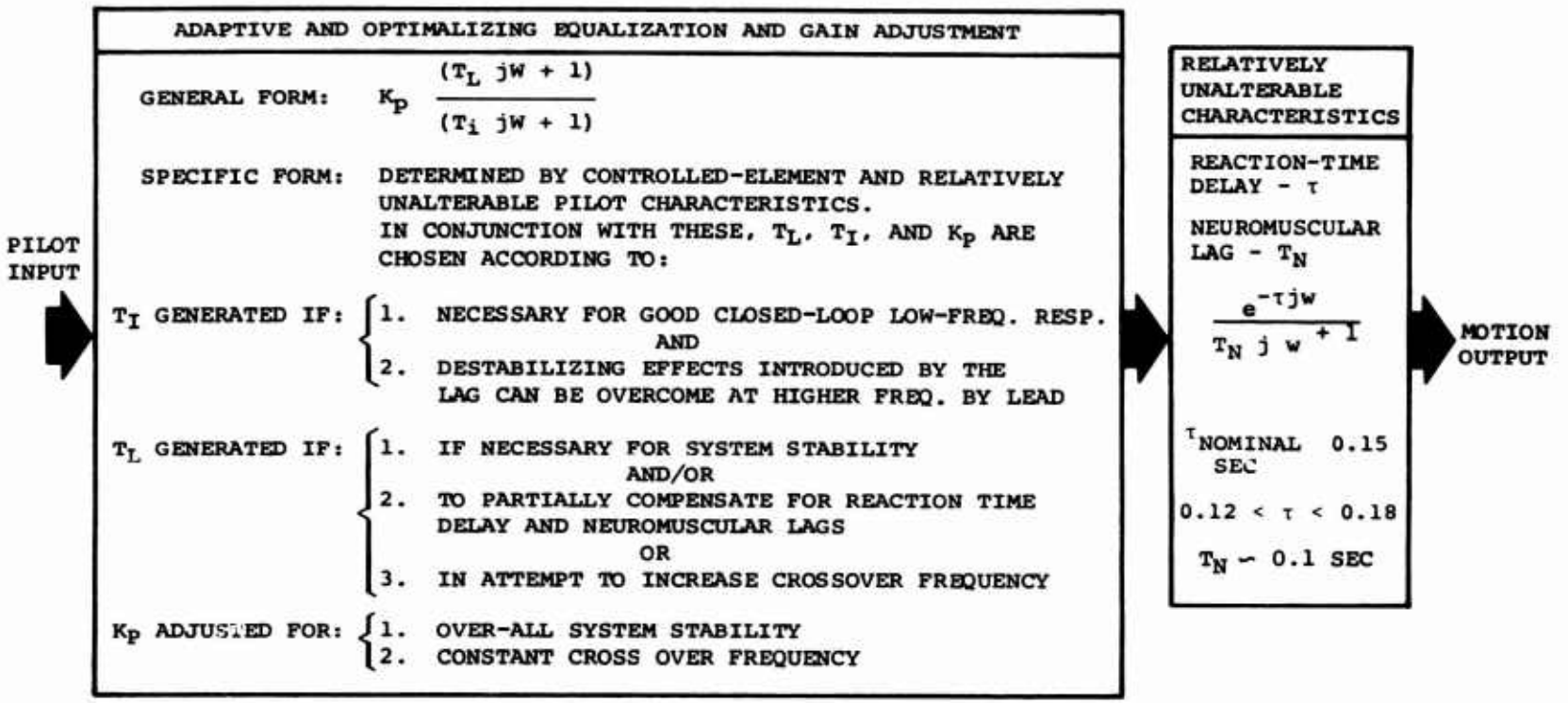

Figure 48. Generalized Human Pilot Describing-Function Model for a Compensatory System With Random-Appearing Visual Inputs.

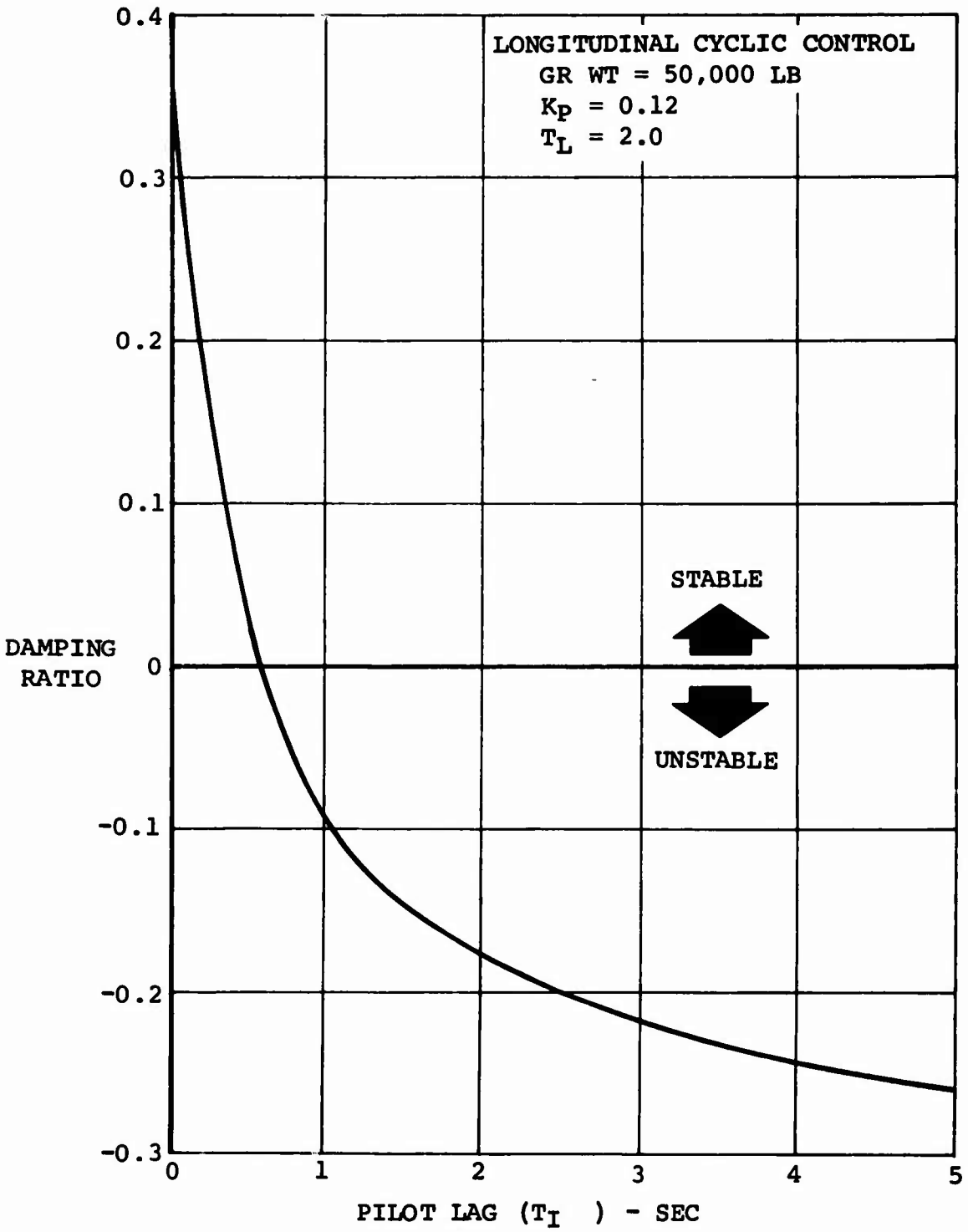

Figure 49. Effect of Adjustable Pilot Lag on Longitudinal Position Loop Closure Stability.

$$Y_p = K_p \frac{(T_L\ S+1)e^{-TS}}{(T_N\ S+1)}$$

$$= K_p \frac{(T_L\ S+1)(-\frac{T}{2}S+1)}{(T_N\ S+1)(\frac{T}{S}S+1)}$$

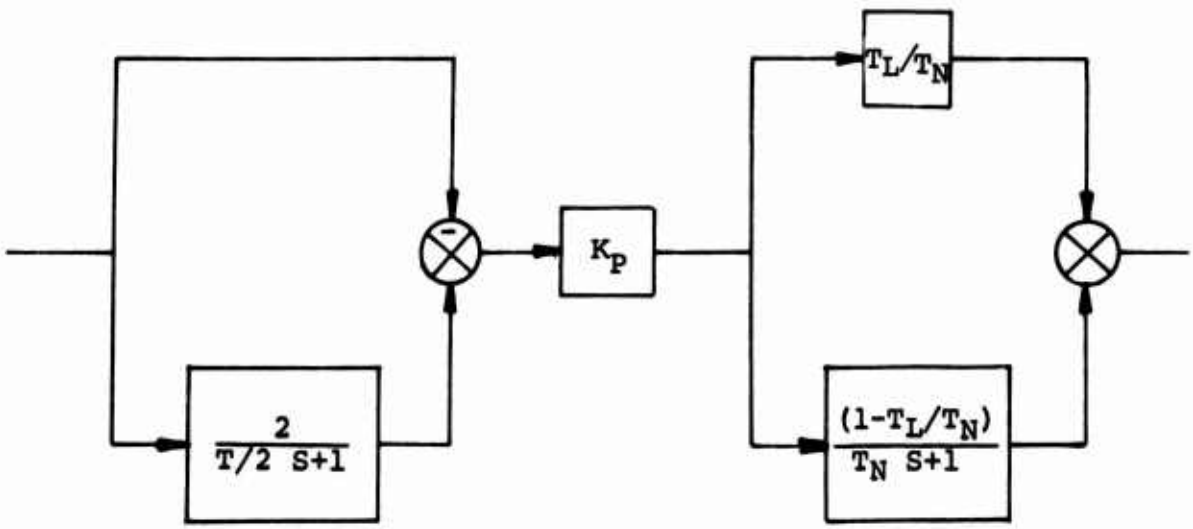

Figure 50. Pilot Model (Block Diagram Used in the Analysis).

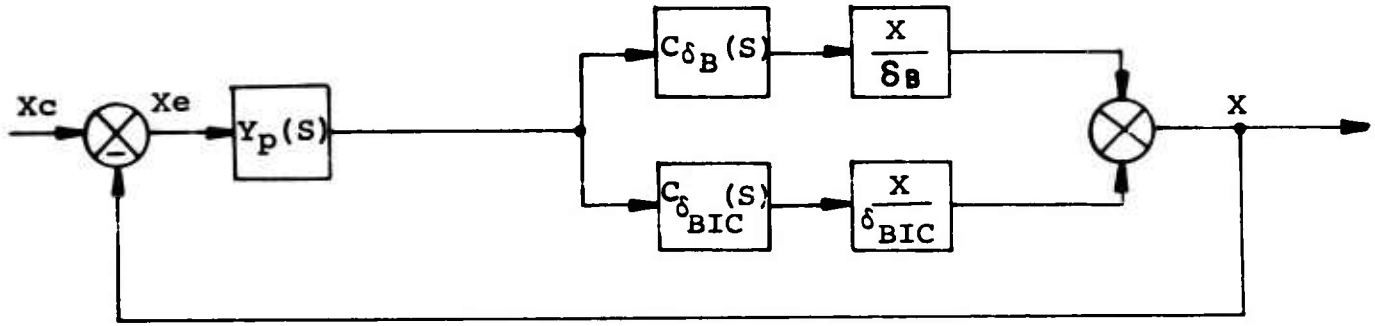

$$Y_p(S) = K_p \frac{-\tau/2S+1}{\tau/2S+1} \frac{T_L\ S+1}{T_N\ S+1}$$ LINEAR PILOT MODEL

$$C_{\delta_B}(S) = \left(\frac{K_{\delta_B}}{\tau_{\delta_B}\ S+1}\right)$$ DIFFERENTIAL COLLECTIVE PITCH SHAPING

$$C_{\delta_{BIC}}(S) = \left(\frac{K_{\delta_{BIC}}}{\tau_{\delta_{BIC}}\ S+1}\right)$$ LONGITUDINAL CYCLIC SHAPING

$\left(\frac{X}{\delta_B}\right), \left(\frac{X}{\delta_{BIC}}\right)$ HELICOPTER POSITION RESPONSE TO DCP AND LONGITUDINAL CYCLIC INPUTS, RESPECTIVELY, WITH SAS LOOPS CLOSED

Figure 51. Pilot Closure of Longitudinal Position Loop.

1. Longitudinal Control Type 1: longitudinal cyclic control only ($K_{\delta_{BIC}} = 0.1$, $\tau_{\delta_{BIC}} = 0.1$, $K_{\delta_B} = 0$)

2. Longitudinal Control Type 2: differential pitch control only ($K_{\delta_{BIC}} = 0$, $K_{\delta_B} = 1$, $\tau_{\delta_B} = 0$)

3. Longitudinal Control Type 3: longitudinal cyclic plus lagged differential pitch control ($K_{\delta_{BIC}} = 0.1$, $\tau_{\delta_{BIC}} = 0.1$, $K_{\delta_B} = 1$, $\tau_{\delta_B} = 2$)

Figure 52 shows the control options and assist functions available in the lateral axis.

1. Lateral Control Type 1: lateral cyclic control with no pickoffs ($K_{LCP} = 0$)
2. Lateral Control Type 2: lateral cyclic control with roll quickening through stick pickoff ($K_{LCP} = 1$, $T_{L_3} = 0.8$, $T_{L_2} = 3$).

In addition to the above lateral options, one further possibility will be investigated in an effort to evaluate the usefulness of velocity feedback in aiding the pilot to perform his task. This option is similar to option 1 except that there will be no velocity stabilization through the SAS.

3. Lateral Control Type 0: lateral cyclic control with no pickoffs ($K_{LCP} = 0$) and no velocity feedback through SAS ($G_{\dot{Y}} = 0$)

Pilot Closure of the Position Loop

In this study, it is assumed that the pilot is concerned with one axis at a time, either longitudinal or lateral. Thus only single-axis pilot closures will be addressed. According to Reference 4, the pilot will adjust his transfer function to perform the task and provide good closed-loop stability. The question arises as to which takes priority. Reference 3 suggests that the pilot tends to minimize pilot rating as a weighted function of performance and pilot leads. It also suggests, however, that a minimum 20% gain margin for stability be satisfied. Reference 4 quotes numbers like 40 to 80 degrees phase margin and closed-loop damping ratios greater than 0.350. Preliminary results showed that position error in turbulence decreased with increasing pilot gain, but that above a certain

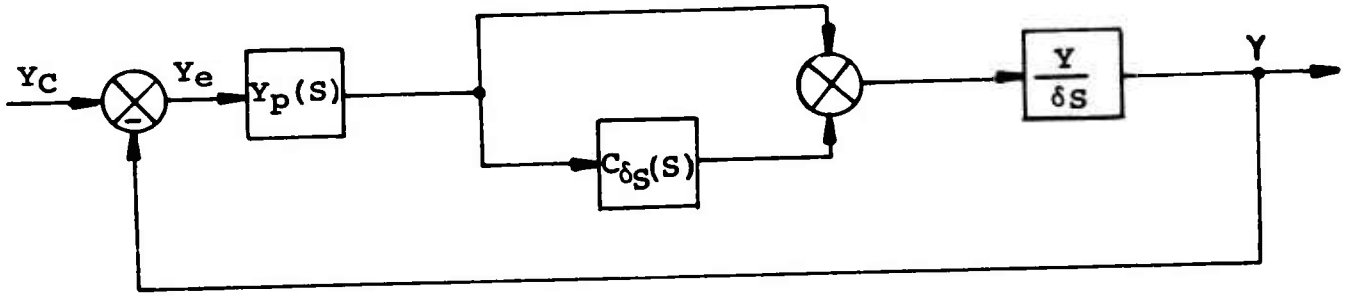

$$Y_p(S) = K_p \left(\frac{-\tau/2S+1}{\tau/2S+1}\right)\left(\frac{T_L\ S+1}{T_N\ S+1}\right)$$ LINEAR PILOT MODEL

$$C_{\delta_S}(S) = K_{LCP} \left(\frac{1}{T_{L_3}\ S+1}\right)\left(\frac{T_{L_2}S}{T_{L_2}\ S+1}\right)$$ LATERAL STICK PICK-OFF SHAPING

$\left(\frac{Y}{\delta S}\right)$ HELICOPTER LATERAL POSITION RESPONSE TO LATERAL STICK INPUT, WITH SAS LOOPS CLOSED

Figure 52. Pilot Closure of Lateral Position Loop.

value the stability of the system decreased. Therefore, it is felt that the pilot, in order to perform the task, will sacrifice as much stability as he can. Thus, a minimum level of 0.350 for closed-loop damping of the position mode will be assumed to form a boundary for possible combinations of pilot gain and lead time constants. For a second-order system, this damping level corresponds roughly to 35-40 degrees of phase margin. In situations where it is felt that a second-order response is not a good approximation for the position response, phase margins will be used as a lower stability bound, along with the requirement that no mode will have a damping ratio less than 35%. Once these stability limits on pilot gain and lead are determined, then a probable range of predicted values will be chosen based on hold capability in turbulence. Pilot work load, in terms of pilot lead, will then be estimated.

Longitudinal Position

Each of the three longitudinal control types mentioned above was studied using the 50,000- and 200,000-pound configurations. There are five eigenvalues of interest when the pilot closes the longitudinal position loop. These are the cubic, which represents the predominant pitch response, and the quadratic, which represents the longitudinal position and velocity response. For low pilot gains and even high pilot gains under certain control types, these responses can be considered distinct. However, with the 200,000-pound configuration and control type 3, the responses become highly coupled. For the cases where the pitch response becomes lightly damped, the single tracking pilot loop hypothesis becomes doubtful. In other words, when pitch excursions become significant to the pilot, then the pilot's inputs to the control system are going to be a sensed combination of pitch and position. However, this possibility will not be studied as it is felt to be beyond the scope of this analysis. In these cases the single-axis approach will be used with reservations.

Longitudinal Control Type 1 - Longitudinal Cyclic Control Only

For the 50,000-pound configuration, the pitch cubic of interest is a complex pair at relatively high frequency and a real eigenvalue with a longer time to half amplitude. Pilot closure of the position loop with the range of gains studied has little effect on the complex pair of pitch eigenvalues and tends to drive the real eigenvalue toward the origin.

Figure 53 is a root locus plot of the complex pair of eigenvalues representing the position-velocity response. Since the aperiodic pitch mode remains significantly quicker (time to

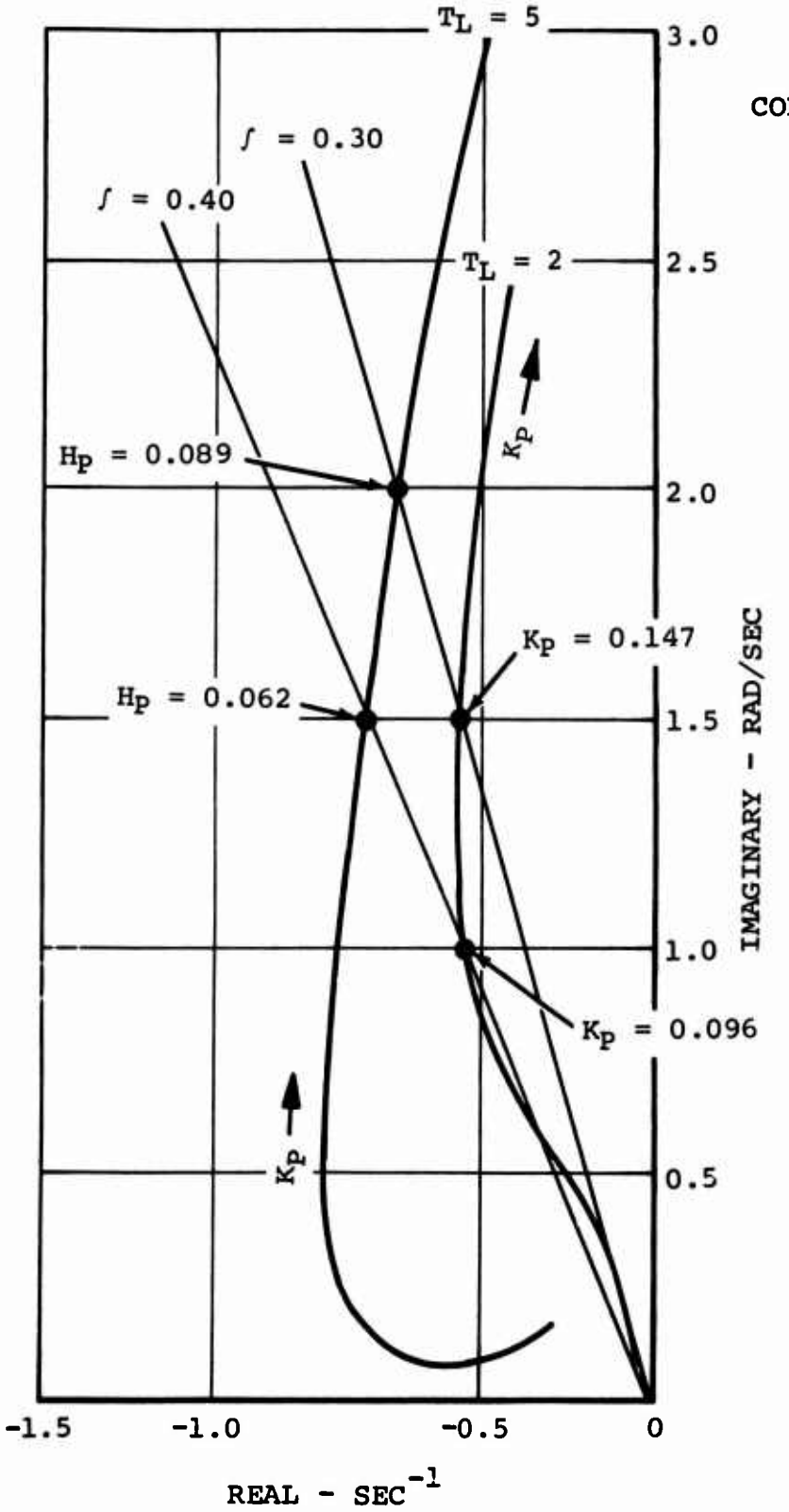

Figure 53. Longitudinal System - Effect of Pilot Gain on Closed-Loop Stability.

half amplitude much less) than the position mode when the imposed stability limits are approached, it can be assumed that the pitch response is uncoupled insofar as distracting the pilot from his precision hover task is concerned.

The damping of the position-velocity mode is plotted in Figure 54 as a function of pilot gain and lead time constant. For constant pilot lead, damping tends to increase and then decrease as pilot gain increases. As lead increases, the shape of the damping ratio versus pilot gain curve shows a sharper peak and greater attenuation following the peak. This points out a definite desirability on the pilot's part to provide a little lead as necessary to perform the task. This is true because the higher the lead, the harder the pilot would have to work to maintain acceptable bounds on his gain and the more the stability of the system would be changing. This point is further emphasized when pilot gain is plotted against pilot lead for constant damping levels. Figure 55 is such a plot for the 50,000-pound configuration with control type 1. As can be seen, a certain amount of pilot lead is needed to reach the proposed stability limit. The pilot will choose to operate on the flat portion of these curves if he can satisfy the task there. The ability of the pilot to perform the task on any portion of these curves will be considered later when the hold capability of this configuration is analyzed in turbulence.

For the 200,000-pound configuration, the pitch cubic is a low-frequency complex pair and a large negative real eigenvalue. Unlike the 50,000-pound configuration, where only the real eigenvalue showed significant movement with pilot gain, the entire pitch cubic is affected significantly with pilot gain. Figure 56 shows the effect of increasing pilot gain at constant pilot leads on the pitch cubic and position-velocity quadratic. As gain increases, one of the complex pair of pitch eigenvalues approaches the origin, while the other approaches the large negative eigenvalue that is moving toward the origin; and finally, as pilot gain further increases, the two larger eigenvalues combine to form a complex pair. This complex pair continues to decrease in damping and increase in frequency. The longitudinal velocity-position eigenvalues move toward each other, with increasing pilot gain, combine to form a complex pair, and then increase in frequency and decrease in damping until they are driven unstable. Figure 57 is the damping ratio of this mode versus pilot gain. The same trends as existed for the 50,000-pound configuration are shown in this plot for the 200,000-pound configuration. Figure 58 shows the damping contours for the 200,000-pound configuration and shows that the minimum acceptable pilot lead is only slightly higher than that for the 50,000-pound configuration, indicating that the position response for this type of control

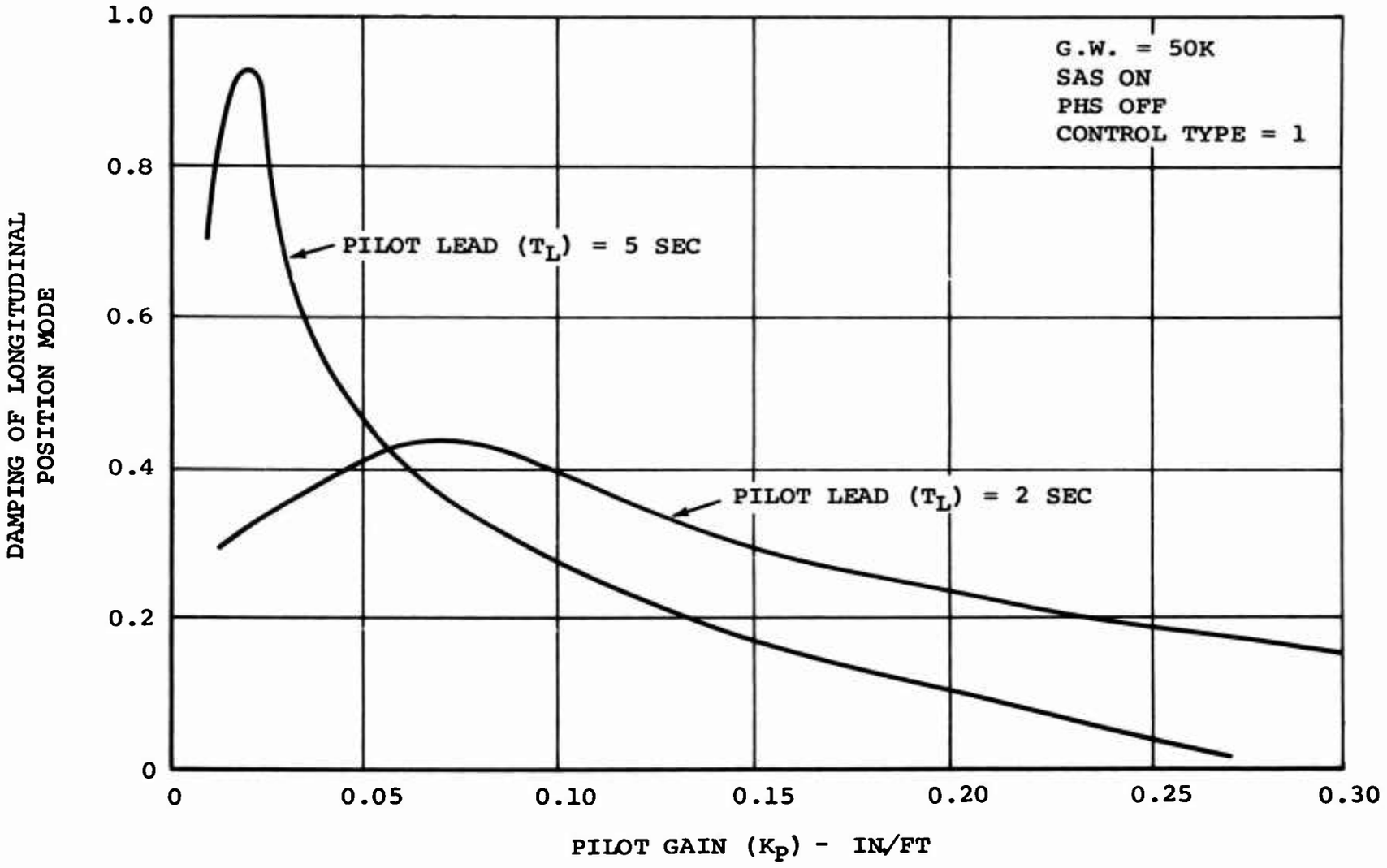

Figure 54. Longitudinal System - Damping of Longitudinal Position Mode.

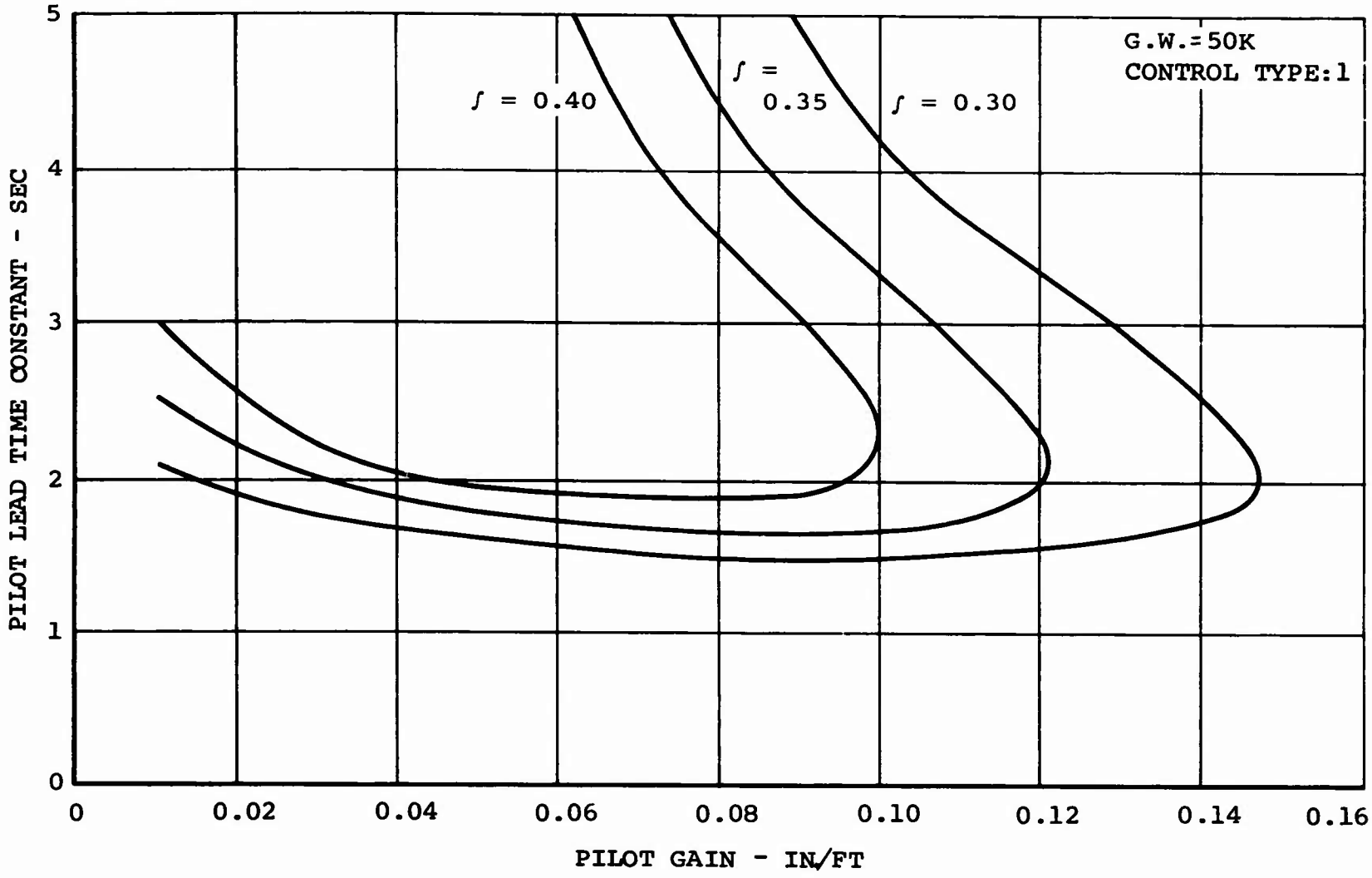

Figure 55. Longitudinal System - Damping Boundaries for Pilot Gain vs Pilot Lead Time Constant.

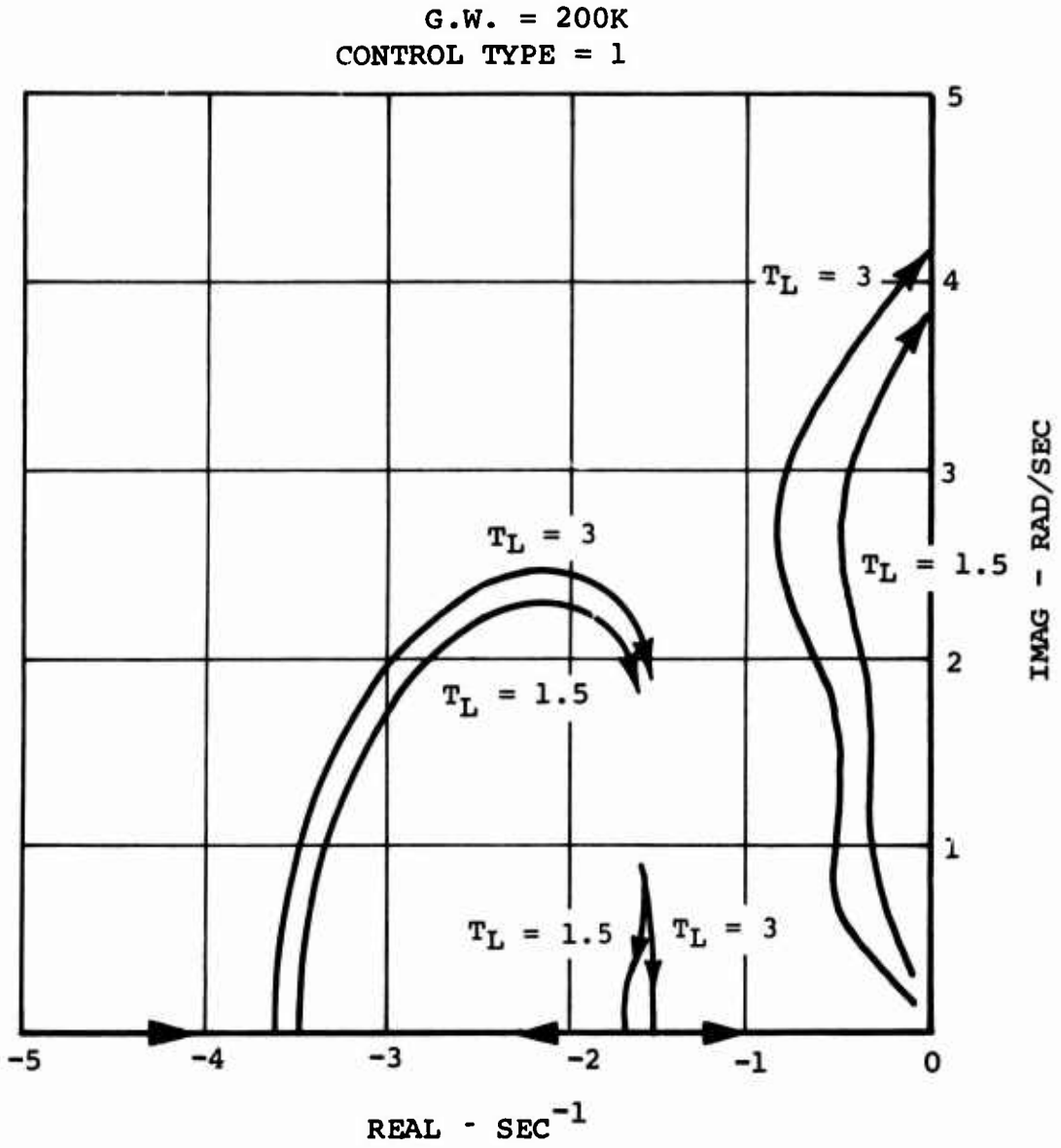

Figure 56. Longitudinal Root Locus.

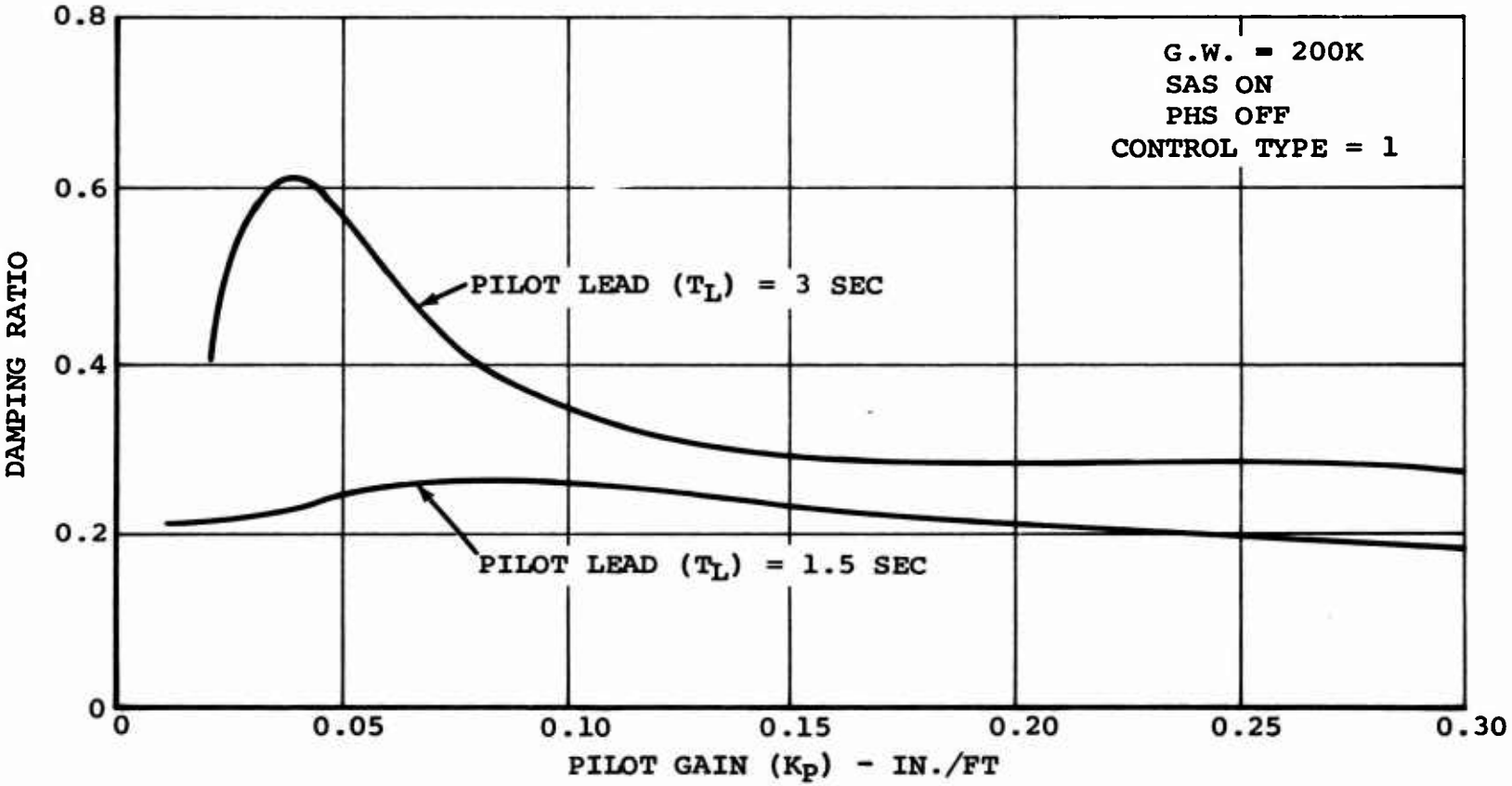

Figure 57. Longitudinal System - Damping of Longitudinal Position Mode.

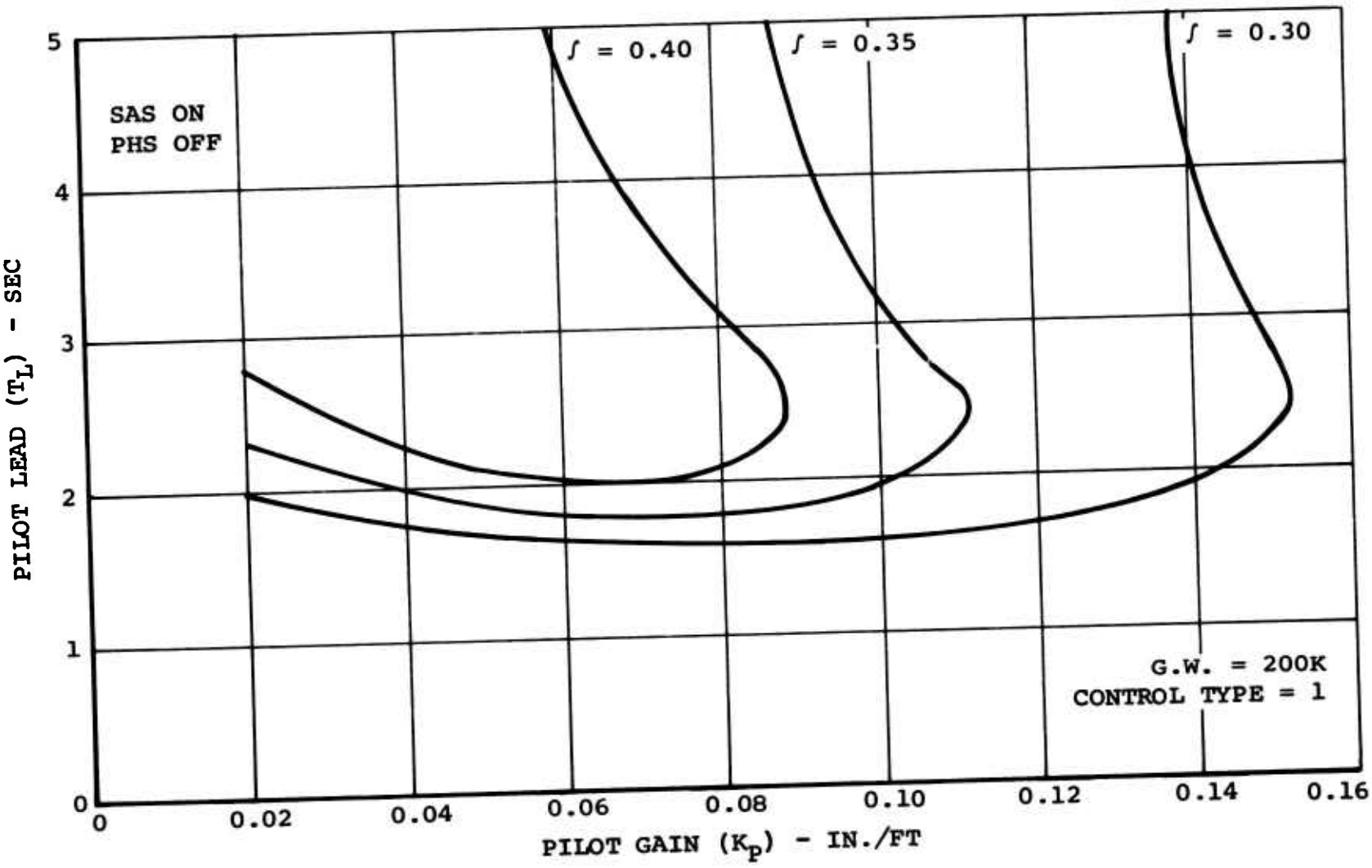

Figure 58. Longitudinal System - Damping Boundaries for Pilot Gain and Lead.

is rather invariant with size. However, the pilot might find the strong pitch coupling in the 200,000-pound configuration undesirable.

Longitudinal Control Type 2 - Differential Collective Pitch Control Only

As with control type 1, the closure of the position loop with this type of control has little effect on the high-frequency complex pair of pitch roots for the 50,000-pound configuration. However, as shown in Figure 59, the aperiodic pitch mode increases in time constant until the time to half amplitude of this mode is about the same as that for the position mode. This is not surprising with this type of control, since the pilot is trying to generate position changes with primarily pitch changes. The crossover frequency for the position mode using this type of control is much less than that for control type 1. Figure 60 is a plot of damping versus pilot gain for control type 2. The trend is similar to that for the other control type and gross weight. Figure 61 is a plot of the stability limits. When compared with Figure 55, the necessary minimum pilot lead seems to be about 1.0 second higher with DCP than with LCP, implying a greater work load. Also, the maximum acceptable gain is slightly less with DCP.

With the 200,000-pound configuration, an aperiodic pitch mode tends toward the origin with pilot closure of the position loop. However, the aperiodic mode for the 200,000-pound configuration is formed from the splitting of the low-frequency second-order pitch mode, as shown in Figure 62. The characteristics of the second-order position response are similar to the 50,000-pound case, but the crossover frequencies are less. As Figure 63 shows, the damping ratio is less for the 200,000-pound configuration for a given gain and lead. Consequently, as Figure 64 shows, the minimum allowable pilot gain is less.

Longitudinal Control Type 3 - Longitudinal Cyclic With Lagged Differential Collective Pitch Control

Figure 65 is the root locus plot for the 50,000-pound configuration with this type of longitudinal control. The high-frequency second-order pitch mode is not significantly affected and consequently is not plotted. The aperiodic pitch response falls between LCP only (type 1) and DCP only (type 2) as discussed in the above paragraphs. This aperiodic response is closer in time to half amplitude to the position mode than with LCP only, but farther than with DCP only. The crossover frequencies for the second-order position response are also between those for the LCP only and DCP only types of control. Figure 66 shows the damping ratio variation of the position mode with pilot gain and lead time constant. The trend of

G.W. = 50K
CONTROL TYPE = 2

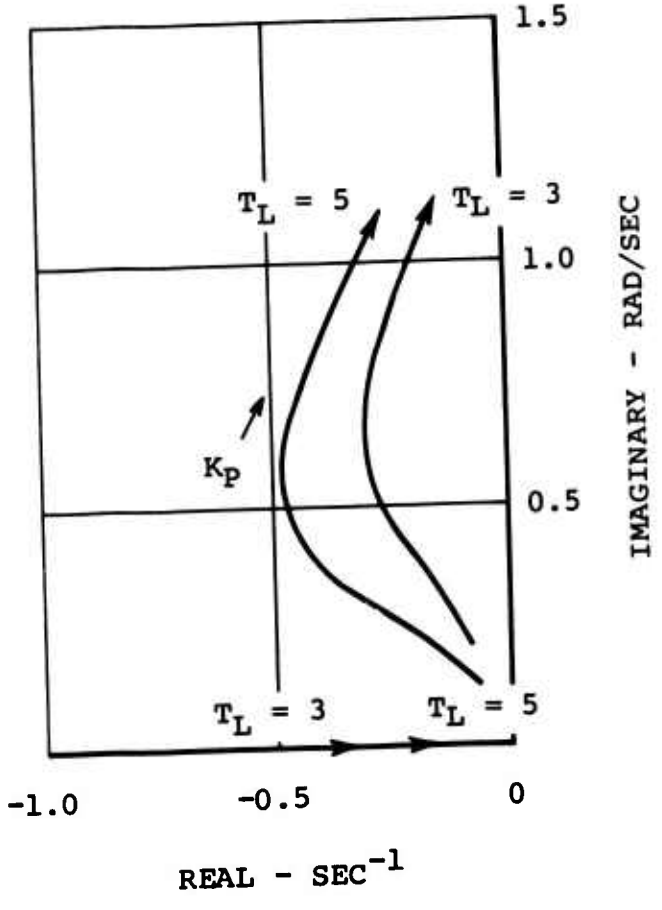

Figure 59. Longitudinal Root Locus.

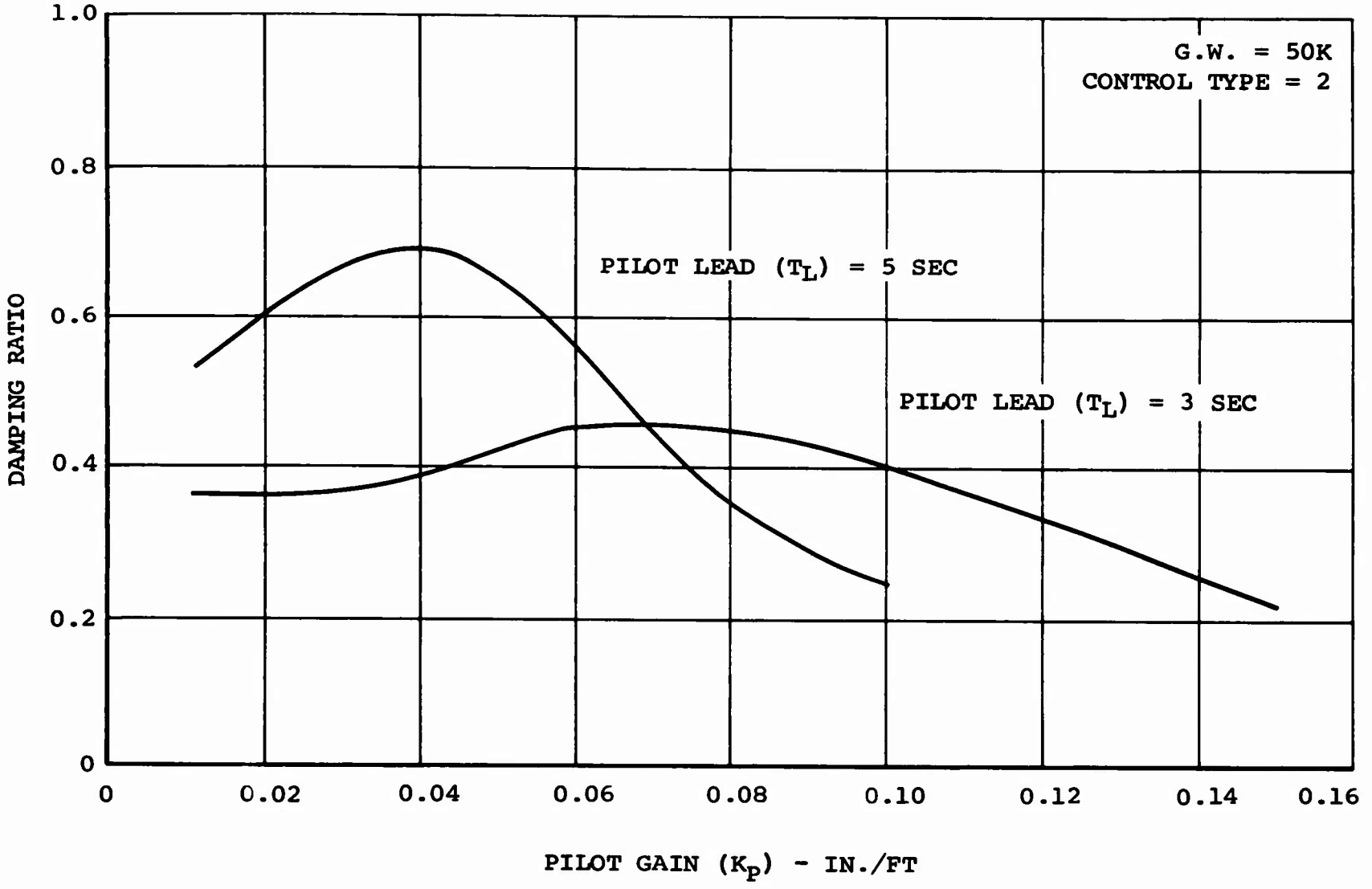

Figure 60. Longitudinal System - Position Modal Damping.

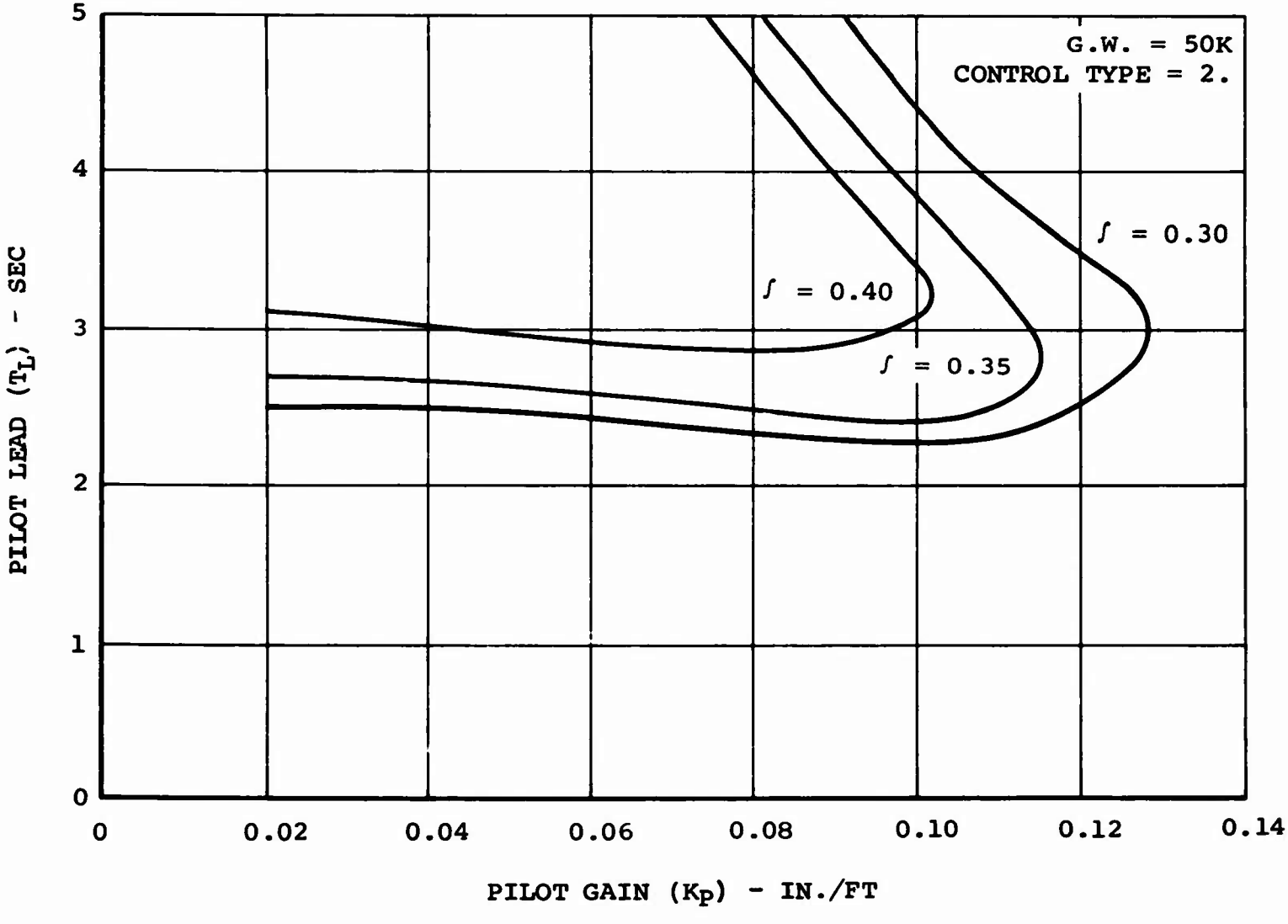

Figure 61. Longitudinal System - Damping Ratio Boundaries.

G.W. = 200K
CONTROL TYPE = 2

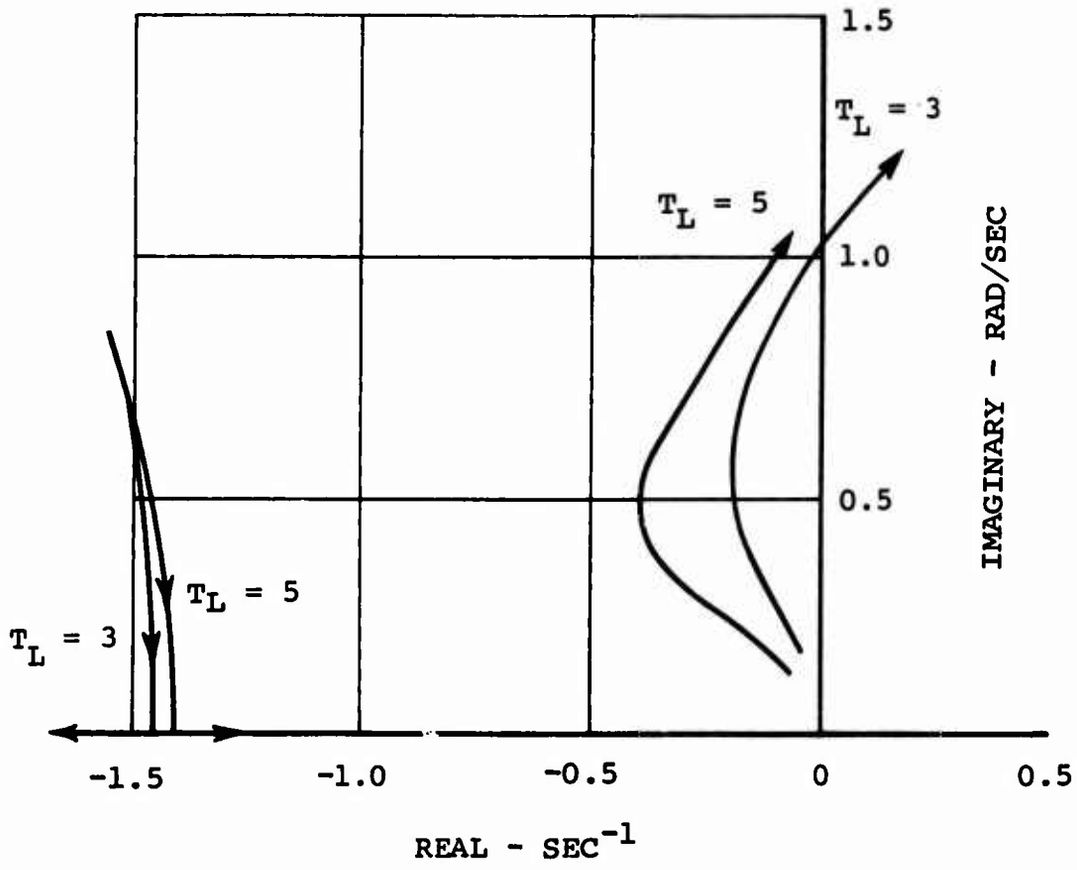

Figure 62. Longitudinal Root Locus.

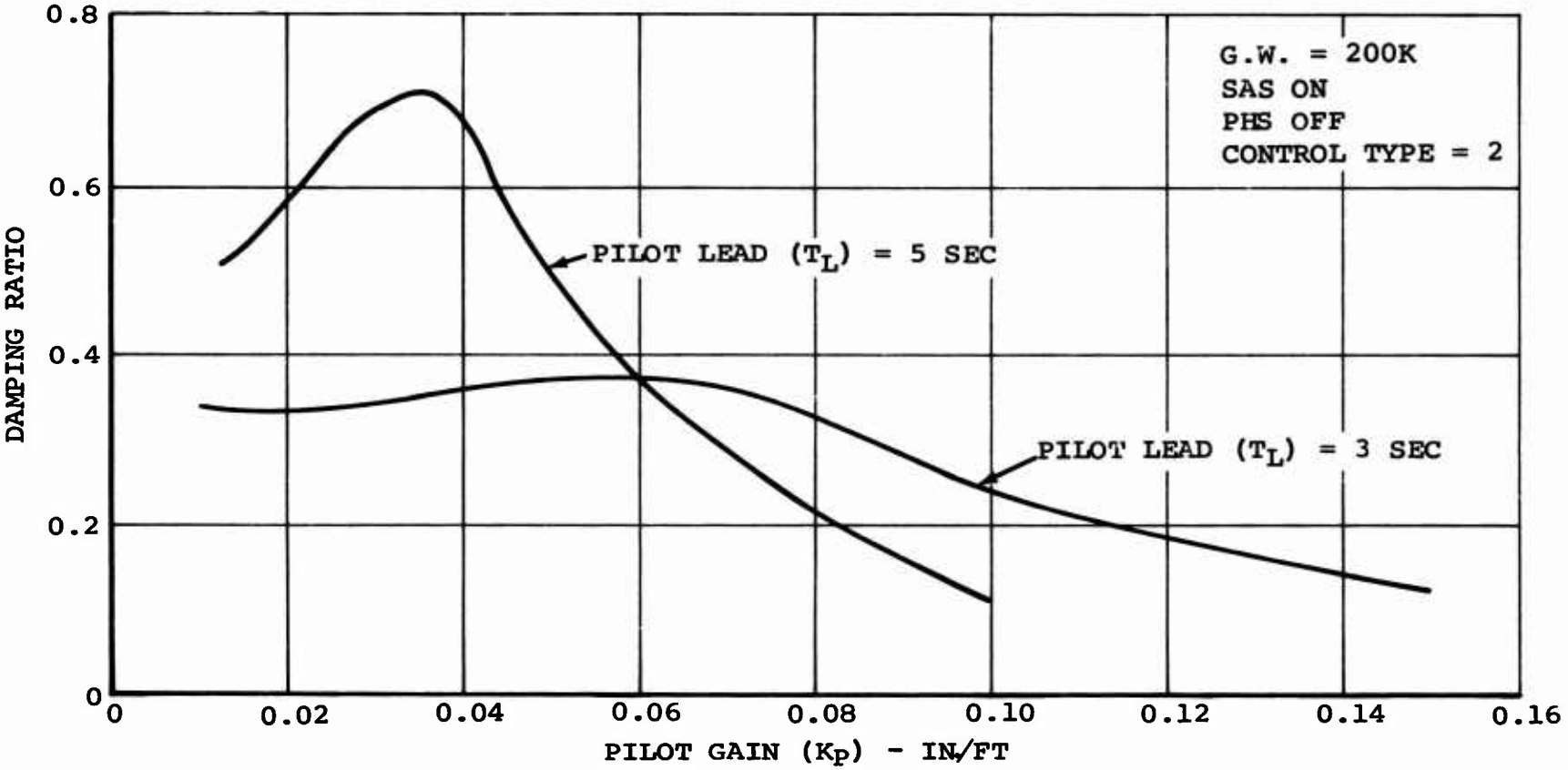

Figure 63. Longitudinal System - Damping of Longitudinal Position Mode.

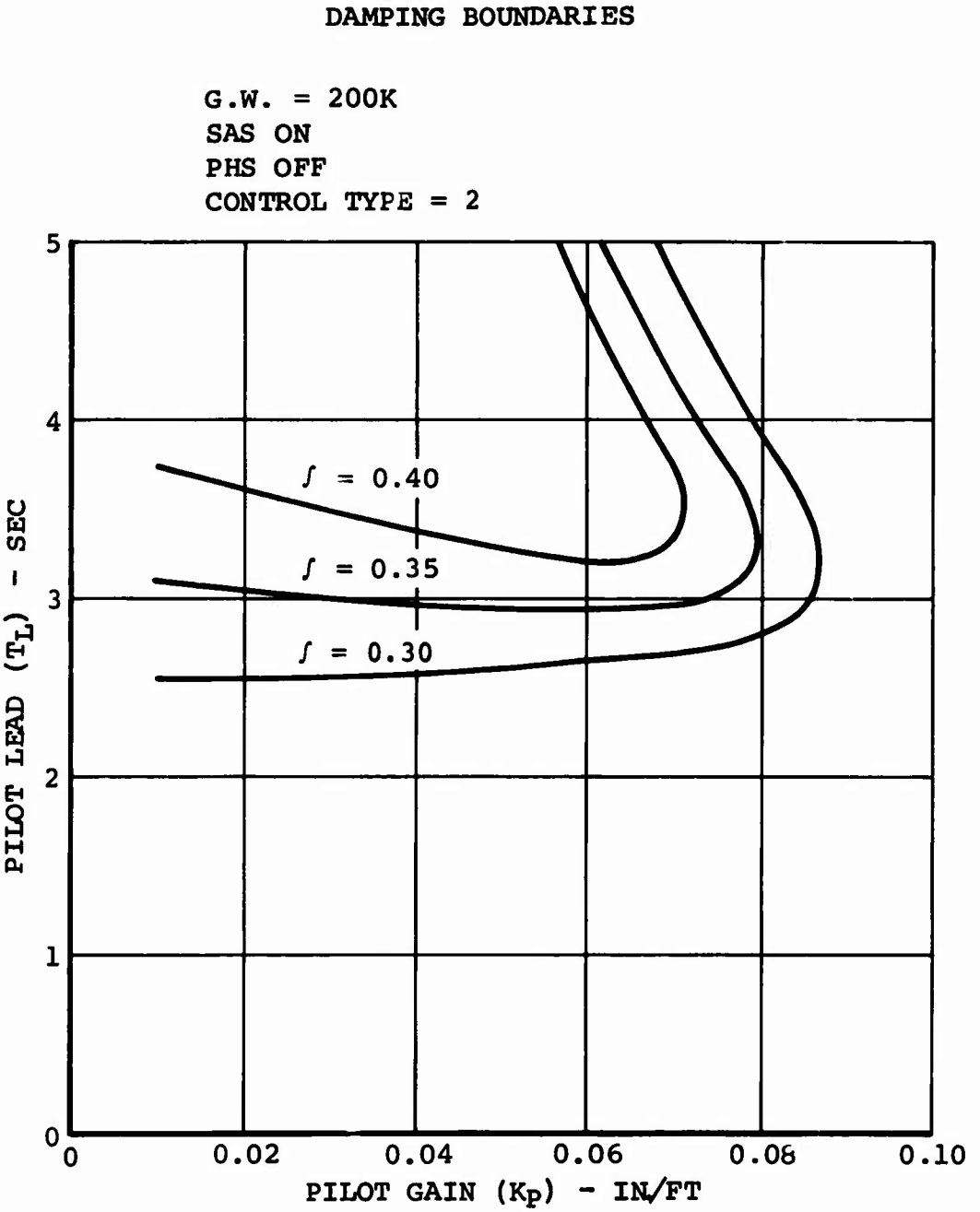

Figure 64. Longitudinal System - Damping Boundaries.

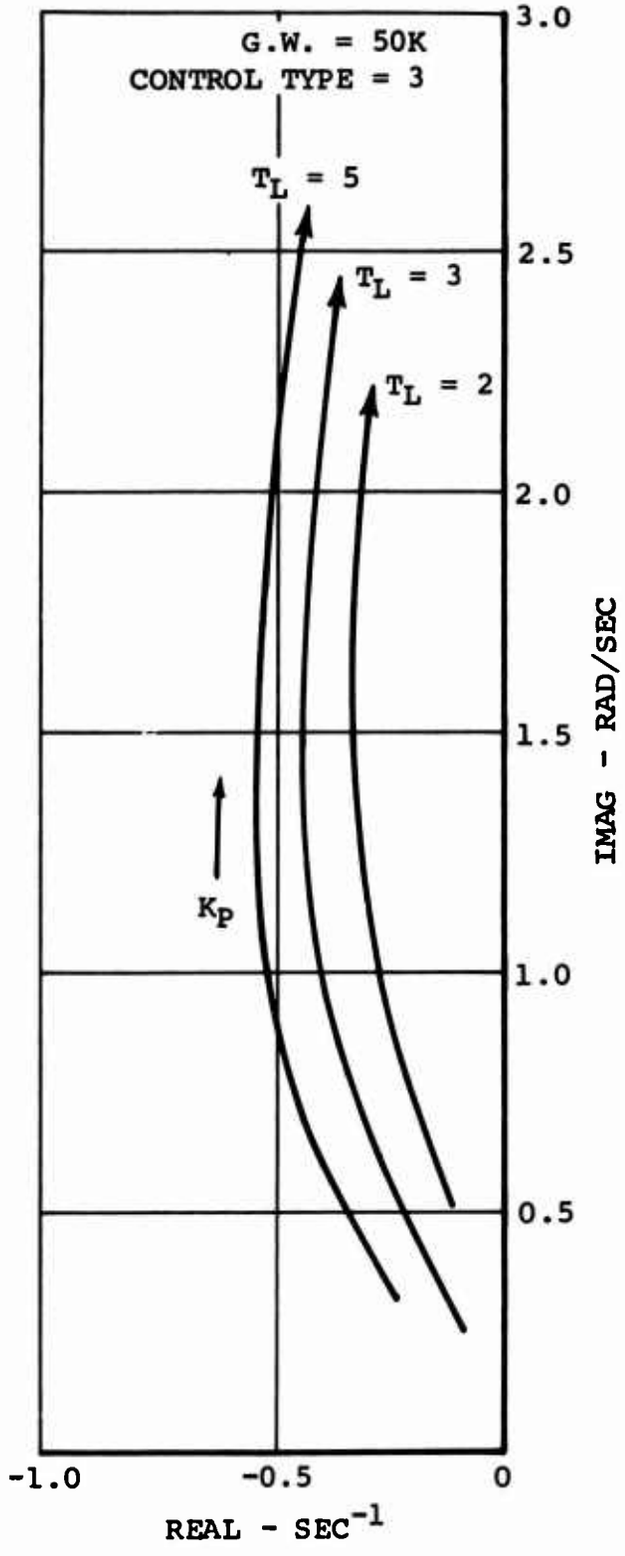

Figure 65. Longitudinal Root Locus.

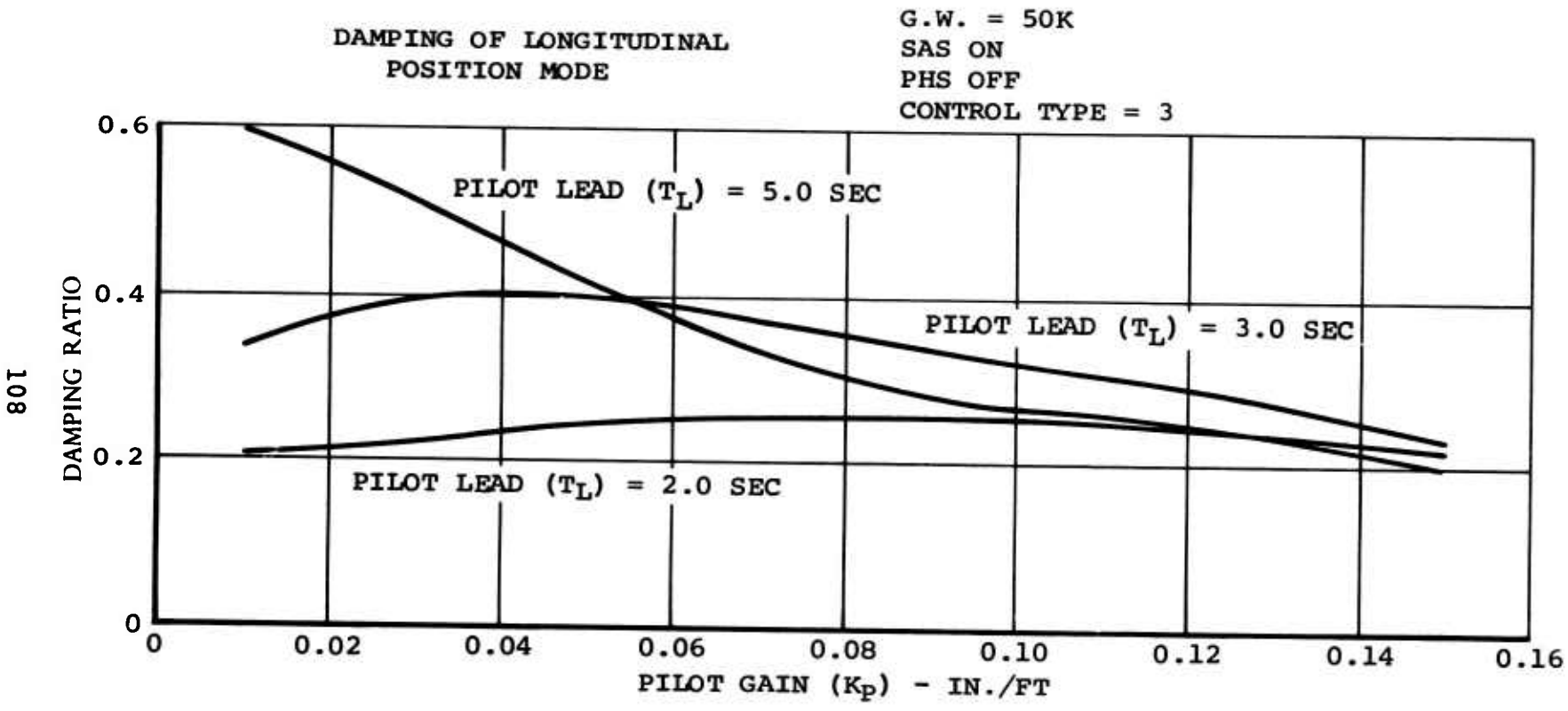

Figure 66. Longitudinal System - Damping of Longitudinal Position Mode.

these curves is again similar to the other control types. Figure 67 shows the stability boundaries for varying pilot gain and lead. The minimum acceptable pilot lead is close to that for DCP only, and the maximum allowable pilot gain is somewhat less. This is a little surprising in that one might expect the results to lie somewhere between that for LCP only and DCP only. Obviously, the DCP, even though lagged, still dictates a stronger pilot lead. However, as will be seen later, the performance in terms of rms position error in turbulence is more like LCP only, indicating that the shorter rise times (for constant overshoot) associated with LCP control allow for a tighter hold capability.

Figure 68 is the root locus for the significant eigenvalues of the 200,000-pound configuration with control type 3. This plot shows the strong effect that pilot closure of the position loop has on the pitch cubic. For the low pilot gains, the locus starts out looking like that for the LCP only control. However, as pilot gain increases, the mode which started out as a pitch mode is driven unstable and not the position mode. Thus, as the pilot tries to minimize the position, he becomes aware of the pitch response, until eventually his concern is in controlling both. At this time, our single-loop approach becomes dubious. Since in the high gain area, the second-order response that started as the combined position-velocity mode is no longer a good representation of the position response, the damping of this second-order response will not determine the stability limits. It was felt that phase margin versus pilot gain and lead offered a better feel for the stability bounds. Figure 69 shows the effect of pilot gain and lead on position error phase margin. The attenuation of the phase margin with gain is greater for the higher leads. Figure 70 shows the relationship between pilot gain and phase margin for constant phase margin. A lower limit of 40 degrees will be used for the stability boundary for this configuration and control type 1. The probable reason that the minimum lead is less stringent for the 200,000-pound configuration than for the 50,000-pound configuration is that DCP control sensitivity decreases at 200,000 pounds, while LCP sensitivity remains relatively constant.

Lateral Position

Each of the three lateral control types mentioned previously will be studied using the 50,000- and 200,000-pound configurations. There are six eigenvalues of interest when the pilot closes the lateral position loop. These are the eigenvalues representing the lateral motion of the helicopter. The three eigenvalues representing the directional motion are affected by this pilot closure.

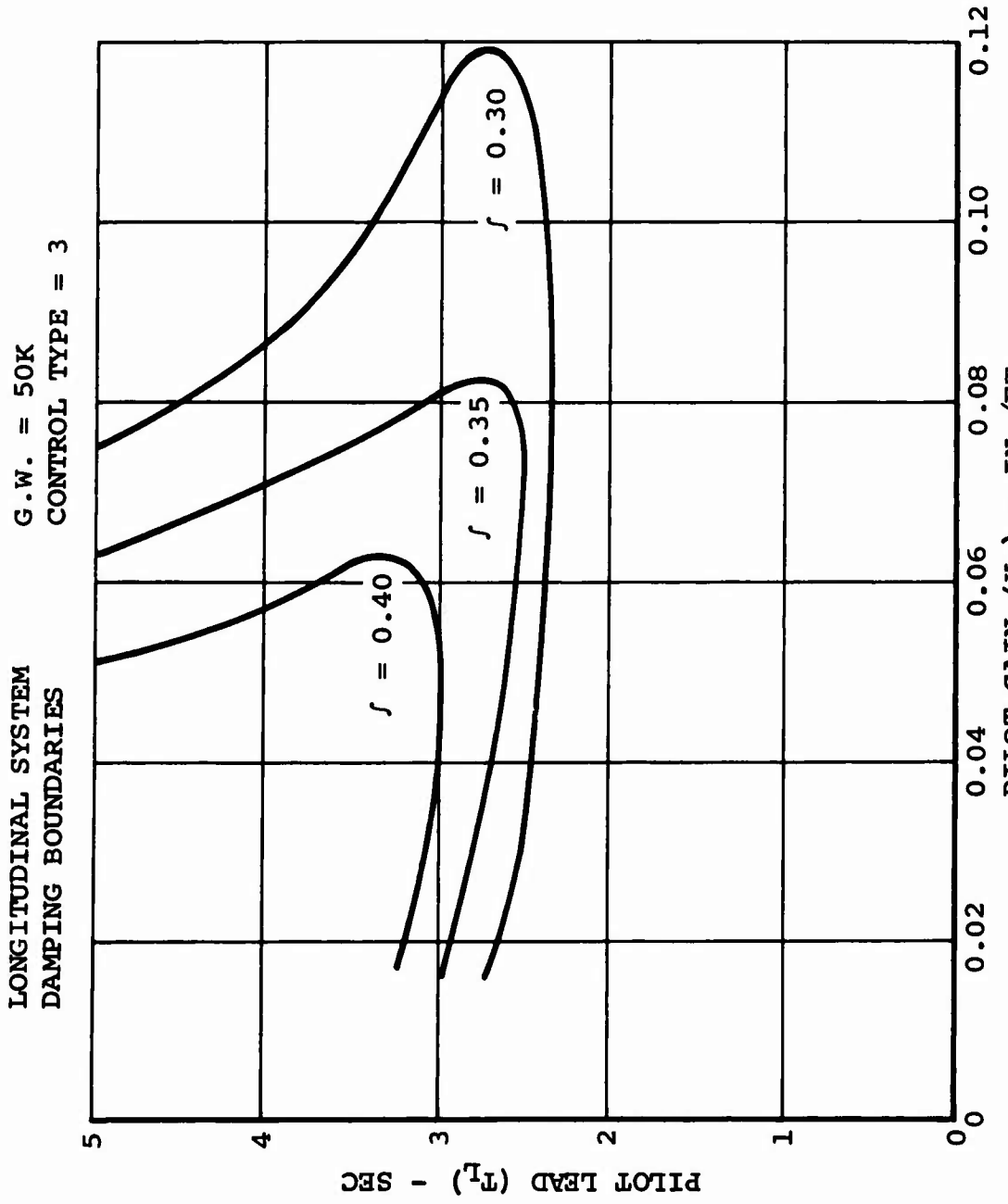

Figure 67. Longitudinal System - Damping Boundaries.

G. W. = 200K
CONTROL TYPE = 3

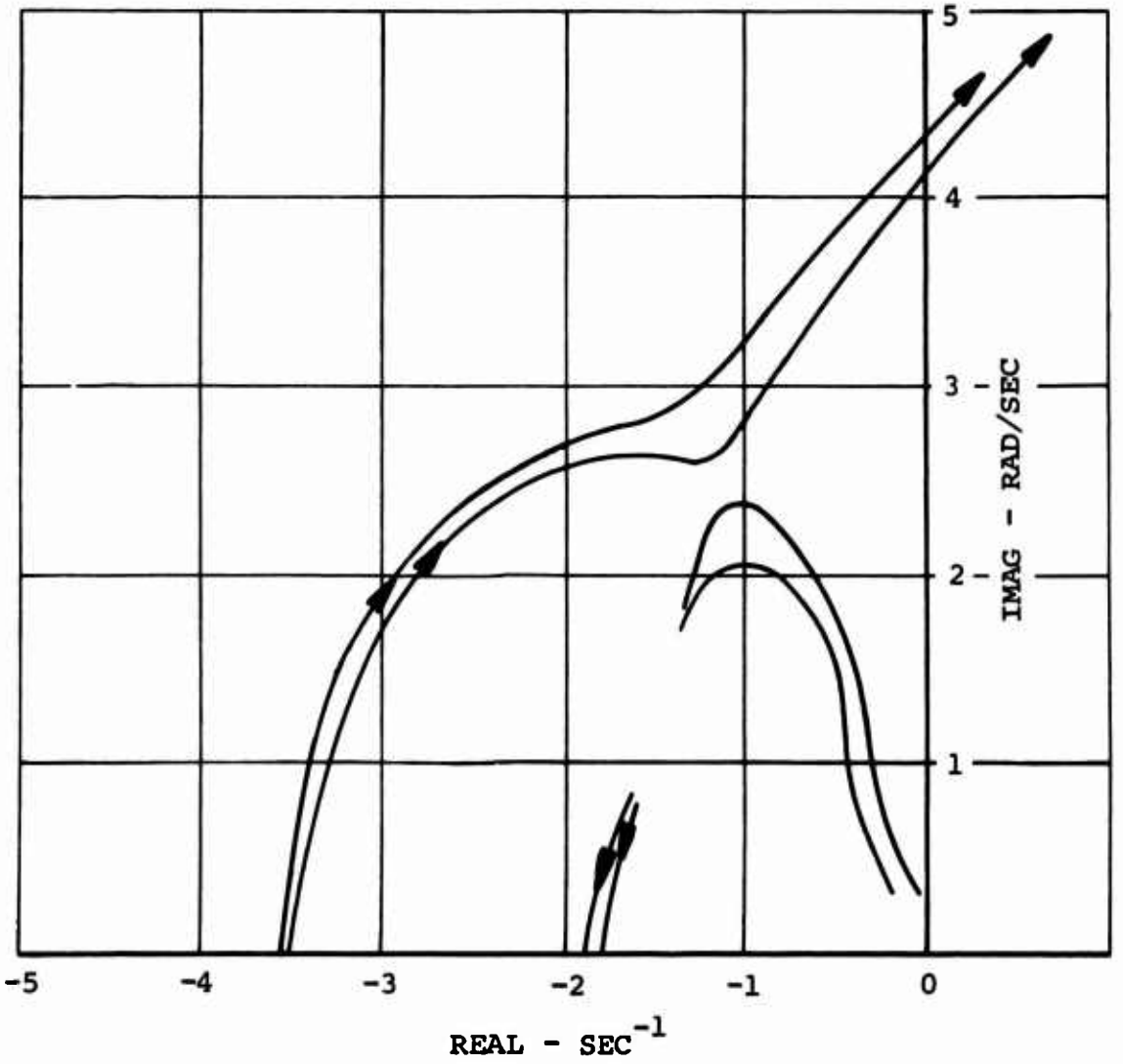

Figure 68. Longitudinal Root Locus.

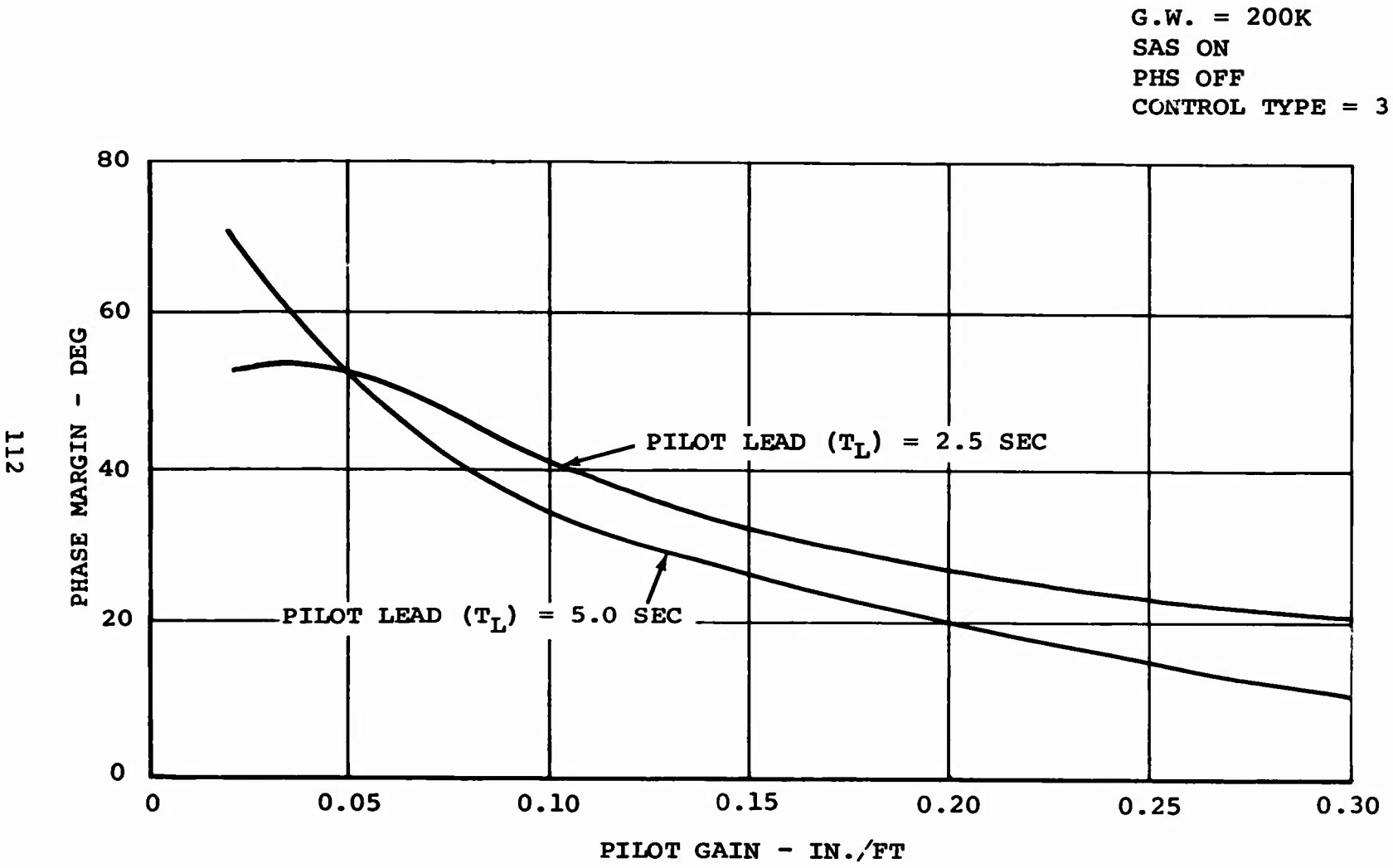

Figure 69. Longitudinal System - Open Loop Phase Margin of Output Position to Position Error.

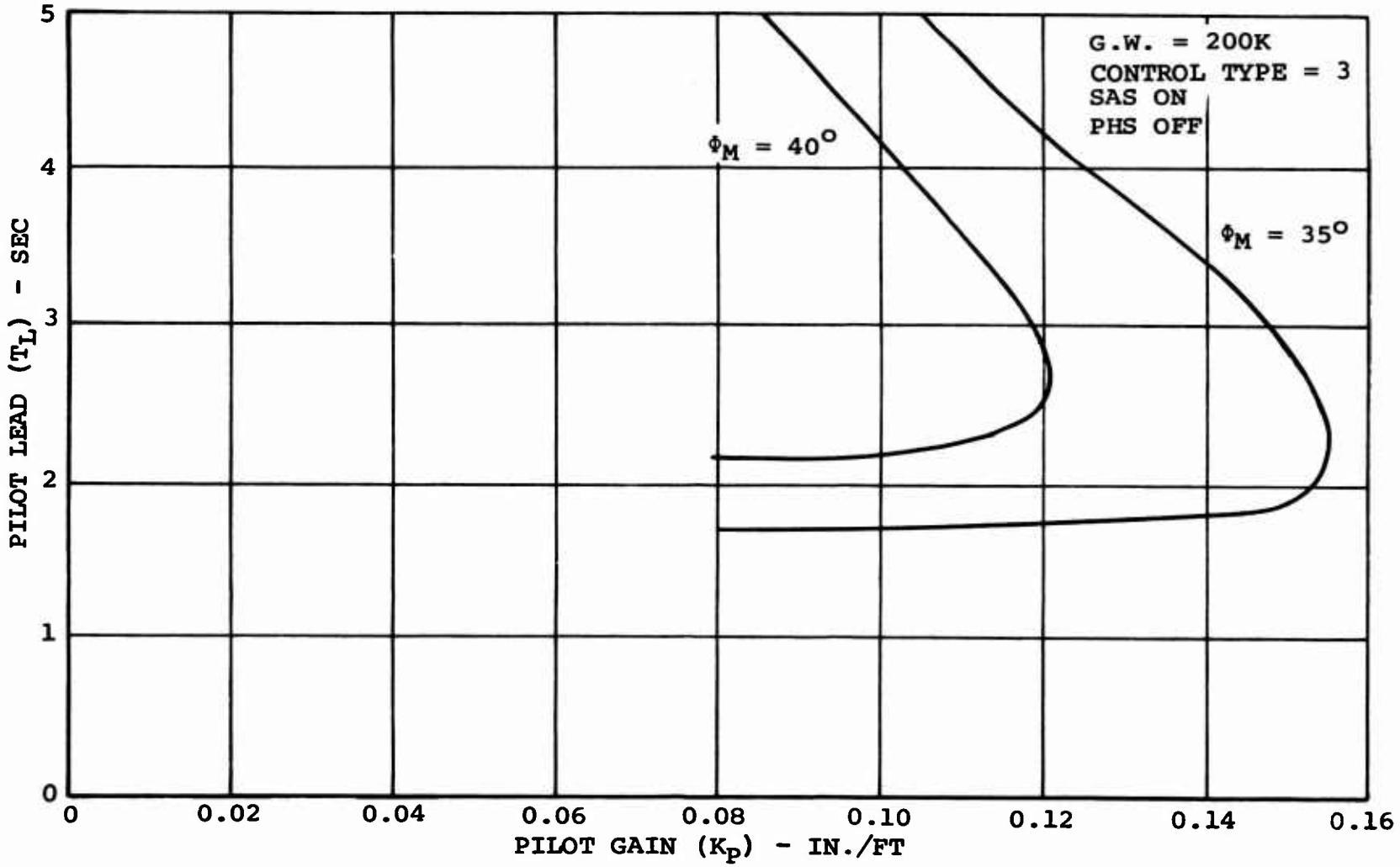

Figure 70. Longitudinal System - Phase Margin Stability Boundaries.

Lateral Control Type 0 - Lateral Cyclic Control With No Pickoffs and No Lateral Velocity Feedback Through SAS

This control type is simply the pilot controlling lateral position with lateral stick motion, with no stick pickoffs and no lateral velocity damping through the stability augmentation system. Any additional lateral velocity damping over and above the helicopter's inherent damping must be provided by the pilot through his lead compensation. When comparing this type of control with type 1 below, the benefit of velocity feedback in the SAS for relief of pilot work load is obvious.

For the 50,000-pound configuration, the eigenvalues of interest are the lateral complex pair near the origin, as shown in Figure 28 for $G_y = 0$, and the eigenvalue which starts out at the origin with the position loop open. Figure 71 shows the result of position loop closure on the complex pair of eigenvalues. Again, as with other control types, the greater the pilot lead compensation, the higher the crossover frequency. The eigenvalue which originates at the origin is driven out the negative real axis until it approaches the value of the roll attitude-lateral velocity washout. Figure 72 represents the variation of damping ratio of the complex pair of eigenvalues as a function of pilot gain and lead. The curves show the peakiness which results from increasing pilot lead. The result is that higher pilot leads make possible higher damping ratios but over smaller ranges of pilot gain. Therefore, as before, the pilot will seek a lead value that will satisfy his minimum stability level and no more. Figure 73 shows the damping ratio contours for this configuration. Due to the slower stability changes associated with the flatter portion and the smaller work load, the pilot would tend to operate on this portion of the curves. A minimum pilot lead of 1.5 seconds is necessary for 35% damping.

For the 200,000-pound configuration, the trends are the same, as shown in Figures 74, 75, and 76. However, the damping levels attainable at the same pilot leads are slightly less for the 200,000-pound configuration. Thus, the minimum pilot lead for minimum stability would be slightly greater with the 200,000-pound configuration, as shown in Figure 76.

Lateral Control Type 1 - Lateral Cyclic Control With No Pickoffs

This control type is the same as just discussed except that the stability augmentation system is providing lateral damping through lateral velocity feedback. The advantage of this automatic damping is immediately obvious. As shown in Figures 77, 78, and 79 for the 50,000-pound configuration, the added damping provided by the control system allows the pilot to

G.W. = 50K
CONTROL TYPE = 0

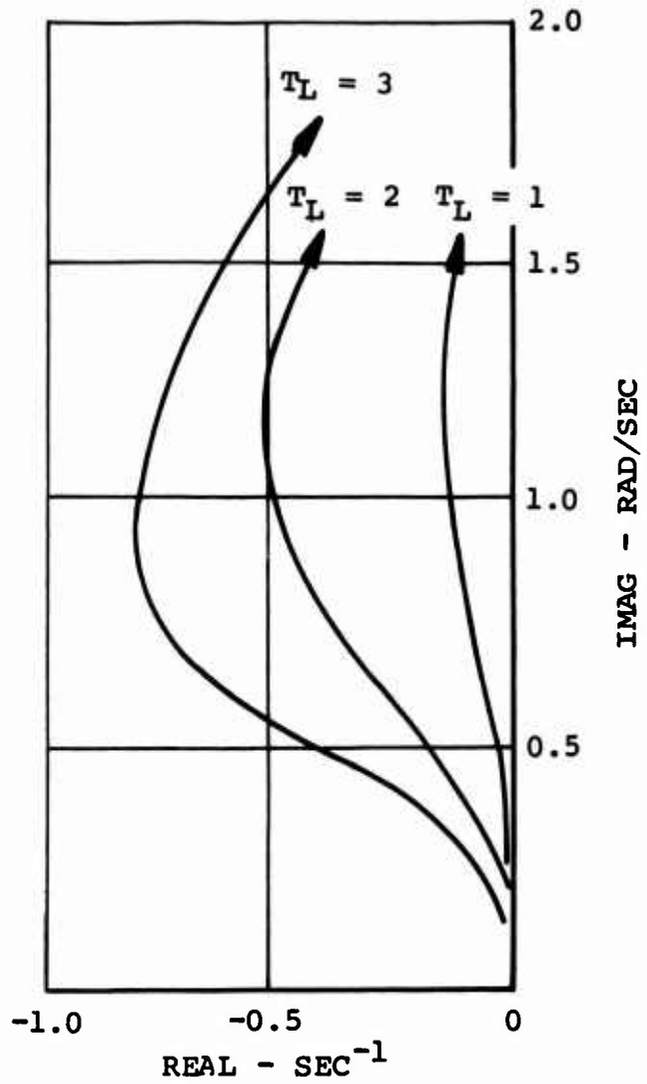

Figure 71. Lateral Root Locus.

G.W. = 50K
CONTROL TYPE = 0

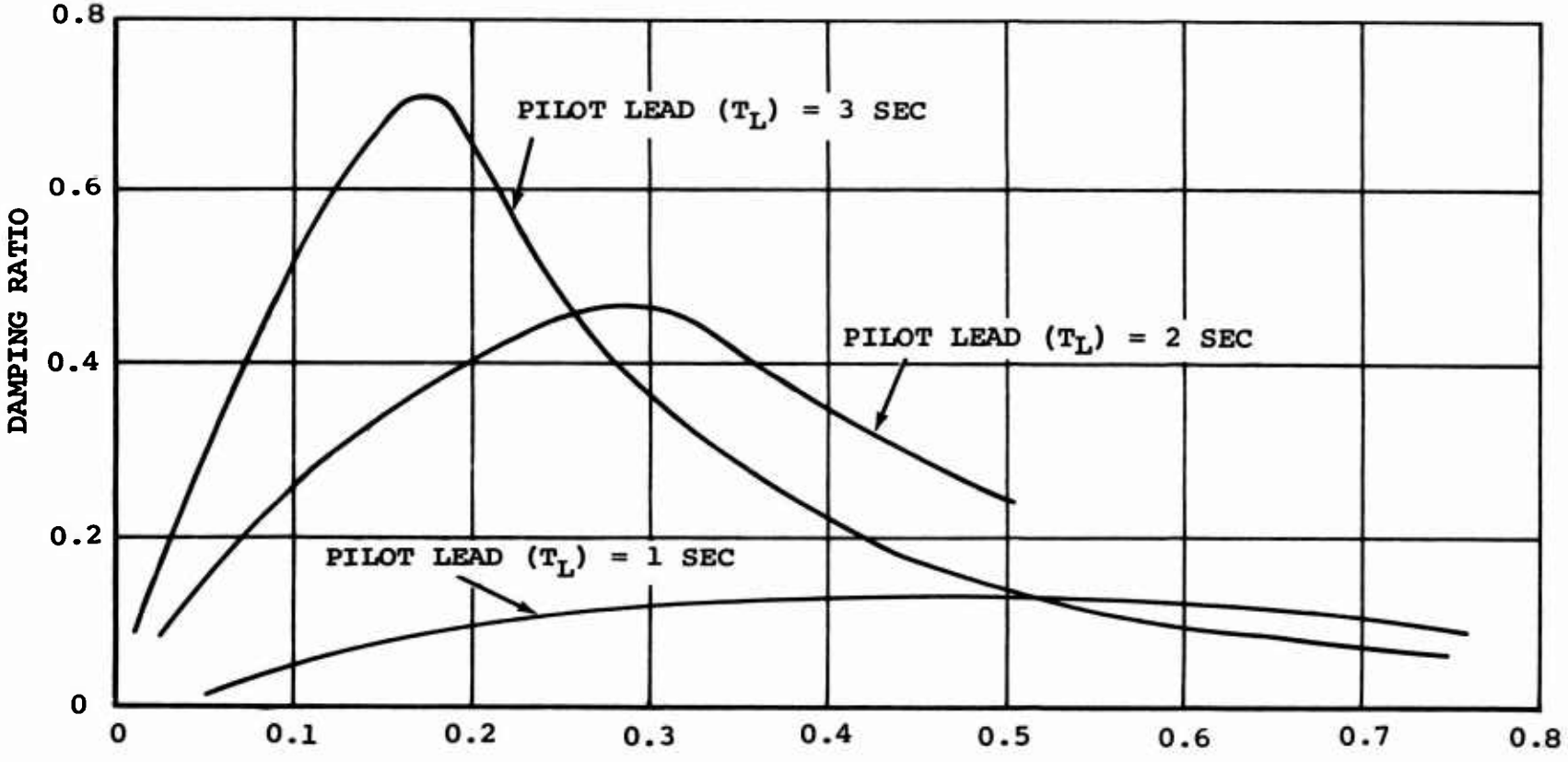

Figure 72. Lateral System.

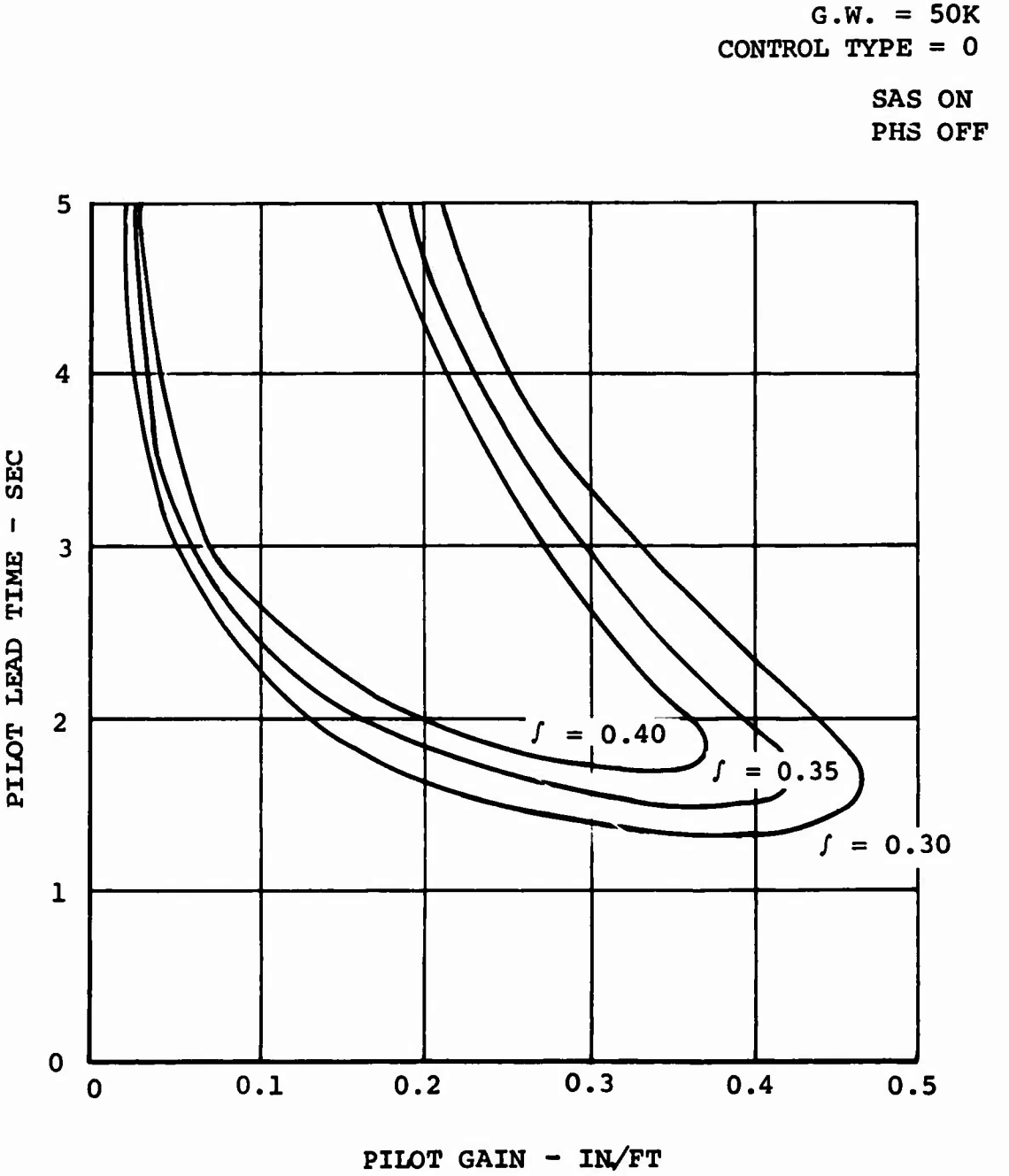

Figure 73. Lateral System - Damping Ratio Boundaries.

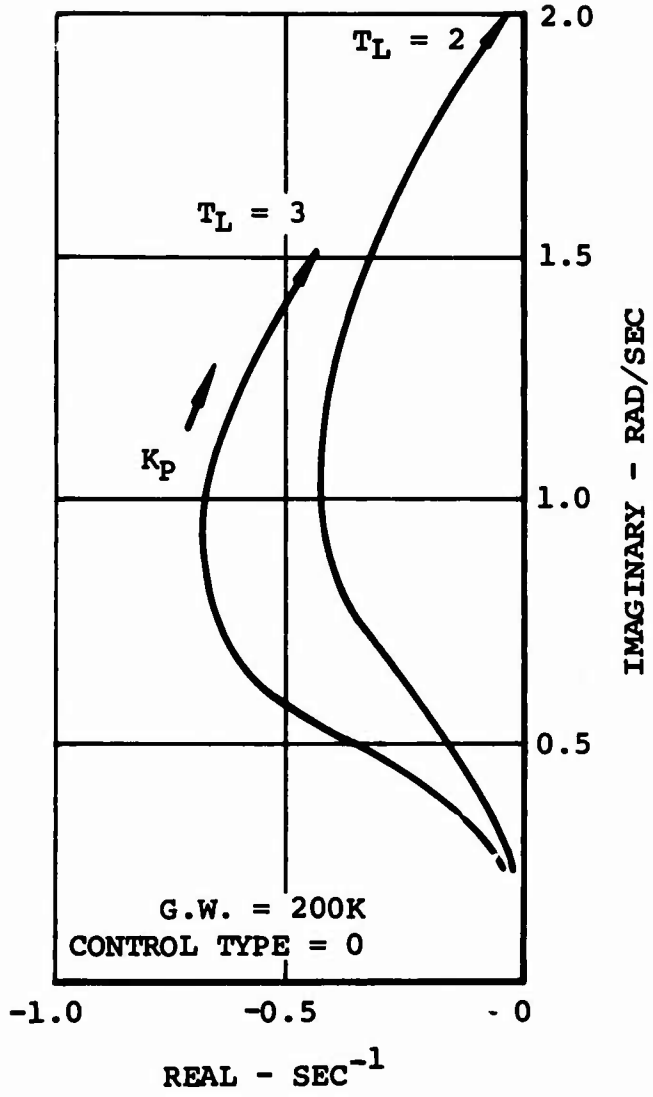

Figure 74. Lateral Root Locus.

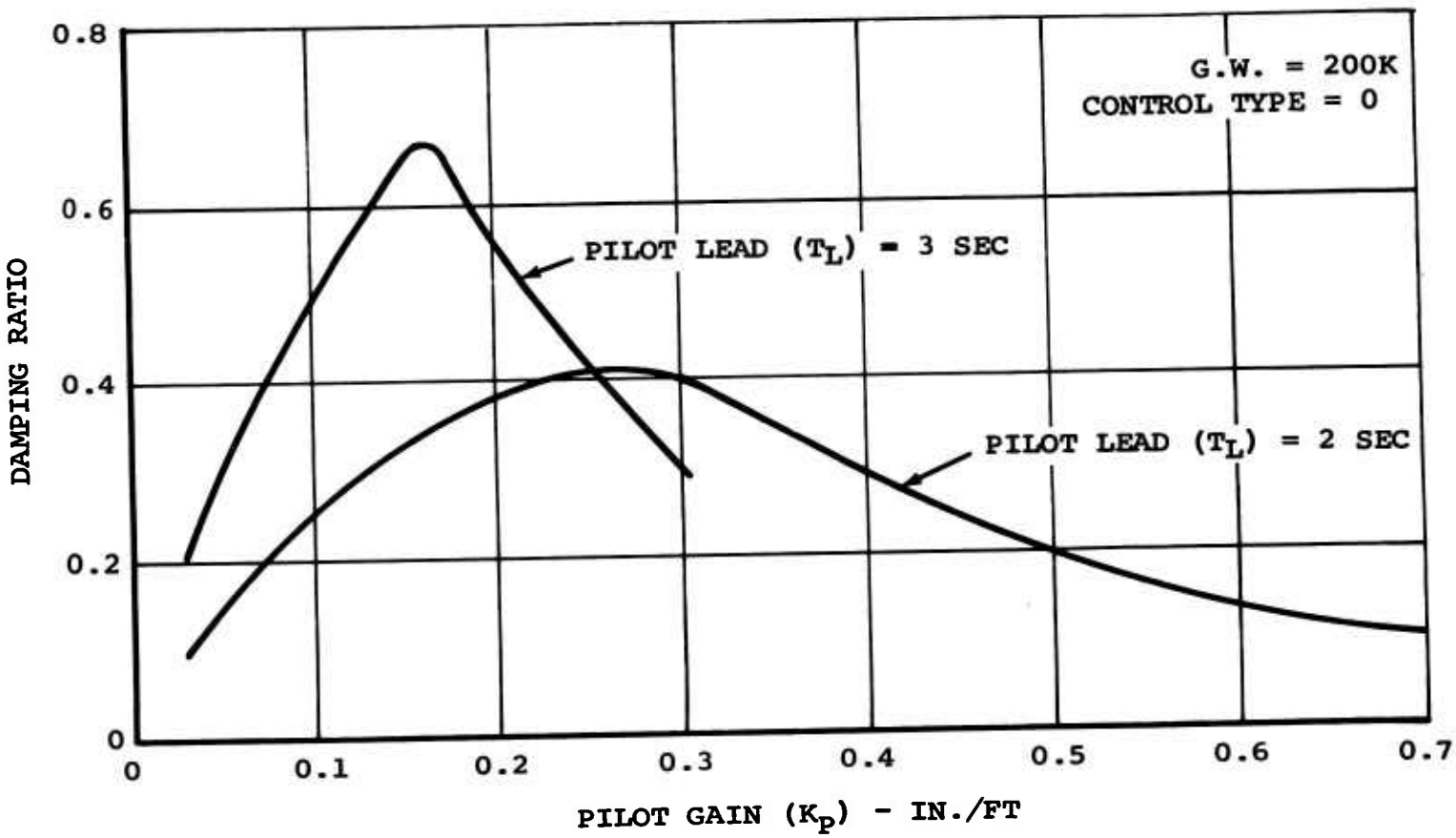

Figure 75. Lateral System - Lateral Position Modal Damping.

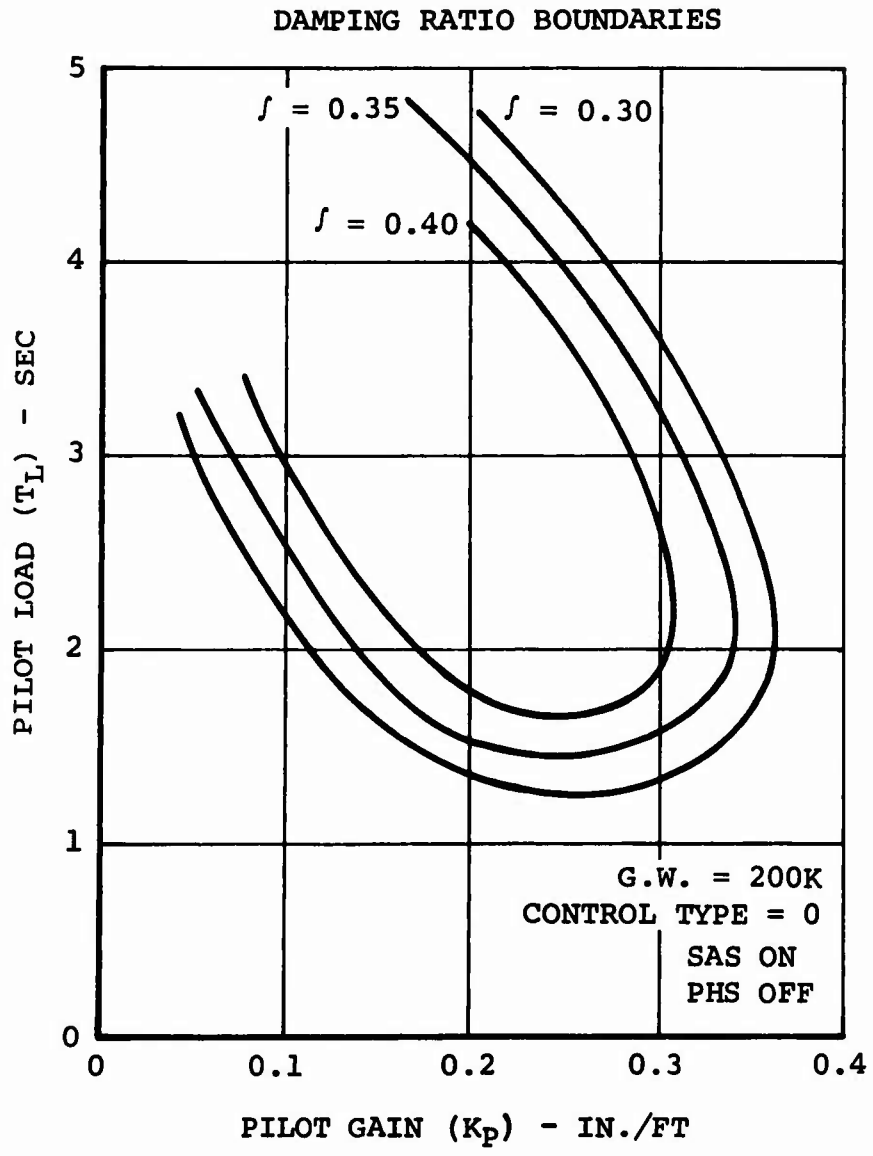

Figure 76. Lateral System - Damping Ratio Boundaries.

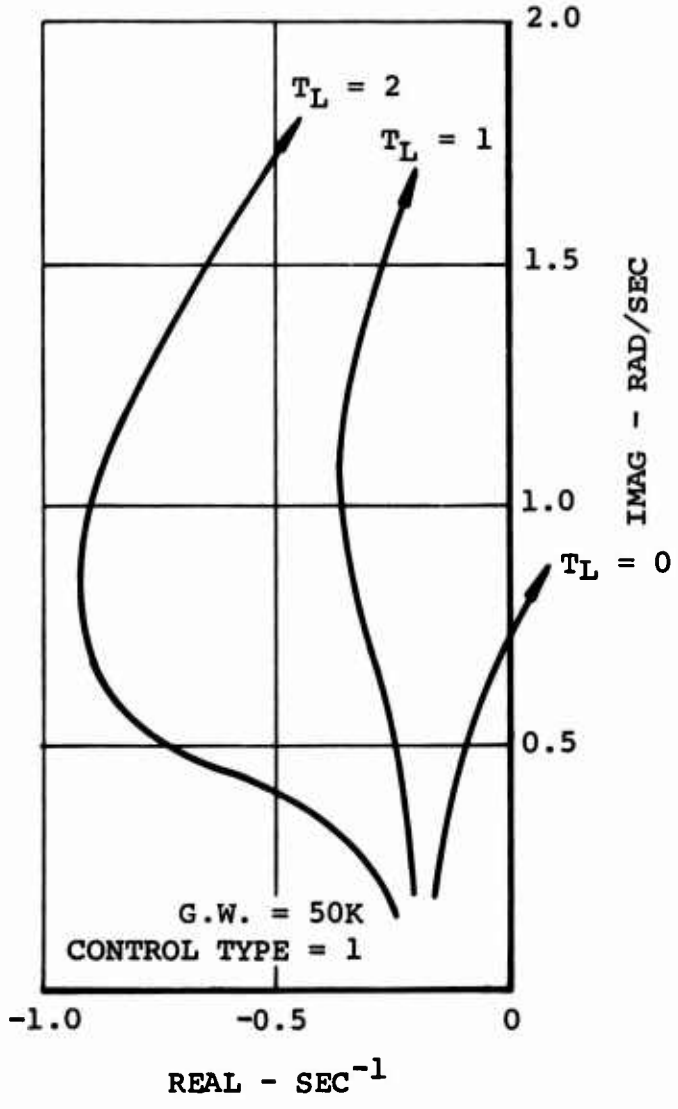

Figure 77. Lateral Root Locus.

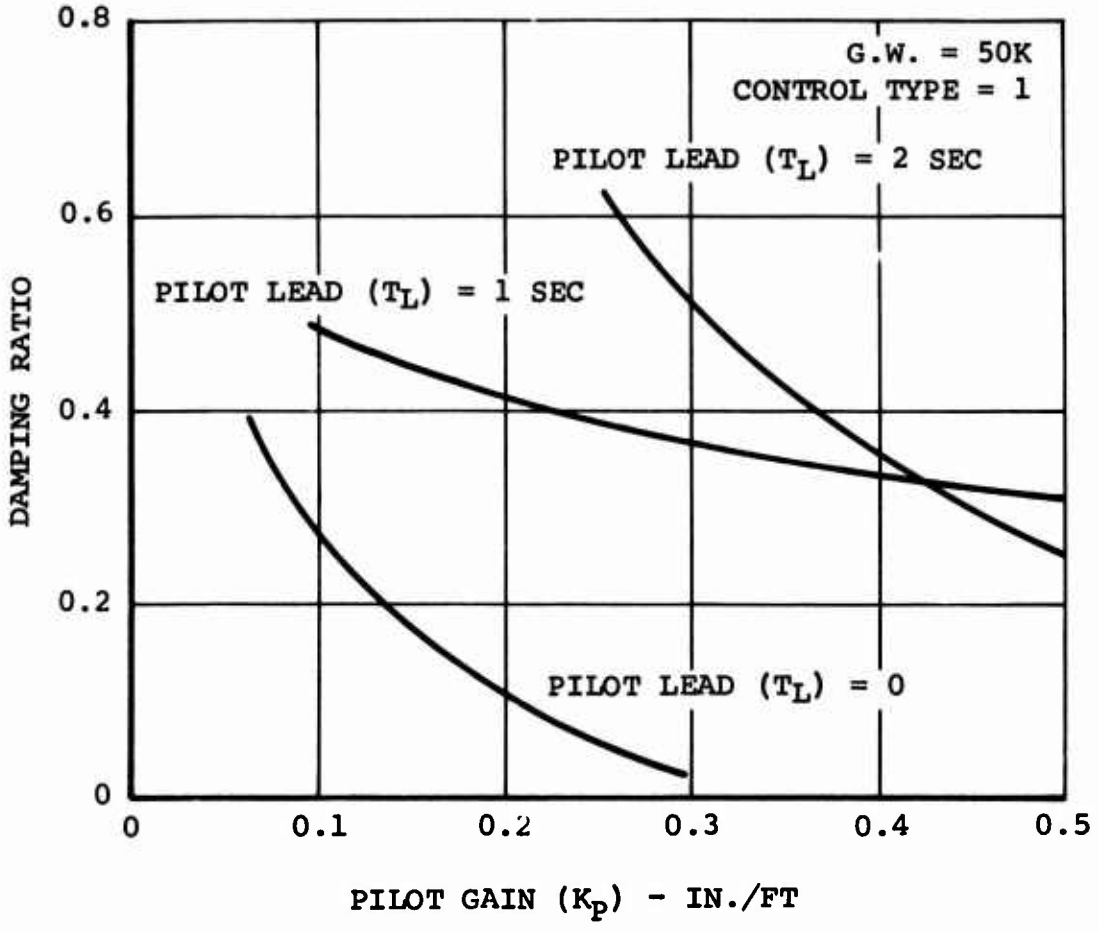

Figure 78. Lateral System.

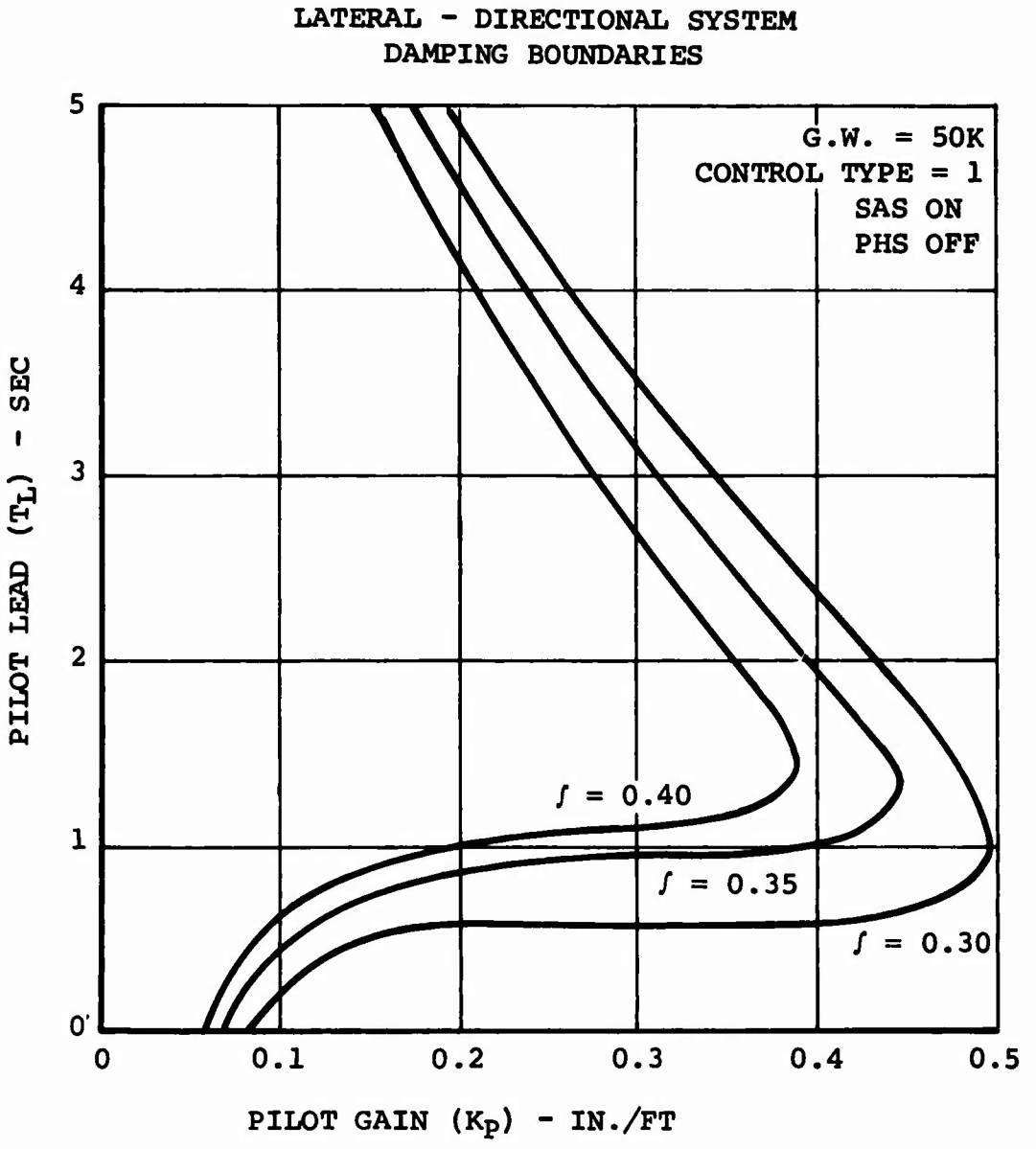

Figure 79. Lateral-Directional System Damping Boundaries.

close the position loop with lower lead compensation. And, indeed, he can close the loop with no lead compensation at all for low pilot gains. Figure 79 shows the variation of the stability boundaries with pilot gain and lead, and depending on task requirements, a minimum pilot lead of zero is possible.

The results for the 200,000-pound configuration are similar to those for the 50,000-pound configuration except that the maximum pilot gain possible for a given pilot lead for a desired minimum damping ratio is less for the 200,000-pound configuration. Figures 80, 81, and 82 present the results for the 200,000-pound configuration with this control type.

Lateral Control Type 2 - Lateral Cyclic Control With Roll Quickening Through Stick Pickoff

This control type is the same as just discussed except that roll quickening has been added through a lateral stick pickoff through a lag and washout. The results are not favorable. As shown in Figures 83, 84, and 85 for the 50,000-pound configuration, much lower maximum pilot gains are possible at a given pilot lead for a desired stability level. Figure 85 shows the further disadvantage of rapid stability changes with pilot gain changes. The 200,000-pound configuration results, Figures 86, 87, and 88, are similar with even lower maximum pilot gains possible.

Piloted Hover Hold Performance in Turbulence

In an effort to restrict the acceptable ranges of pilot parameters, the previous section showed the effect on stability of these parameters. This section will attempt to further pinpoint the pilot's selection of parameters by relating them to the precision hover task in turbulence.

Longitudinal Hold Capability

Using the three longitudinal control types discussed and the 50,000- and 200,000-pound configurations, longitudinal position error due to random U-gusts will be investigated.

Figures 89 and 90 are the results for the 50,000-pound configuration with control type 1. Figure 89 shows the rms position error versus pilot gain for constant stability levels, where the pilot lead is adjusted at each gain to provide desired stability. Figure 90 shows the rms position error versus pilot lead for constant stability levels, where the pilot gain is adjusted at each lead to provide desired stability. For a damping ratio of 0.35, an optimum pilot lead of about 2 seconds and an optimum pilot gain of about 0.12 in./ft will result in an rms position error of about 0.35 feet. If this error is assumed to be sinusoidal for the time being, then an rms of

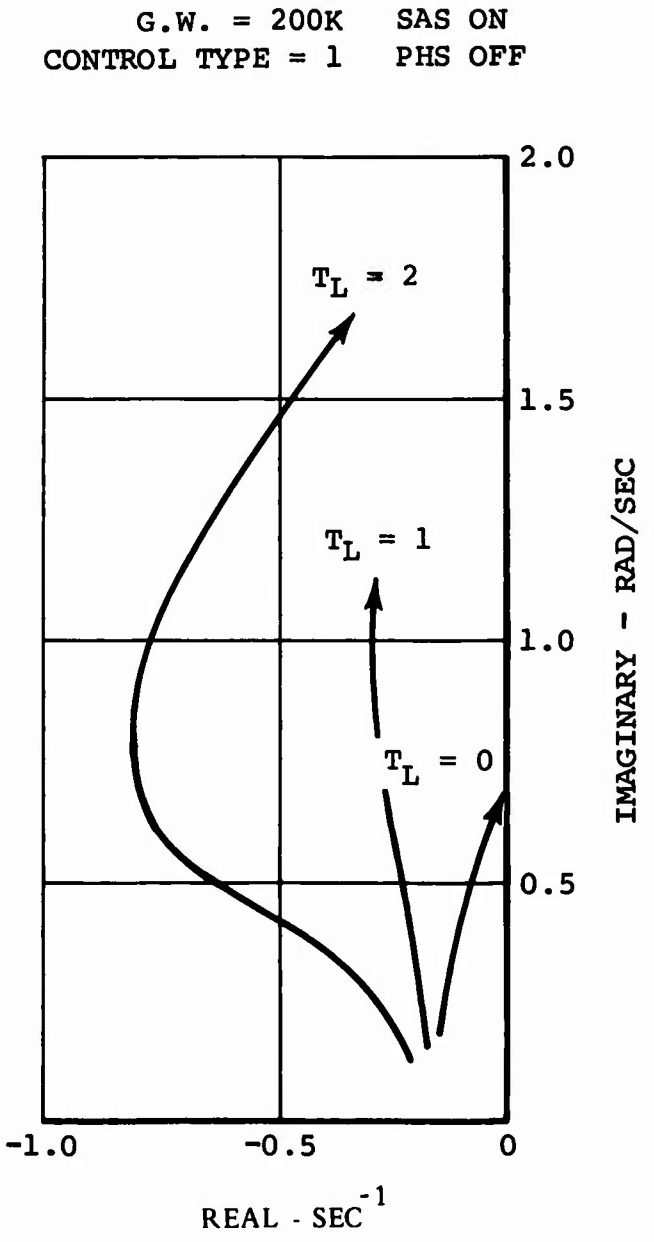

Figure 80. Lateral-Directional System.

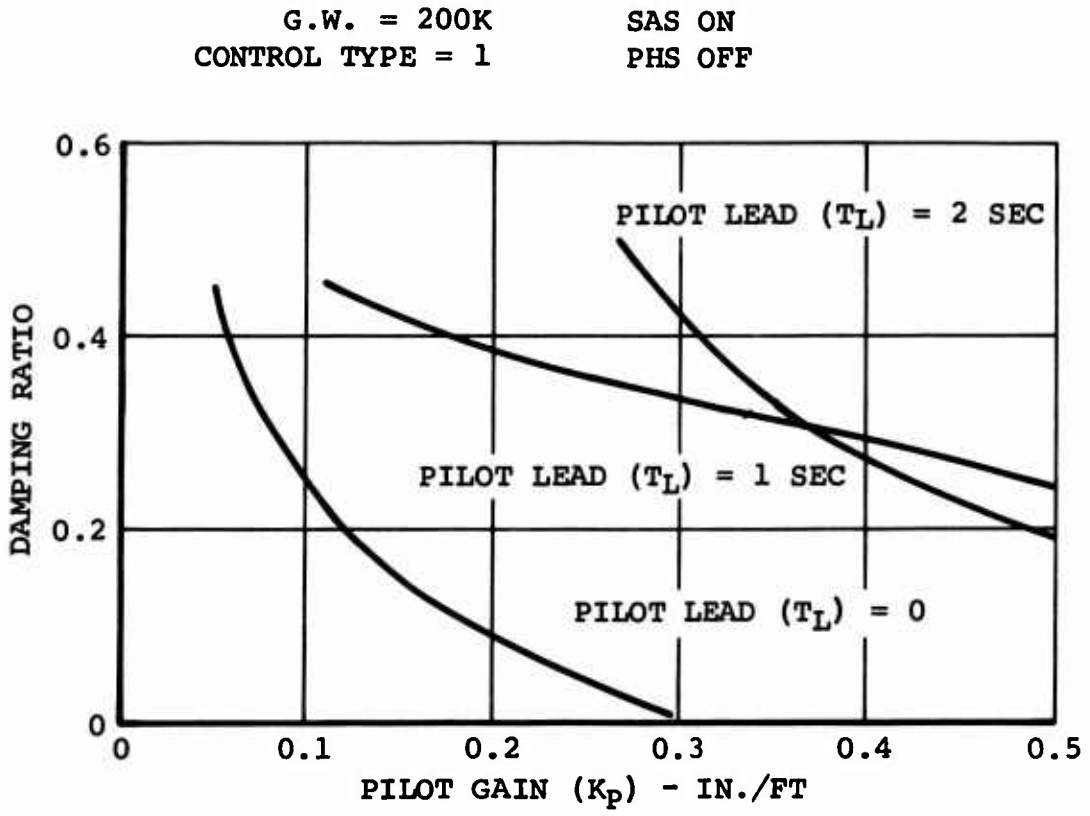

Figure 81. Lateral-Directional System - Lateral Position Modal Damping.

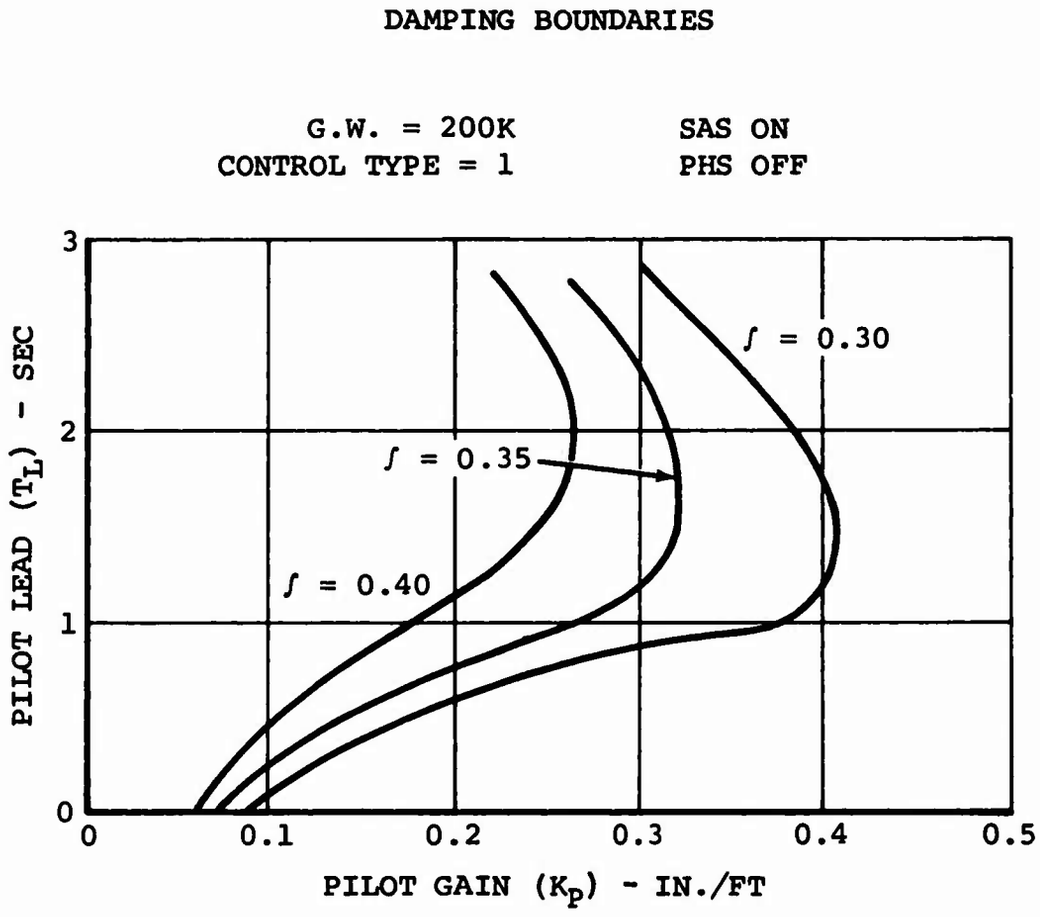

Figure 82. Lateral-Directional System Damping Boundaries.

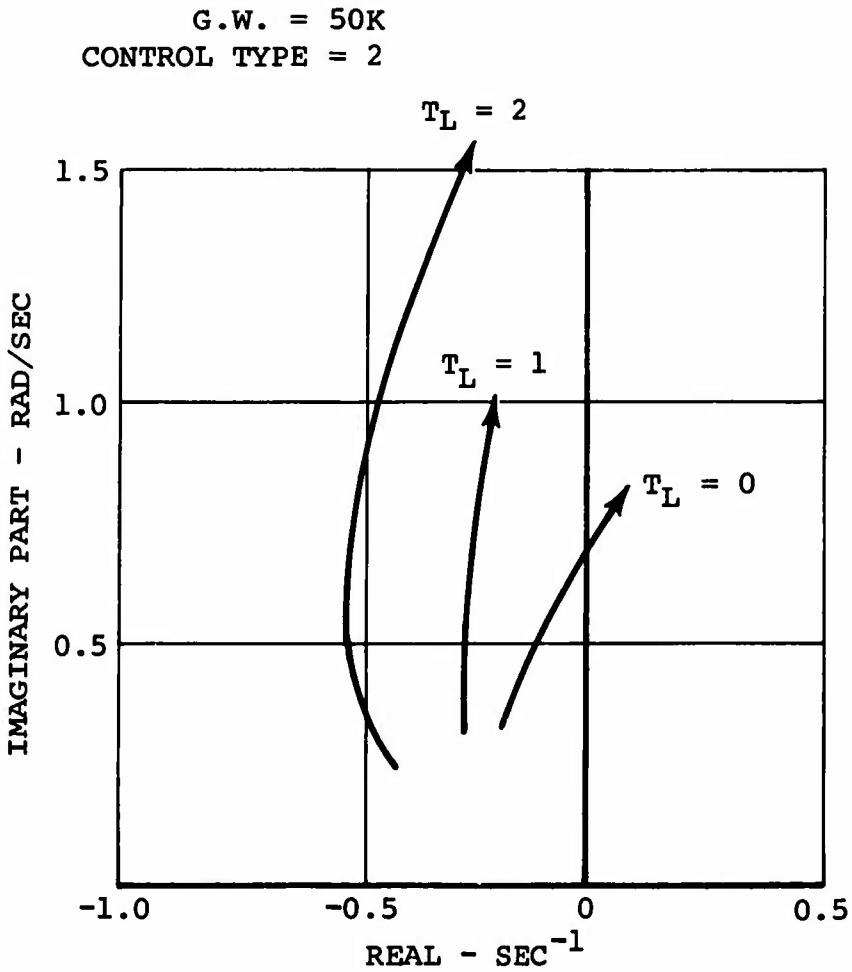

Figure 83. Lateral Root Locus.

G.W. = 50K
CONTROL TYPE = 2

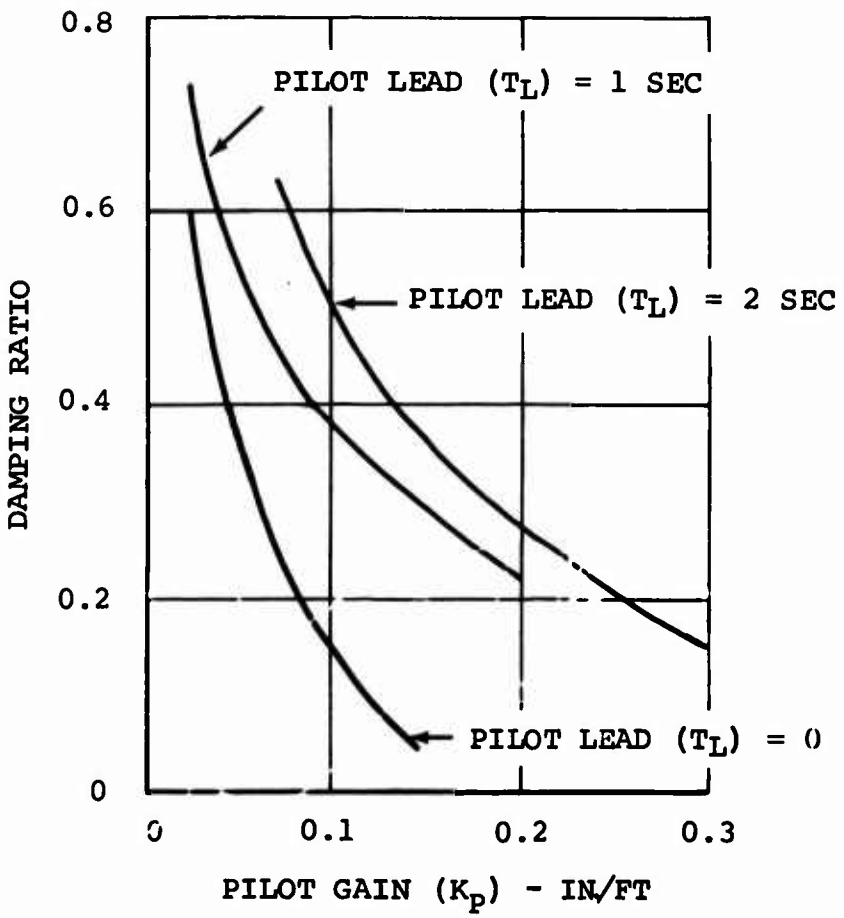

Figure 84. Lateral System.

G.W. = 50K
CONTROL TYPE = 2

SAS ON
PHS OFF

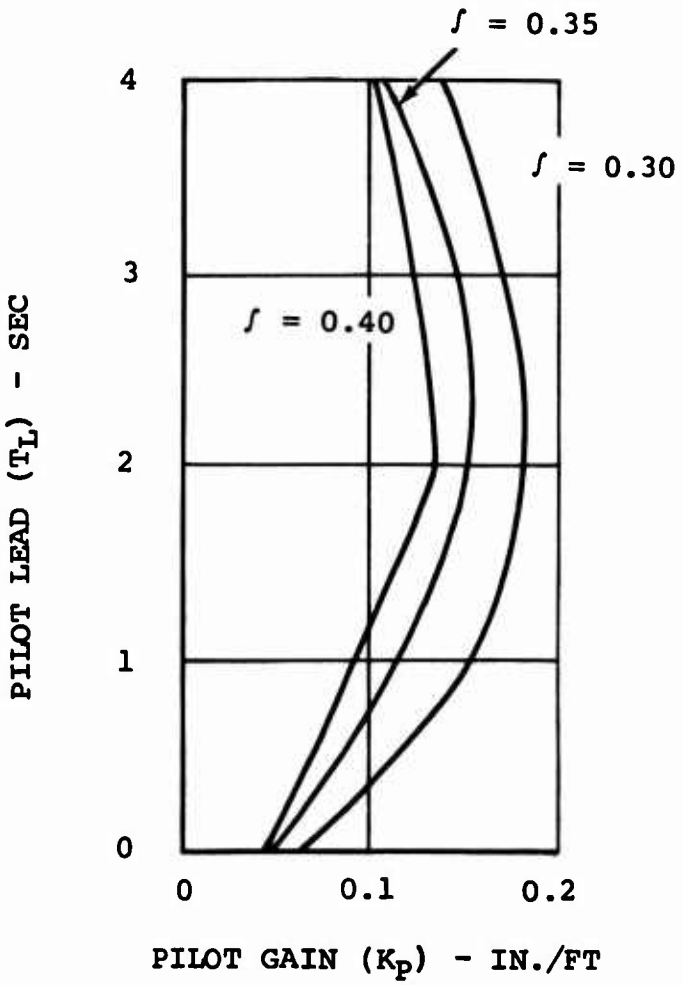

Figure 85. Lateral-Directional System Damping Boundaries.

G.W. = 200K
CONTROL TYPE = 2

SAS ON
PHS OFF

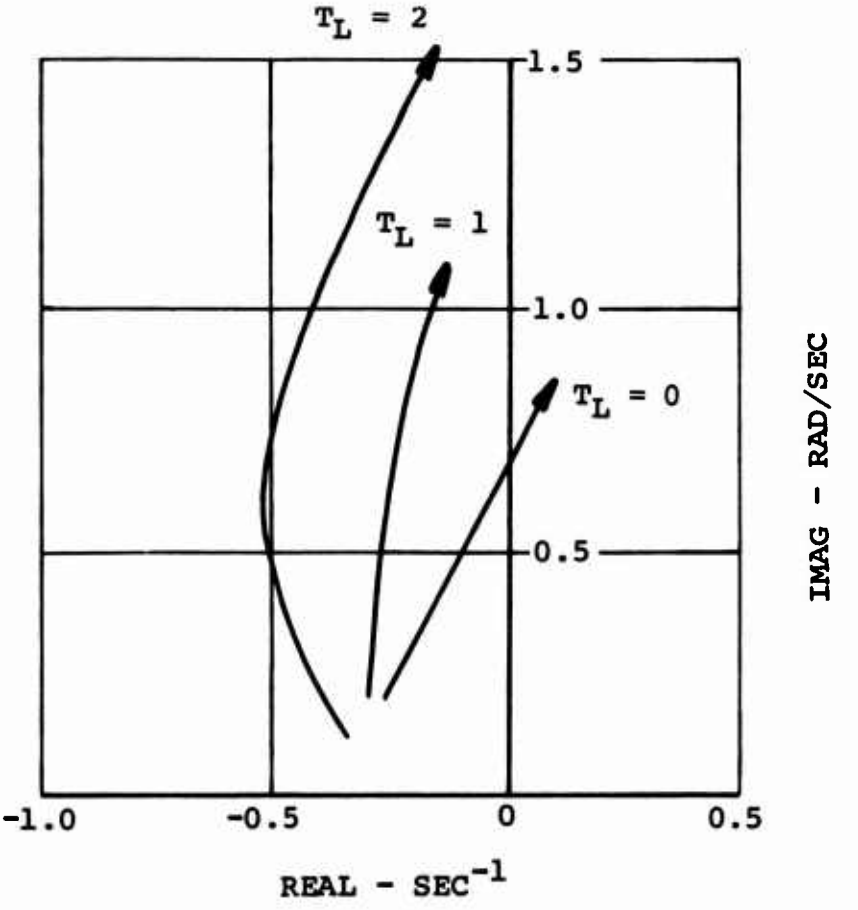

Figure 86. Lateral-Directional System.

G.W. = 200K
CONTROL TYPE = 2

SAS ON
PHS OFF

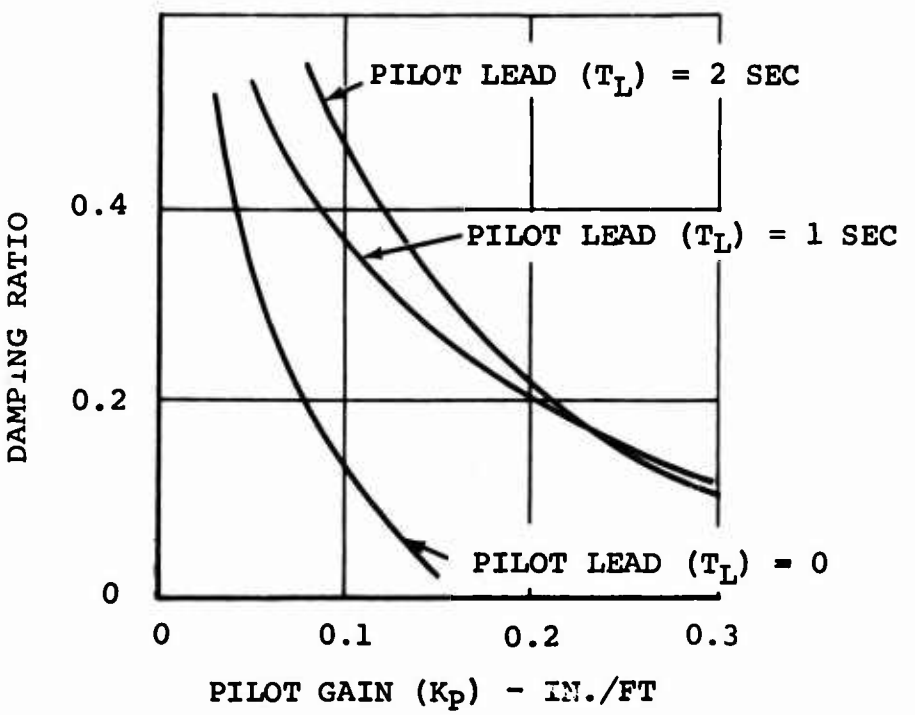

Figure 87. Lateral-Directional System.

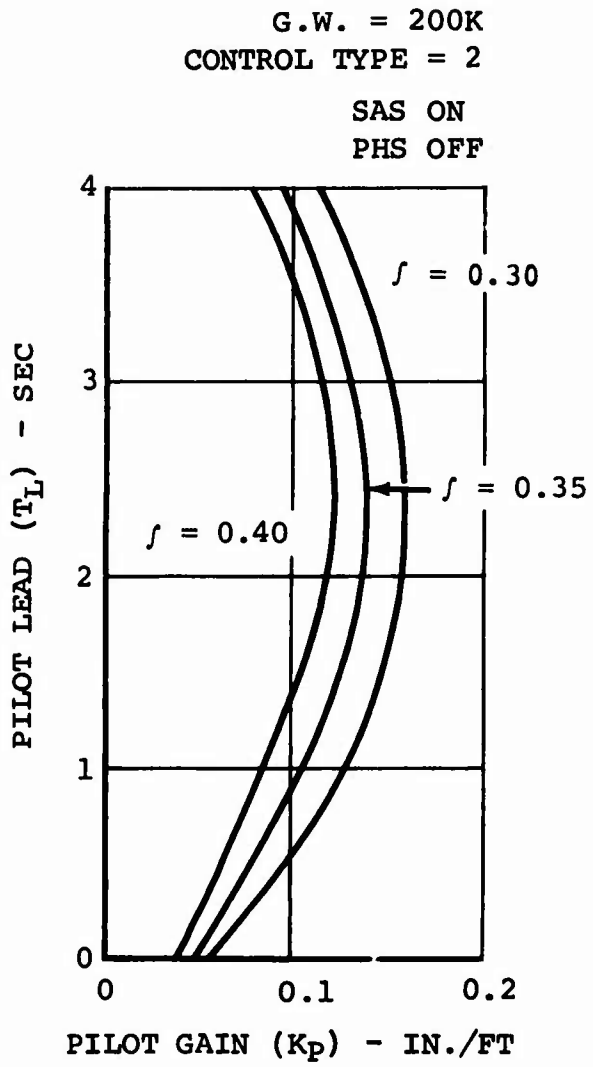

Figure 88. Lateral-Directional System Damping Boundaries.

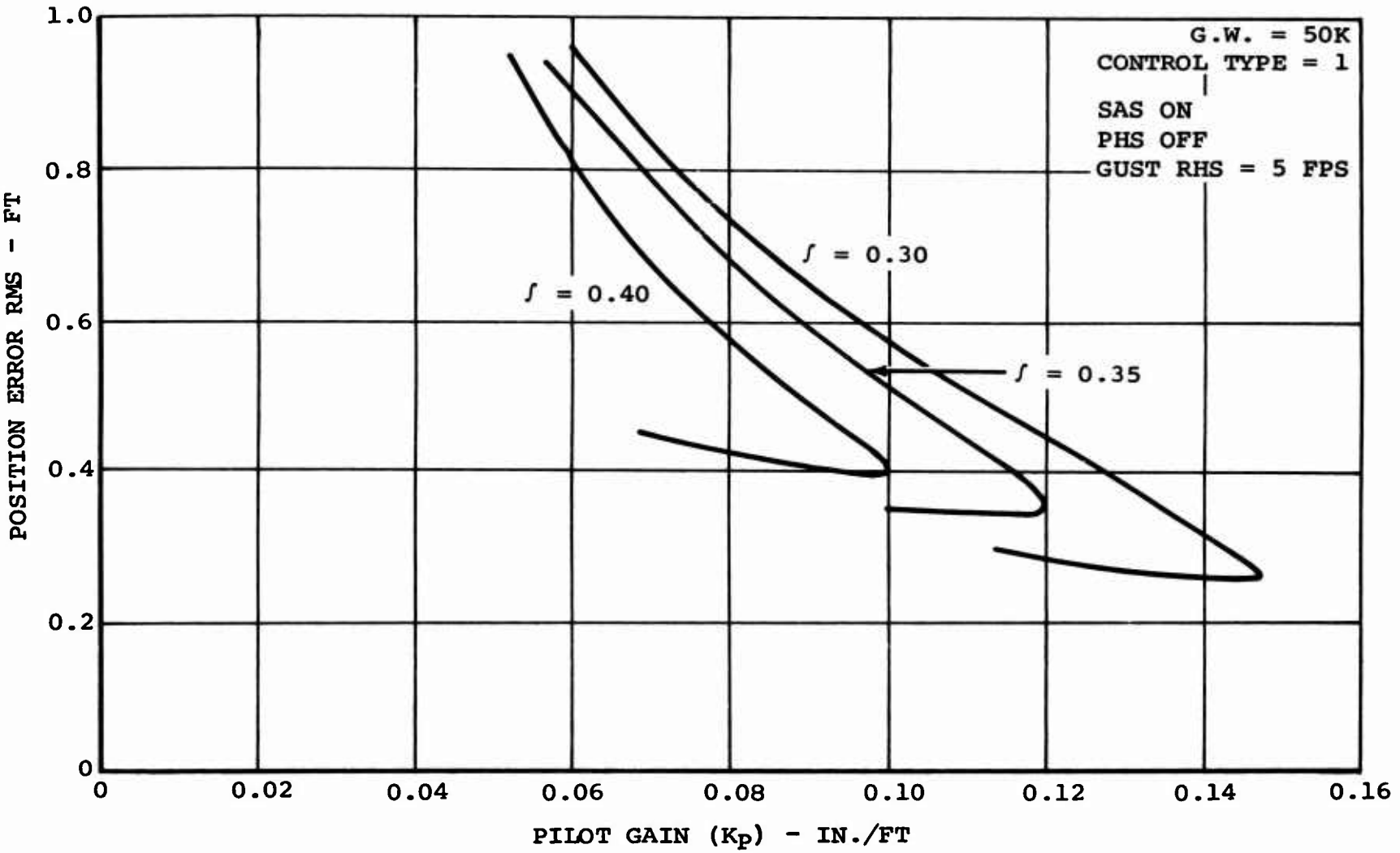

Figure 89. Piloted Longitudinal Hold Capability.

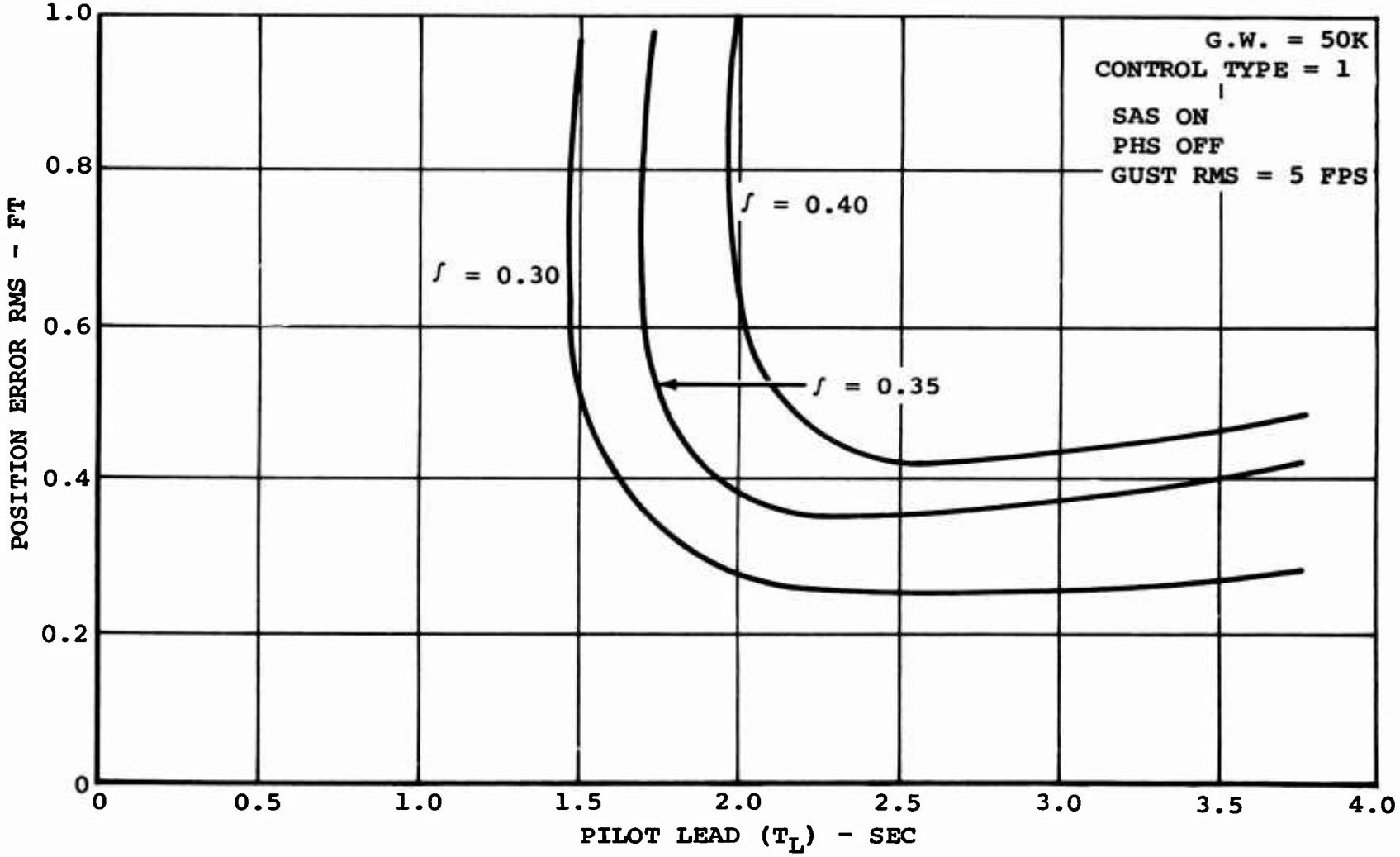

Figure 90. Piloted Longitudinal Hold Capability.

0.35 would mean a peak value of ± 0.5 feet, which for a pilot gain of 0.12 in./ft would mean pilot inputs of ± 0.06 inch. Whether this sensitivity is below the pilot's capability will be one item to be investigated on the simulator. If control sensitivities need to be changed, then all affected feedback gains will have to be reevaluated. However, most of the analysis will be valid, since pilot gain times control sensitivity is usually a constant multiplying factor. Thus, a change in control sensitivity would result in a proportional change in pilot gain. Table XII presents the optimum longitudinal pilot parameters and associated errors for the other control types and gross weights.

Lateral Hold Capability

Using the three lateral control types discussed and the 50,000- and 200,000-pound configurations, lateral position error due to random V-gusts will be investigated. Table XIII presents the optimum lateral pilot parameters and associated lateral position errors for the various control types and configurations.

Pilot Rating

In previous studies, efforts to relate pilot work load and pilot rating to stick activity were based on rms levels and were unsuccessful. However, References 3 and 4 associate pilot lead to pilot rating, in that increased compensation results in decreased ratings. Figure 91 is produced from Reference 4 and shows the incremental pilot ratings associated with lead compensation. Tables XII and XIII also include the incremental change in pilot ratings for the predicted pilot leads.

TABLE XII. ADJUSTABLE LONGITUDINAL PILOT PARAMETERS PREDICTED "OPTIMAL" OPERATION(1)

Gross Weight (Lb)	Control Type	Pilot Gain K_p (In./Ft)	Pilot Lead T_L (Sec)	Pilot Lag (Sec)	Position Error σx (Rms Ft)	Pilot Rating Change
50,000	1	0.12	2.0	0	0.35	1.5
200,000	1	0.11	2.0	0	0.40	1.5
50,000	2	0.11	3.0	0	1.20	2.5
200,000	2	0.08	3.0	0	1.60	2.5
50,000	3	0.08	2.5	0	0.45	2.0
200,000	3	0.11	2.0	0	0.35	1.5

(1) Based on K_p and T_L Yielding Min σ_x at 0.35 Damping Ratio.

REFERENCES

(1) NASA TN-D-1328 MAY 1962
"A FLIGHT DETERMINATION
OF THE ATTITUDE CONTROL
POWER AND DAMPING REQ.
FOR A VISUAL HOVERING TASK"

(2) NASA TN-D-792 APRIL 1961
"ATTITUDE CONTROL REQ.
FOR HOVERING CONTROL
THROUGH THE USE OF A
PILOTED FLIGHT SIMULATOR"

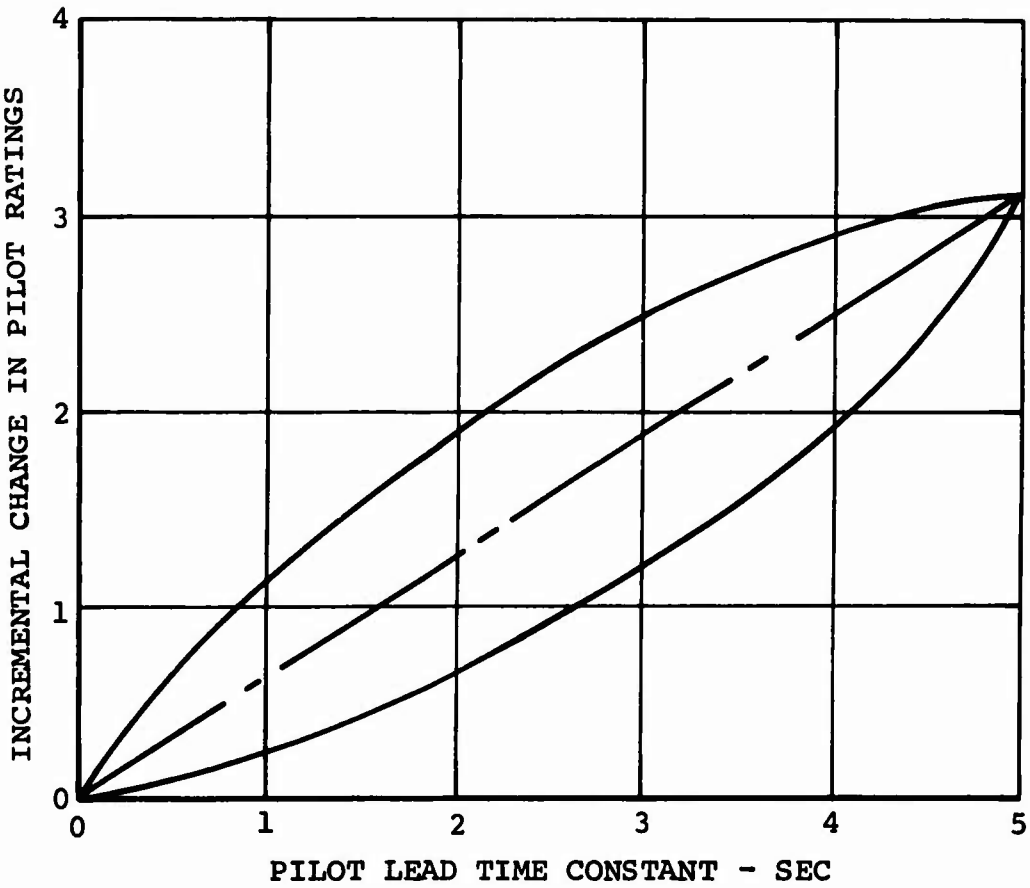

Figure 91. Approximate Variation of Incremental Pilot Rating With Pilot Lead Time Constant.

TABLE XIII. ADJUSTABLE LATERAL PILOT PARAMETERS PREDICTED "OPTIMAL" OPERATION (1)

Gross Weight (Lb)	Control Type	Pilot Gain K_p (In./Ft)	Pilot Lead T_L (Sec)	Pilot Lag (Sec)	Position Error σy (Rms Ft)	Pilot Rating Change
50,000	0	0.20	1.5	0	0.40	1.0
200,000	0	0.20	1.5	0	0.40	1.0
50,000	1	0.30	1.0	0	0.25	0
200,000	1	0.30	1.0	0	0.25	0
50,000	2	0.08	0.5	0	0.60	0
200,000	2	0.08	0.5	0	0.60	0

(1) Based on K_p and T_L Yielding Min σ_y at 0.35 Damping Ratio.

BASIC SIMULATOR MODEL VALIDATION APPROACH

A summary of the Boeing-Vertol flight test data is outlined in this section, and the approach to the hybrid model validation is described. The full-flight envelope hybrid simulation mathematical model used in the Boeing-Vertol simulation facility was validated against flight test data taken on the "wingless" 347 helicopter. The hybrid model configuration for these validation test runs included the "basic" 347 (airframe and control system) and the same vehicle with an external sling load attached. A set of hybrid computer responses was then generated for the future use in the validation of the Northrop simulator program. The complete data validation package, which is fully detailed in Reference 5, was submitted to the Northrop Corporation as scheduled in the contract. This section represents only a short synopsis of the validation approach and Boeing-Vertol simulator validation results.

MATHEMATICAL MODEL VALIDATION APPROACH

The basic approach to obtaining a validated simulator model involved the simulation on the Boeing-Vertol hybrid computer of the full-envelope math model (Reference 5), followed by validation of this model against piloted Model 347 flight test data based on specified pilot inputs or electronically generated SAS inputs. After this simulator model was adequately validated, a set of response data was generated based on an analog representation of the 347 control system. An identical computational setup was then used to program the full-flight envelope model at the Northrop facility, and the total new program was checked out against the validated Boeing-Vertol simulation results.

BASIC MODEL 347 AIRCRAFT FLIGHT TEST AND HYBRID SIMULATION MODEL COMPARISON

AFCS Configuration

The 347 airframe and control system models were first validated with static and dynamic response data generated from theory. Mechanization of the automatic flight control system functions for this program checkout phase was accomplished with an analog computer.

The analog FCS configuration reflected a design version of the system that was later optimized through testing on the 347 flight vehicle. Changes in system gains, time constants, and variations in shaping were made during the flight test optimization.

Prior to comparing hybrid response data with flight test results, it was necessary to modify the 347 control system model to match the final "optimized" flight test installation. This was done by programming the AFCS digitally in the 360/44 computer (through the use of the VECEX modeling tool discussed in Reference 5).

The control system model was synthesized from the larger 347 demonstrator digital AFCS by "enabling" the appropriate rate, attitude, pickoff, and synchronizer loops (with the proper 347 gains, time constants, etc.). Details of this digital control system mechanization are presented in Reference 5.

Correlation Results

Flight test data utilized for model verification included a series of pulses and steps put in by the pilot (at various airspeeds) in the longitudinal, lateral, and directional axes. Selected pulses were also applied through the aircraft SAS.

In the hybrid lab, these test-derived cockpit control deflections were modeled as a function of time with a BCA minicomputer. BCA outputs were trunked to the appropriate "control system" analog console for mixing and summation with model SAS inputs.

Figures 92, 93, and 94 illustrate typical correlations of flight test and hybrid results. Figures 92 and 93 depict an unaugmented control input at medium cruise speed in level flight. This plot indicates clearly (through the good correlation of rate and attitude response data) that the airframe model is adequate for the purposes intended. The SAS ON hover response presented in Figure 94 also shows good agreement with expected results. Other runs made for correlation with flight data are discussed in detail in Reference 5.

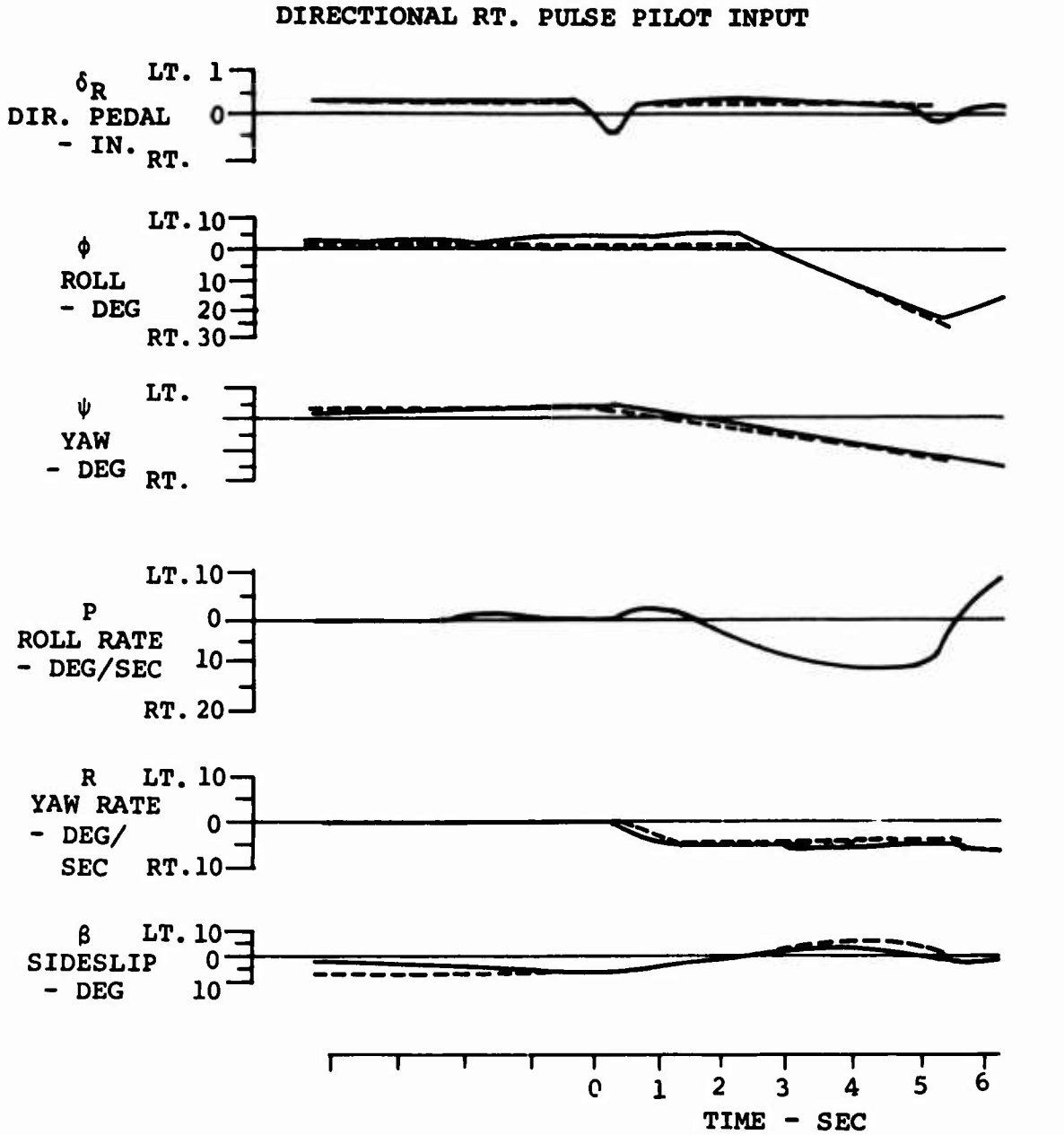

HYBRID DATA		FLT TEST DATA
DATE AUG. 31, 1972	TOGW 45,660 LB	FLIGHT 428
RUN 49	TOGG 9 IN. AFT	RUN 24
VECEX 347 AUTO CONTROL SYSTEM WITH ROLL RATE FEEDBACK COMPENSATION INCLUDED	IAS 80 KT SAS & DASH OFF RPM 220 ALT(H_D) 2,800 FT	AIRCRAFT B-164 FLIGHT TEST CASE 3

Figure 92. Hybrid Model Validation With 347 Flight Test Data.

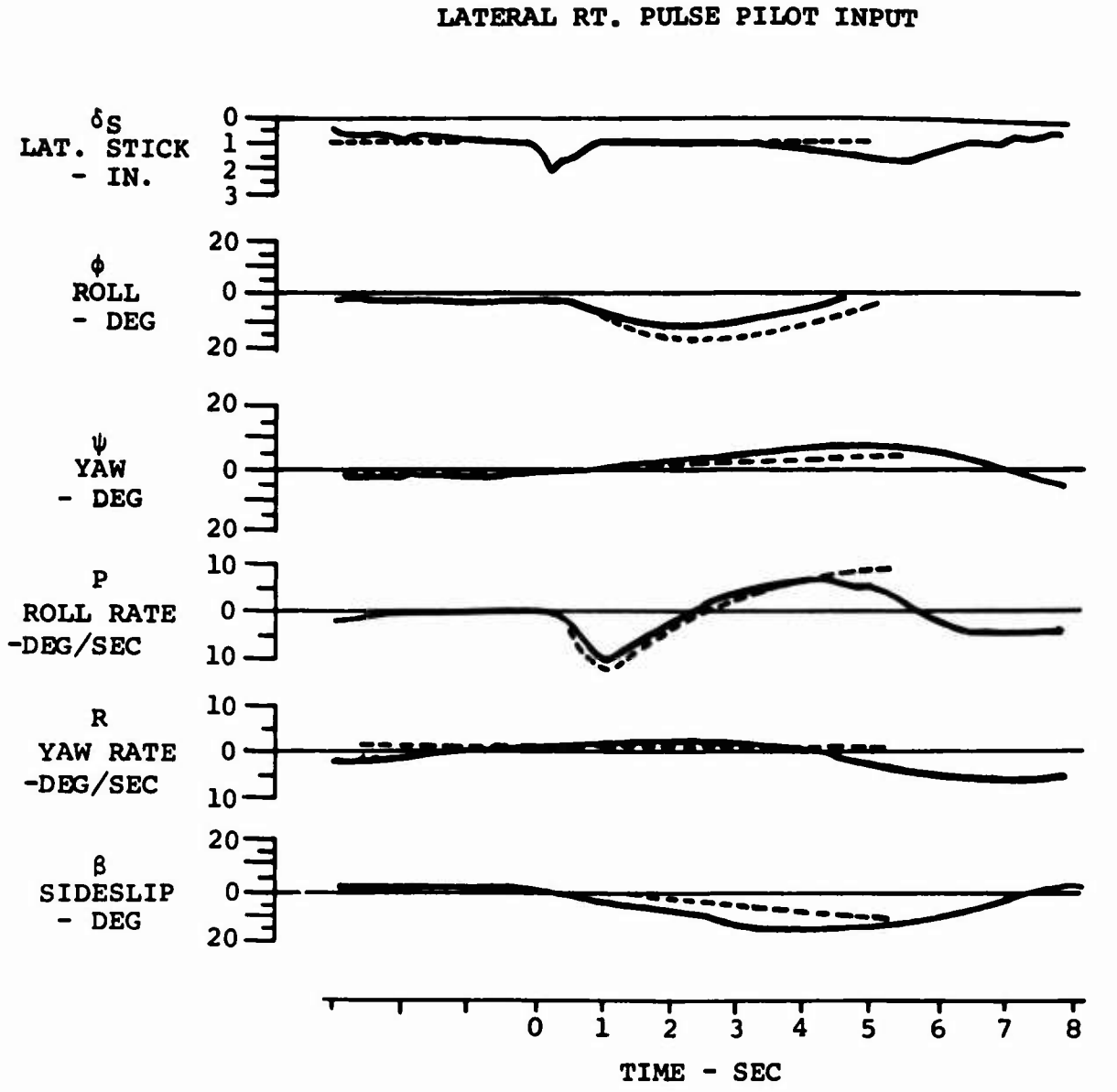

HYBRID DATA		FLT. TEST DATA
UPPER BOOST DYNAMICS - W = 55, τ = .6	T.O. G.W. 45,660 LB	FLIGHT 420
ROLL RATE FEEDBACK COMPENSATION = .24S+1/.12S+1	T.O G.G. 9 IN. AFT	RUN 21
ROLL ATTITUDE GAIN, G_{ϕ}=.5"/DEG	IAS 85 KT	AIRCRAFT B-164
DATE AUG. 31, 1972	SAS & DASH OFF	FLT. TEST CASE 2
RUN NO. 48	RPM 220	
	ALT. (H_D) 2,800 FT	

Figure 93. Hybrid Model Validation With 347 Flight Test Data.

Longitudinal Pulse Pitch Down Pilot Input

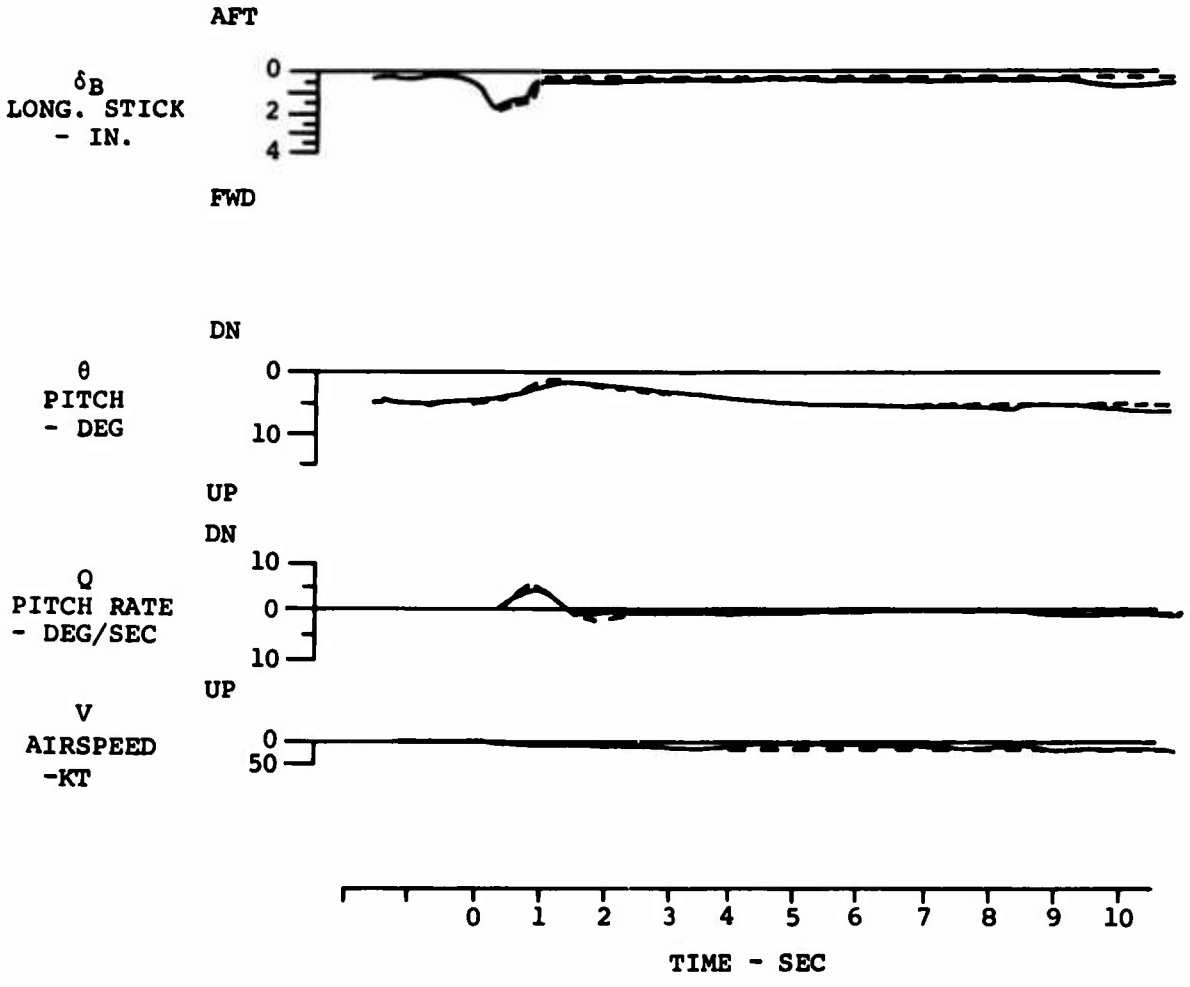

DATE AUG 31, 1972
RUN 47
VECEX 347 AUTO CONTROL SYS.
WITH ROLL RATE FEEDBACK
COMPENSATION INCLUDED

TOGW 43,660 LB
TOC 9 IN. AFT
IAS 0 KT
SAS & DASH ON
RPM 220
ALT (H_D) SL FT

FLIGHT 428
RUN 48
AIRCRAFT B-164
FLIGHT TEST
CASE 5

Figure 94. Hybrid Model Validation With 347 Flight Test Data.

GROUND-BASED SIMULATOR EVALUATION OF HOVER PERFORMANCE

The hover performance evaluation was accomplished at the Northrop Corporation, Aircraft Division, flight simulation facility utilizing the large motion-base simulator. The mathematical model programmed on this simulator is described in FULL-FLIGHT ENVELOPE MATHEMATICAL MODEL and in Reference 1. The precision hover system (PHS) loops were added to the basic helicopter model, and an oscilloscope display of the helicopter position error was installed in the cockpit dashboard. All piloted evaluation was performed by a Boeing-Vertol pilot with extensive experience in experimental and production helicopters, both with and without external load.

PRECISION HOVER SYSTEM MECHANIZATION

The PHS was mechanized on an analog computer with the differential position error computed from integration of lateral and longitudinal helicopter velocities which were resolved into the true horizontal plane. These integrated velocities were used directly as the signals coming from a synchronized position sensor. Appropriate logic signals, actuated by the stick detent and PHS switches, were added for position synchronization whenever the pilot entered the control loop. A continuous velocity integration signal drives the cockpit display of helicopter position with respect to a ground-fixed reference.

FEEDBACK LOOPS AND SYNCHRONIZING LOGIC

The PHS feedback loop mechanization is shown in Figures 95, 96, and 97. These loops are the additional ones to those designed for the Model 347 simulation (see FULL-FLIGHT ENVELOPE MATHEMATICAL MODEL and Reference 5 for details). The most significant feature of the longitudinal PHS is in the longitudinal cyclic pitch (LCP) control loops. The longitudinal velocity and position errors are fed back directly into the LCP control on both rotors. The pilot inputs have the options of direct differential collective pitch (DCP) and/or LCP control. Both of these options were used in the piloted simulator evaluation. The ground speed and the ground position error feedback loops are similar for all three (longitudinal, lateral, and vertical) axes. The ground position reference synchronization is achieved by controlling the operate/reset modes of the ground-speed integrators with switching logic L8 shown in Figure 97. Lateral ground speed and position error actuate the lateral cyclic pitch control; the vertical velocity and the altitude error move the collective pitch control. The horizontal position loops (lateral and longitudinal) go into a synchronizing mode whenever the pilot displaces the cyclic stick out of detent. The altitude hold remains closed unless the collective stick magnetic brake is released.

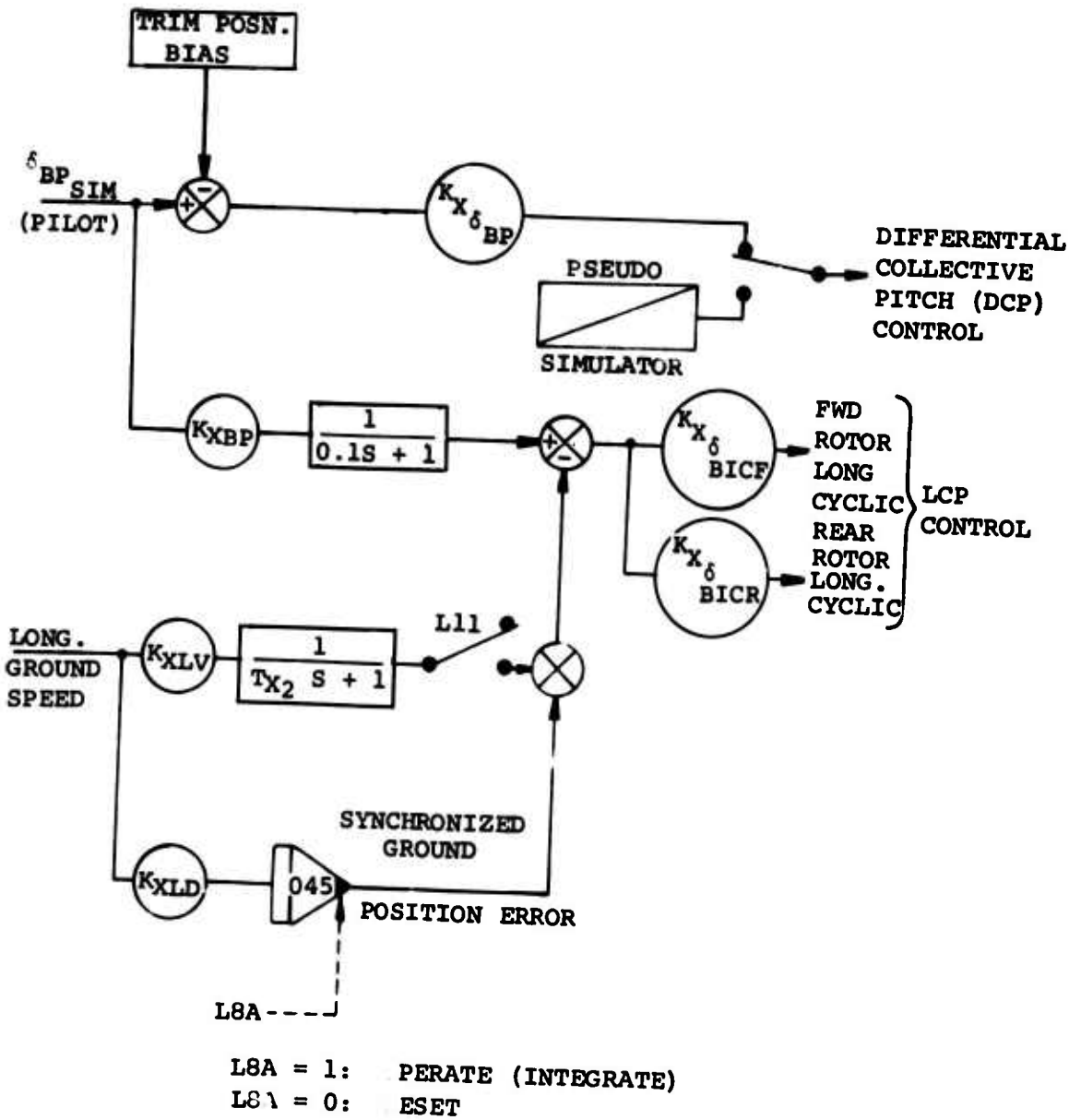

Figure 95. Longitudinal Precision Hover System.

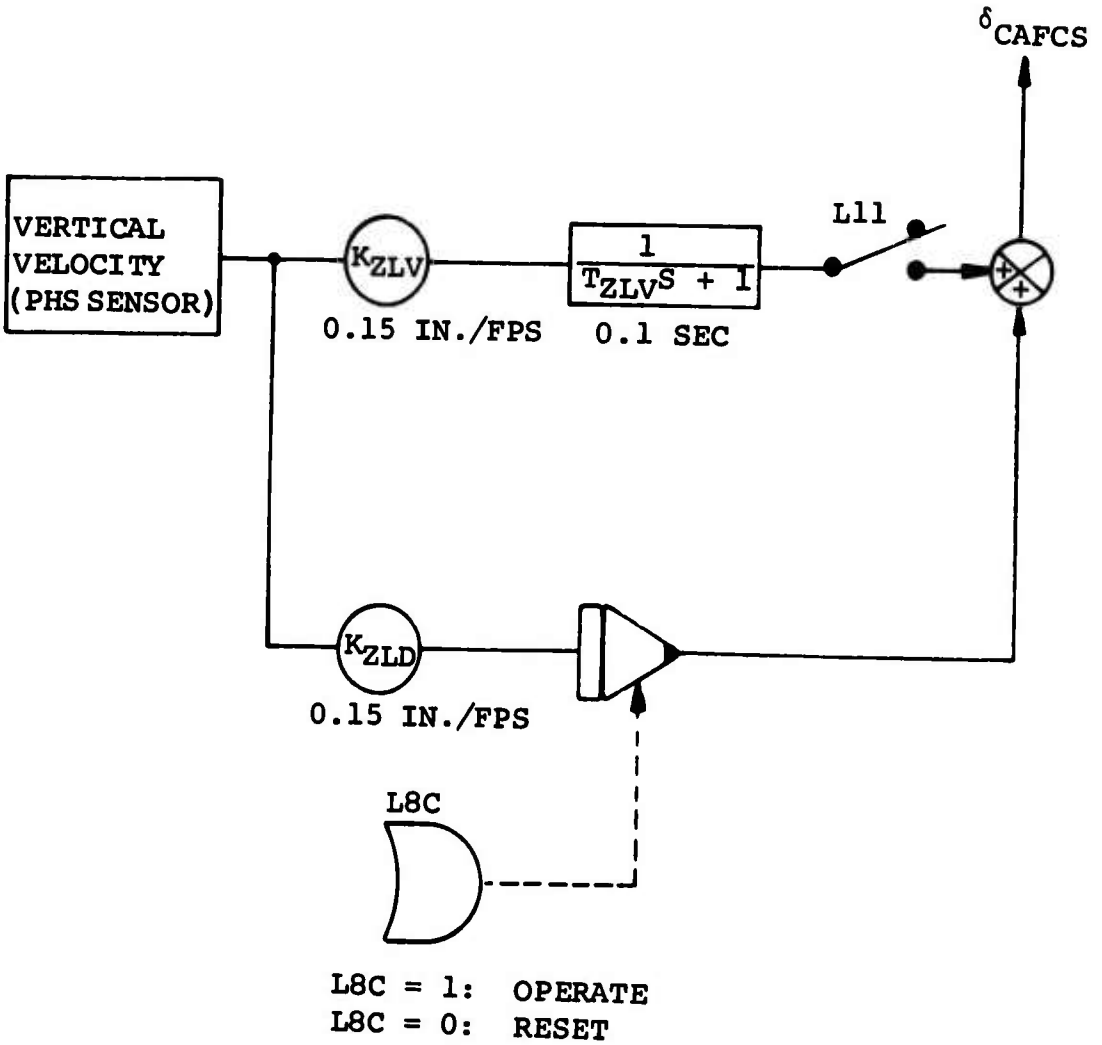

Figure 96. Vertical Hold System.

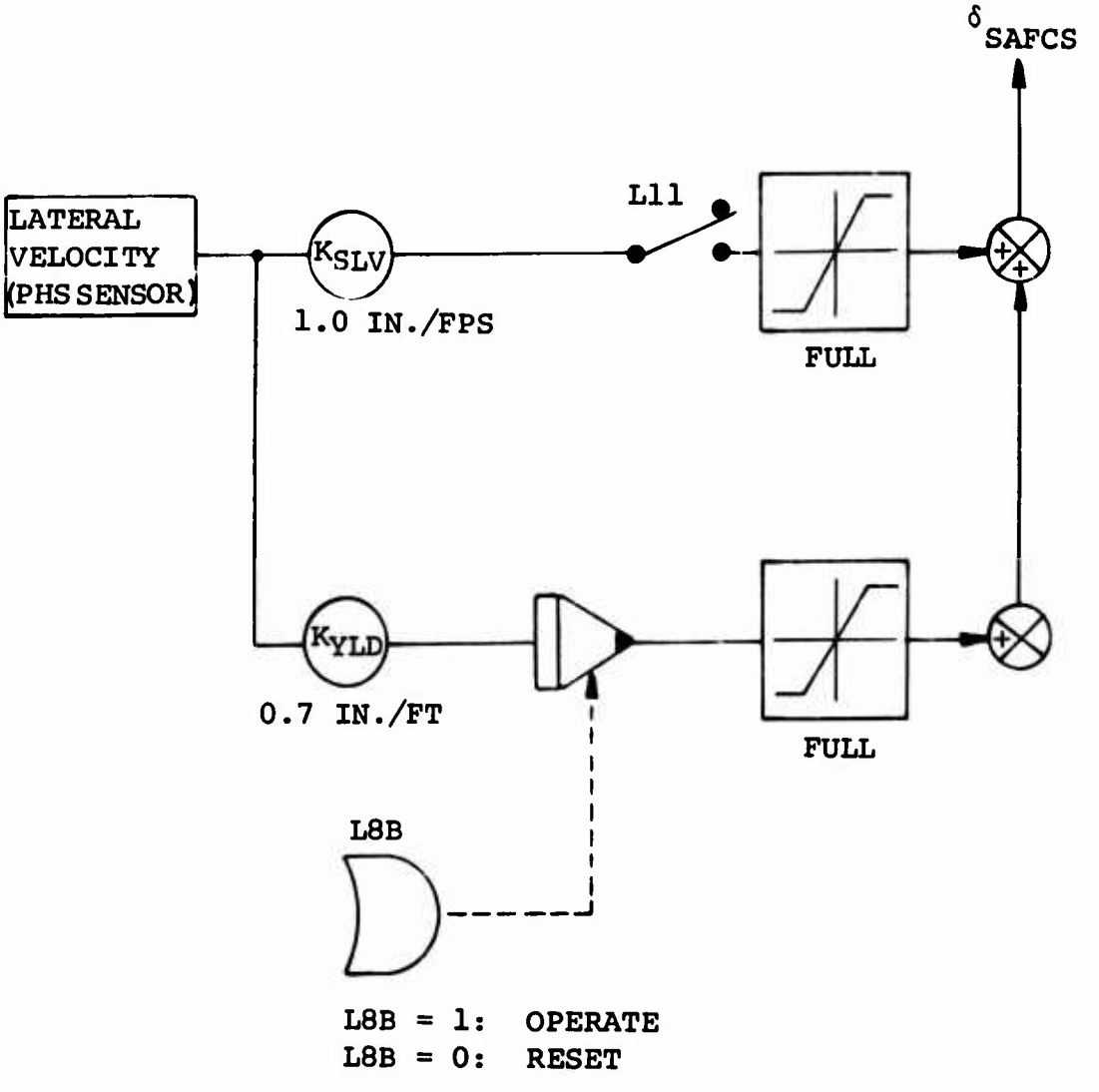

Figure 97. Lateral Precision Hover System (Sheet 1 of 2).

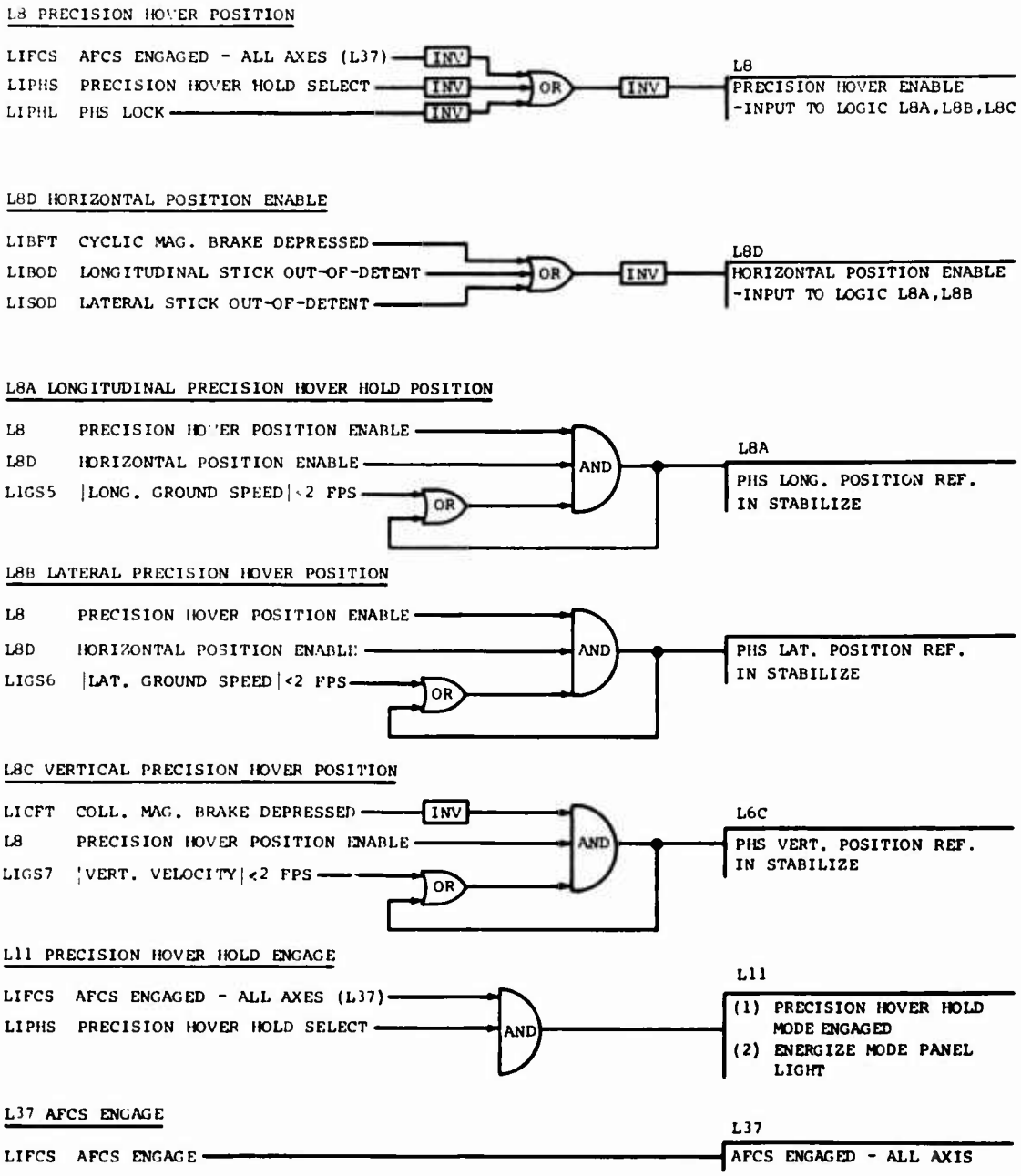

Figure 97. Lateral Precision Hover System (Sheet 2 of 2).

COCKPIT DISPLAY FUNCTIONS

A scope display of this aircraft position with respect to a ground-fixed reference was provided in the cockpit. The display mechanization included two options: an "inside-out" view, in which the motion of the scope displayed "T" represented the view of the ground-fixed reference from the aircraft (i.e., the scope is fixed to the aircraft); and an "outside-in" view, in which the displayed "T" represented the motion of the aircraft as seen by an observer stationed on a ground-fixed platform above the aircraft (i.e., the scope is fixed to the ground). These two options were programmed in deference to the fact that not all pilots like the same view for simulator work. Some pilots prefer to work with the "outside-in" views, and thus are able to interpret the motions on the display screen as the actual aircraft behavior, while other pilots find the opposite arrangement easier to follow. The pilot who was "flying" the simulator in this evaluation used the "outside-in" view exclusively.

The basic variables which were used to generate the two display functions are defined in Figure 98. The transformations for the two options are defined in Figure 99.

PILOT-ASSIST MODES AND CONTROL TYPES

The control types described in the Piloted Hover Hold Performance section were modeled on the simulator for a comparative evaluation in piloted hover performance. In addition, two more control types were simulated in each of the two axes. In the longitudinal axes (see Table XIV), these are control types 4 and 5; in the lateral axes (see Table XV), these are control types 3 and 4. The lateral control types 3 and 4 and the longitudinal control type 4 were added in order to provide the pilot with ground pattern tracking capability over large distances ($\pm$ 50 feet or more). The longitudinal control type 5 was added in order to evaluate the effect of ground speed damping in both axes. It was anticipated that this type of control, obtainable with type 5 in longitudinal and type 1 in lateral axes, should be one of the best available to the pilots for precise tracking tasks over small distances ($\pm$ 5.0 feet around the target). In addition to the control types shown in Tables XIV and XV, the pilot could maneuver within the tight PHS control with automatic position synchronizing on the cyclic control stick. This control type was termed the PHS control. As such, it represented the baseline control type, and all Cooper-Harper rating changes for other controls were compared with respect to the PHS control type.

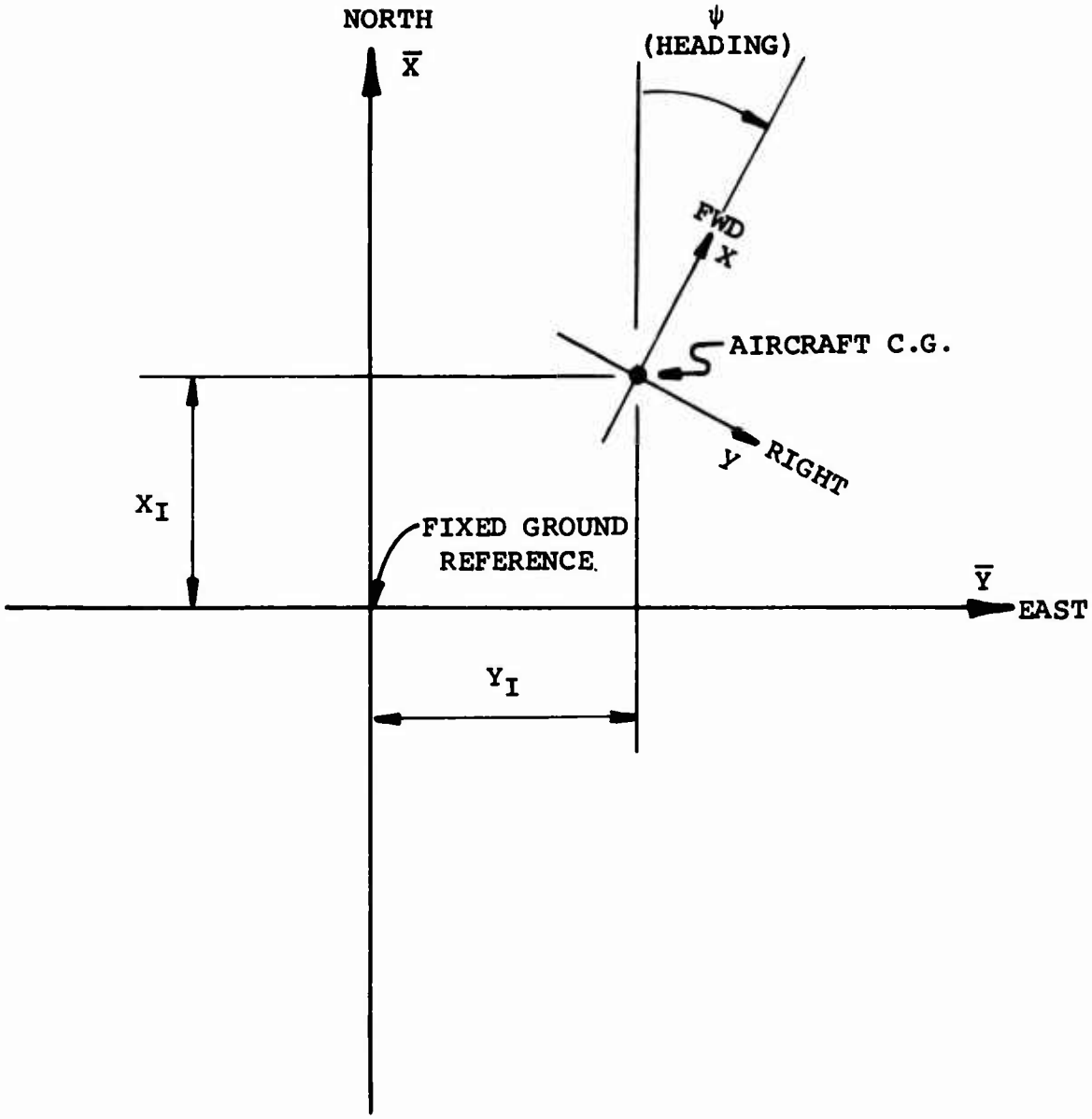

(X_I) = COMPUTED N-S COORDINATE, POSITIVE NORTH

(Y_I) = COMPUTED E-W COORDINATE, POSITIVE EAST

(ψ) = HEADING ANGLE, POSITIVE CLOCKWISE FROM NORTH

($\bar{X}$,$\bar{Y}$) = COORDINATE SYSTEM FIXED TO GROUND (INERTIAL)

(x,y) = AIRCRAFT BODY COORDINATES

Figure 98. Scope Display Variable Definition.

TABLE XIV. LONGITUDINAL CONTROL TYPES

Control Type	Rotor Control Mode	DCP Control			LCP Control			Ground Speed Feedback G_{BU}	Remarks
		$K_{X\delta_{BP}}$	G_{BPO}	Pickoff Washout τ	$K_{X_{BP}}$	K_{XLV}	K_{XLD}		
0	DCP alone	1.0	0.0	2.0	0.0	0.0	0.0	0.2	DCP velocity control $\dot{X}/\delta_B \approx 5.0 \frac{ft/sec}{in.}$
1	LCP alone No pickoff	0.0	0.0	2.0	5.73 deg/in.	0.0	0.0	0.0	LCP linear accel. control $\ddot{X}/\delta_B \approx 3.22 \frac{ft/sec^2}{in.}$ (= 5.73 deg/in.)
2	DCP alone No pickoff	1.0	0.0	2.0	0.0	0.0	0.0	0.0	DCP linear accel through pitch attitude on stick $\theta/S_B \approx 3$ deg/in.
3	LCP + delayed DCP	1.0	1.0	2.0	5.73 deg/in.	0.0	0.0	0.0	LCP and DCP linear accel. control
4	LCP + delayed DCP with pickoff	1.0	1.0	2.0	5.73 deg/in.	0.0	0.0	0.11	Dash pickoff as per ATH 6.5 in./in. with .154 rate limit 0.8 in./in.
5	LCP alone	0.0	0.0	2.0	5.73 deg/in.	1.15	0.0	0.0	LCP velocity control $\dot{X}/\delta_B$ = 5.0 fps/in.

X_{SC}, Y_{SC}, ψ_{SC} = SCOPE DRIVING SIGNALS

OPTION 1

DISPLAY DRIVING VARIABLES:

$X_{SC} = -(X_I COS\psi + Y_I SIN\psi)$

$Y_{SC} = -(-X_I SIN\psi + Y_I COS\psi)$

$\psi_{SC} = -\psi$

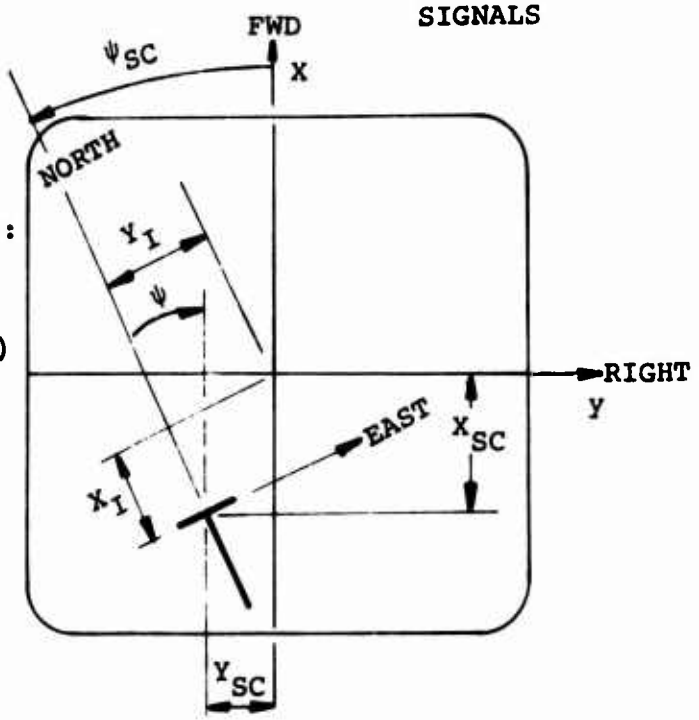

OPTION 2

DISPLAY DRIVING VARIABLES:

$X_{SC} = X_I$

$Y_{SC} = Y_I$

$\psi_{SC} = \psi$

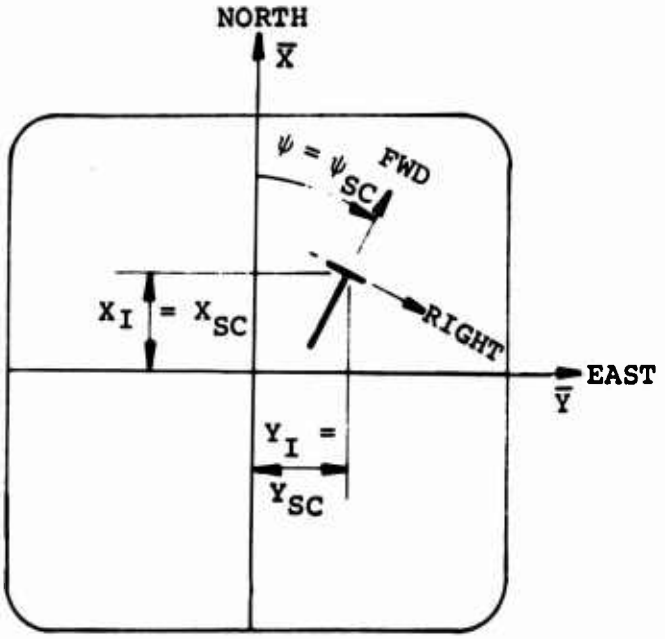

Figure 99. Cockpit Scope Display Driving Functions.

TABLE XV. LATERAL CONTROL TYPES

Control Type	Roll Pickoff			K_{YLD}	K_{SLV}	Remarks
	Gain G_{SPO}	Lag Time Constant	Washout Time Constant			
0	0.0	0.8	3.0	0.0	0.0	Accel. control with ϕ/δ_S = 2.9 deg/in.
1	0.0	0.8	3.0	0.0	0.2	Velocity control without roll quickening $\dot{y}/\delta_S \approx 5.0$ fps/in.
2	1.0	0.8	3.0	0.0	0.2	Velocity control with roll quickening washed out $\dot{y}/\delta_S \approx 5.0$ fps/in.
3	4.0	4.0	No Washout	0.0	0.2	Velocity control with rate limited roll quickening without washout $\dot{y}/\delta_S$ = 25 fps/in.
4	8.0	8.0	No Washout	0.0	0.2	High gain velocity control with rate limited roll pickoff without washout $\dot{y}/\delta_S$ = 45 fps/in.

SIMULATION PROCEDURES AND RESULTS

The simulator evaluation of the hover performance in turbulence was done only for the 50,000-pound configuration. The aircraft performance runs without the pilot control were made with the full motion, PHS-ON, while the pilot kept his hands off the controls. The piloted performance runs were made for several selected control types at nominal turbulence levels of 0.0, 5.0, 10.0, and 15.0 feet per second rms. For presentation purposes, the actual turbulence levels were used, which were calculated from the digital records of the data sampled at five samples per second. In addition, a tracking task (CTR) was performed by the pilot with each of the selected control types, in which the pilot traced a closed triangular path on the ground with the aircraft. An X-Y plotter was used to show how the pilot was able to perform these tasks at various turbulence levels with different control types.

A typical hover performance run was conducted by first letting the aircraft attain a trim configuration, and then switching into the operate mode with the cockpit motion. Several trial runs were then obtained (and recorded digitally) to check on the natural drift characteristics of the cockpit display functions. The unpiloted hover performance runs then followed, in which the turbulence level was varied while the pilot kept his hands off the controls. The pilot's comments with respect to the acceleration level acceptability and general realism of the cockpit motion were noted. Then the pilot was given the hover hold task (HH) and the closed path tracking task (CTR) for the different control types at various turbulence levels. The aircraft response data was recorded at the selected intervals, and the pilot's comments regarding Cooper-Harper rating and general aircraft response were noted in the log. The full log of all runs is shown in Appendix III.

Hover Hold Tasks

The piloted hover hold tasks are described in this section. These tasks were performed by requiring the pilot to hold the displayed aircraft position (display option 2, Figure 99) over the fixed ground point. This particular pilot preferred to work with "outside-in" display exclusively. The pilot was given the hover hold task with the baseline PHS control capability (synchronized position hold) and with control type combinations 5/1 (long. type 5/lateral type 1), 1/2, 1/0, 2/0, and 1/1. On the initial runs, the pilot found control combinations 1/0 and 2/0 hard to work with, apparently because these controls did not have either lateral or longitudinal velocity feedback. With the additional complication of small display motions ($\pm$ 5.0 feet in both directions), the pilot had difficulty in his attempts to remain within the display limitations in higher than 5.0-fps turbulence levels. The set

of X-Y plots shown here is therefore limited to control types 5/1, 2/1, and the PHS mode. The reduced data for other control combinations is discussed in the Simulator Evaluation and Analytical Results section.

The baseline PHS control type hover hold capabilities in turbulence are shown in Figure 100. This control was considered to be the best by the pilot, with an approximate Cooper-Harper rating of 3.0. On the statistical basis, this control shows the capability to hold the hover position with about 4.0 inches (standard duration) in 15.0-fps nominal turbulence level. In practical terms this means that in high turbulence the pilot will be able to hold the aircraft within 4.0 inches of the fixed ground position 68.3% of the total duration of the task, and about 95.6% of the task duration the aircraft position error will not be greater than 8.0 inches in either direction. Figures 101 and 102 compare the piloted performance at 5.0 fps nominal turbulence level with control type combinations 5/1 and 1/2 (longitudinal/lateral). The advantage of the longitudinal velocity feedback (type 5/1) is clearly visible in the significantly better position hold shown in Figure 101 compared with Figure 102 (control type 1/2). A similar advantage can be discerned at 10.0 fps nominal turbulence levels shown in Figures 103 and 104. Performance with control combination 5/1 at 15.0 and 20.0 fps turbulence levels is displayed in Figures 105 and 106. Comparison of these control combinations with the baseline PHS control mode performance of Figure 100 clearly indicates the powerful effect of a good precision hover system on hover hold performance in turbulence.

Hover Tracking Tasks

In addition to the hover hold tasks on the simulator, the pilot performed closed-path tracking tasks (CTR), in which he was instructed to fly the aircraft around a triangular path, with 4.0-ft rectangular sections. This section describes the pilot's performance of the CTR tasks at different turbulence levels using control type combinations 5/1, 1/2, and the baseline PHS control mode.

The basic tracking capability of the three control types (in calm air) is compared in Figures 107, 108, and 109. The baseline PHS mode (Figure 107) emerges as the best control type, control type 5/1 (Figure 108) rates second, and control type 1/2 rates third. In terms of Cooper-Harper scale, this pilot rated the baseline PHS and control type 5/1 as 3.0. Control type 1/2 was rated as 5.0 at the full design longitudinal control sensitivity, and 4.0 when the longitudinal stick sensitivity was reduced to one-half of the design setting. An improvement in longitudinal tracking capability with reduced stick sensitivity is evident when the traces in Figure 111 are compared with those of Figure 110. The tracking capability

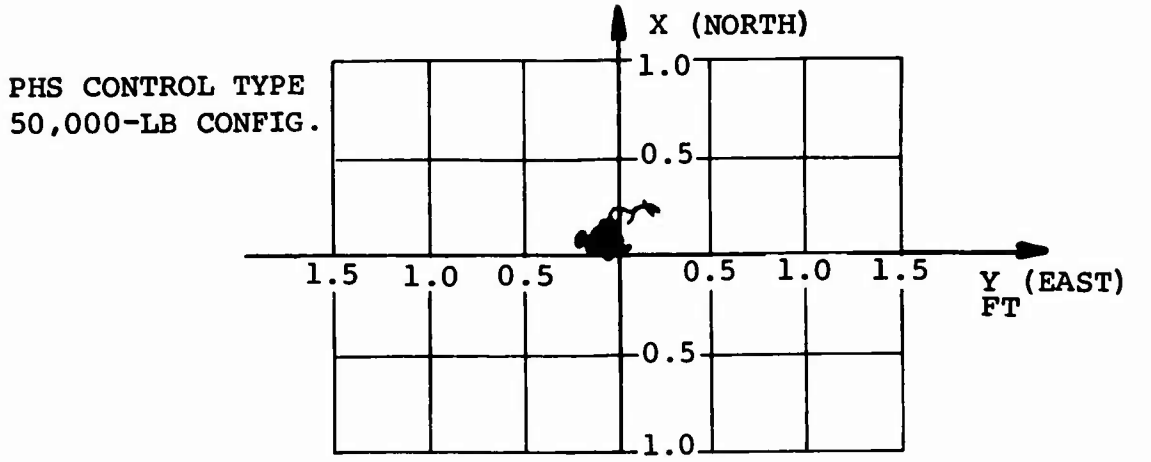

(a) 5.0 FT/SEC NOMINAL TURB. LEVEL

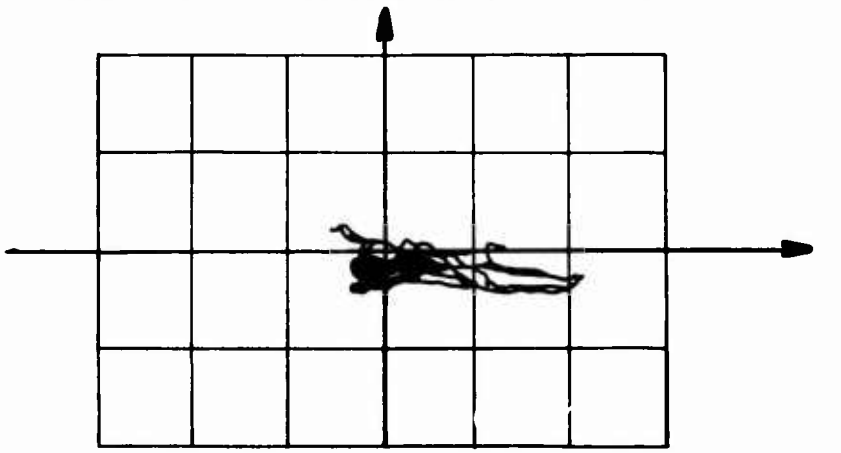

(b) 10.0 FT/SEC NOMINAL TURB. LEVEL

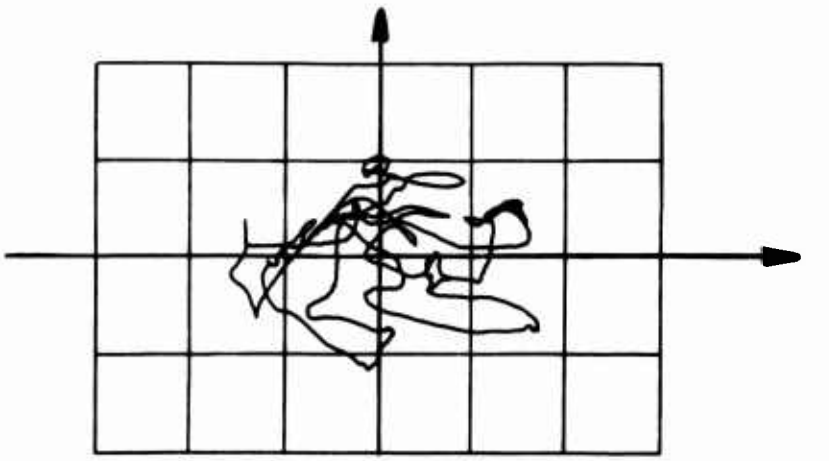

(c) 15.0 FT/SEC NOMINAL TURB. LEVEL

Figure 100. Simulator Results: Piloted Hover Hold Performance in Turbulence.

3 JULY 1973
RUN NO. 14

5.0 FPS NOMINAL TURB.LEVEL

COMPUTED RESULTS:

$\bar{X}$ = -0.158 FT
σ_X = 0.427 FT
$\bar{Y}$ = -0.130 FT
σ_Y = 0.515 FT
$\bar{U}_g$ = -1.66 FPS
σ_{U_g} = 4.45 FPS
$\bar{V}_g$ = -2.56 FPS
σ_{V_g} = 8.56 FPS

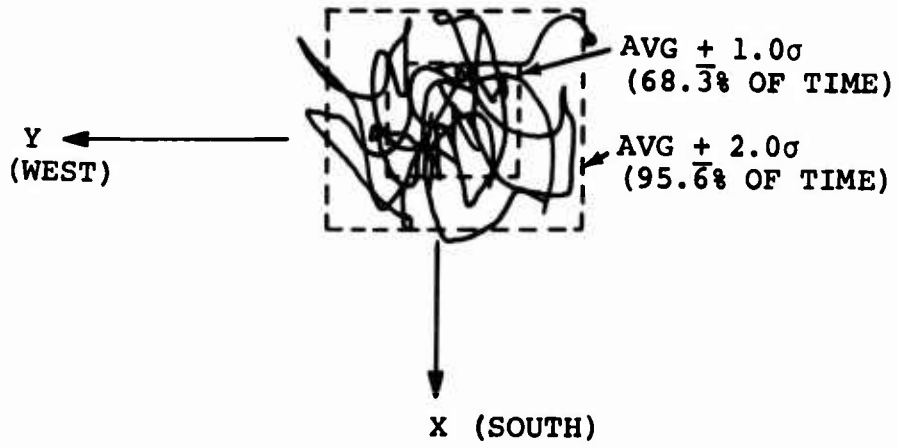

SCALE: 1.0 FT/IN.

Figure 101. Piloted Hover Hold Control Type 5/1.

3 JULY 1973
RUN NO. 10

5.0 FPS NOMINAL TURB.LEVEL

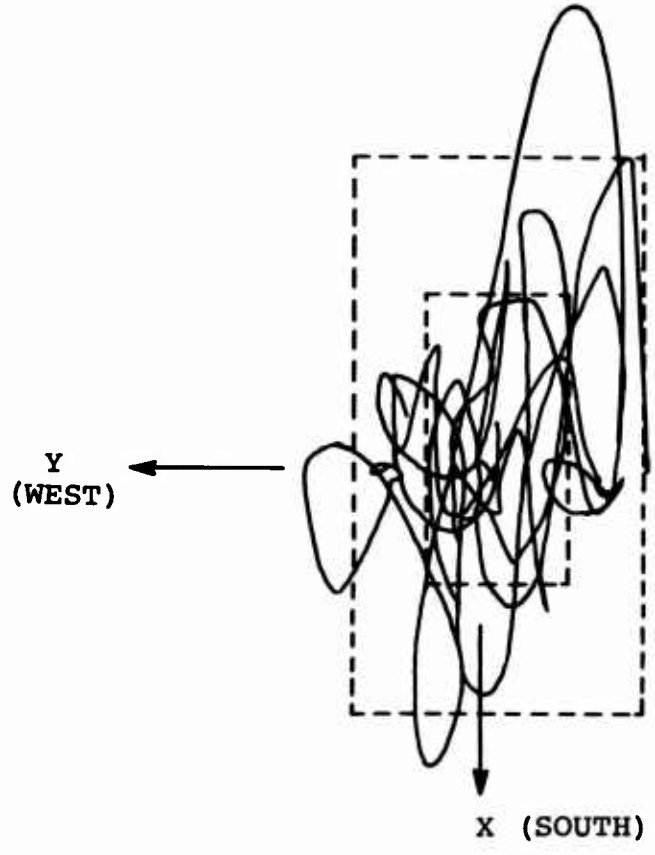

SCALE: 1.0 FT/IN.

COMPUTED RESULTS:

$\bar{X}$ = -0.252 FT
σ_X = 1.127 FT
$\bar{Y}$ = -0.140 FT
σ_Y = 0.570 FT

$\bar{U}_g$ = -1.64 FPS
σ_{ug} = 4.39 FPS
$\bar{V}_g$ = -2.58 FPS
σ_{Vg} = 8.57 FPS

Figure 102. Piloted Hover Hold Control Type 1/2.

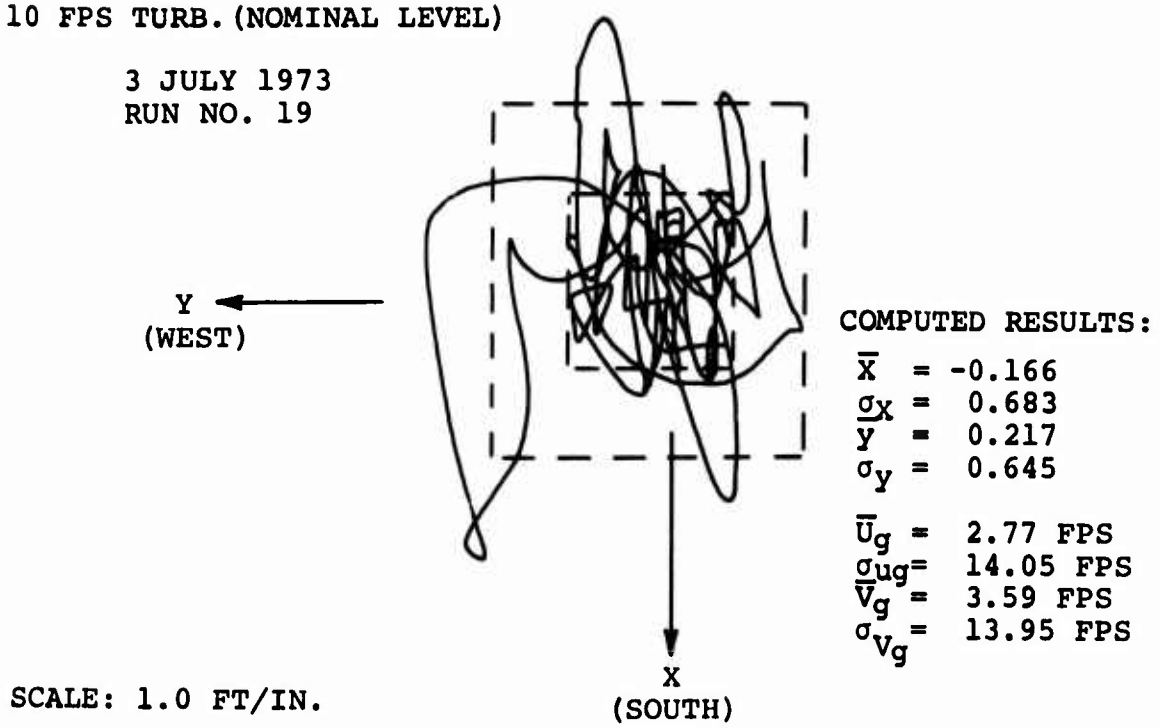

Figure 103. Piloted Hover Hold Control Type 5/1.

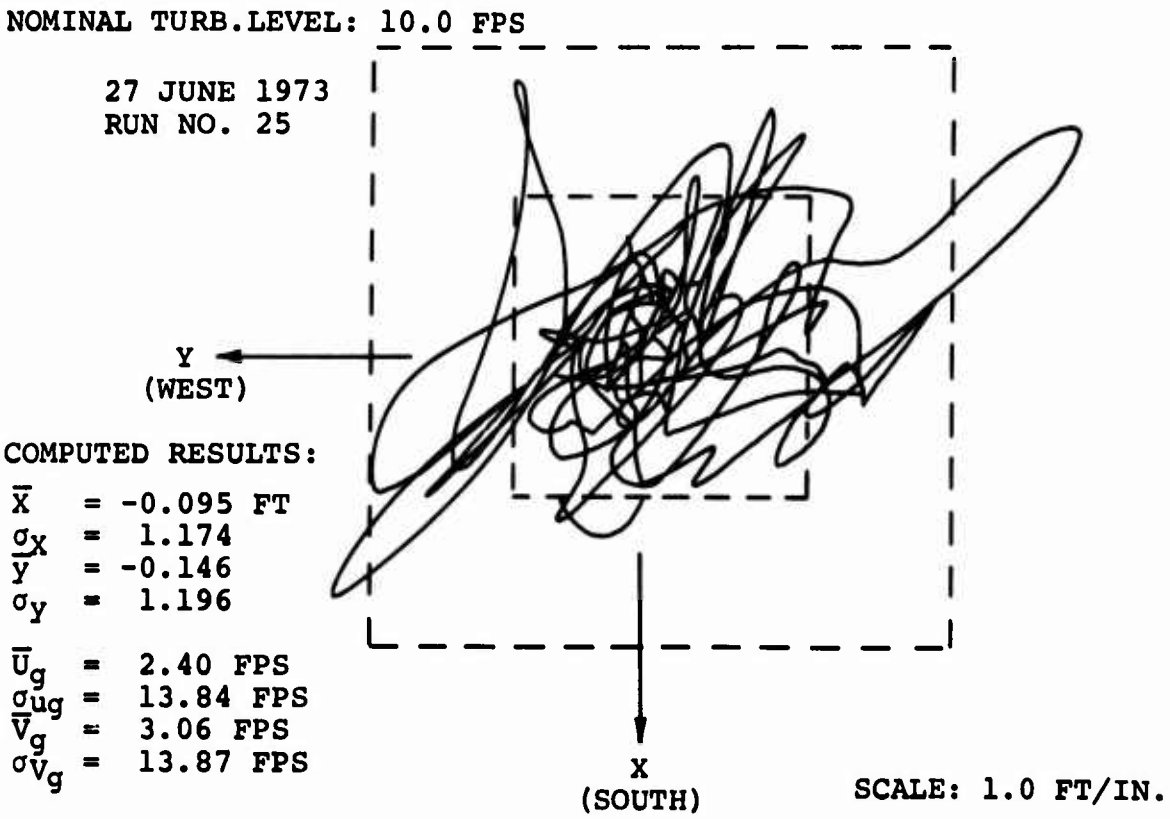

Figure 104. Piloted Hover Hold Control Type 1/2.

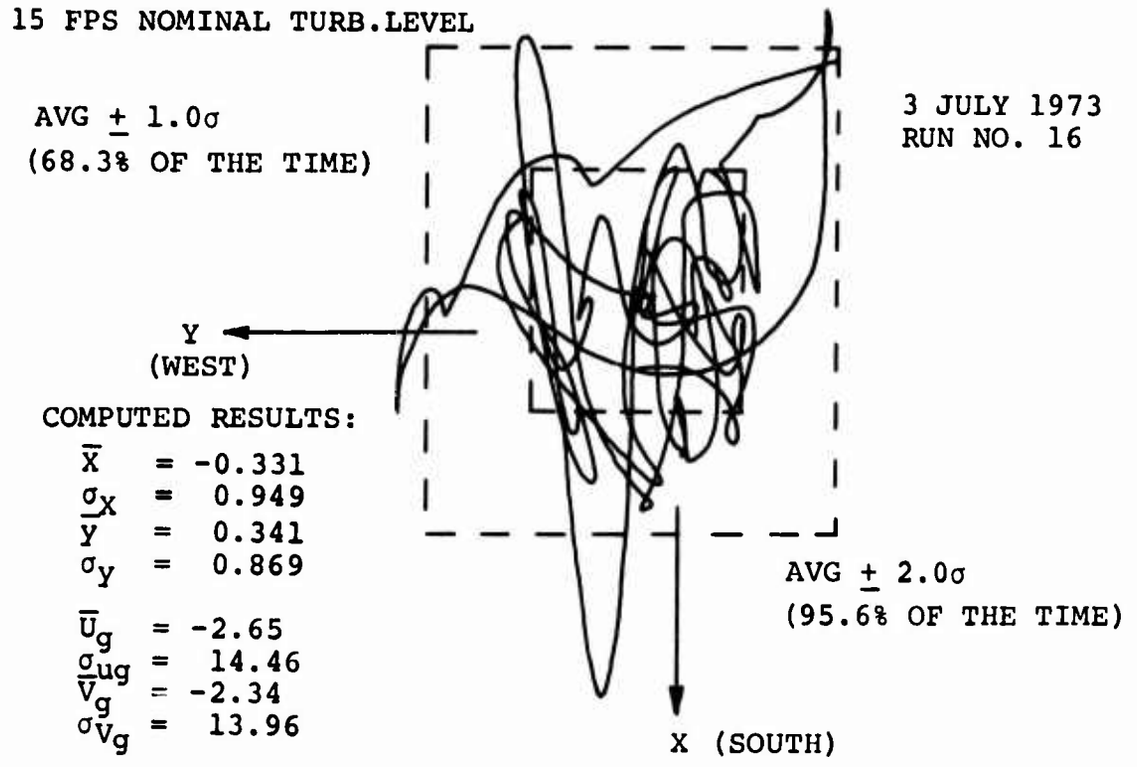

Figure 105. Piloted Hover Hold Control Type 5/1.

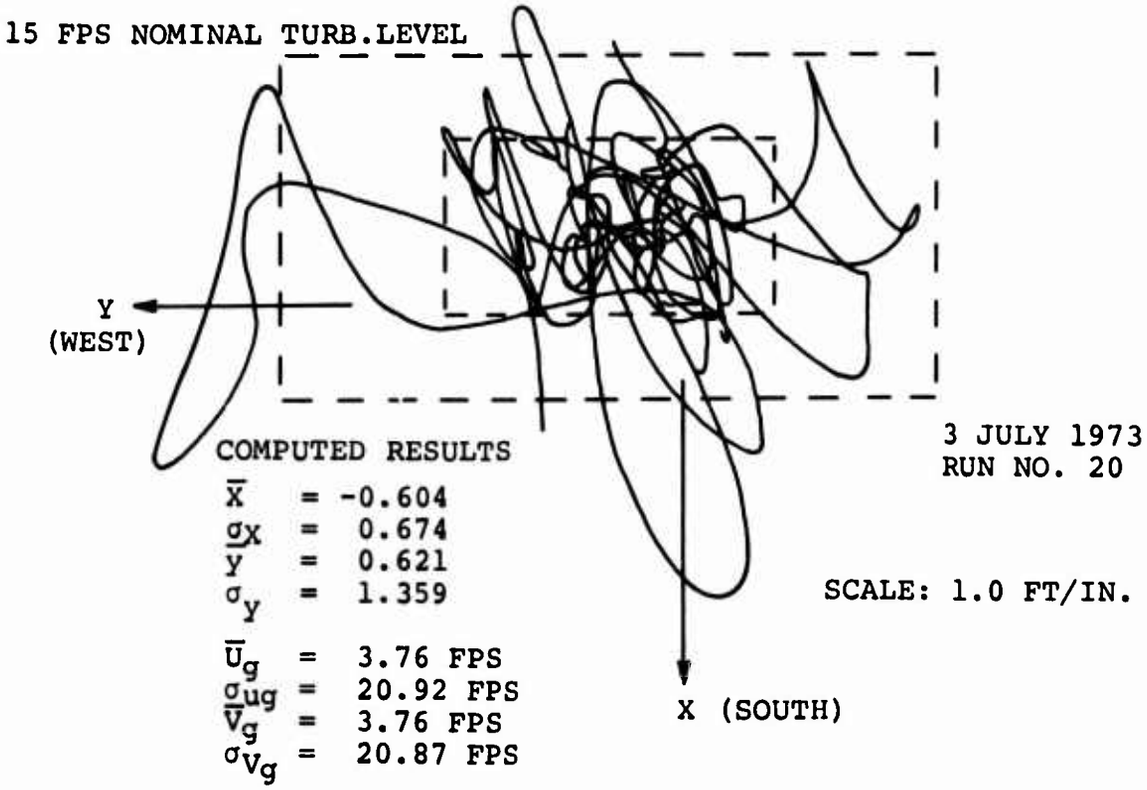

Figure 106. Piloted Hover Hold Control Type 5/1.

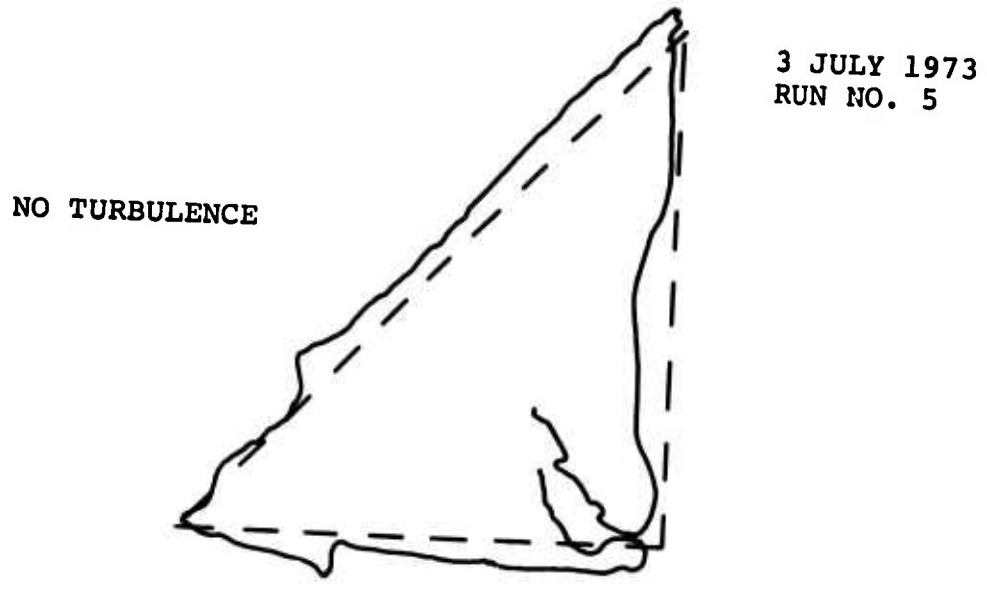

Figure 107. Piloted CTR Task Control Type PHS.

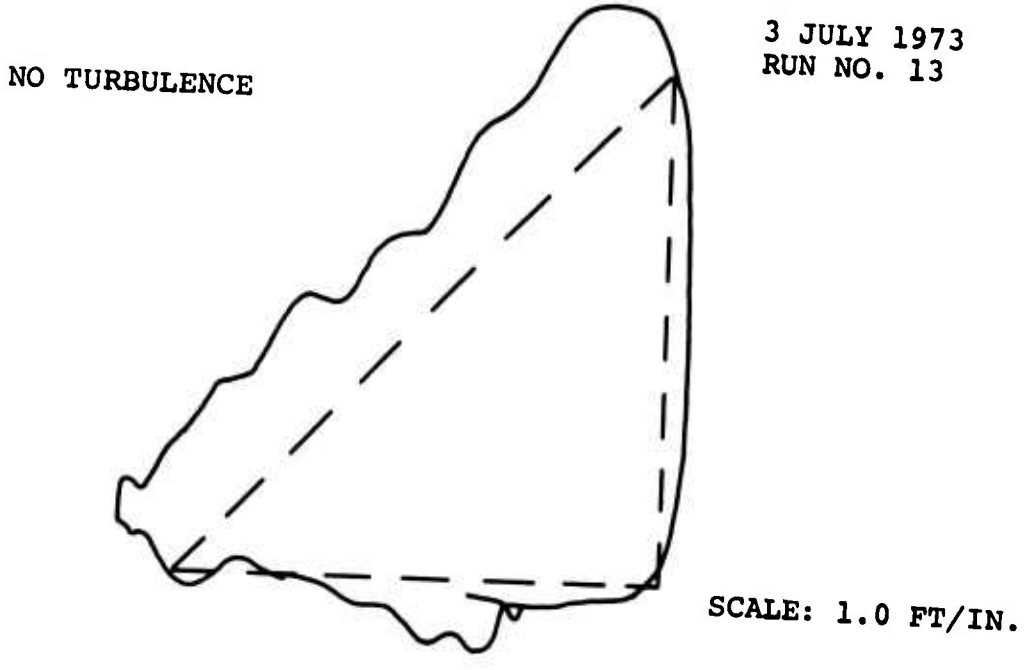

Figure 108. Piloted CTR Task Control Type 5/1.

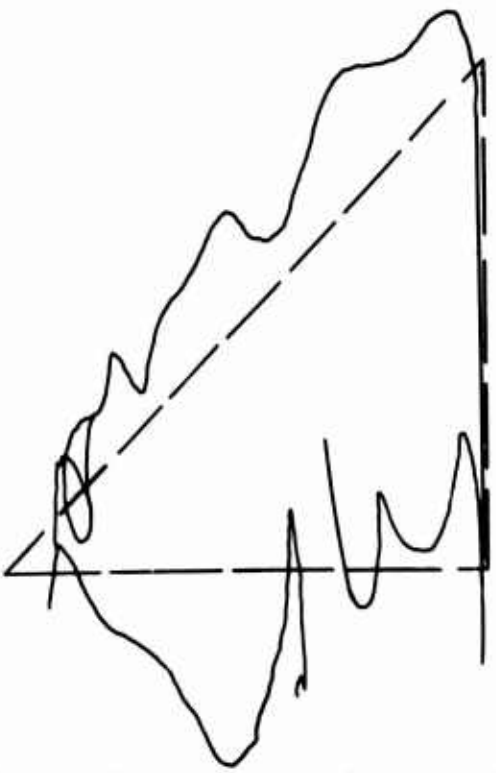

Figure 109. Piloted CTR Task Control Type 1/2 (Full Gains).

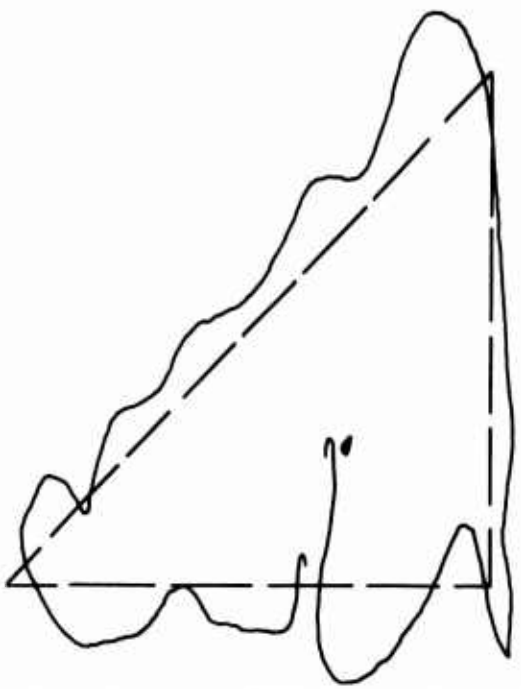

Figure 110. Piloted CTR Task Control Type 1/2 (With 1/2 X Longitudinal Gain).

27 JUNE 1973
RUN NO. 42

PILOT TASK: CTR
TURB LEVEL: 10.0 fps
CONTROL TYPE: PHS

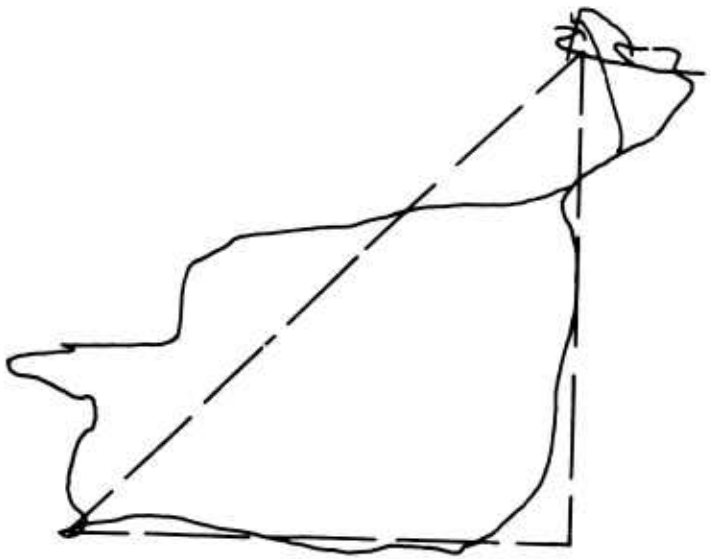

Figure 111. Pilot CTR Task Control Type PHS.

3 JULY 1973
RUN NO. 18

10.0 FPS NOMINAL TURBULENCE LEVEL

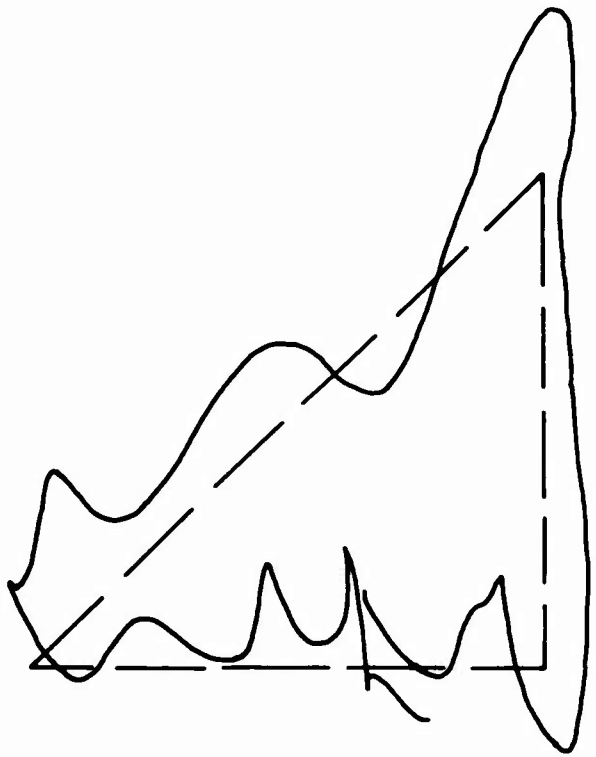

Figure 112. Piloted CTR Task Control Type 5/1.

27 JUNE 1973
RUN NO. 44

15.0 FPS NOMINAL TURBULENCE LEVEL

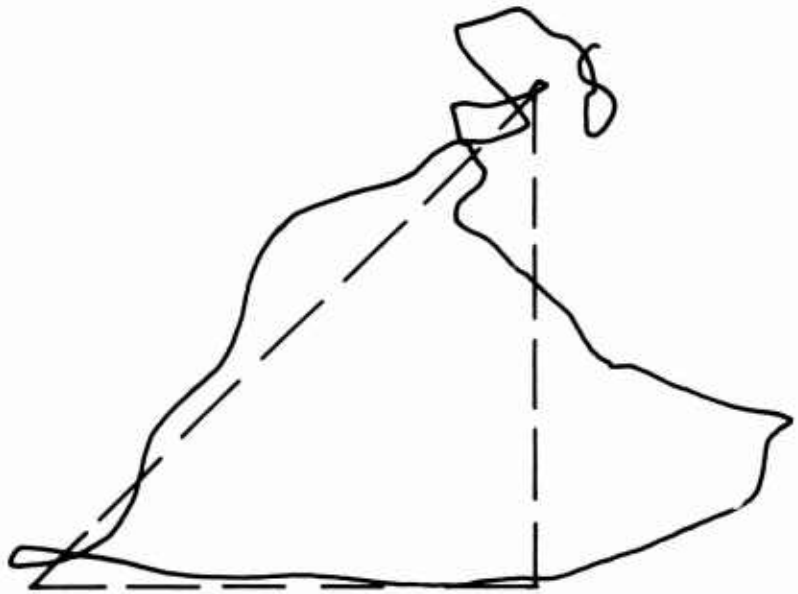

Figure 113. Pilot CTR Task Control Type PHS.

is further compared with PHS and control type 5/1 at higher turbulence levels in Figures 112 and 113.

Effects of Limited Simulator Motion

The simulator motion cues as they might affect the piloted hover hold performance were explored only in a cursory manner. Two piloted hover hold tasks were performed with and without the cockpit motion. Figure 114 shows a piloted hover hold run, fixed base in a 5.0-fps turbulence level; Figure 115 shows the same run repeated with the moving cockpit. A comparison in absolute performance terms clearly indicates that cockpit motion cues helped the pilot in performing the same task. Figure 116 shows another fixed-base hover hold run at 10.0 fps turbulence level. A comparable run with cockpit motion is shown in Figure 117, but this run was performed at a later date when the pilot evidently had learned the system. In any case, judging from these runs and the pilot's comments, good cockpit motion significantly improves the pilot's ability to perform comparable tasks.

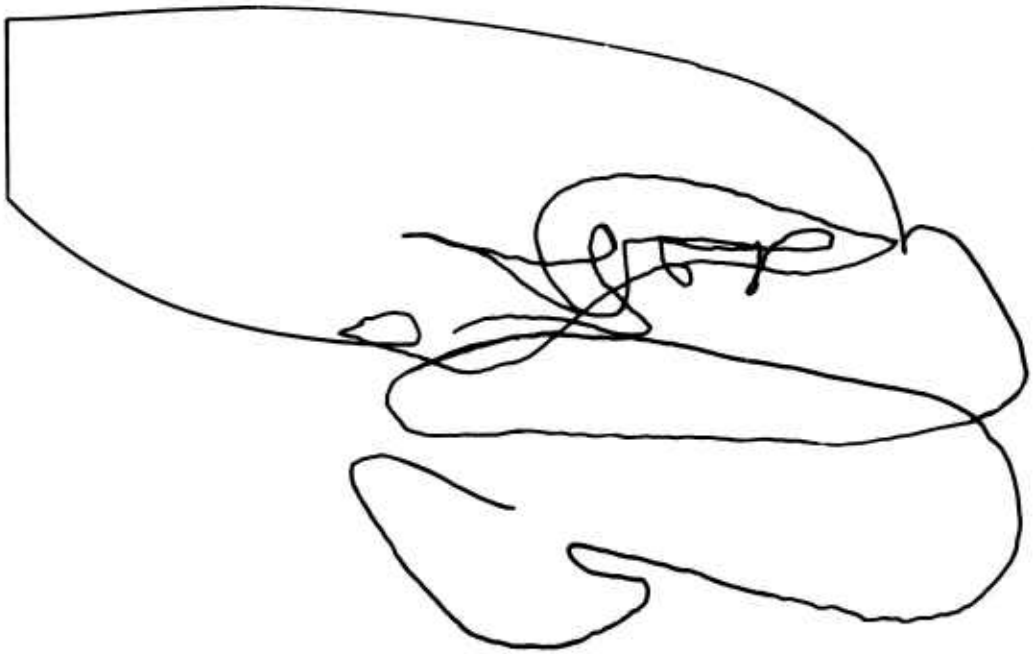

27 JUNE 1973
RUN NO. 36
(DIGITAL FILE NO. 29)

FIXED-BASE RUN

CONTROL TYPE: 5/1
PILOT TASK: HH
TURB. LEVEL: 5.0 FPS

Figure 114. Piloted Hover Hold Task Control Type 5/1.

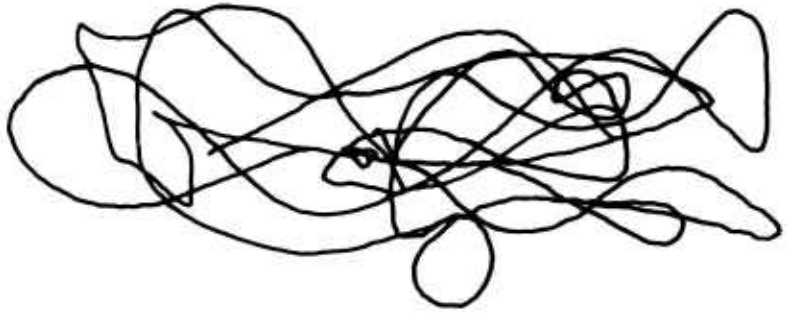

27 JUNE 1973
RUN NO. 37
(DIGITAL FILE NO. 30)

MOVING BASE

CONTROL TYPE: 5/1
PILOT TASK: HH
TURB LEVEL: 5.0 FPS

Figure 115. Piloted HH Task Control Type 5/1.

CONTROL TYPE: 5/1
PILOT TASK: HH
TURB. LEVEL: 10.0 FPS

FIXED-BASE RUN

27 JUNE 1973
RUN NO. 35
(DIGITAL FILE 28)

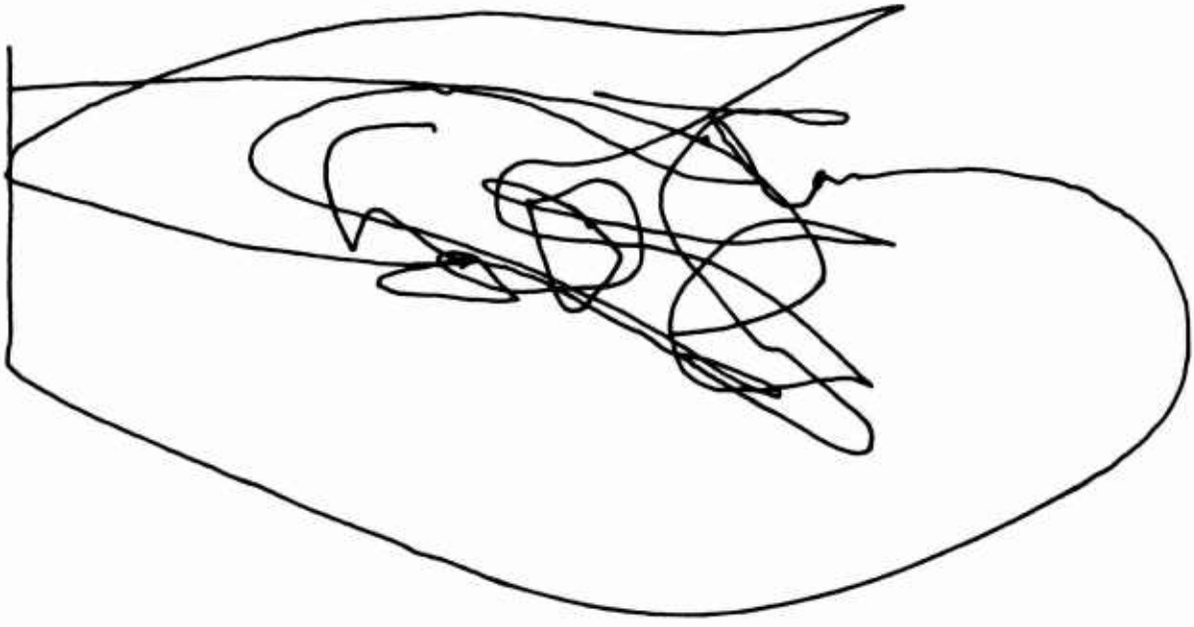

Figure 116. Piloted Hover Hold Task Control Type 5/1.

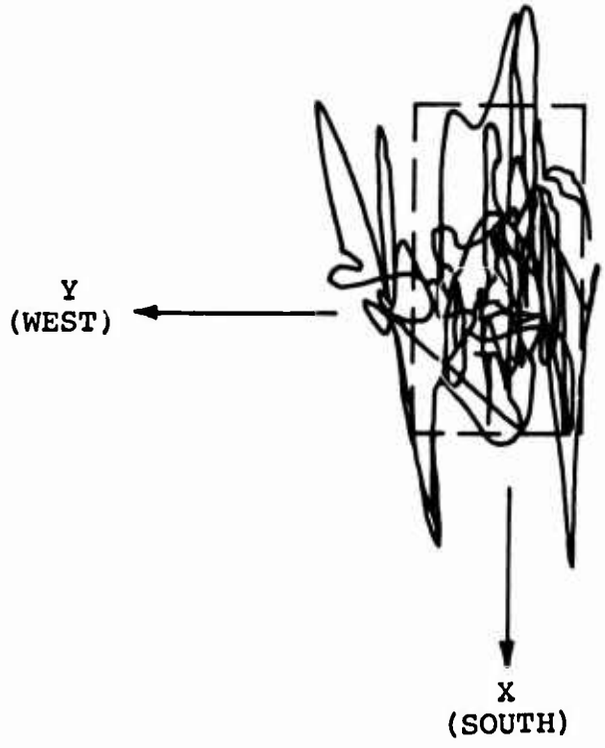

3 JULY 1973
RUN NO. 15

10 FPS NOMINAL
TURBULENCE LEVEL

COMPUTED RESULTS

$\bar{X}$ = -0.356 FT
σ_X = 0.645 FT
$\bar{y}$ = 0.103 FT
σ_y = 0.339 FT

$\bar{U}_g$ = 1.96 FPS
σ_{ug} = 10.81 FPS
$\bar{V}_g$ = -0.95 FPS
σ_{Vg} = 6.87 FPS

Figure 117. Piloted Hover Hold Task Control Type 5/1.

GROUND-BASED SIMULATOR EVALUATION AND ANALYTICAL RESULTS

The simulator results at 50,000 pounds gross weight are compared in this section with the analytical predictions described in ANALYTICAL STUDY OF ADVANCED TANDEM-ROTOR HELICOPTER (ATH) HOVER PERFORMANCE. The unpiloted (SAS-ON, PHS-ON) simulator results for hover hold performance are compared with the theoretical predictions at turbulence levels up to about 20.0 fps. The comparison is made in terms of standard duration position errors, with the inherent assumption that over a long duration of the hover hold task, the average drift is either small or nonexistent. The piloted results for hover position hold are compared on the same basis, with the additional comparison of how the actual pilot behaves compared to the theoretical, "optimal", pilot controller. The "optimal" pilot controller is defined here as that controller which performs with minimum at minimum position error at a total system damping ratio of 0.35. As will be seen from the simulator data, the real pilot does not always behave in this "optimal" fashion, but tends to adjust his equivalent transfer function with learning to the point of sacrificing stability for good performance, or searching for a comfortable work load at the sacrifice of performance. The pilot's Cooper-Harper rating changes are also compared for the selected control type combinations.

COMPARISON OF UNPILOTED HOVER PERFORMANCE

The aircraft performances with all automatic systems operational (SAS-ON, PHS-ON), but without active pilot control, are compared directly in Figure 118. The solid lines in this figure represent the theoretical, linear system estimates for longitudinal and lateral-directional aircraft position errors as a function of rms turbulence levels. Since the theoretical systems are linear, the errors vary linearly with the turbulence levels. The simulator data points are plotted directly on this figure. However, it must be pointed out that the simulator points have not been corrected for the drift due to a parallel digital integration of position error displayed, compared to the analog feedback error. As such, the simulator results will inherently show significantly larger errors, in a somewhat random fashion, with larger durations at higher turbulence levels. As seen from Figure 118, the simulator results compare well with the theoretical predictions at normal turbulence levels (5.0 fps), but diverge somewhat at high turbulence levels.

COMPARISON OF PILOTED HOVER PERFORMANCE

The theoretical basis for piloted performance prediction during precise hover position hold (see Piloted Hover Hold Performance section for details) reduces the pilot transfer

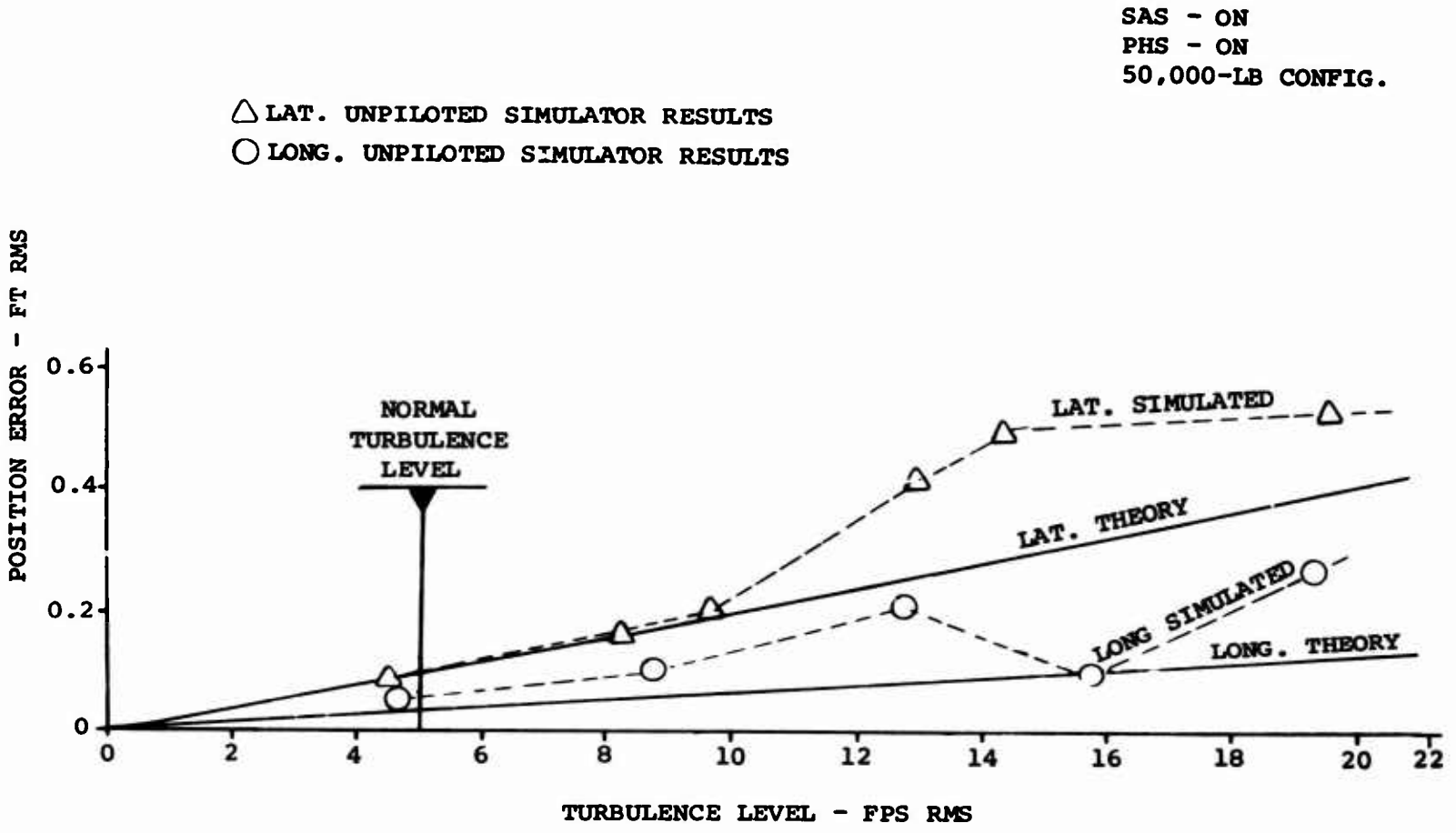

Figure 118. Unpiloted Hover Hold Performance Analysis and Simulator Results.

function variation to two basic parameters: the pilot anticipation factor (pilot lead time, T_L), representing his work load, and the pilot gain factor (K_p), denoting the pilot's stick motion per unit of observed position error. In the analysis, these two factors determine the actual closed-loop performance of the pilot and the aircraft. The theoretical pilot is treated as an "optimal" controller in the sense that the pilot will try to adjust his lead time and gain factor so as to minimize the aircraft position while still maintaining the total (closed-loop pilot and aircraft) system damping in the principal control mode at a comfortable level. In most of the references dealing with the study of pilot dynamics, this total system damping level is found to be in the neighborhood of 0.35 damping ratio. For a given control type, the analytical results may be summarized in the form of typical maps such as the one shown schematically in Figure 119. This map defines the total pilot-aircraft, closed-loop system characteristics plotted in terms of constant damping ratio and position error (for a given level of turbulence) contours plotted versus pilot lead time and gain factor. The solid curves indicate the closed-loop system damping ratio contours; the dashed curves denote the closed-loop system position errors for a constant turbulence level. For this particular control type, the "optimal" pilot controller should operate in the designated cross-hatched area where the position error is about 0.2 ft rms and the total system damping ratio is 0.35. Operation in the upper right-hand side of this area denotes regions of good performance with high work load (high pilot lead time). Operations in the lower right-hand region represent good performance with lower than the "optimal" damping ratio. On the simulator, the real pilot will adjust his transfer function as he learns the system, until he strikes a balance between a satisfactory performance and the total system damping. Intuitively, one might expect the pilot to work in the regions of high damping when he begins to learn the system, and to sacrifice the damping levels as he becomes more confident of his control capability. Most of the initial runs with various control types tend to indicate the real pilot operation in the area denoted as "observed pilot performance". This is the region in which the total system damping remains constant with pilot gain adjustment, so the pilot is able to concentrate on error minimization with little change in work load.

The reduction and interpretation of piloted simulator hover hold performance follow this general line of thought. Once a particular form of pilot transfer function is assumed, time histories of position errors and stick motion can be used to calculate pilot parameters. By assuming that the pilot's neuromuscular lag and reaction time delay are constant, then pilot gain and lead can be calculated using a least-squares error technique. With time histories generated from the piloted simulation effort at Northrop, the data on the

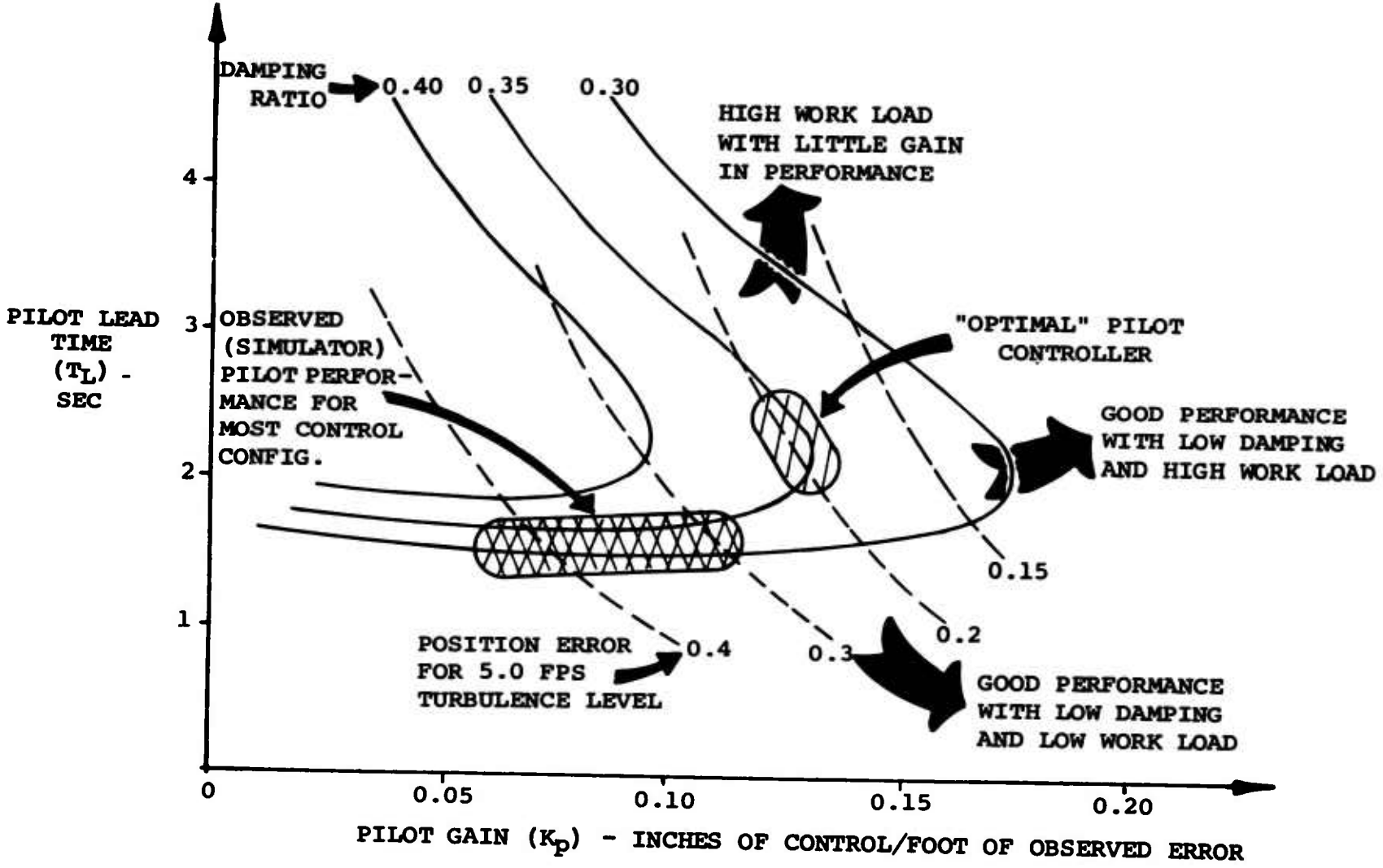

Figure 119. Schematic of Closed-Loop Pilot-Aircraft Hover Performance.

left-hand side of Tables XVI and XVII was calculated. It shows pilot gain and lead, root-mean-square gust, and root-mean-square position error. For comparison with theory, each combination of pilot gain, pilot lead, and gust level was inputted into the analytical model, and root-mean-square position error and modal damping were calculated. Also, the theoretically predicted optimums for pilot gain and lead for each configuration are shown.

Lateral Piloted Performance

At this time, certain results pertaining to the lateral axis have been reduced (see Table XVI). The agreement between simulator position errors and the corresponding analytically calculated position errors is, in general, quite good. Predicted optimum pilot gains also show good agreement. The optimum predicted leads are not bad for lateral control types 0 and 1; however, the predicted lead for control type 2 is considerably less than those calculated from simulator results. Certain conclusions will be drawn from the data presented in Table XVI, but it must be remembered that not all the simulator data has been reduced.

Looking at the one data point for the 0 type lateral control, the gain and lead show good agreement with predicted optimums. However, only one point has been reduced, and certain questions arise. Referring to Figure 73, the analytical results show that the pilot has chosen a gain below the optimum, which yields only about 25% modal damping with the lead chosen. Speculating on one data point, a preliminary conclusion may be that the pilot was still feeling the system out and had not yet determined its optimums. Indeed, the pilot did not fly this configuration for very long. More familiarization with this type of control might have led to increased performance, but the work load would have remained relatively high.

The data points for the lateral control type 1 show a gain variation which encompasses the predicted optimum. The pilot leads are, in general, slightly less than the predicted optimum. Referring to Figure 120, it shows that stability is relatively constant over a rather wide gain range for damping ratios of 35% and less. Therefore, as the pilot becomes more confident with the control type, he is able to increase his gain and decrease the stability level in an effort to minimize position error.

The simulator-generated position errors as a function of turbulence level for control type 1 are compared in Figure 121. It shows that the assumption of pilot performance in the region of constant system damping at a damping ratio slightly less than 0.35 gives an excellent correlation with the simulator results, although this is not the "optimal" controller operation point.

TABLE XVI. LATERAL PILOTED HOVER PERFORMANCE COMPARISON OF SIMULATOR-MEASURED AND ANALYTICALLY CALCULATED DATA

Gross Weight (lb)	Control Type	Simulator Data				Analytical Data				
						Actual Pilot Controller (Based on Simulator K_P and T_L)		"Optimal" Pilot Controller		
		σ_{v_g} Lateral Turbulence (fps)	K_P Pilot Gain (in./ft)	T_L Pilot Lead (sec)	σ_y Lateral Position Error (ft)	σ_y Lateral Position Error (ft)	Total System Damping Ratio	K_P (in./ft)	T_L (sec)	σ_y (ft)
50,000	Lateral (1)	8.56	0.22	0.69	0.52	0.60	0.287	0.30	1.0	0.43
		6.87	0.30	1.27	0.34	0.31	0.474			0.34
		13.96	0.24	0.59	0.87	0.95	0.234			0.7
		13.95	0.40	0.23	0.65	1.02	0.045			0.7
	Lateral (1)	20.87	0.31	0.54	1.36	1.18	0.191	0.30	1.0	1.04
	Lateral (2)	8.57	0.13	1.88	0.57	0.58	0.413	0.08	0.50	1.03
		16.22	0.09	2.35	1.18	1.49	0.510			1.95
		17.45	0.08	2.78	1.89	1.73	0.511			2.09
	Lateral (2)	-	0.11	2.48	1.20	-	0.425	0.08	0.50	-
50,000	Lateral (0)	-	0.16	1.69	1.54	-	0.261	0.20	1.50	-

TABLE XVII. LONGITUDINAL PILOTED HOVER PERFORMANCE COMPARISON OF SIMULATOR-MEASURED AND ANALYTICALLY CALCULATED DATA

		Simulator Data				Analytical Data				
						Actual Pilot Controller (Based on Simulator K_P and T_L)		"Optimal" Pilot Controller		
Gross Weight (lb)	Control Type	σ_{u_g} Longitudinal Turbulence (fps)	K_P Pilot Gain (in./ft)	T_L Pilot Lead (sec)	σ_x Longitudinal Position Error (ft)	σ_x Longitudinal Position Error (ft)	Total System Damping Ratio	K_P (in./ft)	T_L (sec)	σ_y (ft)
50,000	Longitudinal (2)	4.80	0.03	1.29	6.18	5.94	0.150	0.11	3.0	1.20
↕	Longitudinal (1)	4.39	0.04	0.87	1.13	1.76	0.108	0.12	2.0	0.35
↕	Longitudinal (5)	4.45	0.08	0.38	0.43	0.46	0.670	0.22	0.75	0.21
↕	↕	10.81	0.11	0.28	0.65	0.85	0.543	↕	↕	0.46
↕	↕	14.21	0.19	0.09	0.95	0.81	0.259	↕	↕	0.60
50,000	Longitudinal (5)	14.05	0.14	0.01	0.68	0.99	0.345	0.22	0.75	0.59

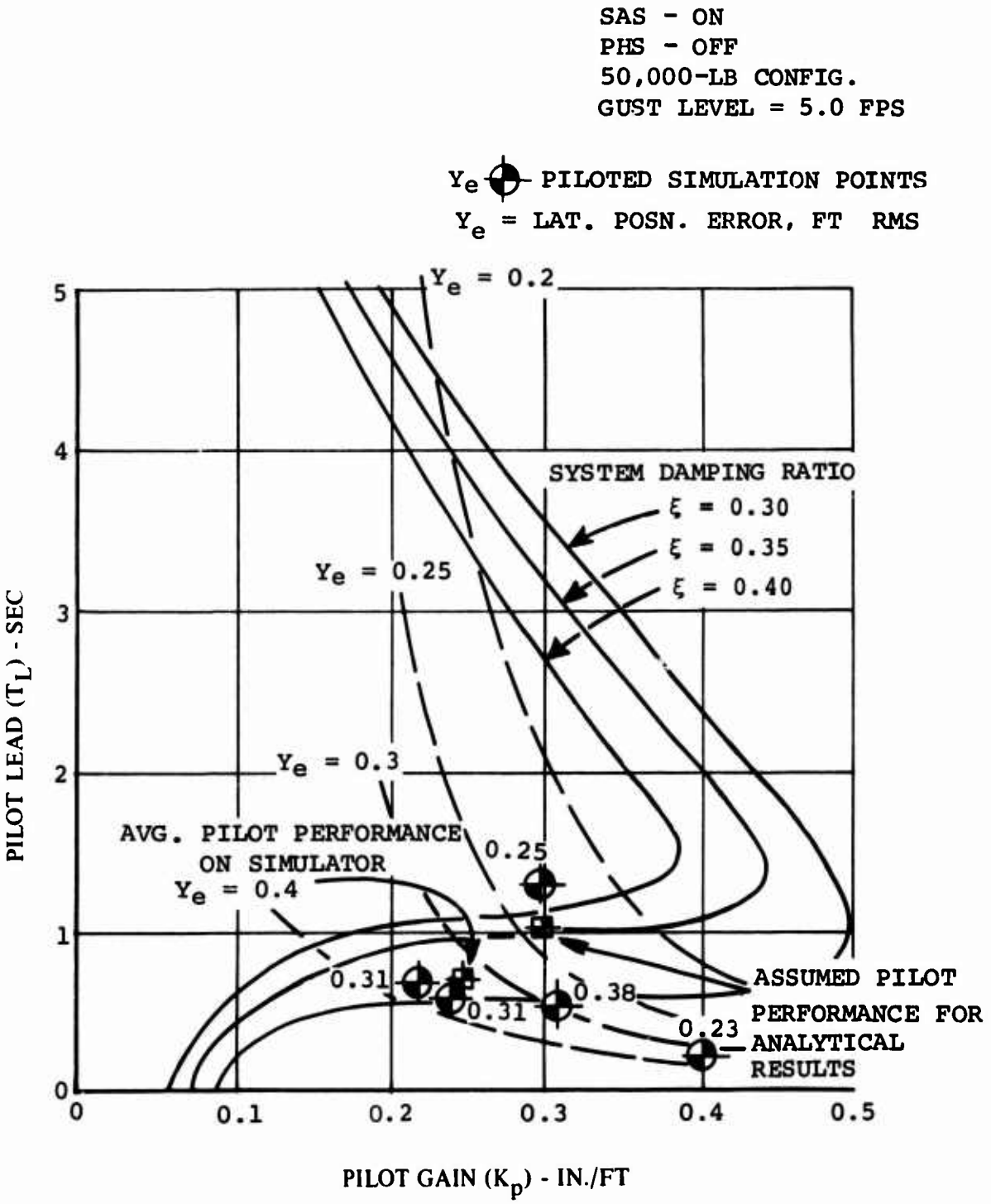

Figure 120. Lateral-Directional Piloted Performance Analysis and Simulation Results Control Type 1.

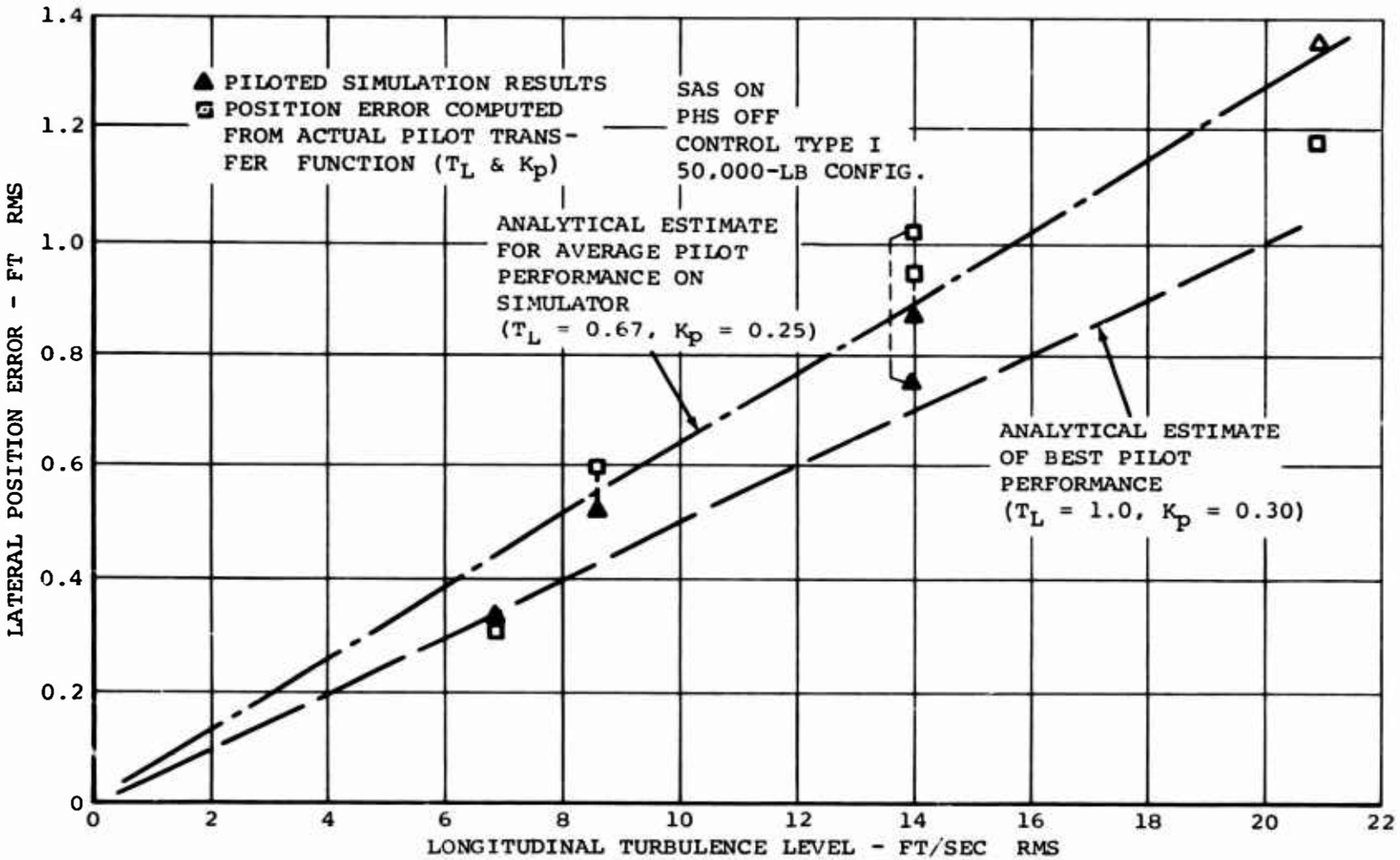

Figure 121. Lateral-Directional Piloted Performance Analysis and Simulation Results.

Finally, looking at control type 2, the simulator pilot gains show good agreement with the predicted optimum. However, the pilot leads generated by the pilot on the simulator are considerably higher than the predicted optimum. Referring to Figure 122, the stability sensitivity of the position mode is high with respect to pilot gain. In other words, small changes in pilot gain cause rather large stability changes, as measured by modal damping. In predicting an optimum, it was assumed that such a system would encourage the pilot to sacrifice some performance in order to minimize lead; thus, instead of predicting a pilot gain of 0.16 and pilot lead of 2.25, a pilot gain of 0.08 and a lead of 0.5 were chosen. In comparison with the simulator results, the gain predicted looked good, but the pilot chose to create a larger lead. This higher lead at this gain yielded higher damping ratios, 45% to 50% critical. With more familiarization with the control type, the pilot may have relaxed his stability criteria and either increased his gain for increased performance, decreased his lead for decreased work load, or both.

Longitudinal Piloted Performance

The tabulated results for longitudinal piloted performance are shown in Table XVII. The analytical predictions based on the "optimal" controller operation show the same trends as the simulator results; the best performance is obtainable with control type 5 and the poorest with control type 2 (pure DCP control), with control type 1 in the middle. The computed position errors based on actual simulator results for pilot lead and pilot gain are generally in agreement.

The comparative results for control type 5 are examined in detail in Figures 123 and 124. Several data points are available for this control type, so the following comparison is valid. The position errors in terms of turbulence levels (Figure 123) indicate that the "optimal" pilot controller predicts the best operation capability, which is much better than the average attained by the pilot from the simulator evaluation. In Figure 124, this discrepancy is revealed to be the result of the different real-pilot operation from the theoretical "optimal". On the average, the real pilot performed in the area of good damping but with very little work load (T_L = 0.4 second). It is conceivable that the pilot chose this region because the total system's damping level gradient is relatively steep for this control type, but good performance can be obtained even with no pilot lead requirement.

Pilot Rating Summary

The pilot ratings for different control types obtained from the simulator evaluation are based on only one pilot's opinion, who had a limited time available for evaluating the different

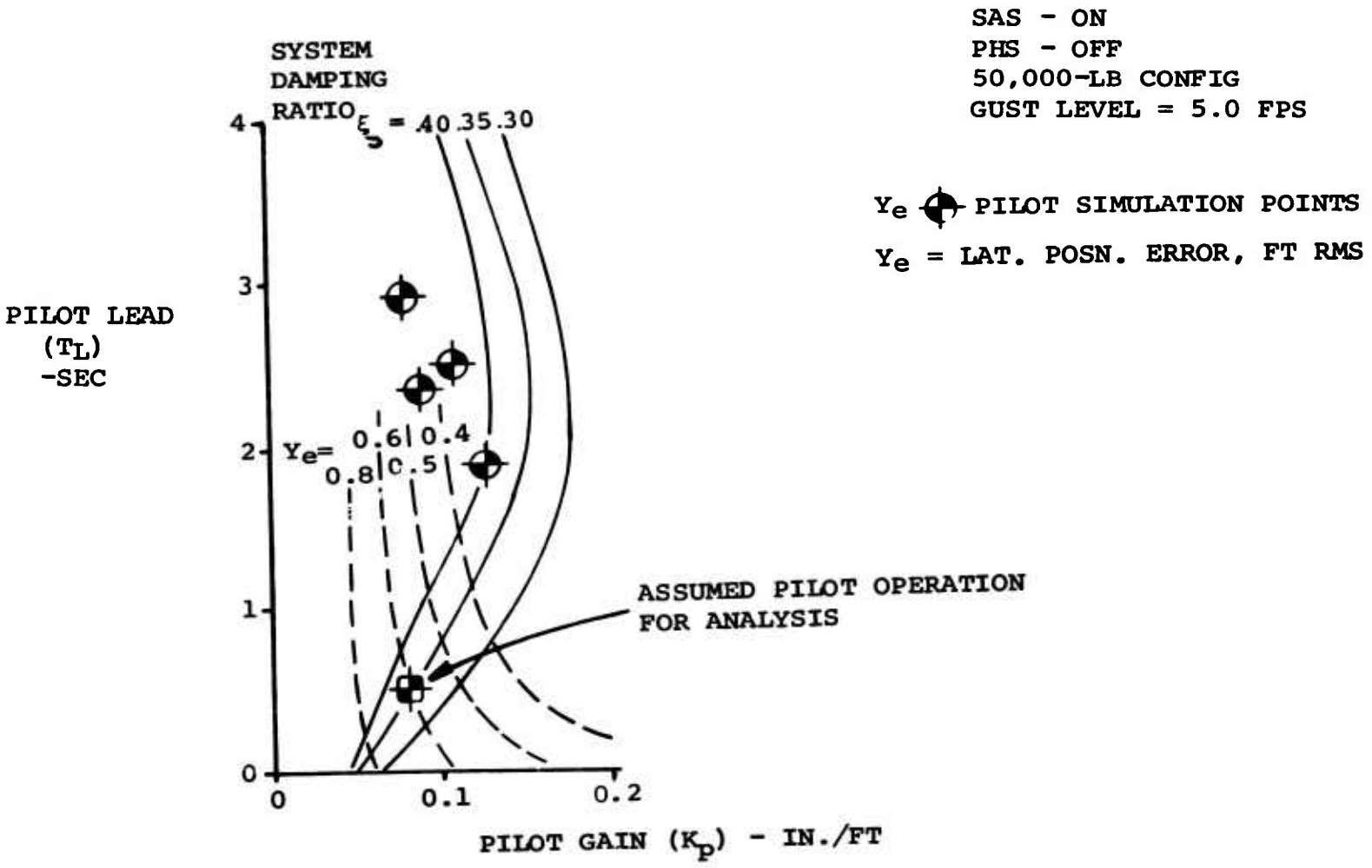

Figure 122. Lateral-Directional Piloted Performance Analysis and Simulation Results Control Type 2.

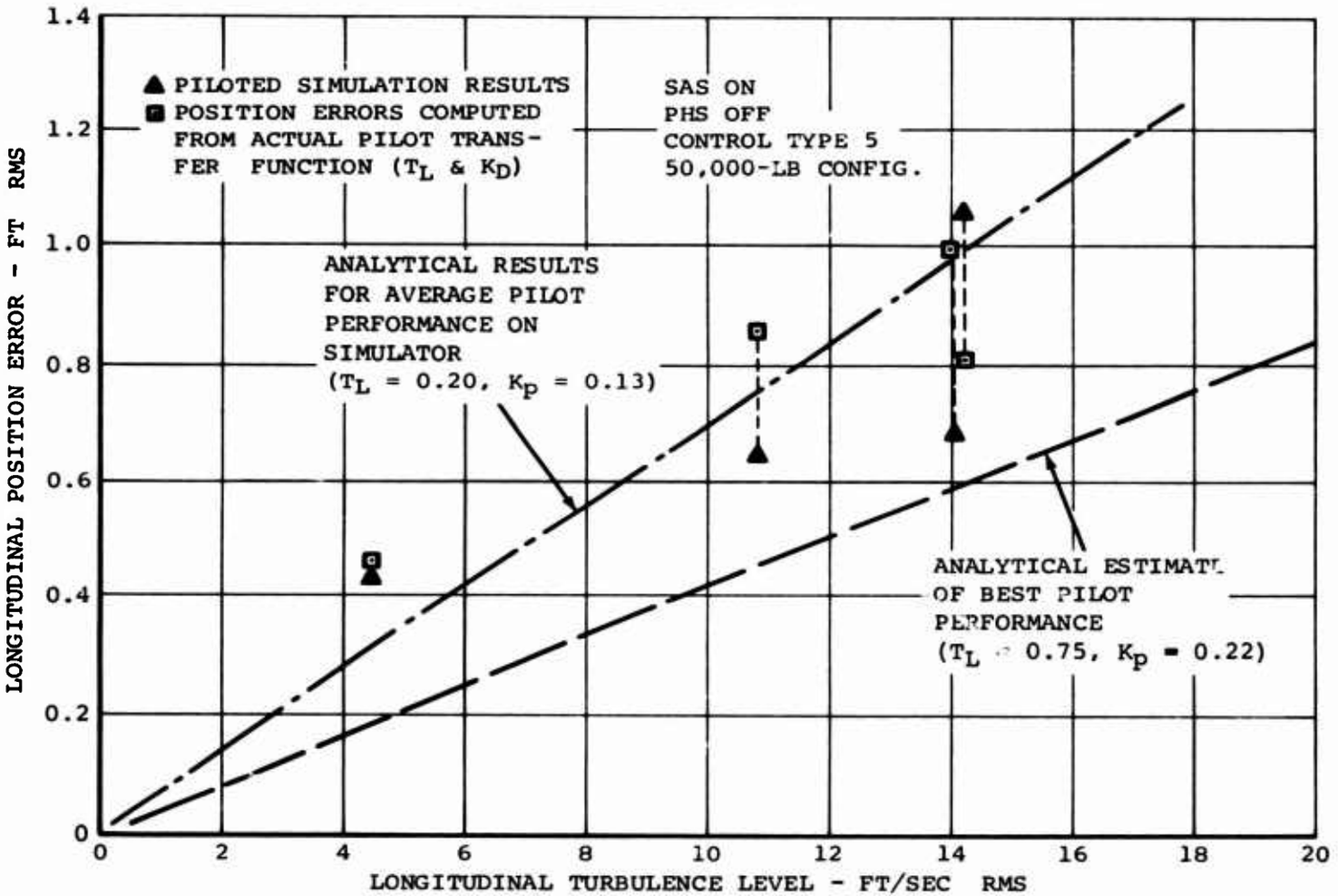

Figure 123. Longitudinal Piloted Hover Hold Performance Analysis and Simulation Results.

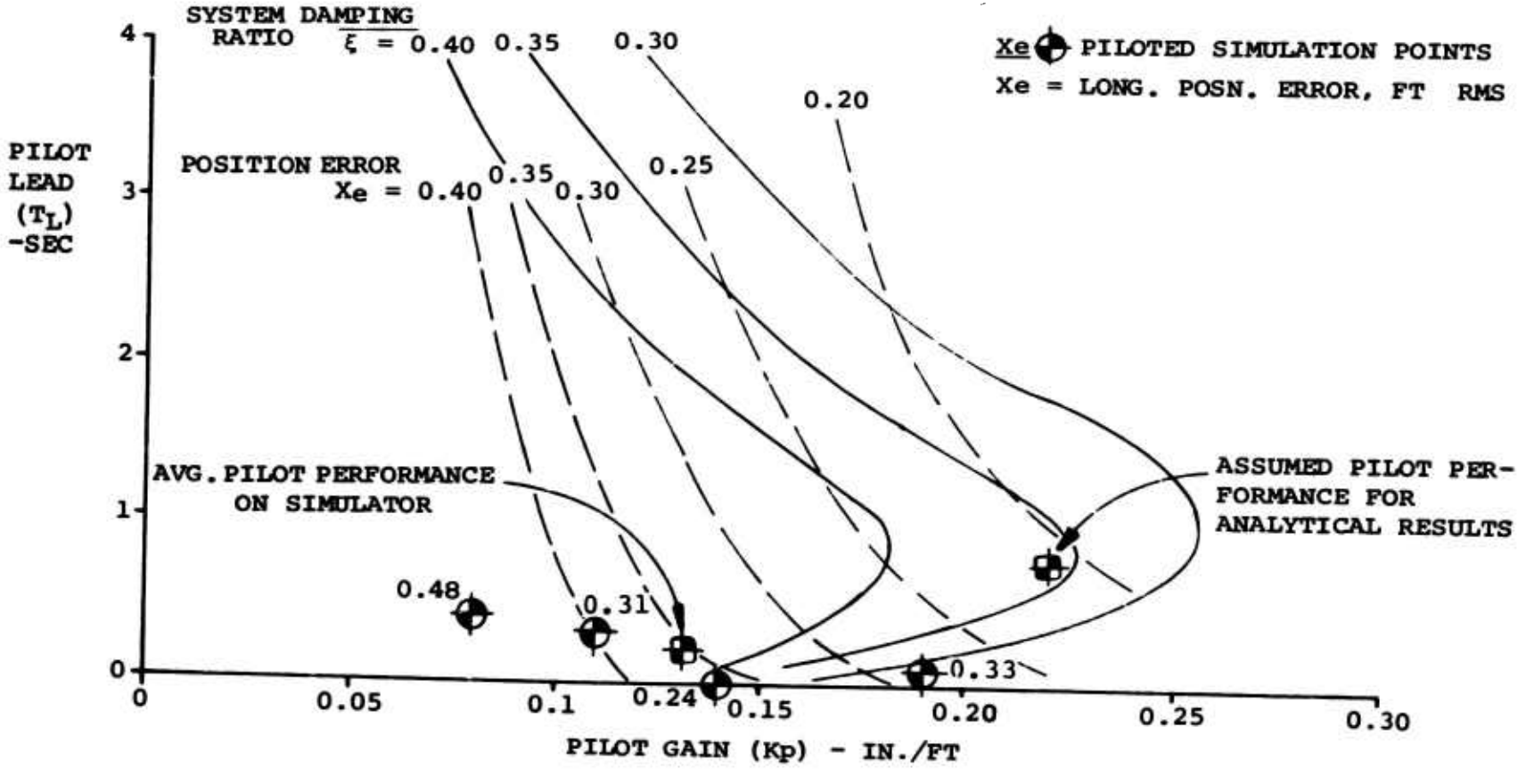

Figure 124. Longitudinal Piloted Hover Performance Analysis and Simulation Results Control Type 5.

systems. In addition, the limited scope display (± 5.0) made the pilot apprehensive during operations with the relatively poor control configurations, because of the tendency for the display to run rapidly off the scope. However, several important points may be noted upon examination of the pilot's Cooper-Harper ratings shown in Table XVIII. First, the baseline PHS and the control combination 5/1 were rated by the pilot as equal. This is in agreement with the analytical predictions. Second, the least acceptable control was the 2/0 combination, representing pure DCP control combined with roll acceleration. This is also in agreement with the theory, although the absolute magnitude of predicted rating changes is considerably smaller than that obtained from the real pilot. As was indicated before, the main apparent reason was disagreement in the absolute magnitudes, which stems from the fact that the pilot does not behave exactly like the theoretical optimal controller. In addition, he becomes concerned when the display has limited displacement capabilities and tends to rate the poorer systems lower, sometimes uncontrollable, because once he loses the display, he is not able to locate it and bring it back within the visible scope area.

GENERAL ASSESSMENT OF GROUND-BASED SIMULATOR RESULTS

Conclusions Based on Present Data

Two basic conclusions were reached. The first is that velocity feedback is desirable in that it relaxes the need for the pilot to create large leads. The velocity feedback thus reduces the pilot's work load and improves his ratings of the system. The other conclusion deals with the part that system stability plays in influencing the pilot's choice in compensation. This relates also to the pilot's learning curve. If the stability of the system changes rapidly with pilot gain or lead, then the pilot will tend to choose his parameters such as to close the position loop with rather significant damping (data reduced to date shows damping ratios in the order of 50%). On the other hand, if stability remains fairly constant with pilot gain, for instance, then the pilot will tend to operate at a lower stability level if it yields greater performance. Also, as the pilot becomes more confident in the system, he will tend to push the system to its limits if performance is improved. As stated earlier, the task is of primary concern in selection of pilot compensation, with stability characteristics playing a key secondary role.

TABLE XVIII. PILOT RATING OF CONTROL TYPES

Control Type Longitudinal/Lateral	Cooper-Harper Rating Simulator Results	Change in Pilot C-H Rating With Respect to PHS Baseline		
		Simulator Results	Analytical Predictions	
			"Optimal" Controller	Average Pilot Controller
PHS (Baseline)	3.0	0	0	0
5/1	3.0	0	0	0/0.5
1/2 (Full Sensitivity)	5.0	2.0	1.5/0	1.5/2.0
1/2 (½ x Longitudinal Sensitivity)	4.0	1.0	1.5/0	1.5/2.0
1/0	7.0-8.0(1)	4.0-5.0	1.5/1.0	1.5/2.0
2/0	8.0(1)	5.0	2.5/1.0	
1/1	6.0	3.0	1.5/0	

(1) The pilot rated these systems very low because of limited display motion (± 5.0 ft). The display moved off the screen too rapidly and he often was unable to reposition the display back to the scaled position.

CONCLUSIONS

The following conclusions are derived from the studies conducted during this program:

1. The tandem-rotor helicopter configurations in the VHLH class can be configured so that their hover hold performance is similar to (or directly scalable from) the existing MLH class. In particular, the control system configurations, required for precise automatic hover position hold and pilot control, can be synthesized from the MLH applicable designs and related experience. The singular exception to this rule might be in the rotor-induced coupled elastic fuselage and blade lead-lag modes. Special filtering might be required to preclude an undesirable aggravation of these low damping modes by the cyclic control feedbacks.

2. The pilot acceptance (rating) level is primarily a function of the automatic control and hover hold functions, and does not appear to be strongly dependent on the gross weight configuration of the augmented stability aircraft.

3. The best hover performance (position hold) capabilities, within the scope of the control augmentation types considered here, are offered by the longitudinal cyclic pitch (LCP) control on the stick, combined with the conventional roll control to give essentially a velocity control system in the horizontal axes. Pilot work load, and consequently pilot rating, is improved if inertial velocity feedback is included in the stability augmentation system. However, such systems are inherently sensitive to the turbulence, and their total position hold capabilities will degrade with the turbulence level. An improvement over the velocity control system, in case of precise hover hold tasks, will be a positive position command system.

4. The least desirable and the least effective control capabilities are those which employ pure attitude control, such as are typical of the differential collective pitch controlled tandem-rotor helicopters or conventional single-rotor aircraft.

5. The simulator model (Reference 5), which is presently used for HLH prototype work, has good response fidelity at all normal operating flight conditions, as evidenced by the response comparison with Model 347 flight response data. The model, including the simplified

representation of the external load equations (Reference 5), should be entirely satisfactory for the simulator evaluation tasks of this contract.

6. The results for the piloted simulator evaluation of the hover performance task in general confirm the validity of the analytical approach for defining the relative performance capability of various control augmentation modes. In absolute performance terms (RMS, or standard deviation of the aircraft position error), the analysis predicts well the best pilot performance capability for any specific augmentation system. On the simulator, the real pilot will approach this performance level only with sufficient practice. On the average, the pilot seems to choose a performance point in which the total (pilot-aircraft) system damping level is nearly constant with pilot gain, rather than the "optimal" point (defined by 0.35 damping ratio at minimum position error).

LITERATURE CITED

1. Seckel, Edward, STABILITY AND CONTROL OF AIRPLANES AND HELICOPTERS, Academic Press, New York, 1964.

2. LONGITUDINAL HANDLING QUALITIES FOR HOVERING, Report No. 594, Department of Aeronautical Engineering, Princeton University, Princeton, N.J.

3. A NEW APPROACH TO THE SPECIFICATION AND EVALUATION OF FLYING QUALITIES, AFFDL-TR-69-120.

4. PILOT DYNAMICS AND AIRCRAFT HANDLING QUALITIES, AIAA Professional Study Series.

5. Cogan, C., Gajkowski, B. J., and Garnett, T. S., FULL FLIGHT ENVELOPE MATH MODEL FOR 347/HLH CONTROL SYSTEM ANALYSIS, Boeing Vertol Report D301-10148-1, July 1972.

6. A METHOD FOR OBTAINING AIRCRAFT MODES SHAPES AND STABILITY CHARACTERISTICS WITH AN APPLICATION TO TANDEM ROTOR HELICOPTERS, Boeing Vertol Report Aero Inv. III-304, January 1966.

APPENDIX I
FULL-FORCE EXTERNAL LOAD MODEL

ELASTIC AND INEXTENSIBLE CABLE FORMULATION FOR A TWO-POINT SUSPENSION SYSTEM

The method presented here enables the evaluation of helicopter and external load accelerations at any instant in time, given the following information:

$\dot{X}_{BH}$, $\dot{Y}_{BH}$, $\dot{Z}_{BH}$	Helicopter body axis velocities
p_H, q_H, r_H	Helicopter body axis rotational rates
Φ_H, θ_H, Ψ_H	Helicopter euler orientation angles
$\dot{X}_{BL}$, $\dot{Y}_{BL}$, $\dot{Z}_{BL}$	External load body axis velocities
p_L, q_L, r_L	External load body axis rotational rates
Φ_L, θ_L, Ψ_L	External load euler orientation angles
γ_1, γ_2	Forward cable angles relative to inertia axes
γ_2, γ_4	Aft cable angle relative to inertia axes
Q_i's	Forces and moments on helicopter and external load, including gravity

The following is a list of physical constants used in the calculations:

m_H	Mass helicopter
I_{XX_H}, I_{YY_H}, I_{ZZ_H}, I_{XZ_H}	Helicopter inertias relative to body axes
m_L	Mass of external load
I_{XX_L}, I_{YY_L}, I_{ZZ_L}, I_{XZ_L}	External load inertias relative to body axes

h_{X_1}, h_{Y_1}, h_{Z_1}	Location of forward hook in helicopter body axis coordinates
h_{X_2}, h_{Y_2}, h_{Z_2}	Location of aft hook in helicopter body axis coordinates
e_{X_1}, e_{Y_1}, e_{Z_1}	Location of forward sling and load attachment point in external load body axis coordinates
e_{X_2}, e_{Y_2}, e_{Z_2}	Location of aft sling and load attachment point in external load body axis coordinates
L_1	Length of forward sling
L_2	Length of aft sling

DERIVATION OF EXTERNAL LOAD EQUATIONS

Inextensible Cables

If a dynamical system can be described by a Lagrangian L (q_m, $\dot{q}_m$, t) involving f coordinates, and if k constraints Φ_s (q_1, q_2, . . ., q_m, t) = 0 are imposed, then the Lagrangian equations of motion can be written as

$$\frac{d}{dt}\left(\frac{\partial L}{\partial \dot{q}_M}\right) - \left(\frac{\partial L}{\partial q_M}\right) = Q_{q_M} + \sum_{s=1}^{k} \lambda_s(t) \left(\frac{\partial \Phi_s}{\partial q_M}\right)$$

The $\lambda_s(t)$'s are unknown functions of t, usually referred to as Lagrangian multipliers. The f equations of motion described above, plus the k constraint equations, provide a system of (f + k) equations in (f + k) unknowns. The constraint equations can be written in dynamical form as

$$\sum_{M=1}^{f} \left(\frac{\partial \Phi_s}{\partial q_M}\right) \dot{q}_M + \frac{\partial \Phi_s}{\partial t} = 0$$

For the system at hand, we chose the normal six-degree-of-freedom coordinates for the helicopter and external load. These plus two constraint equations representing the constraints imposed by the two slings result in a system of 14 equations.

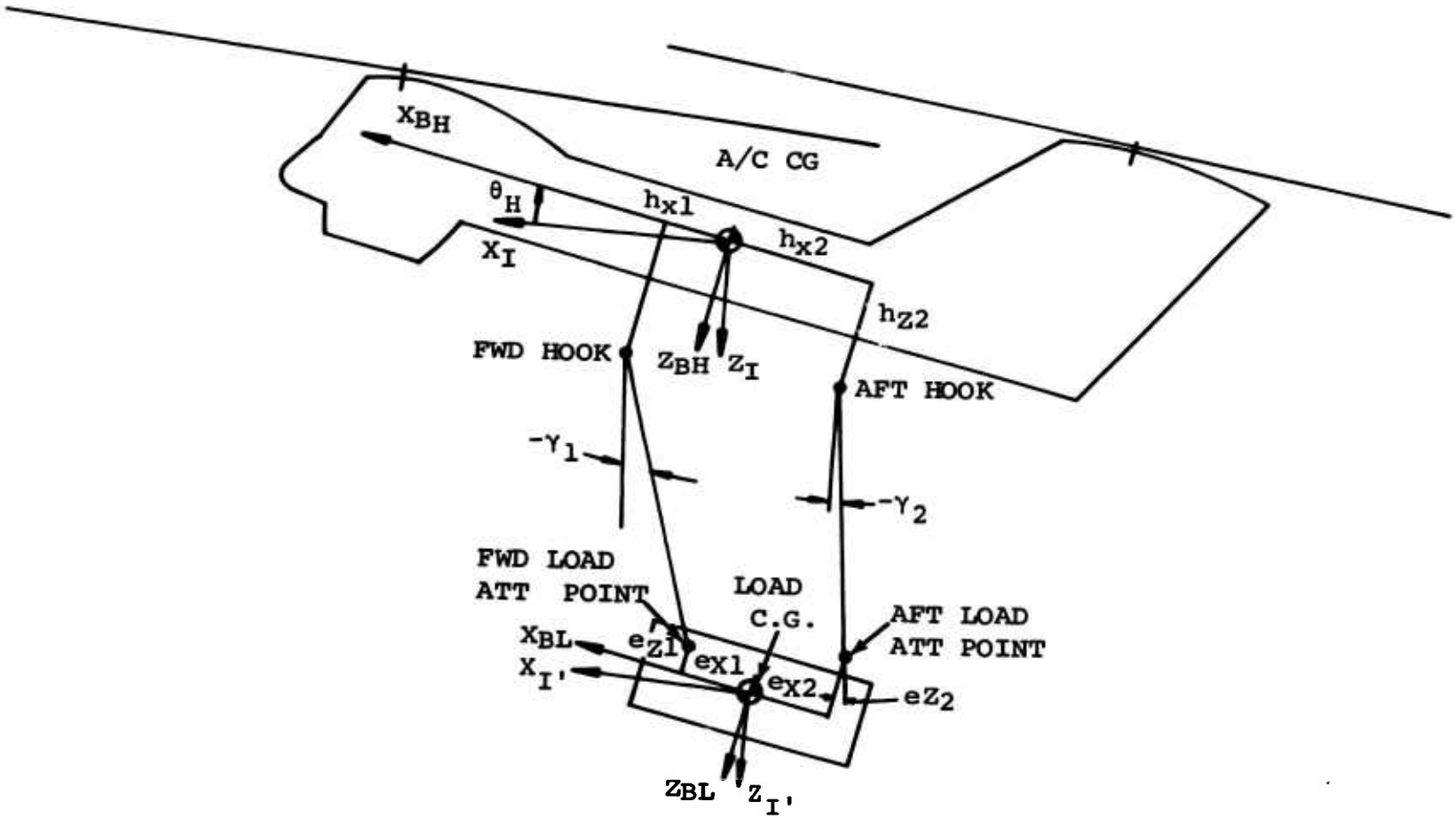

NOTE: 1. (X_I', Y_I', Z_I') ARE PARALLEL TO OUR FIXED INERTIAL AXES (X_I,Y_I,Z_I)

2. h_{x2}, e_{x2}, AND e_{Z2} ARE NEGATIVE AS SHOWN

Figure 125. Full Force External Load Model.

Writing the normal six-degree-of-freedom equations for the rigid-body helicopter as

$$m_H \ddot{X}_{BH} = Q_{XBH} + a_{11} \lambda_1 + a_{12} \lambda_2 \tag{1}$$

$$m_H \ddot{Y}_{BH} = Q_{YBH} + a_{21} \lambda_1 + a_{22} \lambda_2 \tag{2}$$

$$m_H \ddot{Z}_{BH} = Q_{ZBH} + a_{31} \lambda_1 + a_{32} \lambda_2 \tag{3}$$

$$I_{XX_H} \dot{p}_H - I_{XZ_H} \dot{\Gamma}_H = Q'_{p_H} + a_{41} \lambda_1 + a_{42} \lambda_2 \tag{4}$$

$$I_{YY_H} \dot{q}_H = Q'_{q_H} + a_{51} \lambda_1 + a_{52} \lambda_2 \tag{5}$$

$$I_{ZZ_H} \dot{\Gamma}_H - I_{XZ_H} \dot{p} = Q'_{\Gamma_H} + a_{61} \lambda_1 + a_{62} \lambda_2 \tag{6}$$

and a similar set of equations for the external load as

$$m_L \ddot{X}_{BL} = Q_{XBL} + a_{71} \lambda_1 + a_{72} \lambda_2 \tag{7}$$

$$m_L \ddot{Y}_{BL} = Q_{YBL} + a_{81} \lambda_1 + a_{82} \lambda_2 \tag{8}$$

$$m_L \ddot{Z}_{BL} = Q_{ZBL} + a_{91} \lambda_1 + a_{92} \lambda_2 \tag{9}$$

$$I_{XX_L} \dot{p}_L - I_{XZ_L} \dot{\Gamma} = Q'_{p_L} + a_{101} \lambda_1 + a_{102} \lambda_2 \tag{10}$$

$$I_{YY_L} \dot{q}_L = Q'_{q_L} + a_{111} \lambda_1 + a_{112} \lambda_2 \tag{11}$$

$$I_{ZZ_L} \dot{\Gamma}_L - I_{XZ_L} \dot{p}_L = Q'_{\Gamma_L} + a_{121} \lambda_1 + a_{122} \lambda_2 \tag{12}$$

the physical significance of λ_1 and λ_2 is that they represent the tensions in the forward and aft slings exerted through the constraint equations. The a_{ij}'s represent the direction cosines of the cables and relate directly to the two constraint equations. To develop these two constraint equations, we observe the relative motion of the helicopter hook and external load attachment point. Expressing this relative motion between forward hook and forward attachment point in inertia coordinates, using rigid-body motions of the helicopter and load, we obtain

$$\dot{R}_{XI_1} = A_{XX_L} V_{X_{L_1}} + A_{XY_L} V_{Y_{L_1}} + A_{XZ} V_{Z_{L_1}}$$

$$- A_{XX_H} V_{XH_1} - A_{XY_H} V_{Y_{H_1}} - A_{XZ_H} V_{Z_{H_1}} \quad (13)$$

$$\dot{R}_{YI_1} = A_{YX_L} V_{XL_1} + A_{YY_L} V_{Y_{L_1}} + A_{YZ_L} V_{Z_{L_1}}$$

$$- A_{YX_H} V_{XH_1} - A_{YY_H} V_{Y_{H_1}} - A_{YZ_H} V_{Z_{H_1}} \quad (14)$$

$$\dot{R}_{ZI_1} = A_{ZX_L} V_{XL_1} + A_{ZY_L} V_{Y_{L_1}} + A_{ZZ_L} V_{Z_{L_1}}$$

$$- A_{ZX_H} V_{XH_1} - A_{ZY_H} V_{Y_{H_1}} - A_{ZZ_H} V_{Z_{H_1}} \quad (15)$$

We can also describe this relative motion in terms of two angles and the distance between hook and attachment point. If we use as the vector the straight line joining the hook and the attachment, with the direction pointing toward the attachment point, then γ_3 will be the angle through which this vector is rotated in order that it lies in the X-Z inertia plan, and γ_1 will be the angle to rotate this X-Z projection onto the Z inertia axis. Finally, L_1 will represent the magnitude of the vector.

With these definitions, we can write the components (in inertia axes) of this vector as

$$R_{XI_1} = L_1 \cos \gamma_3 \sin \gamma_1 \quad (16)$$

$$R_{YI_1} = L_1 \sin \gamma_3 \quad (17)$$

$$R_{ZI_1} = L_1 \cos \gamma_3 \cos \gamma_1 \quad (18)$$

NOTE: Positive γ_1 and γ_3 are such that the attachment point is to the right and forward of the hook.

We can now differentiate this vector to yield

$$\dot{R}_{XI_1} = \dot{L}_1 \cos \gamma_3 \sin \gamma_1 + L_1 \dot{\gamma}_1 \cos \gamma_3 \cos \gamma_1$$

$$- L_1 \dot{\gamma}_3 \sin \gamma_3 \sin \gamma_1 \quad (19)$$

$$\dot{R}_{YI_1} = \dot{L}_1 \sin \gamma_3 + L_1 \dot{\gamma}_3 \cos \gamma_3 \tag{20}$$

$$\dot{R}_{ZI_1} = \dot{L}_1 \cos \gamma_3 \cos \gamma_1 - L_1 \dot{\gamma}_1 \cos \gamma_3 \sin \gamma_1 - L_1 \dot{\gamma}_3 \sin \gamma_3 \cos \gamma_1 \tag{21}$$

Solving this set of equations for $\dot{\gamma}_1$, $\dot{\gamma}_3$, and $\dot{L}_1$, we get

$$\dot{L}_1 = \dot{R}_{XI1} \cos \gamma_3 \sin \gamma_1 + \dot{R}_{YI_1} \sin \gamma_3 + \dot{R}_{ZI_1} \cos \gamma_3 \cos \gamma_1 \tag{22}$$

$$\dot{\gamma}_3 = -(\dot{R}_{XI_1}/L_1)\sin \gamma_3 \sin \gamma_1 + (\dot{R}_{YI_1}/L_1) \cos \gamma_3 - (\dot{R}_{ZI_1}/L_1) \sin \gamma_3 \cos \gamma_1 \tag{23}$$

$$\dot{\gamma}_1 = (\dot{R}_{XI_1} \cos \gamma_1 - \dot{R}_{ZI_1} \sin \gamma_1)/L_1 \cos \gamma_3 \tag{24}$$

Substituting in our previous expressions for $\dot{R}_{XI_1}$, $\dot{R}_{YI_1}$ and $\dot{R}_{ZI_1}$ in terms of helicopter and external load motions, we now have the relative motion of the forward hook and forward load attachment point completely defined. To arrive at the first constraint equation, we assume that $\dot{L}_1 = 0$ (inelastic cable). Using this equation, we can arrive at our a_{ij}'s associated with the forward cable.

$$a_{11} = -A_{XX_H} \cos\gamma_3 \sin\gamma_1 - A_{YX_H} \sin\gamma_3 - A_{ZX_H} \cos\gamma_3 \cos\gamma_1$$

$$a_{21} = -A_{XY_H} \cos\gamma_3 \sin\gamma_1 - A_{YY_H} \sin\gamma_3 - A_{ZY_H} \cos\gamma_3 \cos\gamma_1$$

$$a_{31} = -A_{XZ_H} \cos\gamma_3 \sin\gamma_1 - A_{YZ_H} \sin\gamma_3 - A_{ZZ_H} \cos\gamma_3 \cos\gamma_1$$

$$a_{41} = -h_{Z_1} a_{21} + h_{Y_1} a_{31}$$

$$a_{51} = h_{Z_1} a_{11} - h_{X_1} a_{31}$$

$$a_{61} = -h_{Y_1} a_{11} + h_{X_1} a_{21}$$

$$a_{71} = A_{XX_L}\cos\gamma_3\sin\gamma_1 + A_{YX_L}\sin\gamma_3 + A_{ZX_L}\cos\gamma_3\cos\gamma_1$$

$$a_{81} = A_{XY_L}\cos\gamma_3\sin\gamma_1 + A_{YY_L}\sin\gamma_3 + A_{ZY_L}\cos\gamma_3\cos\gamma_1$$

$$a_{91} = A_{XZ_L}\cos\gamma_3\sin\gamma_1 + A_{YZ_L}\sin\gamma_3 + A_{ZZ_L}\cos\gamma_3\cos\gamma_1$$

$$a_{101} = -e_{Z_1}\, a_{81} + e_{Y_1}\, a_{91}$$

$$a_{111} = e_{Z_1}\, a_{71} + e_{X_1}\, a_{91}$$

$$a_{121} = -e_{Y_1}\, a_{71} + e_{X_1}\, a_{81} \qquad (25)$$

We can perform a similar analysis on the aft hook and aft attachment point. The results are similar, with the subscripts (1) and (3) replaced by (2) and (4), respectively. Thus, the a_{ij}'s associated with the aft cable are

$$a_{12} = -A_{XX_H}\cos\gamma_4\sin\gamma_2 - A_{YX_H}\sin\gamma_4 - A_{ZX_H}\cos\gamma_4\cos\gamma_2$$

$$a_{22} = -A_{XY_H}\cos\gamma_4\sin\gamma_2 - A_{YY_H}\sin\gamma_4 - A_{ZY_H}\cos\gamma_4\cos\gamma_2$$

$$a_{32} = -A_{XZ_H}\cos\gamma_4\sin\gamma_2 - A_{YZ_H}\sin\gamma_4 - A_{ZZ_H}\cos\gamma_4\cos\gamma_2$$

$$a_{42} = -h_{Z_2}\, a_{22} + h_{Y_2}\, a_{32}$$

$$a_{52} = h_{Z_2}\, a_{12} - h_{X_1}\, a_{32}$$

$$a_{62} = -h_{Y_2}\, a_{12} + h_{X_2}\, a_{22}$$

$$a_{72} = A_{XX_L}\cos\gamma_4\sin\gamma_2 + A_{YX_L}\sin\gamma_4 + A_{ZX_L}\cos\gamma_4\cos\gamma_2$$

$$a_{82} = A_{XY_L}\cos\gamma_4\sin\gamma_2 + A_{YY_L}\sin\gamma_4 + A_{ZY_L}\cos\gamma_4\cos\gamma_2$$

$$a_{92} = A_{XZ_L}\cos\gamma_4\sin\gamma_2 + A_{YZ_L}\sin\gamma_4 + A_{ZZ_L}\cos\gamma_4\cos\gamma_2$$

$$a_{102} = -e_{Z_2}\, a_{82} + e_{Y_2}\, a_{92}$$

$$a_{112} = e_{Z_2}\, a_{72} - e_{X_2}\, a_{92}$$

$$a_{122} = -e_{Y_2}\, a_{72} + e_{X_2}\, a_{82} \qquad (26)$$

In the above expressions for the a_{ij}'s, the A's represent components of euler transformations from body axes to inertia axes. They, along with the V's, are defined as follows:

$$A_{XX_L} = \cos\theta_L \cos\psi_L$$

$$A_{XY_L} = \sin\phi_L \sin\theta_L \cos\psi_L - \cos\phi_L \sin\psi_L$$

$$A_{XZ_L} = \cos\phi_L \sin\theta_L \cos\psi_L + \sin\phi_L \sin\psi_L$$

$$A_{YX_L} = \cos\theta_L \sin\psi_L$$

$$A_{YY_L} = \sin\phi_L \sin\theta_L \sin\psi_L + \cos\phi_L \cos\psi_L$$

$$A_{YZ_L} = \cos\phi_L \sin\theta_L \sin\psi_L - \sin\phi_L \cos\psi_L$$

$$A_{ZX_L} = -\sin\theta_L$$

$$A_{ZY_L} = \sin\phi_L \cos\theta_L$$

$$A_{ZZ_L} = \cos\phi_L \cos\theta_L$$

$$A_{XX_H} = \cos\theta_H \cos\psi_H$$

$$A_{XY_H} = \sin\phi_H \sin\theta_H \cos\psi_H - \cos\phi_H \sin\psi_H$$

$$A_{XZ_H} = \cos\phi_H \sin\theta_H \cos\psi_H + \sin\phi_H \sin\psi_H$$

$$A_{YX_H} = \cos\theta_H \sin\psi_H$$

$$A_{YY_H} = \sin\phi_H \sin\theta_H \sin\psi_H + \cos\phi_H \cos\psi_H$$

$$A_{YZ_H} = \cos\phi_H \sin\theta_H \sin\psi_H - \sin\phi_H \cos\psi_H$$

$$A_{ZX_H} = -\sin\theta_H$$

$$A_{ZY_H} = \sin\phi_H \cos\theta_H$$

$$A_{ZZ_H} = \cos\phi_H \cos\theta_H \tag{27}$$

$$V_{XL_1} = \dot{X}_{BL} + e_{Z_1} q_L - e_{Y_1} \Gamma_L$$

$$V_{YL_1} = \dot{Y}_{BL} + e_{X_1} \Gamma_L - e_{Z_1} P_L$$

$$V_{ZL_1} = \dot{Z}_{BL} + e_{Y_1} P_L - e_{X_1} q_L$$

$$V_{XL_2} = \dot{X}_{BL} + e_{Z_2} q_L - e_{Y_2} \Gamma_L$$

$$V_{YL_2} = \dot{Y}_{BL} + e_{X_2} \Gamma_L - e_{Z_2} P_L$$

$$V_{ZL_2} = \dot{Z}_{BL} + e_{Y_2} P_L - e_{X_2} q_L$$

$$V_{XH_1} = \dot{X}_{BH} + h_{Z_1} q_H - h_{Y_1} \Gamma_H$$

$$V_{YH_1} = \dot{Y}_{BH} + h_{X_1} \Gamma_H - h_{Z_1} P_H$$

$$V_{ZH_1} = \dot{Z}_{BH} + h_{Y_1} P_H - h_{X_1} q_H$$

$$V_{XH_2} = \dot{X}_{BH} + h_{Z_2} q_H - h_{Y_2} \Gamma_H$$

$$V_{YH_2} = \dot{Y}_{BH} + h_{X_2} \Gamma_H - h_{Z_2} P_H$$

$$V_{ZH_2} = \dot{Z}_{BH} + h_{Y_2} P_H - h_{X_2} q_H \tag{28}$$

The two constraint equations are in the form

$$\dot{L}_1 = 0 = a_{11}\dot{X}_{BH} + a_{21}\dot{Y}_{BH} + \ldots + a_{61}\Gamma_H + a_{71}\dot{X}_{BL} + a_{81}\dot{Y}_{BL} + \ldots + a_{121}\Gamma_L \tag{29}$$

$$\dot{L}_2 = 0 = a_{12}\dot{X}_{BH} + a_{22}\dot{Y}_{BH} + \ldots + a_{62}\Gamma_H + a_{72}\dot{X}_{BL} + a_{82}\dot{Y}_{BL} + \ldots + a_{122}\Gamma_L \tag{30}$$

To put these constraint equations in the form useful in solving the system, we differentiate them:

$$a_{11}\dot{X}_{BH} + a_{21}\dot{Y}_{BH} + \ldots = Q_{\lambda_1}$$

$$a_{12}\dot{X}_{BH} + a_{22}\dot{Y}_{BH} + \ldots = Q_{\lambda_2}$$

where

$$Q_{\lambda_1} = -\dot{a}_{11}\dot{X}_{BH} - \dot{a}_{21}\dot{Y}_{BH} - \ldots$$

$$Q_{\lambda_2} = -\dot{a}_{12}\dot{X}_{BH} - \dot{a}_{22}\dot{Y}_{BH} - \ldots$$

Now we are ready to solve the system of equations for helicopter accelerations, load accelerations, and our two unknown λ's. First, we modify our roll and yaw acceleration equations. These become

$$(I_{XX_H}I_{ZZ_H}-I^2_{XZ_H})\dot{p}_H = Q''_{p_H} + a'_{41}\lambda_1 + a'_{42}\lambda_2$$

$$(I_{XX_H}I_{ZZ_H}-I^2_{XZ_H})\dot{\Gamma}_H = Q''_{\Gamma_H} + a'_{61}\lambda_1 + a'_{62}\lambda_2$$

$$(I_{XX_L}I_{ZZ_L}-I^2_{XZ_L})\dot{p}_L = Q''_{p_L} + a'_{10,1}\lambda_1 + a'_{10,2}\lambda_2$$

$$(I_{XX_L}I_{ZZ_L}-I^2_{XZ_L})\dot{\Gamma}_L = Q''_{\Gamma_L} + a'_{12,1}\lambda_1 + a'_{12,2}\lambda_2$$

where

$$Q''_{p_H} = I_{ZZ_H}Q'_{p_H} + I_{XZ_H}Q'_{\Gamma_H}$$

$$Q''_{\Gamma_H} = I_{XX_H}Q'_{\Gamma_H} + I_{XZ_H}Q'_{p_H}$$

$$a'_{41} = I_{ZZ_H}a_{41} + I_{XZ_H}a_{61}$$

$$a'_{42} = I_{ZZ_H}a_{42} + I_{XZ_H}a_{62}$$

$$a'_{61} = I_{XX_H} a_{61} + I_{XZ_H} a_{41}$$

$$a'_{62} = I_{XX_H} a_{62} + I_{XZ_H} a_{42}$$

$$Q''_{P_L} = I_{ZZ_L} Q'_{P_L} + I_{XZ_L} Q'_{\Gamma_L}$$

$$Q''_{\Gamma_L} = I_{XX_L} Q'_{\Gamma_L} + I_{XZ_L} Q'_{P_L}$$

$$a'_{10,1} = I_{ZZ_L} a_{10,1} + I_{XZ_L} a_{12,1}$$

$$a'_{10,2} = I_{ZZ_L} a_{10,2} + I_{XZ_L} a_{12,2}$$

$$a'_{12,1} = I_{XX_L} a_{12,1} + I_{XZ_L} a_{10,1}$$

$$a'_{12,2} = I_{XX_L} a_{12,2} + I_{XZ_L} a_{10,2}$$

Our system of equations is now in a form whereby the application of an elimination-type algorithm will yield two simultaneous equations in λ_1 and λ_2.

$$\alpha_{11} \lambda_1 + \alpha_{12} \lambda_2 = F_1 \tag{31}$$

$$\alpha_{21} \lambda_1 + \alpha_{22} \lambda_2 = F_2 \tag{32}$$

where

$$\alpha_{11} = \alpha_{11_H} + \alpha_{11_L}$$

$$\alpha_{11_H} = \frac{(a_{11}^2 + a_{21}^2 + a_{31}^2)}{m_H} + \frac{(a_{41} a_{41}^1 + a_{61} a_{61}^1)}{I_{XX_H} I_{ZZ_H} - I_{XZ_H}^2} + \frac{a_{51}^2}{I_{YY_H}}$$

$$\alpha_{11_L} = \frac{(a_{71}^2+a_{81}^2+a_{91}^2)}{m_L} + \frac{(a_{10,1}a_{10,1}^1+a_{12,1}a_{12,1}^1)}{I_{XX_L}I_{ZZ_L}-I_{XZ_L}^2} + \frac{a_{11,1}^2}{I_{YY_L}}$$

$$\alpha_{12} = \alpha_{12_H} + \alpha_{12_L}$$

$$\alpha_{12_H} = \frac{(a_{11}a_{12}+a_{21}a_{22}+a_{31}a_{32})}{m_H} + \frac{(a_{41}a_{42}^1+a_{61}a_{62}^1)}{I_{XX_H}I_{ZZ_H}-I_{XZ_H}^2} + \frac{a_{51}a_{52}}{I_{YY_H}}$$

$$\alpha_{12_L} = \frac{(a_{71}a_{72}+a_{81}a_{82}+a_{91}a_{92})}{m_L} + \frac{(a_{10,1}a_{10,2}+a_{12,1}a_{12,2})}{I_{XX_L}I_{ZZ_L}-I_{XZ_L}} + \frac{a_{11,1}a_{11,2}}{I_{YY_L}}$$

$$F_1 = Q_{\lambda_1} - F_{1_H} - F_{1_L}$$

$$F_{1_H} = \frac{(a_{11}Q_{X_{BH}}+a_{21}Q_{Y_{BH}}+a_{31}Q_{Z_{BH}})}{m_H} + \frac{(a_{41}Q_{p_H}''+a_{61}Q_{\Gamma_H}'')}{I_{XX_H}I_{ZZ_H}-I_{XZ_H}^2} + \frac{a_{51}Q_{q_H}'}{I_{YY_H}}$$

$$F_{1_L} = \frac{(a_{71}Q_{X_{BL}}+a_{81}Q_{Y_{BL}}+a_{91}Q_{Z_{BL}})}{m_L} + \frac{(a_{10,1}Q_{p_L}''+a_{12,1}Q_{\Gamma_L}'')}{I_{XX_L}I_{ZZ_L}-I_{XZ_L}^2} + \frac{a_{11,1}Q_{q_L}'}{I_{YY_L}}$$

$$\alpha_{21} = \alpha_{21_H} + \alpha_{21_L}$$

$$\alpha_{21_H} = \frac{(a_{12}a_{11}+a_{22}a_{21}+a_{32}a_{31})}{m_H} + \frac{(a_{42}a_{41}^1+a_{62}a_{61}^1)}{I_{XX_H}I_{ZZ_H}-I_{XZ_H}^2} + \frac{a_{52}a_{51}}{I_{YY_H}}$$

$$\alpha_{21_L} = \frac{(a_{72}a_{71}+a_{82}a_{81}+a_{92}a_{91})}{m_L} + \frac{(a_{10,2}a^1_{10,1}+a_{12,2}a^1_{12,1})}{I_{XX_L}I_{ZZ_L}-I^2_{XZ_L}}$$

$$+ \frac{a_{11,2}a_{11,1}}{I_{YY_L}}$$

$$\alpha_{22} = \alpha_{22_H} + \alpha_{22_L}$$

$$\alpha_{22_H} = \frac{(a^2_{12}+a^2_{22}+a^2_{32})}{m_H} + \frac{(a_{42}a^1_{42}+a_{62}a^1_{62})}{I_{XX_H}I_{ZZ_H}-I^2_{XZ_H}} + \frac{a^2_{52}}{I_{YY_H}}$$

$$\alpha_{22_L} = \frac{(a^2_{72}+a^2_{82}+a^2_{92})}{m_L} + \frac{(a_{10,2}a^1_{10,2}+a_{12,2}a^1_{12,2})}{I_{XX_L}I_{ZZ_L}-I^2_{XZ_L}} + \frac{a^2_{11,2}}{I_{YY_L}}$$

$$F_2 = Q_{\lambda_2} - F_{Z_H} - F_{Z_L}$$

$$F_{2_H} = \frac{(a_{12}Q_{X_{BH}}+a_{22}Q_{Y_{BH}}-a_{32}Q_{Z_{BH}})}{m_H} + \frac{(a_{42}Q''_{p_H}+a_{62}Q''_{\Gamma_H})}{I_{XX_H}I_{ZZ_H}-I^2_{XZ_H}} + \frac{a_{52}Q'_{q_H}}{I_{YY_H}}$$

$$F_{2_L} = \frac{(a_{72}Q_{X_{B_L}}+a_{82}Q_{Y_{B_L}}+a_{92}Q_{Z_{B_L}})}{m_L} + \frac{(a_{10,2}Q''_{p_L}+a_{12,2}Q_{\Gamma_L})}{I_{XX_L}I_{ZZ_L}-I^2_{XZ_L}}$$

$$+ \frac{a_{11,2}Q'_{q_L}}{I_{YY_L}}$$

The solution is

$$\lambda_1 = (F_1\alpha_{22} - \alpha_{12}F_2)/(\alpha_{22}\alpha_{11} - \alpha_{12}\alpha_{21}) \qquad (33)$$

$$\lambda_2 = (\alpha_{11}F_2 - F_1\alpha_{21})/(\alpha_{11}\alpha_{22} - \alpha_{12}\alpha_{21}) \qquad (34)$$

Substitution of these values into the appropriate equations will enable us to solve for the unknown accelerations.

$$\ddot{X}_{B_H} = (Q_{X_{B_H}} + a_{11}\lambda_1 + a_{12}\lambda_2)/m_H$$

$$\ddot{Y}_{B_H} = (Q_{Y_{B_H}} + a_{21}\lambda_1 + a_{22}\lambda_2)/m_H$$

$$\ddot{Z}_{B_H} = (Q_{Z_{B_H}} + a_{31}\lambda_1 + a_{32}\lambda_2)/m_H$$

$$\dot{p}_H = (Q''_{p_H} + a^1_{41}\lambda_1 + a^1_{42}\lambda_2)/(I_{XX_H}I_{ZZ_H} - I^2_{XZ_H})$$

$$\dot{q}_H = (Q'_{q_H} + a_{51}\lambda_1 + a_{52}\lambda_2)/I_{YY_H}$$

$$\dot{r}_H = (Q''_{r_H} + a^1_{61}\lambda_1 + a^1_{62}\lambda_2)/(I_{XX_H}I_{ZZ_H} - I^2_{XZ_H})$$

$$\ddot{X}_{B_L} = (Q_{X_{B_L}} + a_{71}\lambda_1 + a_{72}\lambda_2)/m_L$$

$$\ddot{Y}_{B_L} = (Q_{Y_{B_L}} + a_{81}\lambda_1 + a_{82}\lambda_2)/m_L$$

$$\ddot{Z}_{B_L} = (Q_{Z_{B_L}} + a_{91}\lambda_1 + a_{92}\lambda_2)/m_L$$

$$\dot{p}_L = (Q''_{p_L} + a^1_{10,1}\lambda_1 + a^1_{10,2}\lambda_2)/(I_{XX_L}I_{ZZ_L} - I^2_{XZ_L})$$

$$\dot{q}_L = (Q'_{q_L} + a_{11,1}\lambda_1 + a_{11,2}\lambda_2)/I_{YY_L}$$

$$\dot{r}_L = (Q''_{r_L} + a^1_{12,1}\lambda_1 + a^1_{12,2}\lambda_2)/(I_{XX_L}I_{ZZ_L} - I^2_{XZ_L}) \qquad (35)$$

Now, since the helicopter body axes and also the external load body axes are rotating axes, the inputs into the integrators to yield translational velocities are

$$\dot{X}_{B_H} = \int (\ddot{X}_{B_H} - \dot{Z}_{B_H} q_H + \dot{Y}_{B_H} r_H)\, dt$$

$$\dot{Y}_{B_H} = \int (\ddot{Y}_{B_H} - \dot{X}_{B_H} r_H + \dot{Z}_{B_H} p_H)\, dt$$

$$\dot{Z}_{B_H} = \int (\ddot{Z}_{B_H} - \dot{Y}_{B_H} p_H + \dot{X}_{B_H} q_H)\, dt$$

$$\dot{X}_{B_L} = \int (\ddot{X}_{B_L} - \dot{Z}_{B_L}\, q_L + \dot{Y}_{B_L}\, \Gamma_L)\, dt$$

$$\dot{Y}_{B_L} = \int (\ddot{Y}_{B_L} - \dot{X}_{B_L}\, \Gamma_L + \dot{Z}_{B_L}\, P_L)\, dt$$

$$\dot{Z}_{B_L} = \int (\ddot{Z}_{B_L} - \dot{Y}_{B_L}\, P_L + \dot{X}_{B_L}\, q_L)\, dt \qquad (36)$$

Thus far, nothing has been said to adequately define the generalized forces (Q's). These shall be defined in the following ways:

$$Q_{X_{B_H}} = X_H - m_H g \sin \theta_H$$

$$Q_{Y_{B_H}} = Y_H + m_H g \cos \theta_H \sin \Phi_H$$

$$Q_{Z_{B_H}} = Z_H + m_H g \cos \theta_H \cos \Phi_H$$

$$Q_{p_H} = L_H$$

$$Q'_{p_H} = Q_{p_H} + I_{XZ_H}\, p_H\, q_H - (I_{ZZ_H} - I_{YY_H})\, q_H\, \Gamma_H$$

$$Q_{q_H} = M_H$$

$$Q'_{q_H} = Q_{q_H} - I_{XZ_H}\, (p_H^2 - \Gamma_H^2) - (I_{XX_H} - I_{ZZ_H})\, \Gamma_H\, p_H$$

$$Q_{\Gamma_H} = N_H$$

$$Q'_{\Gamma_H} = Q_{\Gamma_H} - I_{XZ_H}\, q_H\, \Gamma_H - (I_{YY_H} - I_{XX_H})\, p_H\, q_H$$

$$Q_{X_{B_L}} = X_L - m_L\, g \sin \theta_L$$

$$Q_{Y_{B_L}} = Y_L + m_L\, g \cos \theta_L \sin \Phi_L$$

$$Q_{Z_{B_L}} = Z_L + m_L\, g \cos \theta_L \cos \Phi_L$$

$$Q_{p_L} = L_L$$

$$Q'_{p_L} = Q_{p_L} + I_{XZ_L}\, p_L\, q_L - (I_{ZZ_L} - I_{YY_L})\, q_L\, \Gamma_L$$

$$Q_{q_L} = M_L$$

$$
\begin{aligned}
Q'_{q_L} &= Q_{q_L} + I_{XZ_L}\,(p_L^2 - r_L^2) - (I_{XX_L} - I_{ZZ_L})\, r_L\, p_L \\
Q_{r_L} &= N_L \\
Q'_{r_L} &= Q_{r_L} - I_{XZ_L}\, q_L\, r_L - (I_{YY_L} - I_{XX_L})\, p_L\, q_L
\end{aligned} \tag{37}
$$

where X_H, Y_H, Z_H, L_H, M_H, and N_H represent the forces and moments exerted on the helicopter from such things as fuselage aerodynamics, rotor thrust, and rotor hub moments. X_L, Y_L, Z_L, L_L, M_L, and N_L represent the forces and moments exerted on the external load from such things as load aerodynamics.

The preceding formulation is valid for all motions of the helicopter and load if we assume rigid cables. This is true since the λ's will always be calculated to maintain the distance from hook to attachment point constant. In other words, if there arose a situation in which the forces on the load were such that the tendency would be for the attachment point to move closer to the hook, the cables, through the λ's, would exert a compressive force to maintain the distance at cable length. To allow for flexible cables, we must eliminate constraint equations when cable forces become compressive. This is done by simply setting the λ's to the maximum compressive force assumed for the cables (for noncompressive cables, the λ's are set to zero). Thus, any degree of rigidity of the cables may be assumed.

Thus, the problem of allowing the cables to go slack is easily handled. The problem of returning the cables to tension when the conditions call for it is somewhat more complicated. The complication arises because we cannot suddenly begin the λ's calculation at some instant in time without assuring that the velocities of the helicopter and load conform to the constraint equations. To solve this problem, we must reinitialize the helicopter and load velocities and rotations at the instant the cables become taut. We do this by applying impulse-momentum theory. The mathematical expression that we will use to relate the velocities before tautness to after tension is returned is

$$
\left(\frac{\partial L}{\partial \dot{q}_j}\right)_f - \left(\frac{\partial L}{\partial \dot{q}_j}\right)_o = I_j \tag{38}
$$

In this expression, $(\partial L/\partial \dot{q}_j)_f$ represents the momentum after impulse in the direction of the q_j variable, while $(\partial L/\partial \dot{q}_j)_o$ represents the momentum before impulse in the q_j direction, and I_j represents the component of the impulse in the q_j direction.

In terms of our specific problem, we have

$$(1)\quad m_H \dot{X}_{B_{H_f}} - m_H \dot{X}_{B_{H_o}} = a_{11}I_1 + a_{12}I_2$$

$$(2)\quad m_H \dot{Y}_{B_{H_f}} - m_H \dot{Y}_{B_{H_o}} = a_{21}I_1 + a_{22}I_2$$

$$(3)\quad m_H \dot{Z}_{B_{H_f}} - m_H \dot{Z}_{B_{H_o}} = a_{31}I_1 + a_{32}I_2$$

$$(4)\quad (I_{XX_H} P_{H_f} - I_{XZ_H} \Gamma_{H_f}) - (I_{XX_H} P_{H_o} - I_{XZ_H} \Gamma_{H_o}) = a_{41}I_1 + a_{42}I_2$$

$$(5)\quad I_{YY_H} q_{H_f} - I_{YY_H} q_{H_o} = a_{51}I_1 + a_{52}I_2$$

$$(6)\quad (I_{ZZ_H} \Gamma_{H_f} - I_{XZ_H} P_{H_f}) - (I_{ZZ_H} \Gamma_{H_o} - I_{XZ_H} P_{H_o}) = a_{61}I_1 + a_{62}I_2$$

$$(7)\quad m_L \dot{X}_{B_{L_f}} - m_L \dot{X}_{B_{L_o}} = a_{71}I_1 + a_{72}I_2$$

$$(8)\quad m_L \dot{Y}_{B_{L_f}} - m_L \dot{Y}_{B_{L_o}} = a_{81}I_1 + a_{82}I_2$$

$$(9)\quad m_L \dot{Z}_{B_{L_f}} - m_L \dot{Z}_{B_{L_o}} = a_{91}I_1 + a_{92}I_2$$

$$(10)\quad (I_{XX_L} P_{L_f} - I_{XZ_L} \Gamma_{L_f}) - (I_{XX_L} P_{L_o} - I_{XZ_L} \Gamma_{L_o}) = a_{10,1}I_1 + a_{10,2}I_2$$

$$(11)\quad I_{YY_L} q_f - I_{YY_L} q_{L_o} = a_{11,1}I_1 + a_{11,2}I_2$$

$$(12)\quad (I_{ZZ_L} \Gamma_{L_f} - I_{XZ_L} P_{L_f}) - (I_{ZZ_L} \Gamma_{L_o} - I_{XZ_L} P_{L_o}) = a_{12,1}I_1 + a_{12,2}I_2 \qquad (39)$$

Since we know the velocities and rotations before the impulse, $\dot{X}_{B_{H_o}}$, $\dot{Y}_{B_{H_o}}$, . . ., Γ_{L_o}, and if we assume that the direction coefficients, a_{11}, a_{12}, . . ., $a_{12,2}$, do not change during the impulse, we see that we have 12 equations in 14 unknowns. However, the final velocities and rotations, $\dot{X}_{B_{H_f}}$, $\dot{Y}_{B_{H_f}}$, . . ., Γ_{L_f}, must conform to the following constraint equations:

$$(13)\quad a_{11}\dot{X}_{B_{H_f}} + a_{21}\dot{Y}_{B_{H_f}} + \cdots + a_{11,1}q_{L_f} + a_{12,1}\Gamma_{L_f} = 0$$

$$(14)\quad a_{12}\dot{X}_{B_{H_f}} + a_{22}\dot{Y}_{B_{H_f}} + \cdots + a_{11,2}q_{L_f} + a_{12,2}\Gamma_{L_f} = 0$$

(39)

Thus, we have a system of 14 equations in 14 unknowns which can readily be solved.

When the external load is restrained within the hull of a stationary ship, the following equations are superimposed:

$$\dot{X}_{B_L} = \dot{Y}_{B_L} = P_L = q_L = \Gamma_L = 0$$

$$a_{71} = a_{81} = a_{10,1} = a_{11,1} = a_{12,1} = 0$$

$$a_{72} = a_{82} = a_{10,2} = a_{11,2} = a_{12,2} = 0$$

$$Q_{X_{B_L}} = Q_{Y_{B_L}} = Q_{P_L} = Q_{q_L} = Q_{\Gamma_L} = 0 \qquad (40)$$

Elastic Cable Formulation

The preceding derivation for inelastic cables can easily be modified to handle elastic cables. In fact, the calculations are somewhat shortened. The difference arises in that for the inelastic cables, we forced $\dot{L}_1 = \dot{L}_2 = 0$; and by doing this, we were able to define two additional system equations relating helicopter and load motions. With these two additional L equations, we were able to calculate the necessary restraining tensions (λ_1, λ_2).

In the case of elastic cables, we allow the distance between hook and attachment point to vary, as if helicopter and load were two completely independent free bodies. We then measure

the distance between hook and attachment point and the rate of change of this difference, exactly as we did for the inelastic cable case; that is,

$$\dot{L}_1 = \dot{R}_{X_{I_1}} \cos \gamma_3 \sin \gamma_1 + \dot{R}_{Y_{I_1}} \sin \gamma_3 + \dot{R}_{Z_{I_1}} \cos \gamma_3 \cos \gamma_1$$

$$\dot{L}_2 = \dot{R}_{X_{I_2}} \cos \gamma_4 \sin \gamma_2 + \dot{R}_{Y_{I_2}} \sin \gamma_4 + \dot{R}_{Z_{I_2}} \cos \gamma_4 \cos \gamma_2$$

However, unlike the inelastic case where the λ's were calculated as necessary internal restraining forces, the λ's for the elastic cable case are calculated directly from L_1, L_2, $\dot{L}_1$, and $\dot{L}_2$ and the physical properties of the cables. If we assume that the cables will exert a force proportional to change in length and rate of change in length, then we can calculate the λ's in tension as

$$(1) \quad \lambda_1 = -k_{T_1} \Delta L_1 - C_{T_1} \dot{L}_1$$

$$(2) \quad \lambda_2 = -k_{T_2} \Delta L_2 - C_{T_2} \dot{L}_2$$

and in compression as

$$(3) \quad \lambda_1 = -k_{C_1} \Delta L_1 - C_{C_1} \dot{L}_1$$

$$(4) \quad \lambda_2 = -k_{C_2} \Delta L_2 - C_{C_2} \dot{L}_2 \qquad (41)$$

where k_{T_1}, k_{T_2}, k_{C_1}, and k_{C_2} are cable spring constants; C_{T_1}, C_{T_2}, C_{C_1}, and C_{C_2} are cable damping rates.

Once these λ's are calculated, the procedure is the same as for the inelastic case.

Digital Computer Mechanization of External Load Equations

The sling load equations were programmed on the IBM 360-65. Numerical integration of these helicopter and load accelerations was performed using fourth-order Runge-Kutta methods. The following is a brief description of the segments of this program, indicating one possible sequence of calculations.

1. Main Routine - Executive program used to read in physical parameters of helicopter and load, set up initial conditions, set up integration cycle, and plot output.

2. Trim Subroutine - Subroutine called from main program during setting up of initial conditions.

3. TENSNS Subroutine - Subroutine called from main program during integration cycle to calculate cable tensions.

4. Impact Subroutine - Subroutine called from main program during integration cycle if either or both cables are going from slack condition to taut condition. This subroutine calculates helicopter and load velocities and rotations after tautness occurs, based on conditions just before tautness.

5. RKS Subroutine - Subroutine employing fourth-order Runge-Kutta method to numerically integrate our equations of motion. Subroutine is called from main program during integration cycle.

6. Plot Subroutine - Subroutine called by main program to plot output data on-line on the IBM 360-65.

APPENDIX II
PARAMETRIC HELICOPTER DATA

The turbulence is represented as random perturbations in longitudinal and lateral velocity. The response of a linear system to a random input, in terms of power spectra, is

$$P_o(\omega) = |G(j\omega)|^2 P_I(\omega)$$

where $G(s)$ is the transfer function of the system

$P_I(\omega)$, $P_o(\omega)$ are the power spectrums of the input and output, respectively

The mean-square response of the output is

$$\bar{v}_o^2 = \frac{1}{2\pi} \int_{-\infty}^{\infty} P_o(\omega)\, d\omega = \frac{1}{2\pi} \int_{-\infty}^{\infty} |G(j\omega)|^2 P_I(\omega)\, d\omega$$

As an example, suppose it is desired to calculate the mean-square longitudinal position error response to a one-dimensional gust, assuming the following gust spectrum:

$$P_I(\omega) = \frac{2\sigma g^2 \omega_N}{\omega^2 + \omega_N^2}$$

where ω_N is gust break frequency

σg is the standard deviation of gust

The desired system transfer function is

$$G(s) = \frac{X_e}{U_g}(s)$$

and the resultant mean-square position error response is

$$x_e^2 = \frac{1}{2\pi} \int_{-\infty}^{\infty} \left| \frac{X_e}{Ug} (j\omega) \right|^2 \frac{2\,\sigma g^2\,\omega_N}{\omega^2 + \omega_N^2}\, d\omega$$

To perform this analysis and also to determine the stability of the system in terms of eigenvalues, phase margin, etc., a digital program was written with the following options.

Calculations of

(1) Eigenvalues and eigenvectors of state matrix.

(2) Zeroes and poles of desired transfer function, including elimination of like poles and zeroes.

(3) Frequency response of transfer function.

(4) Inverse Laplace coefficients of transfer function.

(5) Time response of transfer function to random disturbance (turbulence).

APPENDIX III
SUMMARY OF SIMULATOR EVALUATION DATA

This appendix presents the simulator evaluation run log (Table XIX), and includes the list of all runs which were directly used to obtain the quantitative and the qualitative data summarized in the main sections of this report.

TABLE XIX. ATH SIMULATION LOG

Date 6-27-73
Configuration 50,000 Lb

Constants: A/C Gr Wt 50,000 Lb
External Load None
Wind 10 KT

Notes: Turbulence Level is Ug and Vg.
Wg = 0 For All Runs

Run No.	PHS Status			Control Type		Load Stabiliz. System	Turbul. Level FPS RMS	Pilot Task	Pilot Comments	Remarks	#3 Tape File No.	X-Y Plot	Calculated Results						
	Long.	Vert.	Lat.	Long.	Lat.								K_P	T_L	Posn. Rms Long.	Posn. Rms Lat.	Pilot Sta Acc. Long.	Pilot Sta Acc. Vert.	Pilot Sta Acc. Lat.
1	ON	ON	ON	PHS	PHS	OFF	0.0	None			1	OFF							
2	↓	↓	↓	PHS	PHS	OFF	None	None	Pilot out (hands off)	Initial Digital Record (No Display)	2	OFF							
3										Repeated	3	OFF							
4				PHS	PHS					Repeated	4	OFF							
5								None		With $G_{SPO} = 0$	-	OFF							
6								Ltr	4 C-H	$G_{SPO} = 0$	-	ON							
7	ON		ON					Ctr			-	ON							
8	OFF		OFF	1	0	OFF	0	None	Pilot out		5	ON							
9	↓		↓	1	0	OFF	0	Ctr			-	ON							
10				1	0	OFF	0	HH	7 C-H		6	ON							
11				1	0	OFF	5.0	HH			7	ON							
12				1	0	OFF					-	OFF							
13				1	0	OFF	5.0	HH	7-8 CH		8	ON							
14		↓		1	0	OFF	10.0	HH			9	ON							
15		ON		1	0	OFF	10.0	HH		Concentrated On Long. Position	10	ON							
16		OFF		2	0	OFF	0	HH		Pilot Feeling Out The System	-	ON							
17		OFF		2	0	OFF	0	HH			12	ON							
18		ON		2	0	OFF	5.0	HH	8 C-H Difficult to Control		12	ON							
19	OFF	ON	OFF	2	0	OFF	5.0	HH	Uncontrol-lable		13	OFF							

Intermittent Loss Of Horz. Position Feedback When Ever Pilot Released The Stick

TABLE XIX. ATH SIMULATION LOG (Continued)

Date 6-27-73
Configuration 50,000 Lb

Constants: A/C Gr Wt 50,000 Lb
External Load None
Wind 10 KT

Notes:

Run No.	PHS Status			Control Type		Load Stabiliz. System	Turbul. Level FPS RMS	Pilot Task	Pilot Comments	Remarks	#3 Tape File No.	X-Y Plot	Calculated Results						
	Long.	Vert.	Lat.	Long.	Lat.								K_P	T_L	Posn. Rms Long.	Posn. Rms Lat.	Pilot Sta Acc. Long.	Pilot Sta Acc. Vert.	Pilot Sta Acc. Lat.
20	OFF	ON	OFF	1	1	OFF	0.	HH	6 CH		14	ON							
21	↓	↓	↓	1	1		5.0	HH			15	ON							
22				1	1	OFF	10.0	HH			16	ON							
23				1	1		0	CTR		3RD CTR Recorded In File 18	17	ON							
24				1	2	OFF	0	HH/CTR	5 C-H Good Control Harmony	Trial 1, Recorded On Digital - Trial 2, X-Y	18	ON							
25				1	2	OFF	5.0	HH			19	ON							
26				1	2	OFF	10.0	HH			20	ON							
27				5	1	OFF	0	(Hands Off)		20 Sec Initial Data Run	21	OFF							
28				5	1	OFF	0	HH			23	OFF							
29				5	1	OFF	5.0	HH			23	OFF							
30				5	1	OFF	10.0	HH		Lost Control Soon After Gust Came In	24	OFF							
31				5	1	OFF	10.0	HH			25	OFF							
32				5	1	OFF	0	CTR	Lat. Too Sensitive		26	OFF							
33				5	1	OFF	5	CTR			-								
34				5	1	OFF	10	CTR			-								
35				5	1	OFF	10	HH	Motion Gives Good Cues	Fixed Base Runs	27	ON							
36	↓					OFF	5	HH		Fixed Base Run	28	ON							
37	OFF	↓	OFF			OFF	5	HH		Moving Base	29	ON							
38	ON	ON	ON	PHS	PHS	OFF	0	CTR		G_{SPO}= 0.0 Moving Base, Stick Detent = .2" For All Subsequent Runs	-	ON							

TABLE XIX. ATH SIMULATION LOG (Continued)

Date 6-27-73
Configuration 50,000 LB

Constants: A/C Gr Wt 50,000 Lb
External Load None
Wind 10 KT

Notes: _____

Run No.	PHS Status			Control Type		Load Stabiliz. System	Turbul. Level FPS RMS	Pilot Task	Pilot Comments	Remarks	#4 Tape File No.	X-Y Plot	Calculated Results						
	Long.	Vert.	Lat.	Long.	Lat.								K_p	T_L	Posn. Rms Long.	Posn. Rms Lat.	Pilot Sta Acc. Long.	Pilot Sta Acc. Vert.	Pilot Sta Acc. Lat.
39	ON	ON	ON	PHS	PHS		5.0	HH			1								
40	↓	↓	↓	↓	↓		10.0	HH			2								
41							10.0	CTR			3	OFF							
42							10.0	CTR	4 C-H		-	ON							
43	ON	ON	ON	PHS	PHS		15.0	HH			4								
44							15.0	CTR			5								

TABLE XIX. ATH SIMULATION LOG (Continued)

Date 7-3-73
Configuration 50,000 Lb

Constants: A/C Gr Wt 50,000 Lb
External Load None
Wind 10-Knot Headwind

Notes: Turbulence Level = Ug and Vg Only

Run No.	PHS Status			Control Type		Load Stabiliz. System	Turbul. Level FPS RMS	Pilot Task	Pilot Comments	Remarks	05 Tape File No.	X-Y Plot	Calculated Results						
	Long.	Vert.	Lat.	Long.	Lat.								K_p	T_L	Posn. Rms		Pilot Sta Acc.		
															Long.	Lat.	Long.	Vert.	Lat.
1	ON	ON	ON	PHS	PHS	OFF	5.0	None		Initial Data Run (20 Sec)	1	OFF							
2	↓	↓	↓	↓	↓	↓	5.0	None	Not Much Motion		2	OFF							
3							10.0	None			3	OFF							
4							15.0	None	Good Realistic Motion		4	ON							
5/6	ON		ON	PHS	PHS		0.	CTR	3.0 C-H	Same CTR Repeated No Data Taken For 6.	5	ON/ OFF							
7	OFF		OFF	1	2		0.	CTR	5.0 C-H	Difficult To Control In Longitudinal	6	ON							
8							0.	CTR		(Bombed Out)	7								
9							0.	CTR	Pitch Axes Much Improved 4.0 GH	$K_{X\ BP\ X}\ ^{1}/_{2}$	8								
10							5.	CTR			9								
11							10.	HH	Display Too Small Hanges Up On Sides		10								
12					1	2	5.	CTR	Difficult To Control		11								
13					5	1	0.	CTR	Good Control Balance 3.0 GH	Two CTR Runs, No Records On The Second Run	12								
14							5.0	HH	Good Same Setting		13								
15							10.0	HH	Good Harmony Harder Task, No. Degradation in Control		14								

TABLE XIX. ATH SIMULATION LOG (Continued)

Date 7-3-73
Configuration 50,000 Lb

Constants: A/C Gr Wt 50,000 Lb
External Load None
Wind 10-Knot Headwind

Notes: Turbulence Level = Ug and Vg Only

Run No.	PHS Status			Control Type		Load Stabiliz. System	Turbul. Level FPS RMS	Pilot Task	Pilot Comments	Remarks	#5 Tape File No.	X-Y Plot	Calculated Results						
	Long.	Vert.	Lat.	Long.	Lat.								K_P	T_L	Pcon. Rms Long.	Pcon. Rms Lat.	Pilot Sta Acc. Long.	Pilot Sta Acc. Vert.	Pilot Sta Acc. Lat.
16							15.0	HH	More Difficult To Control No System Degradation		15								
17							5.0	CTR			16								
18							10.0	CTR			17								
19							10.0	HH			18								
20	OFF	ON	OFF	5	1	OFF	15.0	HH			19	ON							